Small Signal Analysis of Converter-Dominated Power Systems

vorgelegt von
M. Sc.
Huoming Yang
ORCID: 0000-0003-3518-5992

an der Fakultät IV - Elektrotechnik und Informatik
der Technischen Universität Berlin
zur Erlangung des akademischen Grades

Doktor der Ingenieurwissenschaften
-Dr.-Ing.-

genehmigte Dissertation

Promotionsausschuss:

Vorsitzender:	Prof. Dr.-Ing. Uwe Schäfer
Gutachterin:	Prof. Dr.-Ing. Sibylle Dieckerhoff
Gutachter:	Prof. Dr. ir. Dr. h. c. Rik W. De Doncker
Gutachter:	Prof. Keyou Wang, PhD

Tag der wissenschaftlichen Aussprache: 30. August 2022

Berlin 2022

Abstract

The legacy power systems are dominated by synchronous generators providing inertia support, frequency and voltage regulation capabilities. The linear time-invariant (LTI) modal analysis has been widely and successfully applied to their small-signal models for the stability and resonance evaluation. Driven by concerns about global climate changes, the modern power system is undergoing the transition in generation technology from fossil fuel-based generation to renewable generation. The number of power electronic converters used for the integration of renewable energy sources has gradually increased to a significant level. The multiple-timescale control loops of converters cause cross interactions with dynamics of loads and power networks. Moreover, frequency coupling effects caused by converter controllers, the pulse-width modulation process and unbalanced operation conditions further increase the system complexity, which makes the modern converter-dominated power grids become complex nonlinear time-periodic (NLTP) systems. The classical LTI theory based modeling, analysis and design approaches become frangible and less valid.

To precisely describe dynamics of converter-dominated power systems operated under different conditions, a linear time-periodic (LTP) modeling framework is developed in the complex-valued domain. The classical modal analysis for the LTI system is generalized to the LTP system. Accordingly, definitions and expressions of damping ratio, participation factor and eigenvalue sensitivity are modified. A time-domain physical interpretation of the LTP system is proposed to quantitatively confirm the necessity of its application. Two accurate and efficient LTP eigenvalue calculation methods are developed, paving the way for easier application of LTP theory. The proposed stability analysis method has been tested with grid-following converter to investigate the interaction between different phase-locked loops, current controllers and power networks on the system stability, and with grid-forming converter to investigate the interaction between its outer power loop and inner voltage-current loop.

To evaluate the impact of integration of converters on harmonic resonances of future power systems, analytical closed form of the harmonic transfer matrix (HTM) is deduced to describe the relation between Fourier series coefficients of inputs and outputs of the LTP system. The classical resonance mode analysis (RMA) is generalized by replacing the constant system impedance matrix with a time-periodic matrix obtained from the reformulation of the HTM. The LTP modal analysis leads to the extension of the participation analysis and the sensitivity analysis for resonance frequency identification and resonance severity evaluation of LTP systems. The proposed method is tested with an exemplary multiple-converter system to investigate the impact of the converter controller, the LCL filter and the passive network on the resonance behavior, considering balanced and unbalanced operation conditions.

Generalized eigenvalue sensitivity and participation factor analysis provides guidelines for the control parameter and structure optimization of the LTP system. A linear programming problem is formulated by using eigenvalue and damping ratio sensitivity indices to shift critical eigenvalues towards the left-half of the complex plane without degrading the damping performance. Moreover, auxiliary damping loop is designed based on participation analysis results to extend stability margins. The theoretical analysis is confirmed by cross-validation between stability and resonance evaluation results obtained from numerical models, analytical models and hardware measurements.

Zusammenfassung

Das konventionelle Stromnetz wird von Synchrongeneratoren dominiert, die Trägheitsunterstützung, Frequenz- und Spannungsregelung bieten. Die lineare zeitinvariante (*engl.*: linear time-invariant, LTI) Modalanalyse wurde weithin und erfolgreich auf ihre Kleinsignalmodelle für die Stabilitäts- und Resonanzbewertung angewandt. Vor dem Hintergrund der globalen Klimaveränderung vollzieht sich in modernen Stromnetzen ein technologischer Wandel von der Stromerzeugung aus fossilen Brennstoffen hin zur Stromerzeugung aus erneuerbaren Energien. Die Zahl der leistungselektronischen Umrichter, die für die Integration erneuerbarer Energiequellen eingesetzt werden, hat allmählich ein signifikantes Ausmaß erreicht. Die mehrstufigen Regelkreise von Umrichtern verursachen Wechselwirkungen mit der Dynamik von Lasten und Stromnetzen. Darüber hinaus erhöhen Frequenzkopplungseffekte, die durch Umrichterregler, den Pulsbreitenmodulationsprozess und unsymmetrische Betriebsbedingungen verursacht werden, die Systemkomplexität weiter, wodurch die modernen, von Umrichtern dominierten, Stromnetze zu komplexen nichtlinearen zeitperiodischen (*engl.*: nonlinear time-periodic, NLTP) Systemen werden. Die klassischen, auf der LTI-Theorie, basierenden Modellierungs-, Analyse- und Entwurfsansätze werden angreifbar und verlieren an Gültigkeit.

Um die Dynamik von umrichterdominierten Stromnetzen, die unter verschiedenen Bedingungen betrieben werden, genau zu beschreiben, wird ein linearer zeitperiodischer (*engl.*: linear time-periodic, LTP) Modellierungsrahmen im komplexwertigen Bereich entwickelt. Die klassische Modalanalyse für das LTI-System wird auf das LTP-System verallgemeinert. Dementsprechend werden die Definitionen und Ausdrücke des Dämpfungsgrads, des Partizipationsfaktors und der Eigenwertsensitivität modifiziert. Es wird eine physikalische Interpretation des LTP-Systems im Zeitbereich vorgeschlagen, um die Notwendigkeit seiner Anwendung quantitativ zu bestätigen. Es werden zwei genaue und effiziente LTP-Eigenwertberechnungsmethoden entwickelt, die den Weg für eine einfachere Anwendung der LTP-Theorie ebnen. Die vorgeschlagene Stabilitätsanalysemethode wurde mit netzfolgenden Umrichtern getestet, um die Wechselwirkung zwischen verschiedenen Phasenregelkreisen, Stromreglern und Stromnetzen auf die Systemstabilität zu untersuchen, und mit netzbildenden Umrichtern, um die Wechselwirkung zwischen dem äußeren Leistungsregelkreis und dem inneren Spannungs-Strom-Regelkreis zu untersuchen.

Um die Auswirkungen der Integration von Umrichtern auf die harmonischen Resonanzen künftiger Stromnetzen zu bewerten, wird eine analytisch geschlossene Form der harmonischen Übertragungsmatrix (*engl.*: harmonic transfer matrix, HTM) abgeleitet, um die Beziehung zwischen den Fourierkoeffizienten der Ein- und Ausgänge des LTP-Systems zu beschreiben. Die klassische Resonanzmodenanalyse (*engl.*: resonance mode analysis, RMA) wird verallgemeinert, indem die konstante Systemimpedanzmatrix durch eine zeitperiodische Matrix ersetzt wird, die

sich aus der Umformulierung der HTM ergibt. Die LTP-Modalanalyse führt zu einer Erweiterung der Partizipationsanalyse und der Sensitivitätsanalyse zur Identifizierung der Resonanzfrequenz und zur Bewertung des Einflusses dieser Resonanzfrequenzen. Die vorgeschlagene Methode wird mit einem beispielhaften Mehrfachumrichtersystem getestet, um die Auswirkungen des Umrichterreglers, des LCL-Filters und des passiven Netzwerks auf das Resonanzverhalten zu untersuchen, wobei symmetrische und unsymmetrische Betriebsbedingungen berücksichtigt werden.

Die verallgemeinerte Eigenwertsensitivitäts- und Partizipationsfaktoranalyse liefert Leitlinien für die Optimierung der Regelparameter und der Struktur des LTP-Systems. Ein lineares Programmierproblem wird unter Verwendung von Eigenwert- und Dämpfungsgrad-Sensitivitätsindizes formuliert, um kritische Eigenwerte in Richtung der linken Halbebene zu verschieben, ohne die Dämpfungsleistung zu verschlechtern. Darüber hinaus wird auf der Grundlage der Ergebnisse der Partizipationsanalyse eine Hilfsdämpfungsschleife entworfen, um die Stabilitätsbereiche zu erweitern. Die theoretische Analyse wird durch eine Kreuzvalidierung von Stabilitäts- und Resonanzbewertungsergebnissen aus numerischen Modellen, analytischen Modellen und Hardwaremessungen bestätigt.

Acknowledgement

First, I would like to express my most sincere gratitude to my supervisor Prof. Sibylle Dieckerhoff, for offering me the chance to pursue my PhD at FG Leistungselektronik and for her trust and support in the sharpening and realization of my research ideas. Her enthusiasm and attitude towards research have always inspired me to develop critical thinking and conduct meticulous researches with high motivations. I am also grateful for her understanding and encouragement, allowing me to explore possibilities for the next step in my career.

I would like to thank Prof. Keyou Wang with Shanghai Jiao Tong University and Prof. Rik W. De Doncker with RWTH Aachen University for their interest in my work and for taking the time to evaluate it.

In addition, I want to thank all my colleagues at FG Leistungselektronik. I feel very lucky to be part of this great team. The time we spent together, Mensa lunches, coffee breaks, department trips and technical conferences, etc. will all be treasured memories for me. Special thanks go to our Netzgruppe for sharing your experience with hardware, so that I can avoid the risk of learning from explosions.

Last but not least, I want to thank my parents for their understanding and mental support. Though they know very little about my research, they are always willing to listen to my ups and downs. Their unconditional love is my power source during these stressful academic years.

Huoming
Berlin, September 2022

Table of Contents

Glossary of Acronyms

DDSRF-PLL decoupled double synchronous reference frame 14

DP dynamic phasor 9

DSOGI-PLL dual second order generalized integrator PLL 20

DSRF-PLL dual synchronous reference frame PLL 20

EHD extended harmonic domain 9

FLL frequency-locked loop 5

FSA frequency scanning analysis 15

GA generalized averaging 8

GFL grid-following 5

GFM grid-forming 5

HSS harmonic state-space 10

HTM harmonic transfer matrix 10

LPF low-pass filter 21

LTI linear time-invariant 2

LTP linear time-periodic 6

NLTP nonlinear time-periodic 8

OAT one-at-a-time 116

PHIL power-hardware-in-the-loop 47

PI proportional-integral 21

PLL phase-locked loop 5

PoC point of connection 5

PR proportional-resonant 21

PSCD positive-sequence component detector 22

PWM pulse-width modulation 6

RMA resonance mode analysis 15

SCR short-circuit ratio 20

SG synchronous generator 5

SRF-PLL synchronous reference frame PLL 7

VSC voltage source converter 19

VSG virtual synchronous generator 27

1

Introduction

1.1 Motivation and Objectives

The conventional power system is dominated by fossil fuel and nuclear power generation. The growth in electricity consumption brings increased greenhouse gas emissions and the risk of nuclear power plant accidents [1], which force people to reconsider the energy structure. To achieve efficient, safe and environmentally friendly energy generation and use, renewable generation technologies (e.g., photovoltaic and wind energy systems) are considered promising solutions. In Figure 1.1, it can be observed that electricity production with renewable sources in Germany is gradually replacing coal-based and nuclear-based generation. The overall ambition is to achieve a 100% renewable German energy system by 2050 [2].

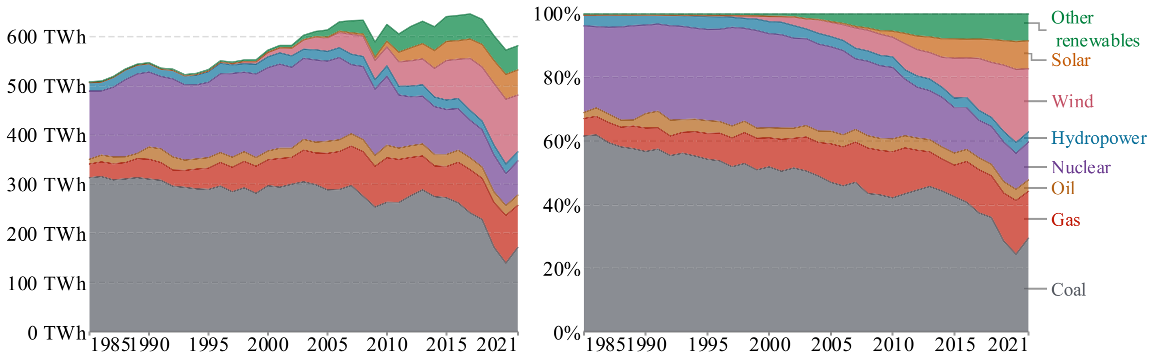

Figure 1.1: Electricity production in Germany by sources [3]

With the increasing share of renewable based power generation, the large synchronous generators providing rotational inertia, frequency and voltage stability are gradually replaced with power electronics converters with small time constants but flexible and fast control properties. The control flexibility facilitates converters to emulate dynamics of the synchronous generators. However, physical differences, such as limited energy storage capacity and overcurrent withstand capability, make it still difficult for converters to fully shoulder the frequency and voltage regulation responsibilities in all operation conditions. The multi-timescale control loops of converters can interact with the dynamics of loads, synchronous generators and the electric network, which brings unexpected harmonics, resonances or even instability over a wide frequency range. Those unique characteristics of converters raise new challenges to the stability of future converter-dominated/only power systems (see Figure 1.2). Moreover, the time-periodic steady-state operation trajectory caused by unbalanced conditions and switching frequency harmonics makes the classical linear time-invariant (LTI) theory based modeling, analysis and design approaches become frangible and less valid.

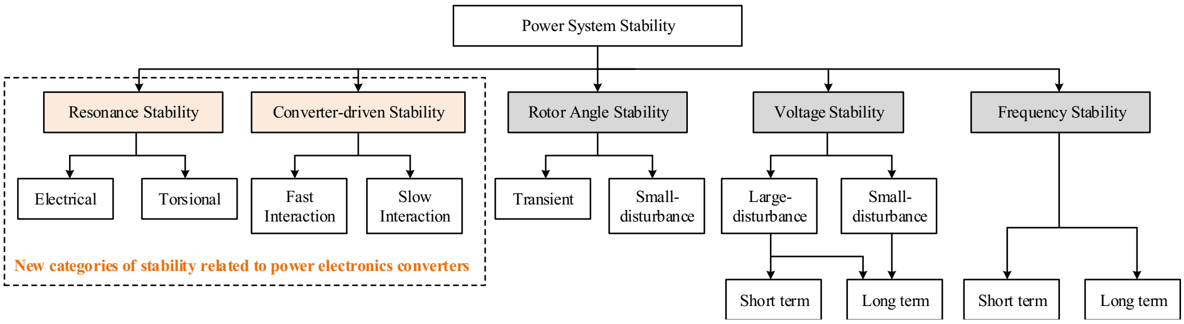

Figure 1.2: Extended classification of power system stability [4]

To pave the way towards converter-dominated or even converter-only power systems, this thesis aims to develop efficient and accurate modeling and stability analysis methods to reveal instability mechanisms and develop countermeasures. The main objectives are summarized as follows:

- *Develop a modular analytical and numerical modeling framework for converter-dominated power systems considering different types of converters and operation conditions.*
- *Develop small-signal stability and resonance analysis methods to evaluate the impact of high penetration levels of converters on dynamics of future power systems.*
- *Develop control parameters and structures optimization methods to improve system stability margins and damping performance.*

1.2 Thesis Structure

This thesis is composed of seven chapters:

- **Chapter 1** is the Introduction.
- **Chapter 2** reviews the state-of-the-art modeling, stability and resonance analysis methods for converter-dominated power systems, after which the main contributions of this thesis are clarified.
- In **Chapter 3**, the nonlinear average models of different converters, loads and power networks are developed in the complex value domain. Then, steady-state power flow analysis and small-signal linearization techniques are proposed to build a modular and flexible numerical and analytical modeling framework. A general description of the software platform and hardware test setup is given.

- **Chapter 4** generalizes the classical modal analysis for linear-time periodic small-signal models of the converter-dominated power systems. Stability analysis, damping ratio analysis, participation factor analysis and eigenvalue sensitivity analysis are performed to evaluate the dynamic performance of different types of power converters.
- **Chapter 5** focuses on the impact of high penetration levels of converters on resonance characteristics of modern power systems.
- In **Chapter 6**, the aforementioned analytical methods are used as design-oriented tools to guide the optimization of control parameters and structures to improve stability margins and damping performance of different converter systems.
- **Chapter 7** concludes this thesis.

1.3 List of Publications

The journal and conference publications originating from this thesis are:

- **H. Yang**, H. Just, M. Eggers and S. Dieckerhoff, "Linear Time-Periodic Theory-Based Modeling and Stability Analysis of Voltage-Source Converters," in *IEEE Journal of Emerging and Selected Topics in Power Electronics*, vol. 9, no. 3, pp. 3517-3529, June 2021, DOI: 10.1109/JESTPE.2020.3003379.
- **H. Yang**, M. Eggers, H. Just, P. Teske and S. Dieckerhoff, "Linear Time-Periodic Theory-Based Harmonic Resonance Analysis of Converter-Dominated Power System," in *IEEE Journal of Emerging and Selected Topics in Power Electronics*, vol. 9, no. 6, pp. 7422-7435, Dec. 2021, DOI: 10.1109/JESTPE.2020.3041945.
- **H. Yang** and S. Dieckerhoff, "Truncation Order Selection Method for LTP-Theory-Based Stability Analysis of Converter Dominated Power Systems," in *IEEE Transactions on Power Electronics*, vol. 36, no. 11, pp. 12168-12172, Nov. 2021, DOI: 10.1109/TPEL.2021.3076877.
- **H. Yang**, M. Eggers, P. Teske and S. Dieckerhoff, "Comparative Stability Analysis and Improvement of Grid-Following Converters using Novel Interpretation of Linear Time-Periodic Theory," *IEEE Journal of Emerging and Selected Topics in Power Electronics*, early access, 2022, DOI: 10.1109/JESTPE.2022.3194411.
- **H. Yang**, M. Eggers, P. Teske and S. Dieckerhoff, "Modeling and Stability Analysis of Converter-Dominated Grids with Dynamic Loads," *2021 6th IEEE Workshop on the Electronic Grid (eGRID)*, 2021, pp. 01-07, DOI: 10.1109/eGRID52793.2021.9662151.
- **H. Yang**, H. Just, M. Eggers and S. Dieckerhoff, "Modeling and Stability Analysis of Grid-Following Voltage-Source Converters Utilizing Individual Channel Design Method," *2020 IEEE 21st Workshop on Control and Modeling for Power Electronics (COMPEL)*, 2020, pp. 1-6, DOI: 10.1109/COMPEL49091.2020.9265666.

- **H. Yang**, H. Just, M. Eggers and S. Dieckerhoff, "Wirtinger Calculus Based Modeling and Analysis of VSG-Dominated Grids," *2020 IEEE 21st Workshop on Control and Modeling for Power Electronics (COMPEL)*, 2020, pp. 1-6, DOI: 10.1109/COMPEL49091.2020.9265753.

- **H. Yang** and S. Dieckerhoff, "Modeling and Stability Analysis of Advanced PLLs Based on LTP Theory," *2019 21st European Conference on Power Electronics and Applications (EPE '19 ECCE Europe)*, 2019, pp. P.1-P.10, DOI: 10.23919/EPE.2019.8915382.

- **H. Yang**, H. Just and S. Dieckerhoff, "Identification of Critical Parameters Affecting the Small-Signal Stability of Converter-based Microgrids," *2019 20th Workshop on Control and Modeling for Power Electronics (COMPEL)*, 2019, pp. 1-6, DOI: 10.1109/COMPEL.2019.8769621.

2

State of the Art

Power systems are currently undergoing the transition in generation technology from fossil fuel-based generation to renewable generation. The number of power electronic converters required to integrate renewable energy sources has gradually increased to a significant level. In three-phase power systems, the control of these converters can be generally classified into two categories, namely the grid-following (GFL) control [5] and the grid-forming (GFM) control [6, 7, 8, 9, 10, 11].

The GFL converter aims to inject the reference current determined by the maximum available power of the regenerative source and the estimation of the voltage at the point of connection (PoC). This simple concept has been widely used in the integration of wind parks and photovoltaic power plants. However, GFL converters are not able to undertake the frequency and voltage regulation responsibility of the conventional synchronous generator (SG). Instability issues caused by voltage synchronization units, namely phase-locked loop (PLL) [12] and frequency-locked loop (FLL) [13] units, hinder the further integration of GFL converters under weak grid conditions. To pave the way towards stable and resilient operation of future 100% renewable grids, the GFM control emulating the primary control and swing dynamics of synchronous generators is considered a feasible option. Existing GFM control schemes can be classified into four categories. First, the droop control [6] derived from the primary control of synchronous generators is a simple and robust operation approach for parallel connected converters in standalone grids. To limit the change rate and nadir of frequencies after large disturbances, the second group (VISMA [7], synchronverter [8] and virtual synchronous generator [9]), mimicking the inertia response through the emulation of electromechanical and electromagnetic dynamics of synchronous generators at different levels of detail, have been proposed. Inspired by the similarities between the DC-link capacitor of the three-phase DC/AC converter system and swing dynamics of the synchronous generator, the matching control is proposed in [10], which requires only measurements of the DC-link capacitor voltage. The fourth category is the virtual oscillator control [11] which makes converters reproduce dynamics of a weakly nonlinear oscillator. The virtual oscillator control guarantees almost global asymptotic stability, nevertheless, its active and reactive power control capability remains to be solved. Although GFM control algorithms enable converters to share similar dynamics with rotational generators, two major physical differences, namely

1. GFM converters require extra energy storage devices to absorb and inject power during transients,

2. Constrained by the thermal capacity of power electronic switches, converters are not comparable to synchronous generators to withstand the significant overcurrent during faults,

make the replacement of synchronous generators with GFM converters still a challenge.

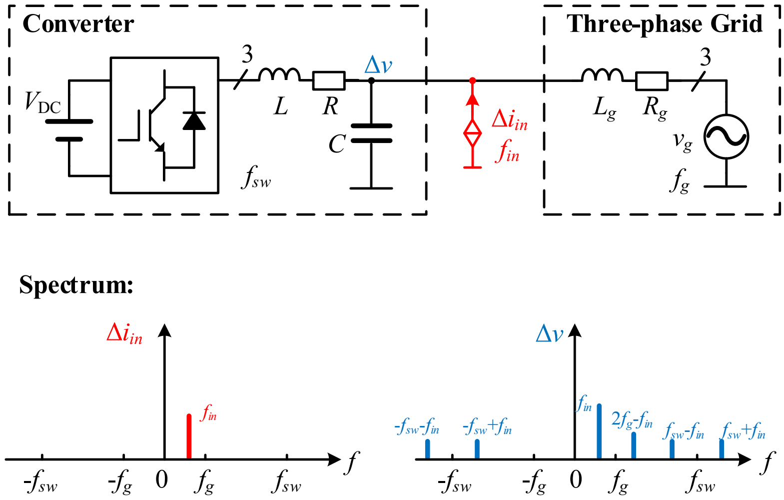

Figure 2.1: Qualitative illustration of the frequency coupling effect, current disturbance Δi_{in} at the frequency of f_{in} can excite voltage response Δv at multiple frequencies.

Both GFL and GFM converters are equipped with fast and coupled controls that can dynamically interact with loads and electric networks. Such interaction may result in unexpected harmonics, resonances or even instability over a wide frequency range. Moreover, the asymmetric controller (e.g., the PLL brings only the q-component of input voltages to zero) and the pulse-width modulation (PWM) cause a frequency coupling effect [14, 15], shown in Figure 2.1. In summary, the high penetration level of converters poses new challenges to the stability and resonance analysis of future power systems [4].

2.1 Modeling

The small-signal analysis has been widely used in the stability and resonance analysis of the conventional power systems [16, 17]. To gain insightful understanding of the impact of the increasing penetration of power electronic converters on the dynamic behavior of the modern power grids, continuous efforts have been made to develop adequate and efficient small-signal models for converter systems. Those models can be grouped into two categories, time-domain state-space models and frequency-domain impedance models. On the other hand, depending on whether the linear approximation is performed around a constant operation point or a time-periodic trajectory, small-signal models are divided into LTI models and linear time-periodic (LTP) models.

Linear Time-Invariant Model

Based on experience in modeling multiple-synchronous-generator power systems, a linear state-space model in the rotational *dq* reference frame is proposed in [18] for microgrids with droop-controlled GFM converters. This modeling method divides the microgrid into converters, networks and loads. The state-space model of each converter is first developed in its individual *dq* reference frame. Then, one of the converters is selected to provide the common *dq* frame. The complete state-space model of the microgrid is obtained by translating that of other converters to the common *dq* frame and combining state-space models of networks and loads on the common *dq* frame. This modularity concept is called component connection method. It is adopted and extended in [19, 20, 21, 22, 23, 24] by including other types of converters and loads, such as GFL converters, electric springs and induction motor loads. Based on state-space models, participation and sensitivity analysis can be performed to gain insightful evaluation of the system dynamic performance [25, 26]. Nevertheless, to build such full-order state-space models, all details of the converter topology, control structure and parameters need to be known, which are generally confidential information of the converter vendors. To tackle this limitation, the frequency-domain impedance model draws increasing attention in power electronics community. The basic idea is to derive the terminal equivalent impedance of the converters, namely the transfer function between the converter output voltage and current. The *dq*-frame impedance models of the grid-following converter are developed in [27, 28, 29, 30] to investigate the negative impact of the synchronous reference frame PLL (SRF-PLL) on system stability. The impact of advanced PLLs is addressed in [31, 32, 33]. The impedance model of GFM converters has been reported in [34]. The impedance modeling method provides the possibility for black-box modeling with measurement results. However, it might give inaccurate stability assessment results when the poorly damped or unstable oscillation modes do not participate in the system outputs. Generally, the selection of the modeling method depends on application scenarios and the purpose of applications. It is inappropriate to draw conclusions about which modeling method is superior.

The models reviewed above are all in the rotational *dq* reference frame. The *dq*-frame modeling enables to describe the system steady state with constant values, which guarantees that the linearized small-signal model is time invariant. However, the physical meaning of voltages, currents and impedances in the fictitious *dq* frame can be confusing in practice for engineers. Moreover, during impedance measurements, phase angles of the grid and the converter under tests are unknown. The phase angle of the converter injecting voltage/current disturbances is the only choice for the Park transformation. Additional compensation algorithms are required to eliminate the deviation caused by the interaction between the converter injecting perturbations and the system under tests [35]. To gain clear physical interpretation and to simplify the impedance measurement procedure, the sequence-domain impedance models are proposed in [36, 37, 38]. In the sequence-domain modeling framework, two-dimensional real-valued voltage and current vectors $[x_\alpha;\ x_\beta]$ are assembled into complex-valued variables $x_{\alpha\beta} = x_\alpha + jx_\beta$. Both positive-sequence and negative-sequence voltage (or current) perturbations are injected into the system under tests. Corresponding steady-state current (or voltage) responses are deduced by using the harmonic linearization principle for the impedance calculation. This modeling framework becomes questionable when negative-frequency components appear in the positive-sequence variables. To further eliminate such confusion, the authors of [39] propose a complex-valued impedance modeling framework in the stationary $\alpha\beta$ reference frame by introducing so-called base vectors $x_{\alpha\beta} = x_\alpha + jx_\beta$ and $x^*_{\alpha\beta} = x_\alpha - jx_\beta$. Yet the mathematical and physical meaning of these base vectors are unclear. Additionally, real-valued description is still needed for the linearization, complete complex-domain modeling has not been achieved.

Inspired by the fact that similar stability analysis results were obtained from the *dq*-frame impedance model and the sequence-domain impedance model, some work has been motivated to mathematically reveal their equivalence [40, 41, 42, 43, 44]. It is concluded that small-signal models in different reference frames, giving the same stability assessment result, can be bridged by linear transformations.

Linear Time-Periodic Model

The LTI models are only valid for three-phase balanced sinusoidal systems with classical converter controllers, such as the standard SRF-PLL, grid-following and grid-forming control without frequency-adaptive harmonics and negative sequence component extraction structures. The real-world three-phase systems, experiencing voltage imbalance and harmonic distortion [45], or containing converters with advanced grid synchronization units [46], imbalance and harmonic estimation/compensation controllers [47], are actually complex nonlinear time-periodic (NLTP) systems. Their dynamics cannot be fully captured by the LTI theory.

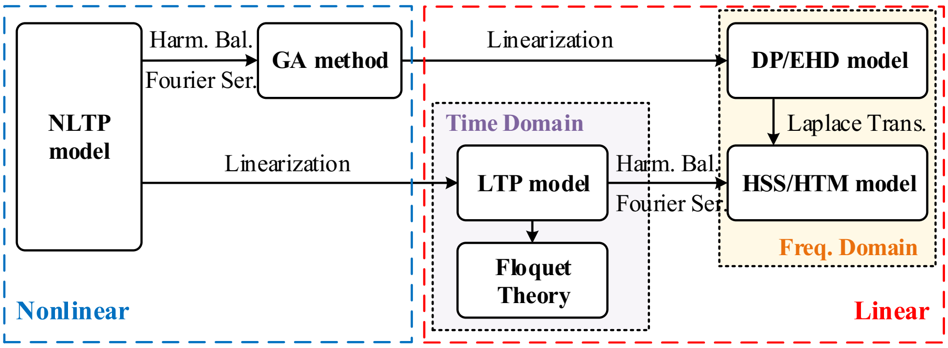

Figure 2.2: Small-signal models of the nonlinear time-periodic system.

To overcome the limitation of the LTI models, linear time-periodic theory gains increasing application in recent years. Various LTP-theory-based linearized models have been proposed for the small-signal analysis of converter systems described with ordinary differential equations

$$\dot{x}(t) = f\left(x(t),\ u(t)\right) \tag{2.1}$$

where $x(t)$ and $u(t)$ denote state and input vectors. Those models share the same theoretical basis, that is the first-order Taylor series approximation, Fourier series expansion and the harmonic balance principle. As shown in Figure 2.2, they are derived through two paths.

First, according to the generalized averaging (GA) method introduced in [48], the waveforms of $x(t)$ and $u(t)$ can be approximated on the time interval $[t - T_0, t]$ to arbitrary precision with the Fourier series

$$\begin{array}{l} x\left(t-T_0+\tau\right)=\sum_k x_k\left(t\right)e^{jk\omega_0\left(t-T_0+\tau\right)} \\ u\left(t-T_0+\tau\right)=\sum_k u_k\left(t\right)e^{jk\omega_0\left(t-T_0+\tau\right)} \end{array} \quad ,\ \tau\in[0,\ T_0]$$

where $T_0 = 2\pi/\omega_0$ is the width of the moving time window, over which the time-dependent Fourier coefficients $x_k(t)$ and $u_k(t)$ are calculated. Defining Fourier coefficient vectors

$$X(t)=[\cdots,\ x_{-1}(t),\ x_0(t),\ x_1(t),\ \cdots]^T$$

and

$$U(t)=[\cdots,\ u_{-1}(t),\ u_0(t),\ u_1(t),\ \cdots]^T,$$

the time-domain finite-dimensional system Eq. (2.1) can be equivalently reformulated as an infinite-dimensional system in the frequency domain

$$\dot{X}(t)=g\left(X(t),\ U(t)\right). \tag{2.2}$$

When the steady-state operation trajectories $\{x_{ss}(t), u_{ss}(t)\}$ are time periodic with fundamental period of T_0, $\{X_{ss}(t), U_{ss}(t)\}$ become constant vectors. Then, a theoretically infinite-dimensional LTI small-signal model can be obtained

$$\begin{aligned} \Delta\dot{X}(t)&=A\Delta X(t)+B\Delta U(t) \\ A&=\left.\frac{\partial g}{\partial X}\right|_{X_{\mathrm{ss}},\ U_{\mathrm{ss}}} \\ B&=\left.\frac{\partial g}{\partial U}\right|_{X_{\mathrm{ss}},\ U_{\mathrm{ss}}} \end{aligned}$$

which is commonly referred to as dynamic phasor (DP) model [49, 50, 51, 52, 53] or extended harmonic domain (EHD) model [54, 55, 56, 57].

The second route is inspired by the pioneer work of Wereley [58], whose primary thrust is to develop an operator for the LTP system, which maps the Fourier coefficients of inputs to those of outputs, comparable to the transfer function for LTI systems. To apply his method, the NLTP model Eq. (2.1) is first linearized around the time-periodic trajectories $\{x_{ss}(t), u_{ss}(t)\}$

$$\begin{aligned} \Delta\dot{x}\left(t\right)&=A\left(t\right)\Delta x\left(t\right)+B\left(t\right)\Delta u\left(t\right) \\ A\left(t\right)&=\left.\frac{\partial f}{\partial x}\right|_{x_{\mathrm{ss}}(t),\ u_{\mathrm{ss}}(t)} \\ B\left(t\right)&=\left.\frac{\partial f}{\partial u}\right|_{x_{\mathrm{ss}}(t),\ u_{\mathrm{ss}}(t)} \end{aligned} \quad . \tag{2.3}$$

If the so-called exponentially modulated periodic inputs

$$\Delta u\left(t\right)=e^{st}\sum\nolimits_{k=-\infty}^{\infty}U_k e^{jk\omega_0 t}$$

are fed to the LTP model Eq. (2.3), the steady-state response are also exponentially modulated periodic signals

$$\Delta x\left(t\right)=e^{st}\sum\nolimits_{k=-\infty}^{\infty}X_k e^{jk\omega_0 t}$$

satisfying the harmonic state-space (HSS) equation [59, 60, 61, 62, 63, 64, 65, 66] obtained from the harmonic balance principle (namely Fourier coefficients of both sides of Eq. (2.3) must be the same)

$$s\mathcal{X} = (\mathcal{A} - \mathcal{N})\mathcal{X} + \mathcal{B}\mathcal{U} \tag{2.4}$$

where s is a complex number and

$$\begin{aligned} \mathcal{X} &= [\cdots,\ X_{-1},\ X_0,\ X_1,\ \cdots]^T \\ \mathcal{U} &= [\cdots,\ U_{-1},\ U_0,\ U_1,\ \cdots]^T \\ \mathcal{N} &= diag[\cdots,\ N_{-k},\ \cdots,\ N_0,\ \cdots,\ N_k,\ \cdots]^T \end{aligned}.$$

Constant matrices $\mathcal{A}$ and $\mathcal{B}$ are Toeplitz matrices of Fourier coefficients of $A(t)$ and $B(t)$. N_k is a diagonal square matrix with diagonal elements equal to $jk\omega_0$, and it shares the same dimension with $A(t)$.

Let $\Delta x\,(t)$ be also the output vector, the infinite-dimensional harmonic transfer matrix (HTM) [67, 68, 69, 70, 71, 72], describing the relation between harmonics in input and output variables, is given by

$$G_{HTM}(s) = (s\mathcal{I} - (\mathcal{A} - \mathcal{N}))^{-1}\,\mathcal{B} \tag{2.5}$$

where $\mathcal{I}$ is the identity matrix.

It is seen that the common idea behind the DP/EHD and HSS/HTM models is to find an LTI approximation of the NLTP system for small-signal stability analysis. To this end, the DP/EHD model replaces time-domain variables with their Fourier series coefficients, resulting in a nonlinear time-invariant model. Then, classical LTI techniques apply. Instead, the HSS/HTM model initially performs first-order Taylor series approximation, resulting in an LTP model. Then, based on Fourier series expansion and harmonic balance principles, a frequency-domain LTI model that maps harmonics of input and output variables is derived. Theoretically, the HSS/HTM models can be regarded as the Laplace transformation of the DP/EHD models. Numerically, the difference between these two categories of models is that the truncation order of DP/EHD models, namely the number of selected harmonics, is determined before the linearization. Therefore, the linearization process must be repeated when more harmonics need to be considered to guarantee the accuracy. Contrarily, the HSS/HTM method is more convenient to adjust the truncation order. It should be mentioned that, different from the HSS/HTM method, the GA method is also valid for the description of general time-varying systems, since the Fourier coefficients can be calculated and updated by online integration.

The LTP small-signal models reviewed above are essentially developed in the frequency domain. Deriving analytical expressions for their free and forced responses is not straightforward because of the need to perform Fourier series expansion of input variables and Fourier series synthesis of state/output variables. Though eigenvalue and participation analysis have been applied to the truncated DP model [51] and HSS model [73] for small-signal stability analysis, some inconveniences of these frequency-domain models can still be identified:

- selection of the truncation order is a trade-off between modeling accuracy and computational efficiency, only empirical recommendation is provided in [74];

- increasing truncation order to ensure modeling accuracy results in more eigenvalues with critical damping ratio, which can mislead the assessment of damping performance;
- the truncation will always bring spurious eigenvalues lying outside vertical lines formed by convergent eigenvalues. Such spurious eigenvalues are commonly distinguished graphically, which requires unnecessarily large truncation orders and hinders automatic stability analysis of LTP systems.

Moreover, the strength of the frequency coupling effect has not been quantitatively evaluated to answer when the LTP theory must be applied.

2.2 Small-Signal Stability Analysis

Linear Time-Invariant Theory

According to the LTI control theory, there exist two types of stability evaluation methods, namely eigenvalue analysis and Nyquist stability criterion, corresponding to the time-domain state-space model and frequency-domain impedance model, respectively.

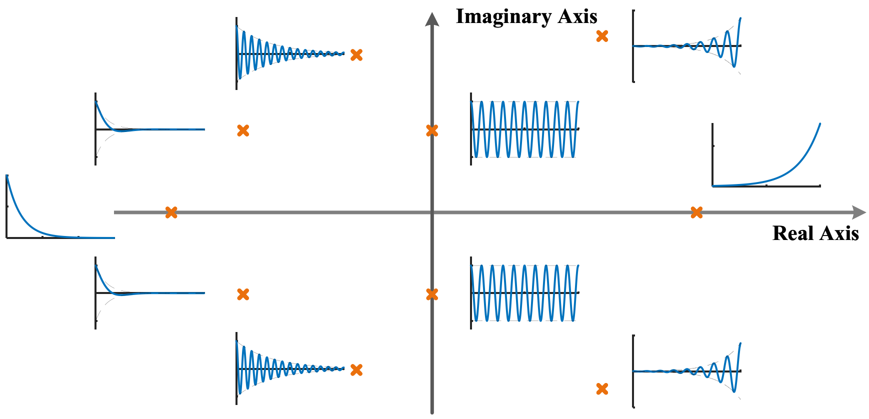

Figure 2.3: Relation between eigenvalues and time-domain free responses

Figure 2.3 qualitatively shows the relation between eigenvalues and time-domain dynamic responses of LTI systems. Eigenvalues of the system matrix in the state-space model provide the complete information of the system dynamics: the system is marginal stable when real parts of all eigenvalues are negative, and the damping performance of each oscillation mode is quantified by the damping ratio. Another useful tool of the eigenvalue-based stability analysis framework is the participation factor analysis, which quantifies the relative contribution of each oscillation mode to different state variables [17]. The participation factor analysis of critical modes can facilitate efficient allocation of monitoring and protection devices. Additionally, eigenvalue sensitivity analysis can be performed to quantify impact of changes of control and physical parameters on the movement of eigenvalues, which provides guidance to the parameter optimization [75, 76]. For example, using the eigenvalue analysis, the authors in [77] concluded that the maximum power transfer limit (obtained from static voltage stability analysis) of a VSC-HVDC system is achievable when the PLL gains become very small. In [18], the eigenvalue analysis result reveals that the low-frequency oscillation modes of droop-controlled converter

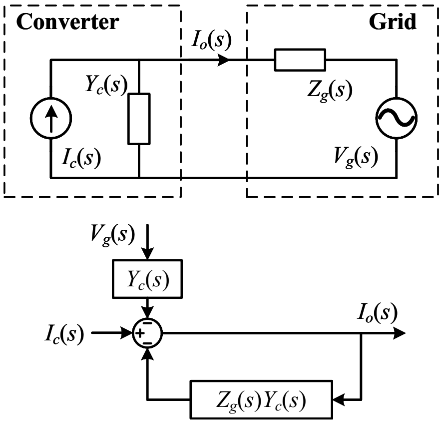

Figure 2.4: Principle of the impedance-based stability analysis. Top: impedance model. Bottom: equivalent control system

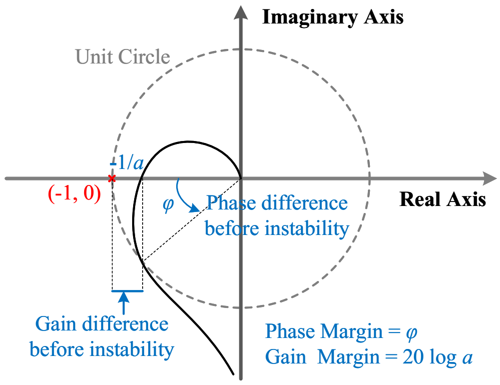

Figure 2.5: Nyquist diagram for single-input-single-output system

systems are highly sensitive to the network configuration and droop coefficients, while the high-frequency modes are largely influenced by the interaction between inner voltage-current controller, load and network dynamics. The interaction between different types of converters has been recently investigated in [19, 78] based on eigenvalue analysis.

In the frequency domain, the impedance-based stability criterion is a well-established technique. It is originally developed for the design-oriented analysis of input filters of DC-DC converters [79]. In [80], it was applied to the analysis of AC power systems, and has gained wide application for the stability assessment of grid-tied converters since the publication of [36]. This method is inspired by the similarity between equivalent electrical circuits and the feedback control system, as shown in Figure 2.4. The converter is described with a Norton equivalent circuit, which is connected to an ideal voltage source in series with a grid impedance. The output current can be determined from the feedback control diagram

$$\begin{aligned} I_o\left(s\right) &= \frac{Y_g\left(s\right)}{Y_c\left(s\right)+Y_g\left(s\right)} I_c\left(s\right) - \frac{1}{Z_g\left(s\right)+Z_c\left(s\right)} V_g\left(s\right) \\ &= \left[I_c\left(s\right) - Y_c\left(s\right) V_g\left(s\right)\right] \frac{1}{1+Z_g\left(s\right) Y_c\left(s\right)} \end{aligned}.$$

When the following conditions are satisfied

1. the voltage source is stable when unloaded (i.e., $V_g(s)$ has no unstable poles);
2. the current source is stable when unloaded (i.e., $I_c(s)$ has no unstable poles),
3. the load is stable when powered with an ideal voltage source (i.e., $Y_c(s)$ has no right-half plane zeros),

the system stability is determined by whether the impedance ratio $Z_g\left(s\right) Y_c\left(s\right)$, namely the minor loop gain, satisfies the Nyquist criterion. The phase margin and gain margin shown in Figure 2.5 can be used to quantify the stability robustness. However, these indicators loose their effectiveness when the converter model becomes an impedance matrix, for which the generalized Nyquist criterion [81] is required for the stability investigation.

An attractive feature of the impedance-based stability analysis method is the black-box modeling capability, since the impedance profile can be measured with frequency scanning technique. However, the equivalent impedance reflects only the input-output dynamics at the converter terminal, which cannot reveal internal instability issues. The generalized Nyquist criterion gives only the conclusion whether the system is stable or not. Indicators with clear physical meaning still need to be developed to quantify the stability margin and guide control optimization. The passivity theory (i.e., when every converter exhibits a non-negative resistance in a certain frequency range, unstable oscillations will not occur in that frequency range) could be a promising option [82, 83], though it is not a necessary condition for the system stability.

In addition, it is commonly assumed that the impedance ratio has no right-half plane poles. Then, the system stability is evaluated by checking whether the Nyquist plot encircles the critical point $(-1,\ 0)$ in the complex plane. In practice, this assumption is not always satisfied [84, 85, 86]. Determination of the right-half plane poles of the impedance ratio from the impedance measurement results deserves further investigation. In contrast, eigenvalue-based analysis yields highly detailed system dynamics assessments, and has been successfully used for positioning and parameter optimization of power system stabilizers to damp low-frequency oscillations in the bulk power systems [16].

Linear Time-Periodic Theory

In the frequency domain, the harmonic transfer matrix given by Eq. (2.5) reveals that the finite dimensional LTP system is equivalent to an infinite-dimensional LTI system. Therefore, the Nyquist stability criterion is also applicable to the stability analysis of the LTP system. To name a few, harmonic impedance models of GFL converters operated under unbalanced conditions are built in [87, 68, 67]. It is concluded that both voltage and current imbalances can reduce the stability margin. In [88], the harmonic transfer matrix is used to address the small-signal stability of voltage-controlled modular multilevel converters. Moreover, its effectiveness for the stability analysis of single-phase converters is confirmed by experimental validation in [64, 89].

In the time domain, stability analysis of LTP systems can be performed by using Floquet theory [90] dating back to 1883. Consider the homogeneous state-space equation, i.e., the free-response problem of Eq. (2.3),

$$\Delta\dot{x}\left(t\right) = A\left(t\right)\Delta x\left(t\right)$$

the Floquet theory gives that the solution is determined by

$$\Delta x\left(t\right) = \mathit{\Phi}\left(t,\ 0\right)\Delta x(0) \tag{2.6}$$

where $\Delta x(0)$ is the initial condition at $t = 0$. $\mathit{\Phi}(t,\ 0)$ is called the state transition matrix, which is T_0-periodic, namely $\mathit{\Phi}\left(t + T_0,\ T_0\right) = \mathit{\Phi}\left(t,\ 0\right)$. It can be obtained by solving the matrix differential equation

$$\dot{\mathit{\Phi}}\left(t,\ 0\right) = A\left(t\right)\mathit{\Phi}\left(t,\ 0\right),\ \text{with}\ \ \mathit{\Phi}\left(0,\ 0\right) = \boldsymbol{I}$$

where $\boldsymbol{I}$ denotes the identity matrix. From Eq. (2.6), the state transition over k full periods is given by

$$\begin{gathered}\Delta x\,(2T_0) = \Phi\,(2T_0,\ T_0)\,\Delta x\,(T_0) = \Phi\,(2T_0,\ T_0)\,\Phi\,(T_0,\ 0)\,\Delta x\,(0) = (\Phi\,(T_0,\ 0))^2 \Delta x\,(0) \\ \Downarrow \\ \Delta x\,(kT_0) = (\Phi\,(T_0,\ 0))^k \Delta x\,(0)\end{gathered}.$$

Inserting the eigendecomposition $\Phi\,(T_0,\ 0) = R\Lambda R^{-1}$, yields

$$\Delta x\,(kT_0) = \underbrace{R\Lambda^k R^{-1}}_{(\Phi(T_0,\,0))^k} \Delta x\,(0)$$

where Λ is the eigenvalue matrix, R is the eigenvector matrix. The state vector $\Delta x\,(kT_0)$ is asymptotically stable, only if eigenvalues of $\Phi\,(T_0,\ 0)$ are located within the open unit circle in the complex plane. In the Floquet theory, matrix $\Phi\,(T_0,\ 0)$ and its eigenvalues are called monodromy matrix and characteristic multipliers, respectively. It was used in [91] for stability analysis of a single-phase asymmetric cascaded H-bridge multilevel inverter operated under the standalone mode. Based on the Floquet theory, the authors of [92] figured out that the stability of the decoupled double synchronous reference frame (DDSRF-PLL) is influenced by both input voltage level and unbalance factors.

The Floquet theory can only predict whether the system is stable or not. It fails to provide more insightful characterization of system dynamics, e.g., damping, sensitivity and participation information. The generalization of the powerful eigenvalue-based analysis for LTI systems to LTP systems remains an open topic. Though eigenvalues of HSS models are calculated in [64, 65] to detect the precise stability boundary of a single-phase converter system, the physical meaning of eigenvalues of the HSS model is still unclear, and the link between these eigenvalues and time domain dynamics has not been revealed, since the HSS model is inherently derived in the frequency domain for periodic inputs. The same problem exists when the eigenvalues of the DP/EHD model is computed for stability analysis [93].

Moreover, some numerical difficulties in the stability analysis of LTP systems remain to be solved. In the time domain, for large-scale converter-dominated systems, solving the numerical matrix equation can be time-consuming. In the frequency domain, the infinite-dimensional matrix must be truncated for the eigenvalue calculation. Though it has been rigorously proved in [94] that eigenvalues of the truncated matrix converge to those of the non-truncated one as the truncation order approaches infinity, selection of the truncation order H is a trade-off between computational accuracy and efficiency. In [58, 94], the truncation order is increased until N unchanged eigenvalues are found in the fundamental strip, where N denotes the number of state variables. Yet this method ignores the rate of convergence of eigenvalues and can result in unnecessarily high truncation orders. An iterative eigenvector sorting method is used in [95], the basic idea behind is that eigenvectors, whose nonzero elements are symmetric about the DC component and within the truncation order, are less influenced by the truncation. However, no rigorous mathematical proof has been achieved. In [74], it is suggested that H should be larger than the maximum harmonic order of nonzero Fourier coefficients of $A(t)$. However, no explicit formula has been established, and the impact of changing the truncation order has not been quantitatively evaluated. An accurate and efficient truncation order selection method is demanded to pave the way for easier application of the LTP theory.

2.3 Harmonic Resonance Analysis

Power systems were previously dominated by synchronous generators with significant mechanical inertia. Since timescales of the electromechanical and electromagnetic dynamics are sufficiently separated, the harmonic resonance analysis of conventional power systems mainly focuses on the inherent characteristics of the passive network [96, 97, 98, 99, 100]. With the increasing penetration of renewable energy generation, the modern power system is gradually evolving as power converter dominated. The multiple-timescale control loops of power converters can cause cross couplings with dynamics of power networks, and frequency coupling effects caused by asymmetric controllers and time-periodic operation trajectories further increase the system complexity. This poses new challenges to the harmonic resonance analysis. As reviewed above, efficient and accurate modeling of power converters has been intensively investigated, however, an effective system-level analysis approach for resonance frequency identification and resonance severity evaluation of converter-dominated systems operating under different conditions is still an open topic.

In power system engineering, two types of harmonic resonances have to be distinguished: parallel and series resonances. The parallel resonance refers to the phenomenon that a small current injection can result in very large bus voltages. The series resonance refers to those cases where a small bus voltage can cause large branch currents. In general, there are mainly two techniques for harmonic resonance analysis. The first method is the frequency scanning analysis (FSA) [96], which can confirm whether the resonance exists and identify the resonance frequency by examining the bus voltage (branch current) responses to harmonic current (voltage) injection. This is actually the same procedure as the impedance measurement. Although the FSA is very straightforward, it fails to provide more insightful information for the design of resonance mitigation strategies. The second method is the resonance mode analysis (RMA) [97, 98, 99, 100] which is based on the eigen-analysis of the network admittance and impedance matrix. Compared with FSA, RMA can further reveal the excitability and observability of a certain resonance mode at each bus by means of participation factor analysis. Meanwhile, the sensitivity analysis in combination with the RMA technique can quantify the impact of each parameter on the system harmonic resonance, which could provide guidelines for the development of the resonance mitigation scheme. The RMA has been utilized in [101, 102] to investigate the resonance interactions between converters and the grid by integrating converters' small-signal equivalent impedance models into the system admittance matrix. However, the converter impedance models used in these papers are obtained from the linearization around the DC operation point. The influence of the frequency coupling effect, caused by the PWM, the PLL and the non-ideal grid conditions (e.g., unbalanced grid voltages and impedance), on the system resonance characteristics cannot be fully captured.

2.4 Thesis Contribution

Aiming to fill in the knowledge gap of recent research, the unique contributions of this thesis can be summarized as follows:

- A modular and flexible modeling, stability and resonance analysis framework is developed in MATLAB/Simulink platform. By introducing the Wirtinger calculus, completely complex-domain nonlinear and small-signal modeling of state-of-the-art converters is achieved. A complex-valued power flow analysis method is developed for converter-dominated power systems to improve the efficiency of development of the small-signal model.
- The conventional modal analysis for LTI systems is generalized to LTP systems. Definitions of damping ratio, participation factor and eigenvalue/eigenvector sensitivity are accordingly modified to evaluate the time-domain dynamic performance of GFL and GFM converters.
- To fully capture the impact of the frequency coupling effect on the harmonic resonance behavior of modern grids, a time-periodic impedance matrix is proposed. A generalized resonance mode analysis method is applied to the time-period impedance matrix to investigate the influence of the converter integration and unbalanced operations on the resonance frequency and severity.
- Based on LTP sensitivity analysis and participation analysis, a design-oriented control parameter and structure optimization method is proposed to improve the damping and stability margin of GFL and GFM converters.

3

Modeling of Converter-Dominated Power Systems

This chapter deals with the time-domain steady-state and small-signal modeling of converter-dominated power systems considering both balanced and unbalanced operation conditions. First, complex-valued description of the state-of-the-art grid-following and grid-forming converters is proposed. Then, by introducing the complex partial derivative defined within the Wirtinger calculus framework, the small-signal models of different types of converters are directly derived in the complex domain. To improve the development efficiency of the small-signal model, a complex-valued power flow analysis method is proposed to determine the steady-state operation trajectory. Next, the component connection method is implemented in the stationary reference frame for system-level modeling. Simulation and experimental tests have been carried out on single-converter and multi-converter systems to validate the analytical methodology.

3.1 Complex-Valued Large-Signal Model

In a three-phase system with no zero-sequence component, a real-valued three-phase voltage/current vector $[x_a,\ x_b,\ x_c]^T$ can be equivalently described with a two-phase Cartesian vector $[x_\alpha,\ x_\beta]^T$ by applying the Clarke transformation $\boldsymbol{T}_{Clarke}$

$$\begin{bmatrix} x_\alpha \\ x_\beta \end{bmatrix} = \boldsymbol{T}_{Clarke} \begin{bmatrix} x_a \\ x_b \\ x_c \end{bmatrix} \quad \boldsymbol{T}_{Clarke} = \frac{2}{3} \begin{bmatrix} 1 & -\frac{1}{2} & -\frac{1}{2} \\ 0 & \frac{\sqrt{3}}{2} & -\frac{\sqrt{3}}{2} \end{bmatrix}.$$

Assembling the in-quadrature entries of the Cartesian vector into a complex scalar, the number of variables and equations for the system description can be halved [103, 104]. Figure 3.1 exemplarily shows the waveform of a three-phase quantity described with two real-valued variables or one complex-valued variable.

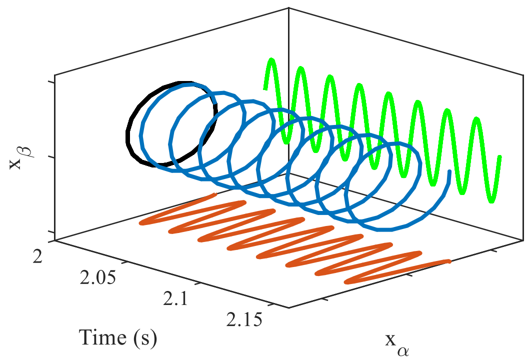

Figure 3.1: Waveform of a three-phase current or voltage. Blue: the complex-valued variable. Red: the real part (α component). Green: the imaginary part (β component).

In the complex plane, fixing the α-axis in the direction of the real axis, the in-quadrature β-axis may coincide with either the imaginary axis or the negative imaginary axis (see Figure 3.2). In this thesis, the obtained two coordinates are defined as the original coordinate and the conjugate coordinate, respectively. This transformation is given by

$$\begin{bmatrix} x_{\alpha\beta} \\ x^*_{\alpha\beta} \end{bmatrix} = \boldsymbol{T}_{r2c} \begin{bmatrix} x_\alpha \\ x_\beta \end{bmatrix} \quad \boldsymbol{T}_{r2c} = \begin{bmatrix} 1 & j \\ 1 & -j \end{bmatrix} \quad \boldsymbol{T}_{c2r} = \boldsymbol{T}_{r2c}^{-1}$$

where $x_{\alpha\beta}$ denotes the complex-valued voltage/current variable in the original coordinate, and the associated variable $x^*_{\alpha\beta}$ is in the conjugate coordinate.

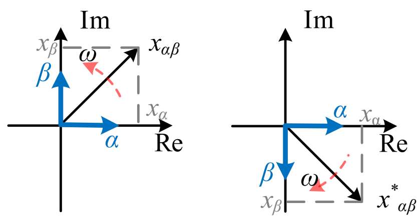

Figure 3.2: Complex-domain description of three-phase variables

Physically, the information provided by $x^*_{\alpha\beta}$ is redundant, since $[x_\alpha,\ x_\beta]^T$ can be fully recovered from either $x_{\alpha\beta}$ or $x^*_{\alpha\beta}$ by separating their real and imaginary parts. Mathematically, it plays an essential role for the power flow analysis and the linearization in the complex domain. For instance, the absolute value function used for the steady-state and dynamic modeling of the power converters

$$f\left(x_{\alpha\beta}\right) = f\left(x_\alpha,\ x_\beta\right) = f_{\mathrm{Re}}\left(x_\alpha,\ x_\beta\right) + j \cdot f_{\mathrm{Im}}\left(x_\alpha,\ x_\beta\right) = \left|x_{\alpha\beta}\right| = \sqrt{x_\alpha^2 + x_\beta^2}$$

does not have the classical complex partial derivative $\partial f/\partial x_{\alpha\beta}$, since the function is non-holomorphic, namely it does not fulfill the Cauchy-Riemann condition:

$$\left(\frac{\partial f_{\mathrm{Re}}}{\partial x_\alpha} = \frac{x_\alpha}{\sqrt{x_\alpha^2 + x_\beta^2}}\right) \neq \left(\frac{\partial f_{\mathrm{Im}}}{\partial x_\beta} = 0\right)$$
$$\left(\frac{\partial f_{\mathrm{Re}}}{\partial x_\beta} = \frac{x_\beta}{\sqrt{x_\alpha^2 + x_\beta^2}}\right) \neq \left(-\frac{\partial f_{\mathrm{Im}}}{\partial x_\alpha} = 0\right)$$

Therefore, the absolute value function cannot be directly linearized in the complex domain. To solve this problem, the relaxed definition of the complex partial derivative, which is called the Wirtinger calculus [105], is adopted in this thesis. The main idea behind the Wirtinger calculus is to reformulate f as a function of both $x_{\alpha\beta}$ and $x_{\alpha\beta}^*$

$$f\left(x_{\alpha\beta}\right) = \left|x_{\alpha\beta}\right| = f\left(x_{\alpha\beta},\ x_{\alpha\beta}^*\right) = \sqrt{x_{\alpha\beta} x_{\alpha\beta}^*}$$

and the complex derivatives are calculated by treating $x_{\alpha\beta}$ and $x_{\alpha\beta}^*$ as independent variables

$$\begin{aligned} \frac{\partial f}{\partial x_{\alpha\beta}} &= \frac{x_{\alpha\beta}^*}{2\sqrt{x_{\alpha\beta} x_{\alpha\beta}^*}} \\ \frac{\partial f}{\partial x_{\alpha\beta}^*} &= \frac{x_{\alpha\beta}}{2\sqrt{x_{\alpha\beta} x_{\alpha\beta}^*}} \end{aligned}.$$

Then, the linearized form is given by

$$\begin{aligned} \Delta f &= \left.\frac{\partial f}{\partial x_{\alpha\beta}}\right|_{X_{\alpha\beta},\, X_{\alpha\beta}^*} \Delta x_{\alpha\beta} + \left.\frac{\partial f}{\partial x_{\alpha\beta}^*}\right|_{X_{\alpha\beta},\, X_{\alpha\beta}^*} \Delta x_{\alpha\beta}^* \\ &= \frac{X_{\alpha\beta}^*}{2\sqrt{X_{\alpha\beta} X_{\alpha\beta}^*}} \Delta x_{\alpha\beta} + \frac{X_{\alpha\beta}}{2\sqrt{X_{\alpha\beta} X_{\alpha\beta}^*}} \Delta x_{\alpha\beta}^* \end{aligned}$$

where $X_{\alpha\beta}$ and $X_{\alpha\beta}^*$ denote the steady-state values of $x_{\alpha\beta}$ and $x_{\alpha\beta}^*$. The variables preceded by Δ denote small-signal ones.

It can be confirmed that the complex conjugate operator, as well as the real and imaginary part extraction operators are also non-holomorphic. The Wirtinger calculus enables the direct linearization in the complex domain. To make this thesis self-contained, details about the Wirtinger calculus are provided in the Appendix A.

In this section, the nonlinear state-space model of the voltage source converter (VSC), power networks and loads will be developed in the complex domain based on the fundamentals introduced above. The notations used in this section follow the rules below:

1. The subscript in the notation defines the reference frame, specifically, α and β are for the stationary $\alpha\beta$ reference frame, d and q for the rotational dq reference frame. Variables with single character are in the real value domain $\mathbb{R}$, e.g., x_α and x_d. The subscript with double characters defines variables in the complex value domain $\mathbb{C}$, e.g., $v_{\alpha\beta}$ and v_{dq}.

2. When the variable comprises a single sequence component, an extra symbol + for the positive-sequence component or symbol − for the negative-sequence component is added into the subscript, e.g., v_{dq+}.

3. Other characters in the subscript are used to denote the physical meaning of variables, e.g., c indicates that $v_{\alpha\beta c}$ is the filter capacitor voltage.

4. Variables of different converters or buses are indexed with comma-separated numbers in the subscript, e.g., $v_{\alpha\beta c,i}$ stands for the filter capacitor voltage of the ith converter.

In addition, the complex conjugate operator is denoted by the symbol star $(\cdot)^*$. $(\cdot)^T$ and $(\cdot)^{-1}$ denote the transpose and inverse operators respectively. $\mathrm{Im}\{\cdot\}$ is the imaginary part extraction operator, and $\mathrm{Re}\{\cdot\}$ stands for the real part extraction operator. If not specified otherwise, boldface is used for vectors and matrices.

3.1.1 Grid-Following Voltage Source Converters

Figure 3.3 depicts the schematic and control of a single GFL converter system. The converter is assumed to be supplied by an ideal DC voltage V_{DC}. Its output is connected to the grid through an LC(L) filter. For the single converter system, the grid is modeled as an ideal voltage source in series with an RL impedance. The grid strength quantified by the short-circuit ratio (SCR)

$$SCR = \frac{V_0^2}{|Z_g|\, S_0} = \frac{V_0^2}{|R_g + j\omega_0 L_g|\, S_0} \tag{3.1}$$

can be modified by changing the grid impedance L_g and R_g. V_0 stands for the rated voltage of the converter, and S_0 is the apparent output power of the converter. $\omega_0 = 2\pi \cdot 50$ rad/s is the fundamental frequency.

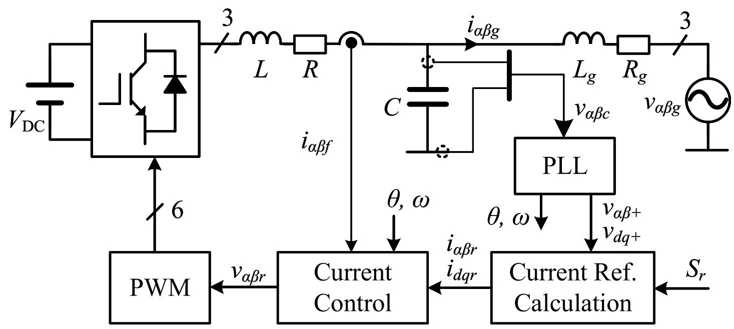

Figure 3.3: Schematic and control of a single grid-following converter system

The control of the GFL converter can be generally divided into three parts. First, the PLL serves as a synchronization unit for the detection of the magnitude, frequency and phase angle of the filter capacitor voltage $v_{\alpha\beta c}$. To realize precise and fast grid synchronization even for unbalanced or harmonically distorted grid voltages, two advanced PLLs are considered, the dual synchronous reference frame PLL (DSRF-PLL) [106] and the dual second order generalized integrator PLL (DSOGI-PLL) [107]. Next, based on the instantaneous power theory [108], the current reference $i_{\alpha\beta r}$ or i_{dqr} is calculated from the given power command S_r and the detected positive-sequence capacitor voltage $v_{\alpha\beta +}$ or v_{dq+}. Third, the current control is realized with either a proportional-integral (PI) controller in the dq frame or a frequency-adaptive proportional-resonant (PR) controller in the $\alpha\beta$ frame [109].

Advanced Three-phase PLLs

Figure 3.4 shows the basic structure of the classical three-phase SRF-PLL. Let

$$v_{\alpha\beta c} = V_+ e^{j\theta_0} = V_+ e^{j\omega_0 t}$$

be the balanced three-phase input voltage. When the SRF-PLL is quasi synchronized, namely the estimated phase angle θ deviates only slightly from θ_0 ($\theta \approx \theta_0$), the phase angle estimation error can be approximated by the Park transformation

$$T_{Park}(\theta) = e^{-j\theta}$$

of the input voltage

$$\begin{aligned} v_{dq} &= T_{Park}(\theta) v_{\alpha\beta c} = e^{-j\theta} v_{\alpha\beta c} = V_+ e^{j(\theta_0 - \theta)} \\ &= V_+ \cos(\theta_0 - \theta) + j V_+ \sin(\theta_0 - \theta) \\ &\approx \underbrace{V_+}_{v_d} + j \underbrace{V_+ (\theta_0 - \theta)}_{v_q} \end{aligned} .$$

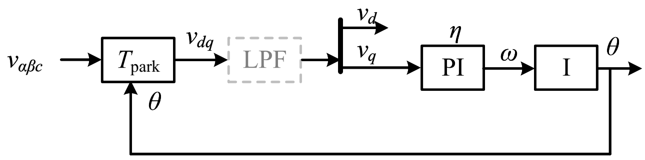

Figure 3.4: Basic scheme of SRF-PLL

To eliminate the phase angle detection error, a PI controller is applied to regulate the imaginary part of v_{dq}, namely $v_q \approx V_+ (\theta_0 - \theta)$, to zero. Under ideal three-phase balanced and harmonic-free conditions, the SRF-PLL yields precise and fast frequency and phase angle tracking performance. However, when the input voltage is unbalanced and/or harmonically distorted, for instance

$$v_{\alpha\beta c} = V_+ e^{j\omega_0 t} + V_- e^{-j\omega_0 t + j\theta_-} \tag{3.2}$$

contains a negative-sequence voltage with magnitude and initial phase angle of V_- and θ_-, the disturbance at the frequency of $2\omega_0$ in v_q resulting from the Park transformation

$$\begin{aligned} v_{dq} = T_{Park}(\theta) v_{\alpha\beta c} &= e^{-j\theta} v_{\alpha\beta c} \\ &= V_+ e^{j(\theta_0 - \theta)} \qquad + e^{-j\theta} V_- e^{-j\omega_0 t + j\theta_-} \\ &\approx V_+ + j V_+ (\theta_0 - \theta) \quad + V_- e^{-j2\omega_0 t + j\theta_-} \end{aligned}$$

will significantly degrade the synchronization accuracy of the SRF-PLL. Although the in-loop low-pass filter (LPF) can be used to suppress harmonics, the low cut-off frequency required to reject disturbances at $2\omega_0$ can result in an unacceptably slow response. To overcome the shortcoming of the SRF-PLL, two advanced PLL schemes, DSRF-PLL and DSOGI-PLL, are commonly used for applications requiring high accuracy and fast dynamic response even under adverse utility voltages. Their common idea is to employ a specific positive-sequence component detector (PSCD) in front of the conventional SRF-PLL.

Dual Synchronous Reference Frame PLL, DSRF-PLL

As shown in Figure 3.5, by taking both θ and $-\theta$ as the input of the Park transformation, the DSRF-PLL implements two dq frames rotating in opposite directions, namely $dq+$ and $dq-$ frames. Assume that the PLL perfectly synchronizes to the positive-sequence voltage, i.e., $\theta = \theta_0$, the unbalanced input voltage expressed in the $dq+$ and $dq-$ frames are

$$\begin{aligned} \bar{v}_{dq+} &= T_{Park}\left(\theta_0\right) v_{\alpha\beta} &&= V_+ &&+ V_- e^{j\theta_-} e^{-j2\omega_0 t} \\ \bar{v}_{dq-} &= T_{Park}\left(-\theta_0\right) v_{\alpha\beta} &&= V_+ e^{j2\omega_0 t} &&+ V_- e^{j\theta_-} \end{aligned} . \tag{3.3}$$

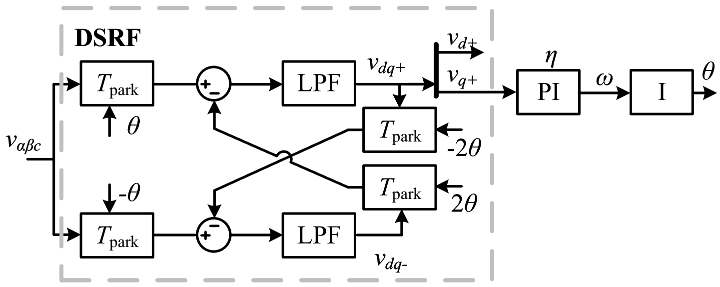

Figure 3.5: Basic scheme of DSRF-PLL

It is observed from Eq. (3.3) that the magnitude of the double fundamental frequency oscillation term present in $dq+$ or $dq-$ frame corresponds to the DC term in the other rotational frame. By subtracting the oscillatory terms, the positive and negative sequence voltage components can be separated. The 1st-oder LPF

$$G_{LPF}(s) = \frac{\omega_f}{s + \omega_f}$$

with a bandwidth of ω_f is used to improve extraction performance of the DC terms. The four LPFs in Figure 3.5 are always designed to have the same cut-off frequency.

Combining the PSCD structure with the SRF-PLL, the complete state-space model of the DSRF-PLL is

$$\begin{aligned} \dot{v}_{dq+} &= -\omega_f v_{dq+} - \omega_f e^{-j2\theta} v_{dq-} + \omega_f e^{-j\theta} v_{\alpha\beta c} \\ \dot{v}_{dq-} &= -\omega_f v_{dq-} - \omega_f e^{j2\theta} v_{dq+} + \omega_f e^{j\theta} v_{\alpha\beta c} \\ \dot{\eta} &= k_i v_{q+} = k_i \mathrm{Im}\left\{v_{dq+}\right\} \\ \dot{\theta} &= \omega = \eta + k_p v_{q+} = \eta + k_p \mathrm{Im}\left\{v_{dq+}\right\} \end{aligned} \tag{3.4}$$

where state variables v_{dq+} and v_{dq-} are for the low-pass filters. k_p and k_i are PI control coefficients, and η is associated with the integrator.

Dual Second Order Generalized Integrator PLL, DSOGI-PLL

The basic scheme of the DSOGI-PLL is illustrated in Figure 3.6. Instead of separating the positive and negative sequence voltage components in different dq frames, the DSOGI-PLL directly realizes the sequence decomposition in the $\alpha\beta$ frame. When the resonance frequency of the DSOGI structure is adapted to that of the positive-sequence component of the input voltage, the DSOGI structure will be able to precisely estimate the input voltage (Eq. (3.2)) and its quadrature signal, namely

$$\begin{aligned} X_{\alpha\beta 1} &= V_+ e^{j\omega_0 t} + V_- e^{-j\omega_0 t + j\theta_-} \\ j\omega_0 X_{\alpha\beta 2} &= V_+ e^{j\omega_0 t} - V_- e^{-j\omega_0 t + j\theta_-} \end{aligned}. \tag{3.5}$$

$X_{\alpha\beta 1}$ and $X_{\alpha\beta 2}$ stand for steady-state values of $x_{\alpha\beta 1}$ and $x_{\alpha\beta 2}$, which are the state variables related to the integrators in the DSOGI structure, as shown in Figure 3.6. The positive-sequence component can be solved from Eq. (3.5), yielding

$$V_+ e^{j\omega_0 t} = \frac{1}{2}\left(X_{\alpha\beta 1} + j\omega_0 X_{\alpha\beta 2}\right). \tag{3.6}$$

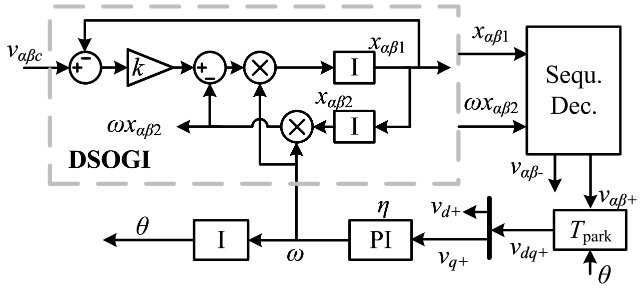

Figure 3.6: Basic scheme of DSOGI-PLL

The complete state-space model of the DSOGI-PLL is

$$\begin{aligned} \dot{x}_{\alpha\beta 1} &= -k\omega x_{\alpha\beta 1} - \omega^2 x_{\alpha\beta 2} + k\omega v_{\alpha\beta c} \\ \dot{x}_{\alpha\beta 2} &= x_{\alpha\beta 1} \\ \dot{\eta} &= k_i v_{q+} = k_i \mathrm{Im}\left\{v_{dq+}\right\} \\ \dot{\theta} &= \omega = \eta + k_p v_{q+} = \eta + k_p \mathrm{Im}\left\{v_{dq+}\right\} \end{aligned} \tag{3.7}$$

along with the algebraic relation

$$v_{q+} = \mathrm{Im}\left\{v_{dq+}\right\} = \mathrm{Im}\left\{e^{-j\theta}\cdot\frac{x_{\alpha\beta 1} + j\omega x_{\alpha\beta 2}}{2}\right\}.$$

Equation (3.3) and (3.6) describe the basic principle of the DSRF and DSOGI structures by assuming that the phase angle and frequency used by those two blocks are perfectly synchronized to those of the positive-sequence component of the input voltage. This assumption is adopted by all existing LTI models. However, as given in Eq. (3.4) and (3.7), the phase angle and frequency are actually estimated by the PLL itself. It will be demonstrated in the next chapter that neglecting the phase angle or frequency feedback coupling in the PSCD structure can result in wrong stability assessment results.

Current Reference Calculation

The power control of the GFL converter is based on the instantaneous power theory. Define

$$S_r = P_r + jQ_r$$

as the complex power reference, the current reference in the *dq* frame and the $\alpha\beta$ frame are determined by

$$i_{dqr} = i_{dr} + ji_{qr} = \frac{2}{3}\left(\frac{S_r}{v_{dq+}}\right)^* \tag{3.8}$$

and

$$i_{\alpha\beta r} = i_{\alpha r} + ji_{\beta r} = \frac{2}{3}\left(\frac{S_r}{v_{\alpha\beta+}}\right)^* \tag{3.9}$$

respectively.

Current Control

Figure 3.7 shows block diagrams of the current controller in the *dq* frame. The complex-valued state-space equation of the PI current controller is given by

$$\dot{x}_{dqC} = k_{iC}\left(i_{dqr} - i_{dqf}\right) \tag{3.10}$$

along with the algebraic relation

$$v_{dqr} = x_{dqC} + k_{pC}\left(i_{dqr} - i_{dqf}\right) + j\omega_0 L i_{dqf} \tag{3.11}$$

where k_{pC} and k_{iC} are PI coefficients, and x_{dqC} is the state variable of the integrator. $i_{\alpha\beta f}$ is the converter-side filter inductor current. Neglecting the switching process and the time delay caused by the modulation and sampling, the voltage command v_{dqr} (or $v_{\alpha\beta r}$) can be regarded as the terminal voltage of the converter.

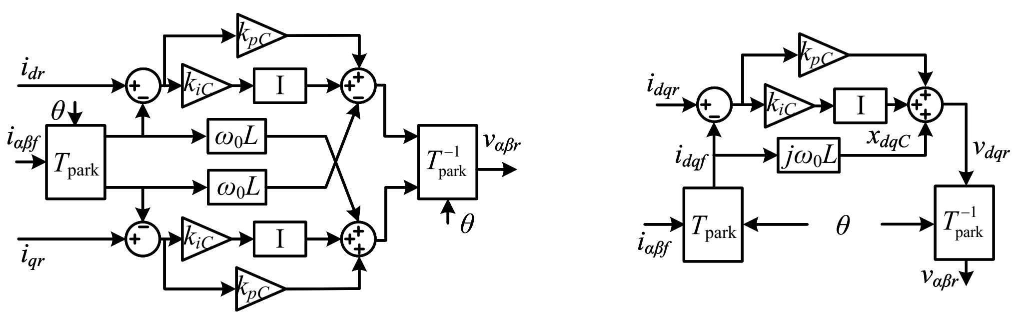

Figure 3.7: Block diagrams of PI current controller. Left: real domain implementation. Right: complex domain representation.

In $\alpha\beta$ frame, the current reference $i_{\alpha\beta r}$ is a time-periodic signal. To achieve zero steady-state control error, the frequency-adaptive PR controller can be used for the current control. To make these two categories of current controllers (PI and PR controllers) comparable, the 1st-order PR controller shown in Figure 3.8 is adopted in this thesis. The state-space description of the PR controller is given by

$$\dot{x}_{\alpha\beta C} = k_{rC}\left(i_{\alpha\beta r} - i_{\alpha\beta f}\right) + j\omega x_{\alpha\beta C} \tag{3.12}$$

with the algebraic relation

$$v_{\alpha\beta r} = x_{\alpha\beta C} + k_{pC}\left(i_{\alpha\beta r} - i_{\alpha\beta f}\right) \tag{3.13}$$

where k_{pC} and k_{rC} are PR coefficients, and $x_{\alpha\beta C}$ is the state variable for the integrator.

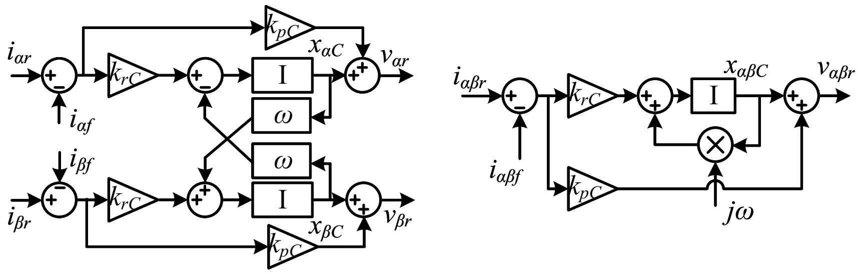

Figure 3.8: Block diagrams of PR current controller. Left: real domain implementation. Right: complex domain representation.

LC(L) Filter and Grid Impedance

Since the grid-side filter inductor shares the same state variable with the grid impedance, it is treated as part of the grid impedance. The passive LC(L) filter and grid impedance are assumed to be linear. In the $\alpha\beta$ frame, their dynamics can be described by

$$\begin{aligned}
\frac{d}{dt} i_{\alpha\beta f} &= -\frac{R}{L} i_{\alpha\beta f} + \frac{1}{L} v_{\alpha\beta r} - \frac{1}{L} v_{\alpha\beta \mathrm{c}} \\
\frac{d}{dt} v_{\alpha\beta \mathrm{c}} &= \frac{1}{C} i_{\alpha\beta f} - \frac{1}{C} i_{\alpha\beta g} \\
\frac{d}{dt} i_{\alpha\beta g} &= -\frac{R_g}{L_g} i_{\alpha\beta g} + \frac{1}{L_{\mathrm{g}}} v_{\alpha\beta \mathrm{c}} - \frac{1}{L_g} v_{\alpha\beta g}
\end{aligned} \tag{3.14}$$

where $i_{\alpha\beta g}$ is the current flowing through the grid impedance, $v_{\alpha\beta g}$ is the voltage at the grid connection point, see Figure 3.3. State variables in different reference frames are linked by the Park respectively inverse Park transformation:

$$\begin{aligned}
&i_{dqf} = e^{-j\theta} i_{\alpha\beta f} \quad i_{dqg} = e^{-j\theta} i_{\alpha\beta g} \\
&v_{dqc} = e^{-j\theta} v_{\alpha\beta c} \quad v_{dqg} = e^{-j\theta} v_{\alpha\beta g} \quad v_{\alpha\beta r} = e^{j\theta} v_{dqr}
\end{aligned} \tag{3.15}$$

Inserting the relation given by Eq. (3.15), the state-space model of the LC filter and grid impedance in the dq frame is obtained

$$\begin{aligned}
\frac{d}{dt} i_{dqf} &= -j\omega i_{dqf} - \frac{R}{L} i_{dqf} + \frac{1}{L} v_{dqr} - \frac{1}{L} v_{dqc} \\
\frac{d}{dt} v_{dqc} &= -j\omega v_{dqc} + \frac{1}{C} i_{dqf} - \frac{1}{C} i_{dqg} \\
\frac{d}{dt} i_{dqg} &= -j\omega i_{dqg} - \frac{R_g}{L_g} i_{dqg} + \frac{1}{L_{\mathrm{g}}} v_{dqc} - \frac{1}{L_g} v_{dqg}
\end{aligned} \quad . \tag{3.16}$$

Nonlinear terms indicated by the red color in Eq. (3.16) result from the transformation between the $\alpha\beta$ and dq frames given by Eq. (3.15).

Steady-State Analysis

Let

$$V_{\alpha\beta c} = V_{\alpha\beta c+}e^{j\omega_0 t} + V_{\alpha\beta c-}e^{-j\omega_0 t}$$

and

$$V_{\alpha\beta g} = V_{\alpha\beta g+}e^{j\omega_0 t} + V_{\alpha\beta g-}e^{-j\omega_0 t}$$

denote steady-state operation trajectories of the unbalanced filter capacitor voltage $v_{\alpha\beta c}$ and the grid voltage $v_{\alpha\beta g}$. The steady-state value of the converter-side filter inductor current $i_{\alpha\beta f}$ will also be unbalanced, which can be written as

$$I_{\alpha\beta f} = I_{\alpha\beta f+}e^{j\omega_0 t} + I_{\alpha\beta f-}e^{-j\omega_0 t}.$$

The current controller ensures that the positive-sequence current $I_{\alpha\beta f+}$ equals the reference value, namely

$$I_{\alpha\beta f+} = \frac{2}{3}\left(\frac{S_r}{V_{\alpha\beta c+}}\right)^*. \tag{3.17}$$

The signal flow graph of the negative-sequence current is shown in Figure 3.9, the algebraic relation for PI and PR controller are given by

$$I_{\alpha\beta f-} = \frac{1}{2j\omega_0 L - R - k_{pC} + k_{iC}/\left(2j\omega_0\right)}V_{\alpha\beta c-} \tag{3.18}$$

and

$$I_{\alpha\beta f-} = \frac{1}{j\omega_0 L - R - k_{pC} + k_{rC}/\left(2j\omega_0\right)}V_{\alpha\beta c-} \tag{3.19}$$

respectively.

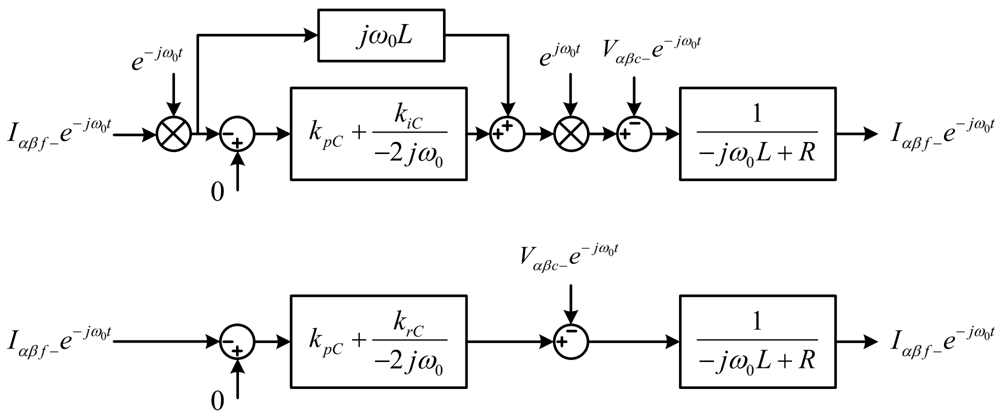

Figure 3.9: Signal flow graphs of the negative-sequence current. Top: the PI current controller. Bottom: the PR current controller.

Based on Kirchhoff's current law, two equations can be derived from the steady-state equivalent circuit shown in Figure 3.10

$$f_{GFL+} = I_{\alpha\beta f+} - j\omega_0 C V_{\alpha\beta c+} - \frac{V_{\alpha\beta c+} - V_{\alpha\beta g+}}{R_g + j\omega_0 L_g} = 0 \tag{3.20}$$

$$f_{GFL-} = I_{\alpha\beta f-} + j\omega_0 C V_{\alpha\beta c-} - \frac{V_{\alpha\beta c-} - V_{\alpha\beta g-}}{R_g - j\omega_0 L_g} = 0 \tag{3.21}$$

which are sufficient for solving of the two unknown voltages $V_{\alpha\beta c+}$ and $V_{\alpha\beta c-}$ of the grid-following converter.

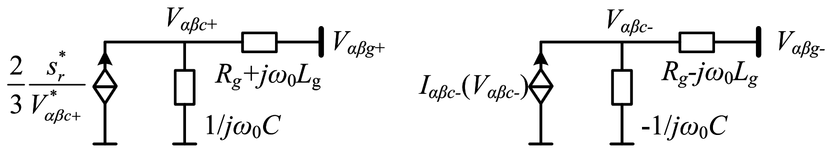

Figure 3.10: Steady-state positive (left) and negative (right) sequence equivalent circuits of the grid-following converter.

3.1.2 Grid-Forming Voltage Source Converters

With increasing penetration of renewable energy sources, grid-connected converters are required to provide voltage and frequency regulation capability instead of just injecting maximum available power. To achieve this, the GFM control draws more and more attention. In this subsection, the state-of-the-art virtual synchronous generator (VSG) algorithm emulating both the stationary droop and dynamic inertia characteristics of the conventional synchronous generator is adopted.

Figure 3.11 illustrates a VSG-controlled single converter system. The VSG algorithm consists mainly of two parts. First, an outer power control loop generates the voltage phase angle θ and magnitude E, as shown in Figure 3.12. Second, an inner cascaded voltage-current control loop shown in Figure 3.13 is designed to reject high frequency disturbances. Additionally, a virtual impedance is introduced in the inner control to improve system stability and power sharing accuracy.

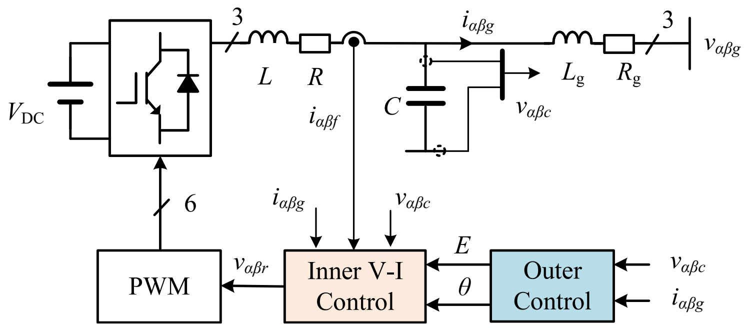

Figure 3.11: Schematic and control of a single VSG converter system

Outer Power Control

As shown in Figure 3.12, the instantaneous power s_{VSG} obtained from

$$s_{VSG} = p + jq = \frac{3}{2} v_{\alpha\beta c} i^*_{\alpha\beta g}$$

is passed through a 1st-order low-pass filter

$$G_{LPF}(s) = \frac{\omega_s}{s + \omega_s}$$

with a cut-off frequency of ω_s. The state-space description is given by

$$\dot{S} = -\omega_s S + \omega_s s_{VSG} \tag{3.22}$$

where $S = P + jQ$ is the state variable of the LPF. Different from the conventional droop control, the swing equation is added in the active power loop of the VSG algorithm to provide inertia support

$$\begin{aligned}
\dot{\omega} &= \frac{1}{J\omega_0}\left(\mathrm{Re}\{S_r\} - \mathrm{Re}\{S\} + k_P(\omega_0 - \omega)\right) \\
&= \frac{1}{J\omega_0}\left(\frac{S_r + S_r^*}{2} - \frac{S + S^*}{2} + k_P(\omega_0 - \omega)\right) \\
\dot{\theta} &= \omega
\end{aligned} \tag{3.23}$$

where $S_r = P_r + jQ_r$ is the power reference. J is the inertia constant. k_P denotes the active power droop coefficient.

The reactive power loop determines the voltage magnitude according to the droop equation

$$\begin{aligned}
E &= E_0 + \frac{\mathrm{Im}\{S_r\} - \mathrm{Im}\{S\}}{k_Q} \\
&= E_0 + \frac{\frac{S_r - S_r^*}{2j} - \frac{S - S^*}{2j}}{k_Q}
\end{aligned} \tag{3.24}$$

with E_0 the rated voltage magnitude. k_Q is the reactive power droop coefficient.

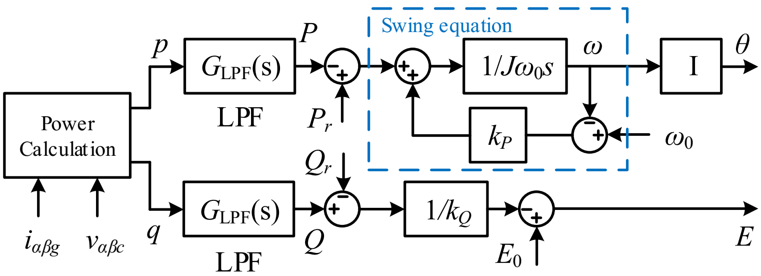

Figure 3.12: Block diagram of the outer power control loop

Inner Cascaded Voltage-Current Control

As shown in Figure 3.13, the inner control consists of three parts, namely the virtual impedance $Z_v(s)$ and voltage as well as current control implemented with standard PI controllers.

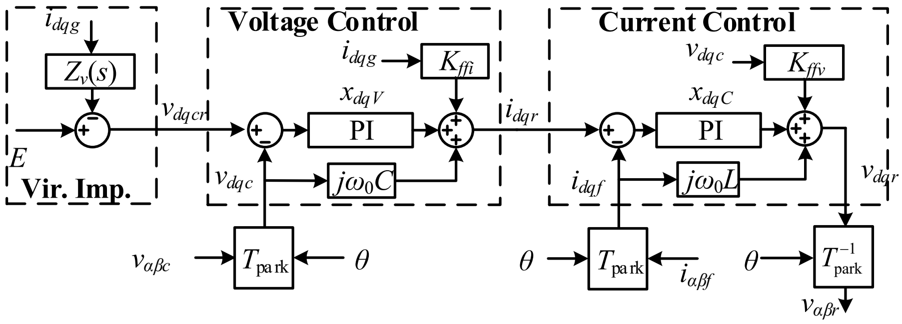

Figure 3.13: Block diagram of the inner cascaded voltage-current control loop with the virtual impedance

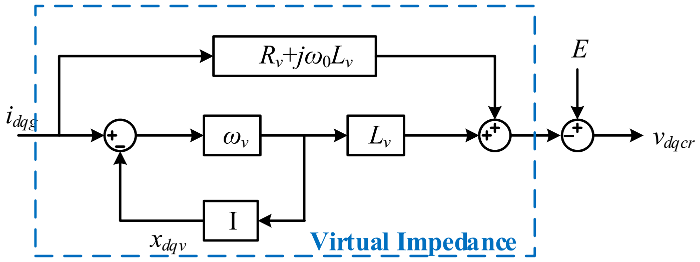

Figure 3.14: Block diagram of the virtual impedance $Z_v(s)$

The virtual impedance

$$Z_v(s) = \frac{\omega_v}{s+\omega_v} sL_v + R_v + j\omega_0 L_v$$

shown in Figure 3.14 is described by the state-space equation

$$\dot{x}_{dqv} = -\omega_v x_{dqv} + \omega_v i_{dqg} \tag{3.25}$$

where ω_v is the bandwidth of the 1st-order low-pass filter $\frac{\omega_v}{s+\omega_v}$ in $Z_v(s)$.

The reference value of the filter capacitor voltage is synthesized from the outputs of the reactive power loop and the virtual impedance unit

$$v_{dqcr} = E - \left(L_v \omega_v \left(i_{dqg} - x_{dqv}\right) + \left(R_v + j\omega_0 L_v\right) i_{dqg}\right). \tag{3.26}$$

The state-space equation of the voltage controller is

$$\dot{x}_{dqV} = k_{iV} \left(v_{dqcr} - v_{dqc}\right) \tag{3.27}$$

together with the algebraic relation for its output

$$i_{dqr} = x_{dqV} + k_{pV} \left(v_{dqcr} - v_{dqc}\right) + j\omega_0 C v_{dqc} + K_{ffi} i_{dqg} \tag{3.28}$$

where k_{pV} and k_{iV} are the proportional and integral coefficients of the voltage PI controller, and the state variable x_{dqV} is related to the integrator. K_{ffi} is the current feedforward gain.

The PI current controller takes the output of the voltage controller as the reference command, and the state-space model is

$$\dot{x}_{dqC} = k_{iC}\left(i_{dqr} - i_{dqf}\right). \tag{3.29}$$

Again, the output of the current controller

$$v_{dqr} = x_{dqC} + k_{pC}\left(i_{dqr} - i_{dqf}\right) + j\omega_0 L i_{dqf} + K_{ffv} v_{dqc} \tag{3.30}$$

is regarded as the terminal voltage of the converter. k_{pC} and k_{iC} are the proportional and integral coefficients of the current controller, and x_{dqC} is the state variable of the integrator. K_{ffv} is the voltage feedforward gain.

The state-space model of the LC filter and grid impedance of the grid-forming converter is the same as that of the grid-following converter given by Eq. (3.14) and Eq. (3.16). Variables in different reference frames share the relations described already by Eq. (3.15).

Steady-State Analysis

Let

$$V_{\alpha\beta c} = V_{\alpha\beta c+} e^{j\omega_0 t}$$

and

$$I_{\alpha\beta g} = I_{\alpha\beta g+} e^{j\omega_0 t}$$

denote steady-state values of the balanced filter capacitor voltage $v_{\alpha\beta c}$ and grid-side current $i_{\alpha\beta g}$. Then, for the fundamental frequency, the virtual impedance defines the relation

$$V_{\alpha\beta v+} = V_{\alpha\beta c+} + \left(R_v + j\omega_0 L_v\right) I_{\alpha\beta g+} \tag{3.31}$$

where $V_{\alpha\beta v+}$ is a virtual voltage constrained by the droop equation

$$f_{VSG+} = S_r - \frac{3}{2} V_{\alpha\beta c+} I^*_{\alpha\beta g+} - k_P\left(\omega - \omega_0\right) - 1j \cdot k_Q\left(\sqrt{V_{\alpha\beta v+} V^*_{\alpha\beta v+}} - E_0\right) = 0. \tag{3.32}$$

Under grid-connected operations, the steady-state value of ω is fixed by the stiff grid to ω_0. Equation (3.32) is sufficient for solving the only unknown variable $V_{\alpha\beta c+}$. The steady-state equivalent circuit is shown in Figure 3.15. For islanded operations, ω becomes another unknown variable. Since no stiff grid bus exists, the capacitor voltage of the grid-forming converter needs to be selected to provide the phase angle reference. If the phase angle of $V_{\alpha\beta c+}$ is set to zero, yields

$$f_{VSG\omega} = V_{\alpha\beta c+} - V^*_{\alpha\beta c+} = 0. \tag{3.33}$$

This additional relation makes the number of equations and unknown variables the same.

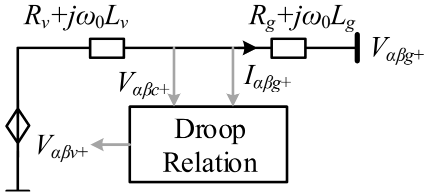

Figure 3.15: Steady-state positive sequence equivalent circuit of the grid-forming converter

3.1.3 Power Networks and Passive Loads

Power Networks

The power networks are modeled as three-phase RL branches. In the natural *abc* reference frame, the state-space equation of the ith three-phase branch connected between the mth bus and the nth bus is given by

$$\boldsymbol{L}_{abc,i}\frac{d}{dt}\begin{bmatrix} i_{a,i} \\ i_{b,i} \\ i_{c,i} \end{bmatrix} = -\boldsymbol{R}_{abc,i}\begin{bmatrix} i_{a,i} \\ i_{b,i} \\ i_{c,i} \end{bmatrix} + \begin{bmatrix} v_{a,m} \\ v_{b,m} \\ v_{c,m} \end{bmatrix} - \begin{bmatrix} v_{a,n} \\ v_{b,n} \\ v_{c,n} \end{bmatrix} \tag{3.34}$$

where $[v_{a,m},\ v_{b,m},\ v_{c,m}]^T$ and $[v_{a,n},\ v_{b,n},\ v_{c,n}]^T$ denote three-phase nodal voltages at the mth bus and the nth bus. $[i_{a,i},\ i_{b,i},\ i_{c,i}]^T$ is the three-phase branch current. Diagonal matrices $\boldsymbol{L}_{abc,i}=\mathrm{diag}\left([L_{a,i},\ L_{b,i},\ L_{c,i}]\right)$ and $\boldsymbol{R}_{abc,i}=\mathrm{diag}\left([R_{a,i},\ R_{b,i},\ R_{c,i}]\right)$ give the inductance and resistance of each phase. The branch can be unbalanced, namely diagonal elements of $\boldsymbol{L}_{abc,i}$ and $\boldsymbol{R}_{abc,i}$ can be different.

In the complex domain, the state-space equation of the branch can be derived from Eq. (3.34) by using the Clarke transformation and the real-complex-domain transformation

$$\boldsymbol{L}_{mn}\frac{d}{dt}\begin{bmatrix} i_{\alpha\beta Branch,i} \\ i^*_{\alpha\beta Branch,i} \end{bmatrix} = -\boldsymbol{R}_{mn}\begin{bmatrix} i_{\alpha\beta Branch,i} \\ i^*_{\alpha\beta Branch,i} \end{bmatrix} + \begin{bmatrix} v_{\alpha\beta,m} \\ v^*_{\alpha\beta,m} \end{bmatrix} - \begin{bmatrix} v_{\alpha\beta,n} \\ v^*_{\alpha\beta,n} \end{bmatrix} \tag{3.35}$$

with

$$\begin{aligned} \boldsymbol{L}_{mn} &= \boldsymbol{T}_{r2c}\boldsymbol{T}_{Clarke}\boldsymbol{L}_{abc,i}\boldsymbol{T}^{-1}_{Clarke}\boldsymbol{T}_{c2r} \\ \boldsymbol{R}_{mn} &= \boldsymbol{T}_{r2c}\boldsymbol{T}_{Clarke}\boldsymbol{R}_{abc,i}\boldsymbol{T}^{-1}_{Clarke}\boldsymbol{T}_{c2r} \\ \left[i_{\alpha\beta Branch,i},\ i^*_{\alpha\beta Branch,i}\right]^T &= \boldsymbol{T}_{r2c}\boldsymbol{T}_{Clarke}\left[i_{a,i},\ i_{b,i},\ i_{c,i}\right]^T \\ \left[v_{\alpha\beta,m},\ v^*_{\alpha\beta,m}\right]^T &= \boldsymbol{T}_{r2c}\boldsymbol{T}_{Clarke}\left[v_{a,m},\ v_{b,m},\ v_{c,m}\right]^T \\ \left[v_{\alpha\beta,n},\ v^*_{\alpha\beta,n}\right]^T &= \boldsymbol{T}_{r2c}\boldsymbol{T}_{Clarke}\left[v_{a,n},\ v_{b,n},\ v_{c,n}\right]^T \end{aligned}. \tag{3.36}$$

Let

$$\begin{aligned} I_{\alpha\beta Branch,i} &= I_{\alpha\beta Branch+,i}e^{j\omega_0 t} + I_{\alpha\beta Branch-,i}e^{-j\omega_0 t} \\ V_{\alpha\beta,m} &= V_{\alpha\beta+,m}e^{j\omega_0 t} + V_{\alpha\beta-,m}e^{-j\omega_0 t} \\ V_{\alpha\beta,n} &= V_{\alpha\beta+,n}e^{j\omega_0 t} + V_{\alpha\beta-,n}e^{-j\omega_0 t} \end{aligned} \tag{3.37}$$

denote steady-state values of $i_{\alpha\beta Branch,i}$, $v_{\alpha\beta,m}$ and $v_{\alpha\beta,n}$. Their complex conjugates are

$$\begin{aligned} I^*_{\alpha\beta Branch,i} &= I^*_{\alpha\beta Branch+,i}e^{-j\omega_0 t} && + I^*_{\alpha\beta Branch-,i}e^{j\omega_0 t} \\ V^*_{\alpha\beta,m} &= V^*_{\alpha\beta+,m}e^{-j\omega_0 t} && + V^*_{\alpha\beta-,m}e^{j\omega_0 t} \\ V^*_{\alpha\beta,n} &= V^*_{\alpha\beta+,n}e^{-j\omega_0 t} && + V^*_{\alpha\beta-,n}e^{j\omega_0 t} \end{aligned} . \tag{3.38}$$

Applying Fourier transform to Eq. (3.35), the red terms in Eq. (3.37) and Eq. (3.38) are linked by

$$\begin{bmatrix} I_{\alpha\beta Branch+,i} \\ I^*_{\alpha\beta Branch-,i} \end{bmatrix} = \boldsymbol{Y}_{mn}\left(\begin{bmatrix} V_{\alpha\beta+,m} \\ V^*_{\alpha\beta-,m} \end{bmatrix} - \begin{bmatrix} V_{\alpha\beta+,n} \\ V^*_{\alpha\beta-,n} \end{bmatrix}\right) \tag{3.39}$$

where the branch admittance matrix $\boldsymbol{Y}_{mn}$ is given by

$$\boldsymbol{Y}_{mn} = (j\omega_0 \boldsymbol{L}_{mn} + \boldsymbol{R}_{mn})^{-1} = \begin{bmatrix} Y^{++}_{mn} & Y^{+-}_{mn} \\ Y^{-+}_{mn} & Y^{--}_{mn} \end{bmatrix} \tag{3.40}$$

Resistive-Inductive Loads

There exist different types of loads in the electric power systems, RL loads are taken as an example here. Mathematically, it can be treated as an RL branch connected between a bus and the ground. When the ith load is connected to the mth bus, according to the aforementioned modeling procedure of RL branches, the complex-domain state-space equation of the load can be derived

$$\boldsymbol{L}_i \frac{d}{dt}\begin{bmatrix} i_{\alpha\beta Load,i} \\ i^*_{\alpha\beta Load,i} \end{bmatrix} = -\boldsymbol{R}_i \begin{bmatrix} i_{\alpha\beta Load,i} \\ i^*_{\alpha\beta Load,i} \end{bmatrix} + \begin{bmatrix} v_{\alpha\beta,m} \\ v^*_{\alpha\beta,m} \end{bmatrix} \tag{3.41}$$

with

$$\begin{aligned} \boldsymbol{L}_i &= \boldsymbol{T}_{r2c}\boldsymbol{T}_{Clarke}\boldsymbol{L}_{Load,i}\boldsymbol{T}^{-1}_{Clarke}\boldsymbol{T}_{c2r} \\ \boldsymbol{R}_i &= \boldsymbol{T}_{r2c}\boldsymbol{T}_{Clarke}\boldsymbol{R}_{Load,i}\boldsymbol{T}^{-1}_{Clarke}\boldsymbol{T}_{c2r} \end{aligned} \tag{3.42}$$

where $\boldsymbol{L}_{Load,i}$ and $\boldsymbol{R}_{Load,i}$ are real-valued three-phase load inductance and resistance matrices.

Let

$$I_{\alpha\beta Load,i} = I_{\alpha\beta Load+,i}e^{j\omega_0 t} + I_{\alpha\beta Load-,i}e^{-j\omega_0 t}$$

denote the steady-state trajectory of the load current $i_{\alpha\beta Load,i}$, it can be deduced from Eq. (3.41)

$$\begin{bmatrix} I_{\alpha\beta Load+,i} \\ I^*_{\alpha\beta Load-,i} \end{bmatrix} = \boldsymbol{Y}_i \begin{bmatrix} V_{\alpha\beta+,m} \\ V^*_{\alpha\beta-,m} \end{bmatrix} \tag{3.43}$$

where load admittance matrix $\boldsymbol{Y}_i$ is given by

$$\boldsymbol{Y}_i = (j\omega_0 \boldsymbol{L}_i + \boldsymbol{R}_i)^{-1} = \begin{bmatrix} Y^{++}_i & Y^{+-}_i \\ Y^{-+}_i & Y^{--}_i \end{bmatrix}. \tag{3.44}$$

3.1.4 Steady-State Power Flow Calculation

For a grid-connected converter-dominated power system with

- one reference bus,
- N_{Load} RL passive loads,

- N_{Bus} feeder buses and N_{GFL} grid-following converters,

considering unbalanced operations, $2N_{Bus}$ unknown bus voltages and $2N_{GFL}$ unknown filter capacitor voltages need to be solved, half positive-sequence voltages and half negative-sequence voltages.

According to Eq. (3.20) and (3.21), $2N_{GFL}$ equations can be formulated for the grid-following converters. The other $2N_{Bus}$ equations can be obtained by applying Kirchhoff's current law to each bus. Specifically, taking the mth bus as an example, following equations can be deduced

$$f_{Bus+,m} = 0 = \begin{cases} \sum_{i=1}^{N_{\text{Bus}}} \delta_{mi}^{Branch} \left(Y_{mi}^{++} \left(V_{\alpha\beta+,m} - V_{\alpha\beta+,i}\right) + Y_{mi}^{+-} \left(V_{\alpha\beta-,m}^{*} - V_{\alpha\beta-,i}^{*}\right)\right) \\ + \sum_{i=1}^{N_{GFL}} \delta_{mi}^{GFL} \frac{V_{\alpha\beta+,m} - V_{\alpha\beta c+,m}}{R_{g,i} + j\omega_0 L_{g,i}} \\ + \sum_{i=1}^{N_{Load}} \delta_{mi}^{Load} \left(Y_{Load,i}^{++} V_{\alpha\beta+,m} + Y_{Load,i}^{+-} V_{\alpha\beta-,m}^{*}\right) \end{cases} \tag{3.45}$$

$$f_{\text{Bus}-,m} = 0 = \begin{cases} \sum_{i=1}^{N_{Bus}} \delta_{mi}^{Branch} \left(Y_{mi}^{-+} \left(V_{\alpha\beta+,m} - V_{\alpha\beta+,i}\right) + Y_{mi}^{--} \left(V_{\alpha\beta-,m}^{*} - V_{\alpha\beta-,i}^{*}\right)\right) \\ + \sum_{i=1}^{N_{GFL}} \delta_{mi}^{GFL} \frac{V_{\alpha\beta-,m}^{*} - V_{\alpha\beta c-,m}^{*}}{R_{g,i} + j\omega_0 L_{g,i}} \\ + \sum_{i=1}^{N_{Load}} \delta_{mi}^{L} \left(Y_{Load,i}^{-+} V_{\alpha\beta+,m} + Y_{Load,i}^{--} V_{\alpha\beta-,m}^{*}\right) \end{cases} \tag{3.46}$$

where $R_{g,i}$ and $L_{g,i}$ denote parameters of the grid impedance of the ith grid-following converter. δ_{mi}^{Branch}, δ_{mi}^{GFL} and δ_{mi}^{Load} are connectivity indicators of branches, grid-following converters and loads, respectively. They follow the definition:

- δ_{mi}^{Branch} equals one when there exists a branch between the mth bus and the ith bus, otherwise it is zero.

- δ_{mi}^{GFL} equals one when the mth grid-following converter is connected to the mth bus, otherwise it is zero.

- δ_{mi}^{Load} equals one when the mth load is connected to the mth bus, otherwise it is zero.

For clarity, Eq. (3.45) is taken as an example to explain the physical meaning behind the power flow equation:

- The first term summarizes all positive-sequence currents flowing from the mth bus to other buses.

- The second term summarizes all positive-sequence currents flowing from the mth bus to all grid-following converters.

- The third term summarizes all positive-sequence currents flowing from the mth bus to all loads.

According to Kirchhoff's current law, the algebraic sum of all those currents flowing away from the mth bus should be zero.

Combine Eq. (3.20), (3.21), (3.45) and (3.46), the steady-state power flow problem can be written in a compact form

$$\boldsymbol{f} = \begin{bmatrix} \left[\underbrace{f_{Bus+,1},\ f_{Bus-,1},\ \cdots,\ f_{Bus+,N_{Bus}},\ f_{Bus-,N_{Bus}}}_{2N_{Bus}} \right]^T \\ \left[\underbrace{f_{GFL+,1},\ f_{GFL-,1},\ \cdots,\ f_{GFL+,N_{GFL}},\ f_{GFL-,N_{GFL}}}_{2N_{GFL}} \right]^T \end{bmatrix} \tag{3.47}$$

with the unknown voltage vector

$$\boldsymbol{V} = \begin{bmatrix} \left[\underbrace{V_{\alpha\beta+,1},\ V_{\alpha\beta-,1},\ \cdots,\ V_{\alpha\beta+,N_{Bus}},\ V_{\alpha\beta-,N_{Bus}}}_{2N_{Bus}} \right]^T \\ \left[\underbrace{V_{\alpha\beta c+,1},\ V_{\alpha\beta c-,1},\ \cdots,\ V_{\alpha\beta c+,N_{GFL}},\ V_{\alpha\beta c-,N_{GFL}}}_{2N_{GFL}} \right]^T \end{bmatrix}. \tag{3.48}$$

Due to the appearance of the non-holomorphic complex conjugate operator and the real/imaginary part extraction operator, the classical complex derivative $\partial \boldsymbol{f}/\partial \boldsymbol{V}$ does not exist, thus, the Newton-Raphson method cannot be directly utilized to solve the nonlinear equations defined by Eq. (3.47) and (3.48). The Wirtinger calculus is used to overcome this issue by extending Eq. (3.47) and (3.48) to

$$\begin{bmatrix} \boldsymbol{f} \\ \boldsymbol{f}^* \end{bmatrix}^{4(N_{Bus}+N_{GFL})\times 1} \qquad \begin{bmatrix} \boldsymbol{V} \\ \boldsymbol{V}^* \end{bmatrix}^{4(N_{Bus}+N_{GFL})\times 1} \tag{3.49}$$

which can now be solved with the Newton-Raphson method by using the Jacobian matrix $\boldsymbol{J}_{PF}$ defined within the Wirtinger calculus framework

$$\boldsymbol{J}_{PF} = \begin{bmatrix} \frac{\partial \boldsymbol{f}}{\partial \boldsymbol{V}} & \frac{\partial \boldsymbol{f}}{\partial \boldsymbol{V}^*} \\ \frac{\partial \boldsymbol{f}^*}{\partial \boldsymbol{V}} & \frac{\partial \boldsymbol{f}^*}{\partial \boldsymbol{V}^*} \end{bmatrix}^{4(N_{Bus}+N_{GFL})\times 4(N_{Bus}+N_{GFL})}. \tag{3.50}$$

It should be clarified that, by separating the real and imaginary parts of Eq. (3.47) and (3.48), i.e.,

$$\begin{bmatrix} \mathrm{Re}\{\boldsymbol{f}\} \\ \mathrm{Im}\{\boldsymbol{f}\} \end{bmatrix}^{4(N_{Bus}+N_{GFL})\times 1} \qquad \begin{bmatrix} \mathrm{Re}\{\boldsymbol{V}\} \\ \mathrm{Im}\{\boldsymbol{V}\} \end{bmatrix}^{4(N_{Bus}+N_{GFL})\times 1}, \tag{3.51}$$

unknown bus voltages can also be solved with the classical real-valued Jacobian matrix. However, the compactness of the complex variables is lost. Besides, compared to Eq. (3.51), the number of independent variables and consequently of derivatives in Eq. (3.49) and (3.50) is halved, requiring less computation time and exhibiting better convergence [110].

Under balanced conditions, only positive-sequence voltages need to be solved. Moreover, considering the existence of grid-forming converters, Eq. (3.45) needs to be modified as

$$f_{\mathrm{Bus}+,m} = 0 = \begin{cases} \sum_{i=1}^{N_{Bus}} \delta_{mi}^{Branch} Y_{mi}^{++} \left(V_{\alpha\beta+,m} - V_{\alpha\beta+,i}\right) \\ + \sum_{i=1}^{N_{GFL}} \delta_{mi}^{GFL} \frac{V_{\alpha\beta+,m} - V_{\alpha\beta c+,m}^{GFL}}{R_{g,i} + j\omega_0 L_{g,i}} \\ + \sum_{i=1}^{N_{Load}} \delta_{mi}^{Load} Y_{Load,i}^{++} V_{\alpha\beta+,m} \\ + \sum_{i=1}^{N_{VSG}} \delta_{mi}^{VSG} \frac{V_{\alpha\beta+,m} - V_{\alpha\beta c+,i}^{VSG}}{R_{g,i} + j\omega_0 L_{g,i}} \end{cases} \tag{3.52}$$

where N_{VSG} is the number of the grid-forming converters. The connectivity indicator δ_{mi}^{VSG} equals one when the ith grid-forming converter is connected to the mth bus. The superscript GFL and VSG is added to the voltage variables to distinguish between the filter capacitor voltages of the GFL converters and VSG converters.

Then, the power flow equations and the unknown voltage vector become

$$\boldsymbol{f} = \begin{bmatrix} \begin{bmatrix} \underbrace{f_{Bus+,1} \ \cdots, \ f_{Bus+,N_{Bus}}}_{N_{Bus}} \end{bmatrix}^T \\ \begin{bmatrix} \underbrace{f_{GFL+,1}, \ \cdots, \ f_{GFL+,N_{GFL}}}_{N_{GFL}} \end{bmatrix}^T \\ \begin{bmatrix} \underbrace{f_{VSG+,1}, \ \cdots, \ f_{VSG+,N_{GFL}}}_{N_{VSG}} \end{bmatrix}^T \end{bmatrix} \tag{3.53}$$

and

$$\boldsymbol{V} = \begin{bmatrix} \begin{bmatrix} \underbrace{V_{\alpha\beta+,1}, \ \cdots, \ V_{\alpha\beta+,N_{Bus}}}_{N_{Bus}} \end{bmatrix}^T \\ \begin{bmatrix} \underbrace{V_{\alpha\beta c+,1}^{GFL}, \ \cdots, \ V_{\alpha\beta c+,N_{GFL}}^{GFL}}_{N_{GFL}} \end{bmatrix}^T \\ \begin{bmatrix} \underbrace{V_{\alpha\beta c+,1}^{VSG}, \ \cdots, \ V_{\alpha\beta c+,N_{VSG}}^{VSG}}_{N_{VSG}} \end{bmatrix}^T \end{bmatrix}. \tag{3.54}$$

When the system is operated in islanded mode, one extra unknown variable, the steady-state system frequency ω, should be added into Eq. (3.54). Accordingly, Eq. (3.33) needs to be included into Eq. (3.53).

3.2 Small-Signal Model

3.2.1 Small-Signal Model of Grid-Following Converters

For the implementation of the GFL converter, there exist different possibilities to combine the PLL and the current controller. Among them, the DSRF-PLL plus the PI current controller and the DSOGI-PLL plus the PR current controller are two straightforward and widely adopted variants, considering that the control is either implemented in the dq frame or the $\alpha\beta$ frame. In this thesis, these two variants are defined as Type I and Type II GFL converter, respectively. Without loss of generality, the Type I GFL converter is taken as an example to explain the derivation of the small-signal model of the GFL converter.

DSRF-PLL

Since the imaginary part extraction operator $\mathrm{Im}\{\cdot\}$ is non-holomorphic, the nonlinear state-space model of the DSRF-PLL given by Eq. (3.4) must be linearized within Wirtinger calculus framework, yielding

$$\begin{aligned}
\Delta\dot{v}_{dq+} &= \omega_f \left(-\Delta v_{dq+} - e^{-j2\theta_0}\Delta v_{dq-} + e^{-j\theta_0}\Delta v_{\alpha\beta c} + j\left(2e^{-j2\theta_0}V_{dq-} - e^{-j\theta_0}V_{\alpha\beta c}\right)\Delta\theta\right)\\
\Delta\dot{v}_{dq-} &= \omega_f \left(-\Delta v_{dq-} - e^{2j\theta_0}\Delta v_{dq+} + e^{j\theta_0}\Delta v_{\alpha\beta c} + j\left(-2e^{j2\theta_0}V_{dq+} + e^{j\theta_0}V_{\alpha\beta c}\right)\Delta\theta\right)\\
\Delta\dot{v}^*_{dq+} &= \omega_f \left(-\Delta v^*_{dq+} - e^{j2\theta_0}\Delta v^*_{dq-} + e^{j\theta_0}\Delta v^*_{\alpha\beta c} - j\left(2e^{j2\theta_0}V^*_{dq-} - e^{j\theta_0}V^*_{\alpha\beta c}\right)\Delta\theta\right)\\
\Delta\dot{v}^*_{dq-} &= \omega_f \left(-\Delta v^*_{dq-} - e^{-2j\theta_0}\Delta v^*_{dq+} + e^{-j\theta_0}\Delta v^*_{\alpha\beta c} - j\left(-2e^{-j2\theta_0}V^*_{dq+} + e^{-j\theta_0}V^*_{\alpha\beta c}\right)\Delta\theta\right)\\
\Delta\dot{\eta} &= k_i \mathrm{Im}\left\{\Delta v_{dq+}\right\} = -\frac{1}{2}jk_i\left(\Delta v_{dq+} - \Delta v^*_{dq+}\right)\\
\Delta\dot{\theta} &= \Delta\eta + k_p \mathrm{Im}\left\{\Delta v_{dq+}\right\} = \Delta\eta - \frac{1}{2}jk_p\left(\Delta v_{dq+} - \Delta v^*_{dq+}\right)
\end{aligned} \tag{3.55}$$

where θ_0 is the steady-state trajectory of θ, and the steady-state trajectories of other state variables are given by the symbols starting with uppercase letters (e.g., V_{dq+} and V_{dq-}). It is noted that the 3rd and 4th equations of Eq. (3.55) are the complex conjugate version of the first two. As given in the 5th and 6th equations, the imaginary extraction operator $\mathrm{Im}\{\cdot\}$ causes the coupling between variables in the original and conjugate coordinates.

The simplified small-signal model shown in Figure 3.16 is commonly used for the parameter design of advanced PLLs [12]. Dynamics of the DSRF and DSOGI structures are approximated by a first-order low-pass filter and a notch filter. The notch filter to remove the disturbance at $2\omega_0$ (caused by the Park transformation of the negative-sequence voltage) is ignored during the parameter design. Then, the open-loop transfer function of the simplified model becomes a type-2 control system given by

$$G_{ol}(s) = V_+ \cdot \frac{\omega_f}{s+\omega_f} \cdot \left(k_p + \frac{k_i}{s}\right) \cdot \frac{1}{s} = \frac{V_+ k_p \omega_f (s+\omega_z)}{s^2(s+\omega_f)} \tag{3.56}$$

where $\omega_z = k_i/k_p$. Based on the extended symmetrical optimum method [45, 111], only the designed bandwidth ω_c needs to be appropriately selected

$$\begin{cases} \omega_f = g\omega_c \\ k_p = \omega_c/V_+ \\ k_i = k_p\omega_c/g \end{cases}$$

where the constant g is solved from Eq. (3.57) for a desired phase margin PM. Usually, a PM within the range of 30° to 60° is selected [112], which corresponds to $1.732 \leq g \leq 3.732$.

$$PM = \tan^{-1} \frac{g^2 - 1}{2g} \tag{3.57}$$

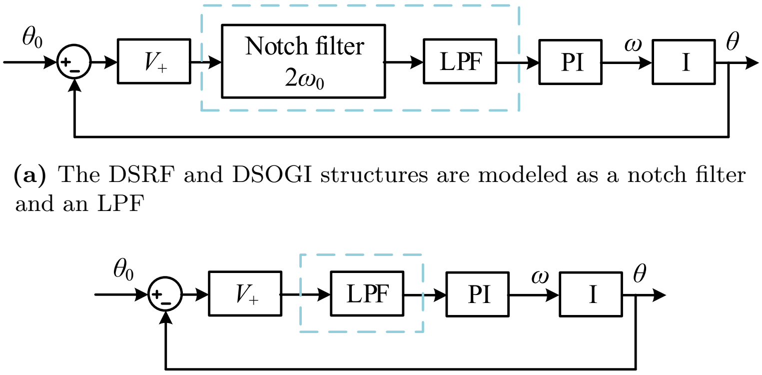

(a) The DSRF and DSOGI structures are modeled as a notch filter and an LPF

(b) Neglecting the notch filter for parameter design

Figure 3.16: Simplified small-signal model of the advanced PLLs.

PI Current Control

Within the Wirtinger calculus framework, the linearization of the current reference calculation unit Eq. (3.8) is given by

$$\begin{aligned} \Delta i_{dqr} &= -\frac{2S_r^*}{3\left(V_{dq+}^*\right)^2}\Delta v_{dq+}^* + \frac{2}{3V_{dq+}^*}\Delta S_r^* \\ \Delta i_{dqr}^* &= -\frac{2S_r}{3(V_{dq+})^2}\Delta v_{dq+} + \frac{2}{3V_{dq+}}\Delta S_r \end{aligned}. \tag{3.58}$$

In the dq frame, the PI current controller described by Eq. (3.10) is inherently linear, the small-signal state-space equation can be directly obtained

$$\Delta \dot{x}_{dqC} = k_{iC}\left(\Delta i_{dqr} - \Delta i_{dqf}\right) \tag{3.59}$$

along with the algebraic equation

$$\Delta v_{dqr} = \Delta x_{dqC} + k_{pC}\left(\Delta i_{dqr} - \Delta i_{dqf}\right) + j\omega_0 L \Delta i_{dqf}. \tag{3.60}$$

LC Filter and Grid Impedance

The state-space model of the LC filter and grid impedance in the $\alpha\beta$ frame given by Eq. (3.14) is linear, of which the small-signal model is

$$\begin{aligned}\frac{d}{dt}\Delta i_{\alpha\beta f} &= -\frac{R}{L}\Delta i_{\alpha\beta f} + \frac{1}{L}\Delta v_{\alpha\beta r} - \frac{1}{L}\Delta v_{\alpha\beta c} \\ \frac{d}{dt}\Delta v_{\alpha\beta c} &= \frac{1}{C}\Delta i_{\alpha\beta f} - \frac{1}{C}\Delta i_{\alpha\beta g} \\ \frac{d}{dt}\Delta i_{\alpha\beta g} &= -\frac{R_g}{L_g}\Delta i_{\alpha\beta g} + \frac{1}{L_g}\Delta v_{\alpha\beta c} - \frac{1}{L_g}\Delta v_{\alpha\beta g}\end{aligned}. \tag{3.61}$$

The linearization of the frame transformation Eq. (3.15) is given by

$$\begin{aligned}\Delta i_{dqf} &= e^{-j\theta_0}\Delta i_{\alpha\beta f} - 1je^{-j\theta_0}I_{\alpha\beta f}\Delta\theta \\ \Delta v_{dqc} &= e^{-j\theta_0}\Delta v_{\alpha\beta c} - 1je^{-j\theta_0}V_{\alpha\beta c}\Delta\theta \\ \Delta v_{dqg} &= e^{-j\theta_0}\Delta v_{\alpha\beta g} - 1je^{-j\theta_0}V_{\alpha\beta g}\Delta\theta \\ \Delta v_{\alpha\beta r} &= e^{j\theta_0}\Delta v_{dqr} + 1je^{j\theta_0}V_{dqr}\Delta\theta\end{aligned}. \tag{3.62}$$

Neglecting the synchronization dynamics of the PLL, in other words, the phase angle of the filter capacitor voltage is assumed to be perfectly known, the block diagram shown in Figure 3.17 can be used to describe the PI current controller and its plant (i.e., the converter-side filter inductor). Based on the pole-zero cancellation principle [113, 114], the closed-loop transfer function of the current control can be simplified as a standard PT1 element

$$G_{clC}(s) = \frac{1}{1+\tau s} \tag{3.63}$$

by choosing the control parameters

$$k_{pC} = \frac{L}{\tau} \quad k_{iC} = \frac{R}{\tau}$$

where τ is defined as the time constant of the current control.

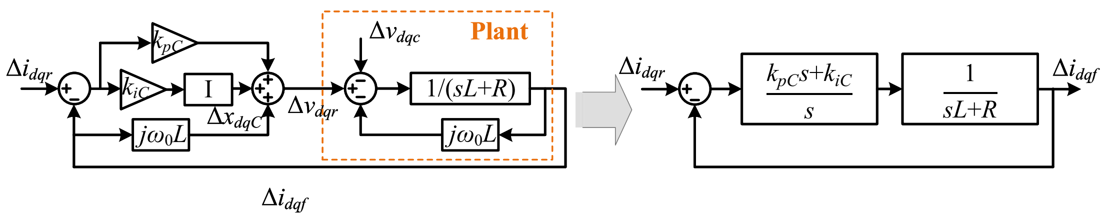

Figure 3.17: Simplified block diagram of the current control loop

Complete Single Grid-Following Converter Model

Combine Eq. (3.55), (3.59) and (3.61), the complete small-signal model of the ith grid-following converter in a power system with N_{Bus} buses can be formulated as

$$\begin{aligned}\Delta\dot{\boldsymbol{x}}_{GFL,i} &= \boldsymbol{A}_{GFL,i}\Delta\boldsymbol{x}_{GFL,i} + \boldsymbol{B}_{GFLS,i}\Delta\boldsymbol{S}_{GFL,i} + \boldsymbol{B}_{GFLV,i}\Delta\boldsymbol{v}_{Bus} \\ \Delta\boldsymbol{y}_{GFL,i} &= \boldsymbol{C}_{GFL,i}\Delta\boldsymbol{x}_{GFL,i}\end{aligned} \tag{3.64}$$

with a 14-dimensional state vector

$$\Delta \boldsymbol{x}_{GFL,i} = \begin{bmatrix} \Delta v_{dq+,i}, \ \Delta v^*_{dq+,i}, \ \Delta v_{dq-,i}, \ \Delta v^*_{dq-,i}, \ \Delta \eta_i, \ \Delta \theta_i, \ \Delta x_{dqC,i}, \ \Delta x^*_{dqC,i}, \\ \Delta i_{\alpha\beta f,i}, \ \Delta i^*_{\alpha\beta f,i}, \ \Delta v_{\alpha\beta c,i}, \ \Delta v^*_{\alpha\beta c,i}, \ \Delta i_{\alpha\beta g,i}, \ \Delta i^*_{\alpha\beta g,i} \end{bmatrix}^T . \tag{3.65}$$

Disturbances of the power reference command and the bus voltage are defined as input variables

$$\begin{aligned} \Delta \boldsymbol{S}_{GFL,i} &= \left[\Delta S_{r,i}, \ \Delta S^*_{r,i}\right]^T \\ \Delta \boldsymbol{v}_{Bus} &= \left[\Delta v_{Bus,1}, \ \Delta v^*_{Bus,1}, \ \cdots, \ \Delta v_{Bus,m}, \ \Delta v^*_{Bus,m}, \ \cdots, \ \Delta v_{Bus,N_{Bus}}, \ \Delta v^*_{Bus,N_{Bus}}\right]^T \end{aligned} \tag{3.66}$$

associated with the input matrices

$$\boldsymbol{B}_{GFLS,i} = \begin{bmatrix} \boldsymbol{0}^{6\times 2} \\ \begin{bmatrix} 0 & \frac{2k_{iC}}{3V^*_{dq+}} \\ \frac{2k_{iC}}{3V_{dq+}} & 0 \end{bmatrix}^{2\times 2} \\ \boldsymbol{0}^{6\times 2} \end{bmatrix}^{14\times 2} \tag{3.67}$$

$$\boldsymbol{B}_{GFLV,i} = \begin{bmatrix} \underbrace{\boldsymbol{0}^{14\times 2}}_{Bus\ 1} & \cdots & \underbrace{\begin{bmatrix} \boldsymbol{0}^{12\times 2} \\ \begin{bmatrix} -\frac{1}{L_{g,i}} & 0 \\ 0 & -\frac{1}{L_{g,i}} \end{bmatrix} \end{bmatrix}}_{Bus\ m} & \cdots & \underbrace{\boldsymbol{0}^{14\times 2}}_{Bus\ N_{Bus}} \end{bmatrix}^{14\times 2N_{Bus}} \tag{3.68}$$

where $\Delta v_{Bus,m}$ is the voltage at the mth bus, to which the ith grid-following converter is connected.

The current injected into the grid is selected as the output signal, $\Delta \boldsymbol{y}_{GFL,i} = \left[\Delta i_{\alpha\beta g}, \ \Delta i^*_{\alpha\beta g}\right]^T$, by defining the output matrix

$$\Delta \boldsymbol{C}_{GFL,i} = \begin{bmatrix} \boldsymbol{0}^{2\times 12} & \begin{bmatrix} 1 & 0 \\ 0 & 1 \end{bmatrix}^{2\times 2} \end{bmatrix} \tag{3.69}$$

Combination of Multiple Grid-Following Converters

Let N_{GFL} denote the total number of grid-following converters, the full state-space model of all grid-following converters can be summaried as

$$\begin{aligned} \Delta \dot{\boldsymbol{x}}_{GFL} &= \boldsymbol{A}_{GFL} \Delta \boldsymbol{x}_{GFL} + \boldsymbol{B}_{GFLS} \Delta \boldsymbol{S}_{GFL} + \boldsymbol{B}_{GFLV} \Delta \boldsymbol{v}_{Bus} \\ \Delta \boldsymbol{y}_{GFL} &= \boldsymbol{C}_{GFL} \Delta \boldsymbol{x}_{GFL} \end{aligned} \tag{3.70}$$

with

$$\Delta \boldsymbol{x}_{GFL} = \begin{bmatrix} \Delta \boldsymbol{x}_{GFL,1} \\ \Delta \boldsymbol{x}_{GFL,2} \\ \vdots \\ \Delta \boldsymbol{x}_{GFL,N_{GFL}} \end{bmatrix} \quad \boldsymbol{A}_{GFL} = \begin{bmatrix} \boldsymbol{A}_{GFL,1} & & & \\ & \boldsymbol{A}_{GFL,2} & & \\ & & \ddots & \\ & & & \boldsymbol{A}_{GFL,N_{GFL}} \end{bmatrix}$$

$$\Delta \boldsymbol{S}_{GFL} = \begin{bmatrix} \Delta \boldsymbol{S}_{GFL,1} \\ \Delta \boldsymbol{S}_{GFL,2} \\ \vdots \\ \Delta \boldsymbol{S}_{GFL,N_{GFL}} \end{bmatrix} \quad \boldsymbol{B}_{GFLS} = \begin{bmatrix} \boldsymbol{B}_{GFLS,1} & & & \\ & \boldsymbol{B}_{GFLS,2} & & \\ & & \ddots & \\ & & & \boldsymbol{B}_{GFLS,N_{GFL}} \end{bmatrix}$$

$$\boldsymbol{B}_{GFLV} = \begin{bmatrix} \boldsymbol{B}_{GFLV,1} \\ \boldsymbol{B}_{GFLV,2} \\ \vdots \\ \boldsymbol{B}_{GFLV,N_{GFL}} \end{bmatrix}$$

$$\Delta \boldsymbol{y}_{GFL} = \begin{bmatrix} \Delta \boldsymbol{y}_{GFL,1} \\ \Delta \boldsymbol{y}_{GFL,2} \\ \vdots \\ \Delta \boldsymbol{y}_{GFL,N_{GFL}} \end{bmatrix} \quad \boldsymbol{C}_{GFL} = \begin{bmatrix} \boldsymbol{C}_{GFL,1} & & & \\ & \boldsymbol{C}_{GFL,2} & & \\ & & \ddots & \\ & & & \boldsymbol{C}_{GFL,N_{GFL}} \end{bmatrix}$$

The small-signal model of the Type II grid-following converter can be derived following the same procedure.

3.2.2 Small-Signal Model of Grid-Forming Converters

In the GFL converters, the PLLs, which aim to estimate the voltage phase angle by bringing v_q to zero, are the asymmetric control units causing couplings between original and conjugate coordinates. An asymmetric control unit can also be found in the outer control loop of the GFM converters, where active and reactive power are controlled separately. Therefore, the Wirtinger calculus is also needed for the complex-domain modeling of GFM converters.

Outer Power Control

The instantaneous power calculation unit in Figure 3.12 is the only nonlinear part in the outer control. Based on the Wirtinger calculus, the linear approximation of the instantaneous power is given by

$$\Delta s_{VSG} = \frac{3}{2}\left(V_{\alpha\beta c}\Delta i^*_{\alpha\beta g} + I^*_{\alpha\beta g}\Delta v_{\alpha\beta c}\right) \tag{3.71}$$

Since the rests of the outer power loop are linear, the small-signal model can be directly obtained by replacing large-signal variables with corresponding small-signal ones

$$\Delta \dot{S} = -\omega_s \Delta S + \omega_s \Delta s_{VSG} \tag{3.72a}$$

$$\Delta \dot{\omega} = \frac{1}{J\omega_0}\left(\mathrm{Re}\left\{\Delta S_r\right\} - \mathrm{Re}\left\{\Delta S\right\} - k_P \Delta\omega\right) \tag{3.72b}$$

$$\Delta \dot{\theta} = \Delta\omega \tag{3.72c}$$

$$\Delta E = \frac{\mathrm{Im}\left\{\Delta S_r\right\} - \mathrm{Im}\left\{\Delta S\right\}}{k_Q} \tag{3.72d}$$

where Eq. (3.72a) describes the dynamic of the low-pass filter. Eq. (3.72b) and Eq. (3.72c) are for the active power control loop. Eq. (3.72d) is related to the reactive power control loop.

The droop coefficients are selected according to the grid codes. For instance, according to EN 50438, it is required that the change of 100% active power corresponds to the change of 2% grid frequency, while the change of 100% reactive power corresponds to the change of 2% nominal voltage. Let H be the desired inertia time constant, the moment of inertia J can be obtained from

$$J = \frac{2H\left|S_r\right|}{\omega_0^2}.$$

The typical value of H of the classical synchronous generator is between 2 and 12 seconds.

Inner Cascaded Voltage-Current Control

The inner control loop described with variables in the dq frame is linear, the small-signal model is summarized as

$$\begin{aligned}\Delta\dot{x}_{dqv} &= -\omega_v\Delta x_{dqv} + \omega_v\Delta i_{dqg}\\ \Delta\dot{x}_{dqV} &= k_{iV}\left(\Delta v_{dqcr} - \Delta v_{dqc}\right)\\ \Delta\dot{x}_{dqC} &= k_{iC}\left(\Delta i_{dqr} - \Delta i_{dqf}\right)\end{aligned} \tag{3.73}$$

with the algebraic relation

$$\begin{aligned}\Delta v_{dqcr} &= \Delta E - \left(L_v\omega_v\left(\Delta i_{dqg} - \Delta x_{dqv}\right) + \left(R_v + j\omega_0 L_v\right)\Delta i_{dqg}\right)\\ \Delta i_{dqr} &= \Delta x_{dqV} + k_{pV}\left(\Delta v_{dqcr} - \Delta v_{dqc}\right) + j\omega_0 C\Delta v_{dqc} + K_{ffi}\Delta i_{dqg}.\\ \Delta v_{dqr} &= \Delta x_{dqC} + k_{pC}\left(\Delta i_{dqr} - \Delta i_{dqf}\right) + j\omega_0 L\Delta i_{dqf} + K_{ffv}\Delta v_{dqc}\end{aligned} \tag{3.74}$$

The small-signal model of the LC filter and grid impedance is the same as that of the grid-following converter given by Eq. (3.63). The linear approximation of the frame transformation is also the same as Eq. (3.56).

The PI coefficients of the current control are designed by using the pole-zero cancellation technique given by Eq. (3.63). Neglecting the dynamics of reference frame transformation, the PI voltage controller and its plant can be described with the block diagram shown in Figure 3.18. The open-loop transfer function

$$G_{olV}\left(s\right) = \frac{k_{pV}\frac{1}{\tau}\left(s + \frac{k_{iV}}{k_{pV}}\right)}{s^2 C\left(s + \frac{1}{\tau}\right)}$$

has the same form as Eq. (3.56). Similarly, the extended symmetrical optimum method can be used for the selection of the PI coefficients of the voltage controller.

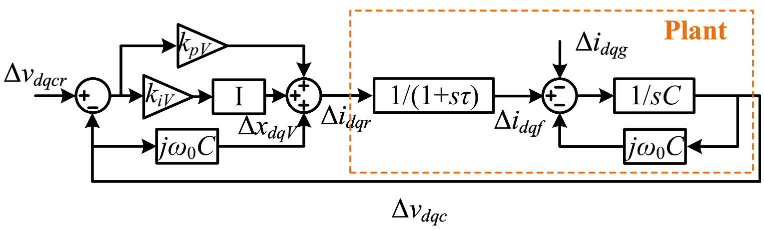

Figure 3.18: Simplified block diagram of the voltage control loop

Complete Single Grid-Forming Converter Model

The complete small-signal model of the ith grid-forming converter is obtained by combining Eq. (3.72), (3.73) and (3.61)

$$\begin{aligned} \Delta\dot{\boldsymbol{x}}_{VSG,i} &= \boldsymbol{A}_{VSG,i}\Delta\boldsymbol{x}_{VSG,i} + \boldsymbol{B}_{VSGS,i}\Delta\boldsymbol{S}_{VSG,i} + \boldsymbol{B}_{VSGV,i}\Delta\boldsymbol{v}_{Bus} \\ \Delta\boldsymbol{y}_{VSG,i} &= \boldsymbol{C}_{VSG,i}\Delta\boldsymbol{x}_{VSG,i} \end{aligned} \tag{3.75}$$

where the 16-dimensional state variable vector is

$$\Delta\boldsymbol{x}_{VSG,i} = \begin{bmatrix} \Delta S_i, & \Delta S_i^*, & \Delta\omega_i, & \Delta\theta_i, & \Delta x_{dqv,i}, & \Delta x_{dqv,i}^*, & \Delta x_{dqV,i}, & \Delta x_{dqV,i}^*, \\ \Delta x_{dqC,i}, & \Delta x_{dqC,i}^*, & \Delta i_{\alpha\beta f,i}, & \Delta i_{\alpha\beta f,i}^*, & \Delta v_{\alpha\beta c,i}, & \Delta v_{\alpha\beta c,i}^*, & \Delta i_{\alpha\beta g,i}, & \Delta i_{\alpha\beta g,i}^* \end{bmatrix}^T. \tag{3.76}$$

Disturbances of the power reference command $\Delta\boldsymbol{S}_{VSG,i} = \left[\Delta S_{r,i}, \ \Delta S_{r,i}^*\right]^T$ and the bus voltage $\Delta\boldsymbol{v}_{Bus}$ are defined as input variables. The current injected into the grid is selected as the output signal $\Delta\boldsymbol{y}_{VSG,i} = \left[\Delta i_{\alpha\beta g,i}, \ \Delta i_{\alpha\beta g,i}^*\right]^T$. Corresponding state-space matrices are given by

$$\boldsymbol{B}_{VSGS,i} = \begin{bmatrix} \mathbf{0}^{2\times2} \\ \begin{bmatrix} \frac{1}{2J\omega_0} & \frac{1}{2J\omega_0} \end{bmatrix}^{1\times2} \\ \mathbf{0}^{3\times2} \\ \begin{bmatrix} \frac{k_{iV}}{2j\cdot k_Q} & \frac{k_{iV}}{-2j\cdot k_Q} \\ \frac{k_{iV}}{-2j\cdot k_Q} & \frac{k_{iV}}{2j\cdot k_Q} \end{bmatrix}^{2\times2} \\ \mathbf{0}^{8\times2} \end{bmatrix}^{16\times2}$$

$$\boldsymbol{B}_{VSGV,i} = \begin{bmatrix} \underbrace{\mathbf{0}^{16\times2}}_{Bus\ 1} & \cdots & \underbrace{\begin{bmatrix} \mathbf{0}^{14\times2} \\ \begin{bmatrix} -\frac{1}{L_{g,i}} & 0 \\ 0 & -\frac{1}{L_{g,i}} \end{bmatrix} \end{bmatrix}}_{Bus\ m} & \cdots & \underbrace{\mathbf{0}^{16\times2}}_{Bus\ N_{Bus}} \end{bmatrix}^{16\times2N_{Bus}}$$

$$\Delta\mathbf{C}_{VSG,i} = \begin{bmatrix} \mathbf{0}^{2\times14} & \begin{bmatrix} 1 & 0 \\ 0 & 1 \end{bmatrix}^{2\times2} \end{bmatrix}^{2\times16}.$$

It is assumed that the ith VSG converter is connected to the mth bus.

Combination of Multiple Grid-Forming Converters

Let N_{VSG} denote the total number of VSG converters, the full state-space model of all VSG converters is summarized as

$$\begin{aligned} \Delta\dot{\boldsymbol{x}}_{VSG} &= \boldsymbol{A}_{VSG}\Delta\boldsymbol{x}_{VSG} + \boldsymbol{B}_{VSGS}\Delta\boldsymbol{S}_{VSG} + \boldsymbol{B}_{VSGV}\Delta\boldsymbol{v}_{Bus} \\ \Delta\boldsymbol{y}_{VSG} &= \boldsymbol{C}_{VSG}\Delta\boldsymbol{x}_{VSG} \end{aligned} \tag{3.77}$$

with

$$\Delta \boldsymbol{x}_{VSG} = \begin{bmatrix} \Delta \boldsymbol{x}_{VSG,1} \\ \Delta \boldsymbol{x}_{VSG,2} \\ \vdots \\ \Delta \boldsymbol{x}_{VSG,N_{VSG}} \end{bmatrix} \quad \boldsymbol{A}_{VSG} = \begin{bmatrix} \boldsymbol{A}_{VSG,1} & & & \\ & \boldsymbol{A}_{VSG,2} & & \\ & & \ddots & \\ & & & \boldsymbol{A}_{VSG,N_{VSG}} \end{bmatrix}$$

$$\Delta \boldsymbol{S}_{VSG} = \begin{bmatrix} \Delta \boldsymbol{S}_{VSG,1} \\ \Delta \boldsymbol{S}_{VSG,2} \\ \vdots \\ \Delta \boldsymbol{S}_{VSG,N_{VSG}} \end{bmatrix} \quad \boldsymbol{B}_{VSGS} = \begin{bmatrix} \boldsymbol{B}_{VSGS,1} & & & \\ & \boldsymbol{B}_{VSGS,2} & & \\ & & \ddots & \\ & & & \boldsymbol{B}_{VSGS,N_{VSG}} \end{bmatrix}.$$

$$\boldsymbol{B}_{VSGV} = \begin{bmatrix} \boldsymbol{B}_{VSGV,1} \\ \boldsymbol{B}_{VSGV,2} \\ \vdots \\ \boldsymbol{B}_{VSGV,N_{VSG}} \end{bmatrix}$$

$$\Delta \boldsymbol{y}_{VSG} = \begin{bmatrix} \Delta \boldsymbol{y}_{VSG,1} \\ \Delta \boldsymbol{y}_{VSG,2} \\ \vdots \\ \Delta \boldsymbol{y}_{VSG,N_{VSG}} \end{bmatrix} \quad \boldsymbol{C}_{VSG} = \begin{bmatrix} \boldsymbol{C}_{VSG,1} & & & \\ & \boldsymbol{C}_{VSG,2} & & \\ & & \ddots & \\ & & & \boldsymbol{C}_{VSG,N_{VSG}} \end{bmatrix}$$

3.2.3 Small-Signal Model of Power Networks and Loads

In the $\alpha\beta$ frame, the small-signal model of the ith linear RL branch and the ith load described by Eq. (3.35) and Eq. (3.41) can be written in a compact form

$$\begin{aligned} \Delta \dot{\boldsymbol{x}}_{Branch,i} &= \boldsymbol{A}_{Branch,i} \Delta \boldsymbol{x}_{Branch,i} + \boldsymbol{B}_{Branch,i} \Delta \boldsymbol{v}_{Bus} \\ \Delta \dot{\boldsymbol{x}}_{Load,i} &= \boldsymbol{A}_{Load,i} \Delta \boldsymbol{x}_{Load,i} + \boldsymbol{B}_{Load,i} \Delta \boldsymbol{v}_{Bus} \end{aligned} \tag{3.78}$$

with

$$\begin{aligned} \boldsymbol{A}_{Branch,i} &= -\boldsymbol{L}_{mn}^{-1} \boldsymbol{R}_{mn} \\ \boldsymbol{B}_{Branch,i} &= \Big[\underbrace{\boldsymbol{0}^{2\times2}}_{Bus\ 1}, \ \underbrace{\boldsymbol{0}^{2\times2}}_{Bus\ 2}, \cdots, \ \underbrace{\boldsymbol{L}_{mn}^{-1}}_{Bus\ m}, \ \cdots, \ \boldsymbol{0}^{2\times2}, \ \cdots, \ \underbrace{-\boldsymbol{L}_{mn}^{-1}}_{Bus\ n}, \ \cdots, \ \underbrace{\boldsymbol{0}^{2\times2}}_{Bus\ N_{Bus}} \Big]^{2\times2N_{Bus}} \\ \boldsymbol{A}_{Load,i} &= -\boldsymbol{L}_{i}^{-1} \boldsymbol{R}_{i} \\ \boldsymbol{B}_{Load,i} &= \Big[\underbrace{\boldsymbol{0}^{2\times2}}_{Bus\ 1}, \ \cdots, \ \underbrace{\boldsymbol{L}_{i}^{-1}}_{Bus\ m}, \ \cdots, \ \underbrace{\boldsymbol{0}^{2\times2}}_{Bus\ N_{\mathrm{Bus}}} \Big]^{2\times2N_{Bus}} \end{aligned}$$

where

$$\Delta \boldsymbol{x}_{Branch,i} = \left[\Delta i_{\alpha\beta Branch,i}, \ \Delta i^{*}_{\alpha\beta Branch,i} \right]^{T}$$

denotes the current of the ith branch flowing from the mth bus to the nth bus.

$$\Delta \boldsymbol{x}_{Load,i} = \left[\Delta i_{\alpha\beta Load,i},\ \Delta i^{*}_{\alpha\beta Load,i}\right]^{T}$$

is the current of the ith load connected to the mth bus.

Define N_{Branch} and N_{Load} as the total number of branches and loads, state-space models of all branches and loads can be written in the compact form

$$\begin{aligned} \Delta\dot{\boldsymbol{x}}_{Branch} &= \boldsymbol{A}_{Branch}\Delta\boldsymbol{x}_{Branch} + \boldsymbol{B}_{Branch}\Delta\boldsymbol{v}_{Bus} \\ \Delta\dot{\boldsymbol{x}}_{Load} &= \boldsymbol{A}_{Load}\Delta\boldsymbol{x}_{Load} + \boldsymbol{B}_{Load}\Delta\boldsymbol{v}_{Bus} \end{aligned} \tag{3.79}$$

with state-space vectors and matrices given by

$$\Delta\boldsymbol{x}_{Branch} = \begin{bmatrix} \Delta\boldsymbol{x}_{Branch,1} \\ \Delta\boldsymbol{x}_{Branch,2} \\ \vdots \\ \Delta\boldsymbol{x}_{Branch,N_{Branch}} \end{bmatrix} \quad \boldsymbol{B}_{Branch} = \begin{bmatrix} \boldsymbol{B}_{Branch,1} \\ \boldsymbol{B}_{Branch,2} \\ \vdots \\ \boldsymbol{B}_{Branch,N_{Branch}} \end{bmatrix}$$

$$\boldsymbol{A}_{Branch} = \begin{bmatrix} \boldsymbol{A}_{Branch,1} & & & \\ & \boldsymbol{A}_{Branch,2} & & \\ & & \ddots & \\ & & & \boldsymbol{A}_{Branch,N_{Branch}} \end{bmatrix}$$

$$\Delta\boldsymbol{x}_{Load} = \begin{bmatrix} \Delta\boldsymbol{x}_{Load,1} \\ \Delta\boldsymbol{x}_{Load,2} \\ \vdots \\ \Delta\boldsymbol{x}_{Load,N_{Load}} \end{bmatrix} \quad \boldsymbol{B}_{Load} = \begin{bmatrix} \boldsymbol{B}_{Load,1} \\ \boldsymbol{B}_{Load,2} \\ \vdots \\ \boldsymbol{B}_{Load,N_{Load}} \end{bmatrix}.$$

$$\boldsymbol{A}_{Load} = \begin{bmatrix} \boldsymbol{A}_{Load,1} & & & \\ & \boldsymbol{A}_{Load,2} & & \\ & & \ddots & \\ & & & \boldsymbol{A}_{Load,N_{Load}} \end{bmatrix}$$

3.2.4 Complete Small-Signal Model of the Converter-Dominated Power System

As shown in Figure 3.19, the converter-dominated power system can be generally decomposed into four parts, grid-following converters, grid-forming converters, power networks and loads. The state-space model of each part is given by Eq. (3.70), (3.75) and (3.79). It is observed that the bus voltages $\Delta\boldsymbol{v}_{Bus}$ are used as common inputs to each individual part. Since the power networks are modeled as series connected RL branches instead of transmission lines described with the π-model, the bus voltages do not represent state variables. To ensure the bus voltages are well-defined, a virtual resistance r_V is assumed to be connected between each bus and the ground. According to Kirchhoff's current law and Ohm's law, the voltage of the mth bus is

$$\begin{bmatrix} \Delta v_{Bus,m} \\ \Delta v^*_{Bus,m} \end{bmatrix} = r_V \begin{pmatrix} \boldsymbol{M}_{GFL}(2m-1:2m,\ :)\,\Delta\boldsymbol{y}_{GFL} \\ +\boldsymbol{M}_{VSG}(2m-1:2m,\ :)\,\Delta\boldsymbol{y}_{VSG} \\ +\boldsymbol{M}_{Load}(2m-1:2m,\ :)\,\Delta\boldsymbol{x}_{Load} \\ +\boldsymbol{M}_{Branch}(2m-1:2m,\ :)\,\Delta\boldsymbol{x}_{Branch} \end{pmatrix} \tag{3.80}$$

where $\boldsymbol{M}_{GFL}((2m-1):2m,\ :)$ gives the (2m-1)th and the 2mth rows of the connectivity matrix of the grid-following converter, which follows the definition that

$$\boldsymbol{M}_{GFL}(2m-1:m,\ 2i-1:2i) = \begin{bmatrix} 1 & 0 \\ 0 & 1 \end{bmatrix}$$

when the ith grid-following converter is connected to the mth bus, otherwise the submatrix is $\mathbf{0}^{2\times 2}$. The same goes for the connectivity matrix of the grid-forming converter $\boldsymbol{M}_{VSG}$.

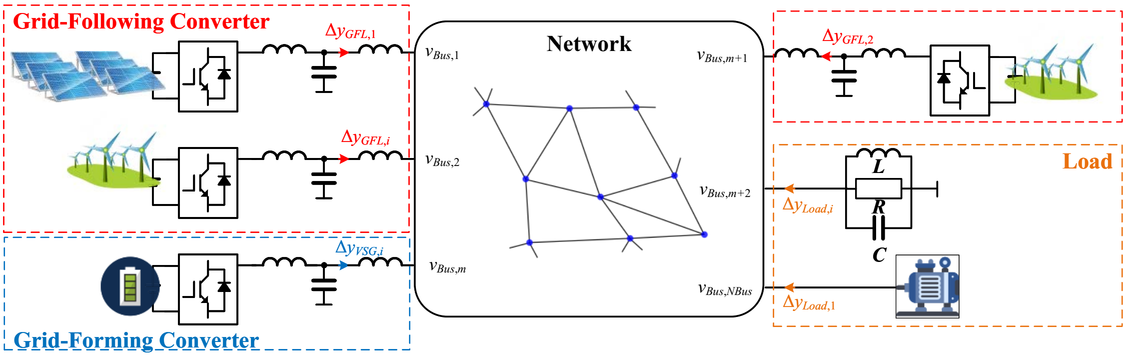

Figure 3.19: Complete small-signal modeling of the converter-dominated power systems

The load connectivity matrix $\boldsymbol{M}_{Load}$ maps the load currents to each bus by defining

$$\boldsymbol{M}_{Load}(2m-1:m,\ 2i-1:2i) = \begin{bmatrix} -1 & 0 \\ 0 & -1 \end{bmatrix}$$

when the ith load is connected to the mth bus.

The branch connectivity matrix $\boldsymbol{M}_{Branch}$ maps the current of the ith branch (flowing from the mth bus to the nth bus) to each bus by defining

$$\boldsymbol{M}_{Branch}(2m-1:m,\ 2i-1:2i) = \begin{bmatrix} -1 & 0 \\ 0 & -1 \end{bmatrix}$$

$$\boldsymbol{M}_{Branch}(2n-1:n,\ 2i-1:2i) = \begin{bmatrix} 1 & 0 \\ 0 & 1 \end{bmatrix}$$

Further, the bus voltage vector can be obtained

$$\Delta\boldsymbol{v}_{Bus} = r_V \begin{pmatrix} \boldsymbol{M}_{GFL}\boldsymbol{C}_{GFL}\Delta\boldsymbol{x}_{GFL} + \boldsymbol{M}_{VSG}\boldsymbol{C}_{VSG}\Delta\boldsymbol{x}_{VSG} \\ +\boldsymbol{M}_{Load}\Delta\boldsymbol{x}_{Load} + \boldsymbol{M}_{Branch}\Delta\boldsymbol{x}_{Branch} \end{pmatrix} \tag{3.81}$$

Insert Eq. (3.81) into (3.70), (3.75) and (3.79), the complete small-signal state-space model of a converter-dominated power system can be obtained by combining them together

$$\Delta\dot{\boldsymbol{x}} = \boldsymbol{A}\Delta\boldsymbol{x} + \boldsymbol{B}\Delta\boldsymbol{S} \tag{3.82}$$

where

$$\Delta\boldsymbol{x} = \begin{bmatrix} \Delta\boldsymbol{x}_{GFL} \\ \Delta\boldsymbol{x}_{VSG} \\ \Delta\boldsymbol{x}_{Branch} \\ \Delta\boldsymbol{x}_{Load} \end{bmatrix} \quad \Delta\boldsymbol{S} = \begin{bmatrix} \Delta\boldsymbol{S}_{GFL} \\ \Delta\boldsymbol{S}_{VSG} \end{bmatrix} \quad \boldsymbol{B} = \begin{bmatrix} \boldsymbol{B}_{GFL} & \boldsymbol{0} \\ \boldsymbol{0} & \boldsymbol{B}_{VSG} \\ \boldsymbol{0} & \boldsymbol{0} \\ \boldsymbol{0} & \boldsymbol{0} \end{bmatrix}$$

$$\boldsymbol{A} = \begin{bmatrix} \boldsymbol{A}_{GFL} + \boldsymbol{B}_{GFLV}\boldsymbol{A}_1 & \boldsymbol{B}_{GFLV}\boldsymbol{A}_2 & \boldsymbol{B}_{GFLV}\boldsymbol{A}_3 & \boldsymbol{B}_{GFLV}\boldsymbol{A}_4 \\ \boldsymbol{B}_{VSGV}\boldsymbol{A}_1 & \boldsymbol{A}_{\mathrm{VSG}} + \boldsymbol{A}_2 & \boldsymbol{B}_{VSGV}\boldsymbol{A}_3 & \boldsymbol{B}_{VSGV}\boldsymbol{A}_4 \\ \boldsymbol{B}_{Branch}\boldsymbol{A}_1 & \boldsymbol{B}_{Branch}\boldsymbol{A}_2 & \boldsymbol{A}_{Branch} + \boldsymbol{B}_{Branch}\boldsymbol{A}_3 & \boldsymbol{B}_{Branch}\boldsymbol{A}_4 \\ \boldsymbol{B}_{Load}\boldsymbol{A}_1 & \boldsymbol{B}_{Load}\boldsymbol{A}_2 & \boldsymbol{B}_{Load}\boldsymbol{A}_3 & \boldsymbol{A}_{Load} + \boldsymbol{B}_{Load}\boldsymbol{A}_4 \end{bmatrix}$$

with

$$\boldsymbol{A}_1 = r_V\boldsymbol{M}_{GFL}\boldsymbol{C}_{GFL} \quad \boldsymbol{A}_2 = r_V\boldsymbol{M}_{VSG}\boldsymbol{C}_{VSG} \quad \boldsymbol{A}_3 = r_V\boldsymbol{M}_{Load} \quad \boldsymbol{A}_4 = r_V\boldsymbol{M}_{Branch}$$

In Eq. (3.82), the state vector $\Delta\boldsymbol{x}$ consists of the state variables of all grid-following and grid-forming converters, the currents of all RL branches and the currents of all loads. The input vector $\Delta\boldsymbol{S}$ contains the power reference commands of all converters. The state space matrices $\boldsymbol{A}$ and $\boldsymbol{B}$ in Eq. (3.82) are time periodic matrices with the fundamental frequency ω_0. The stability and analytical solution of such LTP system will be investigated in the next chapter.

3.3 General Description of the Simulation Platform and Experimental Test Setup

Figure 3.20 shows the software framework for the numerical modeling and analytical stability evaluation of converter-dominated power systems. This framework consists mainly of following procedures:

1. The software *Microsoft Excel* is used for the management of input data, which specifies the power system topology, control and physical parameters of the networks, loads and different types of converters. A MATLAB script is generated from the *Excel* file.

2. A MATLAB/Simulink model is automatically built following the settings specified in the MATLAB script. Meanwhile, the power flow analysis is performed to initialize the state variables of the MATLAB/Simulink model, including currents of inductors, voltage of capacitors and integrators in controllers. This enables that the numerical Simulink model can be started from steady-state operation trajectories.

3. The linear time-periodic small-signal model is established by calling the *jacobian* function provided by MATLAB Symbolic Math Toolbox. The LTP modal analysis (Chapter 4) and resonance modal analysis (Chapter 5) are carried out for the assessment of the system dynamic performance.

The numerical MATLAB/Simulink model serves for the time-domain validation of the small-signal analysis results. To further confirm the analytical and simulation results, a power-hardware-in-the-loop (PHIL) test setup [115] shown in Figure 3.21 is used, which consists of three two-level IGBT converters, a Cinergia grid emulator, a dSPACE MicroLabBox and an OP5600 real-time simulator. The two-level IGBT converter is a scaled version of a low-voltage high-power VSC product with a rated power of 500 kVA and a rated peak phase voltage of 255 V. The switching frequency is 3.2 kHz. The laboratory prototype is down scaled to a power rating of 2 kVA and a rated voltage of 100 V. Other parameters are accordingly scaled to keep per unit values the same. The control of the converter is implemented in the dSPACE MicroLabBox, which serves also as the recorder of all measurements. The grid emulator can be operated as a power amplifier controlled by the OP5600 real-time simulator.

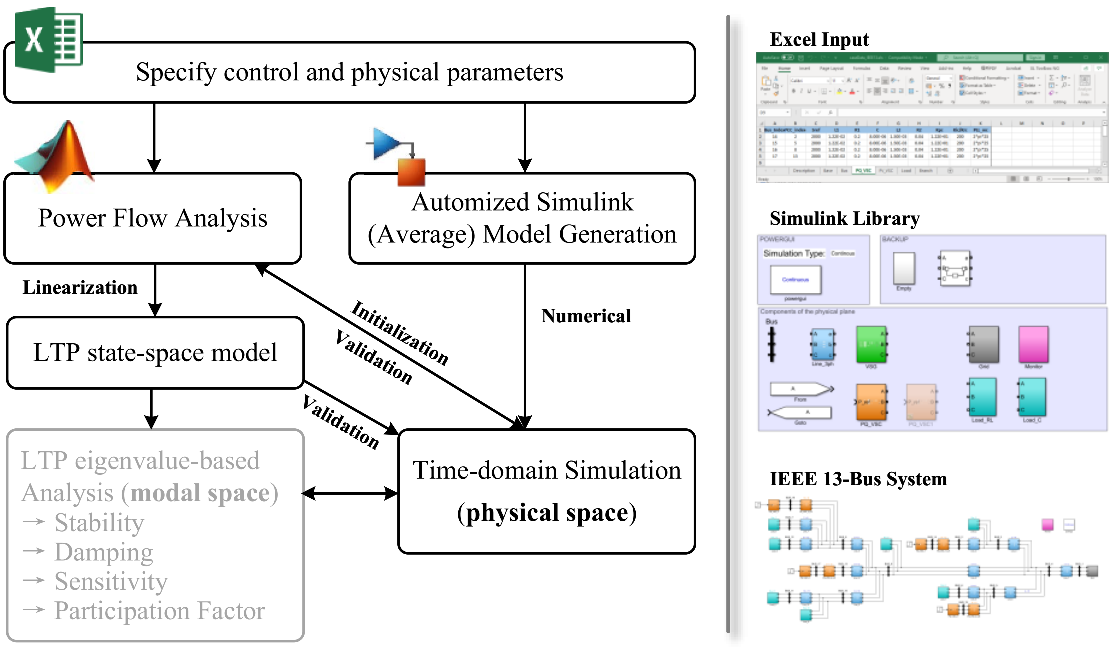

Figure 3.20: General framework for the modeling and stability analysis of converter-dominated power systems.

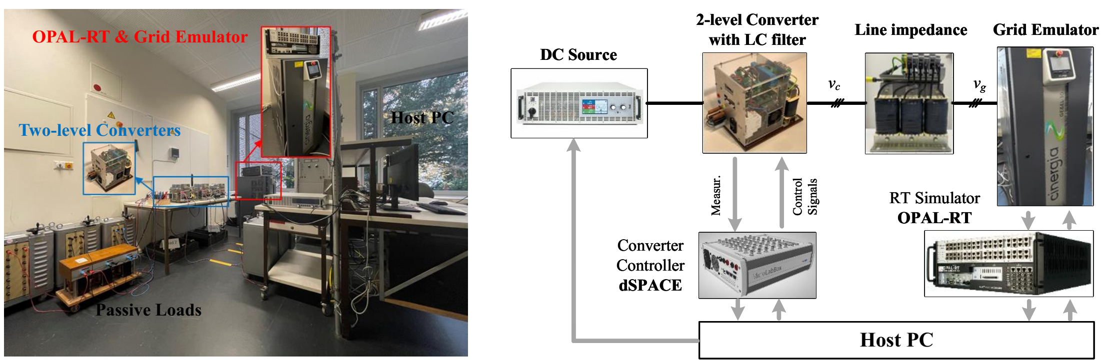

Figure 3.21: Configuration of the laboratory power-hardware-in-the-loop test setup.

3.4 Case Study

3.4.1 Single-Converter System

The proposed power flow analysis and small-signal modeling method is first tested with single-converter scenarios. Following three cases are considered:

- **Case 1**: single GFL converter connected to a balanced grid;
- **Case 2**: single GFL converter connected to an unbalanced grid with 0.8 pu negative-sequence voltage;
- **Case 3**: single GFM converter connected to a balanced grid.

Physical parameters of the analytical model and MATLAB/Simulink model are adapted to those of the physical test bench, given in Table 3.1.

Table 3.1: Physical Parameters of the Two-Level IGBT Converter System

Symbol	Description	Value
L/R	converter-side filter inductance	5.6 mH / 0.1 Ω
C	filter capacitor	16 μF
L_g/R_g	grid impedance	17.4 mH / 0.53 Ω
V_{DC}	voltage of the DC source	300 V
f_{sw}	switching frequency	3200 Hz
$V_{\alpha\beta g+}$	positive-sequence grid voltage (peak value)	100 V
$V_{\alpha\beta g-}$	negative-sequence grid voltage (peak value) for Case 2	80 V

For each case, power flow analysis is performed to compute the steady-state value of the filter capacitor voltage $v_{\alpha\beta c}$, the results are listed in Table 3.2. The voltage magnitude and phase angle obtained from the power flow analysis are exactly the same as those obtained from the numerical simulation in MATLAB/Simulink. This confirms the accuracy of the proposed steady-state model and the power flow analysis method. For Case 1, both types of GFL converters share the same steady-state capacitor voltage, while the negative-sequence component becomes different as the grid becomes unbalanced in Case 2. In Case 3, the use of the nonzero virtual impedance Z_v changes the steady-state capacitor voltage.

To verify the accuracy of the small-signal models, time-domain free and forced responses obtained from the analytical small-signal model, the nonlinear average model in MATLAB/Simulink and experimental tests will be compared. In this thesis, if not specified otherwise, experimental results are plotted as solid gray lines. Dashed lines and solid lines in other colors are for the analytical small-signal model and the nonlinear average Simulink model.

Table 3.2: Power Flow Analysis Results for Single-Converter Cases

	Case 1	**Case 2**				**Case 3**	
		Type I GFL		Type II GFL		$Z_v \neq 0$	$Z_v = 0$
	$V_{\alpha\beta c+}$	$V_{\alpha\beta c+}$	$V_{\alpha\beta c-}$	$V_{\alpha\beta c+}$	$V_{\alpha\beta c-}$	$V_{\alpha\beta c+}$	$V_{\alpha\beta c+}$
Magnitude (V)	96.24	96.24	65.51	96.24	68.11	97.96	99.62
Angle (rad)	0.4688	0.4688	0.3695	0.4688	0.4159	0.3795	0.3715

Grid-Following Converter

The power reference of the GFL converters is set to 1.2 kW. The bandwidth of the PLLs is designed to be 20 Hz. The current controller time constant is chosen to be 0.5 ms.

For Case 1, a disturbance of 2 Hz is first given to the state variable η at $t = 1.0$ s to excite the free response. The dynamic evolution of the estimated frequency of the DSRF-PLL η, the filter capacitor voltage and the grid-side current are plotted in Figure 3.22. It should be clarified that a rotational transformation $e^{-j\omega_0 t}$ is applied to the voltage and current variables to remove the fundamental oscillation at ω_0 for a clear visualization of the dynamic responses. As will be illustrated in the next chapter, such rotational transformation with fixed frequency is linear, which does not change the system stability characteristic. Without loss of generality only the real part of the complex-valued voltage and current variables are plotted. It can be observed that all state variables return to their original steady state trajectory within about 0.2 s after the disturbance. The agreement between results obtained from the small-signal model, the average model and the measurement confirms the correctness of the proposed small-signal modeling method.

In addition, to excite the forced response, a 100 W power reference step is given to the converter at $t = 1.0$ s, the waveforms of the three aforementioned state variables are shown in Figure 3.23. The slight deviation between the small-signal model and the nonlinear average model is caused by the changing of the steady-state operation trajectory.

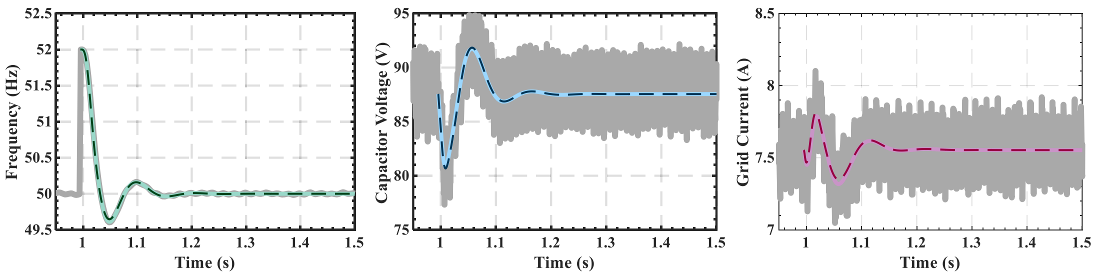

Figure 3.22: Free responses of the Type I GFL converter 2 Hz frequency disturbance at $t = 1.0$ s

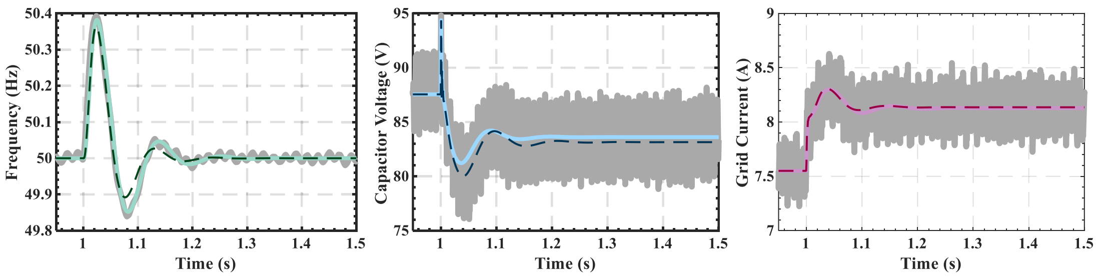

Figure 3.23: Forced responses of the Type I GFL converter to 100 W power reference step at $t = 1.0$ s

The same free and forced response tests have also been carried out on the Type II GFL converter, and the results are plotted in Figure 3.24 and Figure 3.25. Comparing the dynamic responses shown in Figure 3.23 and Figure 3.25 (or Figure 3.22 and Figure 3.24), it is seen that the Type II GFL converter exhibits a better damping performance. This difference cannot be explained by the existing LTI models in literature, according to which the two implementations of grid-following converters should be equivalent.

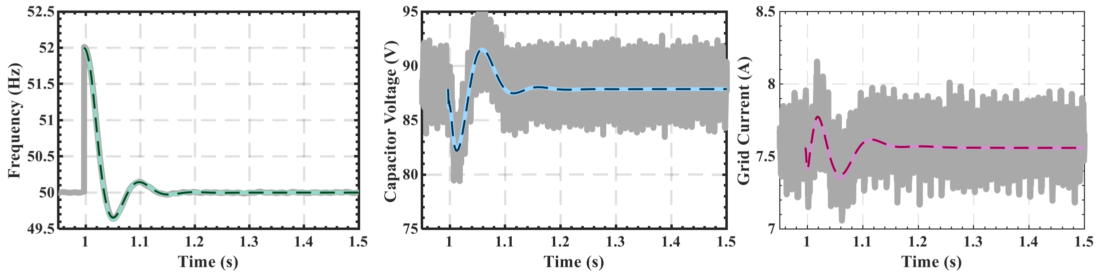

Figure 3.24: Free responses of the Type II GFL converter to 2 Hz frequency disturbance at $t = 1.0\,\mathrm{s}$

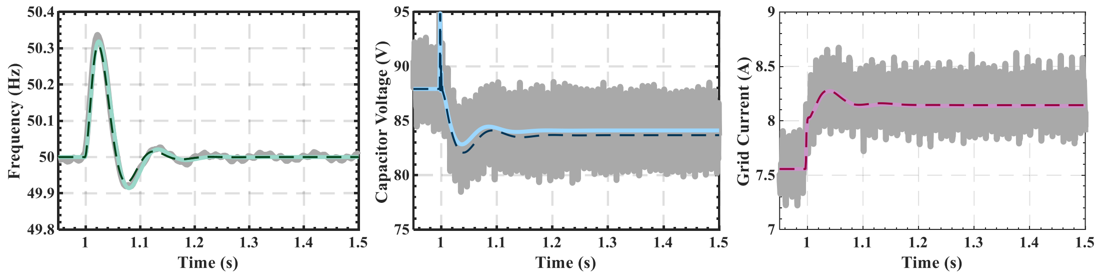

Figure 3.25: Forced responses of the Type II GFL converter to 100 W power reference step at $t = 1.0\,\mathrm{s}$

To test the modeling accuracy under unbalanced conditions, the grid voltage is set to contain a negative-sequence component with a magnitude of 0.8 pu in Case 2. The designed PLL bandwidth is increased to 30 Hz. Free responses to the 2 Hz disturbances are shown in Figure 3.26. It can be observed that more oscillation components appear in the dynamic responses of the two types of GFL converters. As the designed PLL bandwidth increases, the Type II GFL converter is more robust against the appearance of the negative-sequence voltage. Moreover, sustained oscillations can be observed in the filter-capacitor voltage and grid-side current in Figure 3.26, because the system is under unbalanced operation. The steady-state negative-sequence components are transformed into 100-Hz oscillations by the rotational transformation $e^{-j\omega_0 t}$.

Grid-Forming Converter

Case 3 is aimed to verify the accuracy of the proposed small-signal model of the VSG converter. The physical and control parameters are listed in Table 3.3. Forced responses of the frequency ω as well as the output active and reactive power to a 100 W power reference jump are plotted in Figure 3.27. It can be observed that the adoption of the virtual impedance can improve the dynamic performance of the grid-connected VSG converter. Moreover, a large inertia constant J can degrade the damping performance of the grid-connected single VSG converter system, as shown in Figure 3.27c.

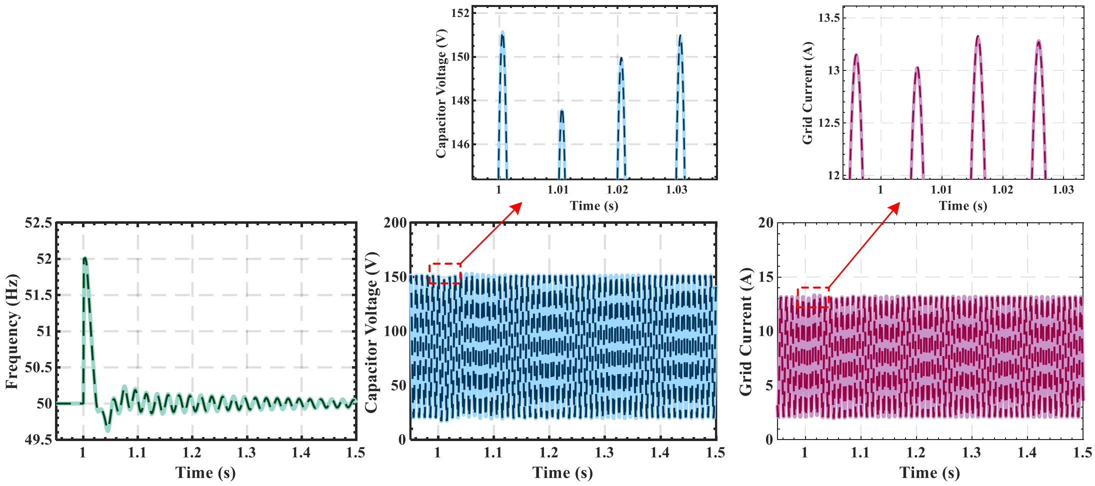

(a) Type I GFL converter

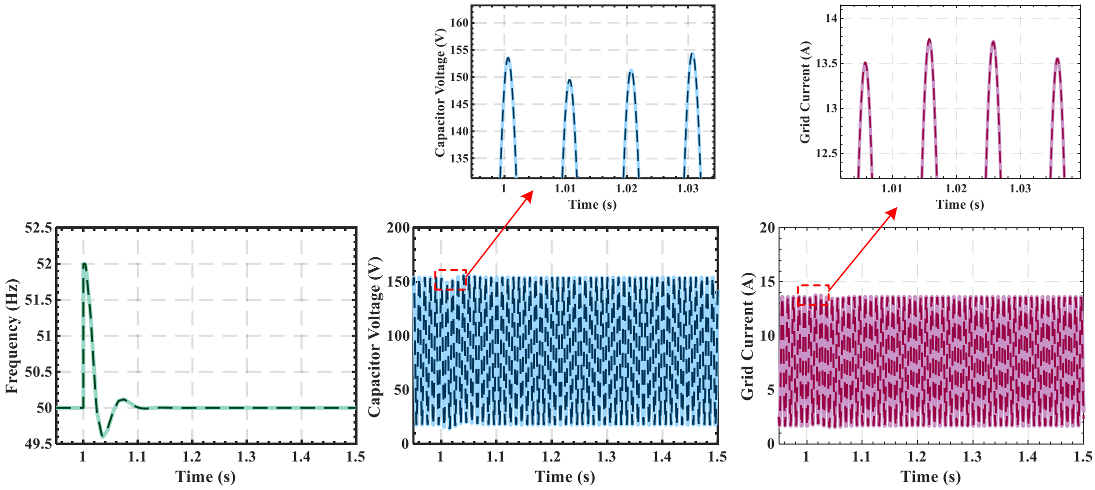

(b) Type II GFL converter

Figure 3.26: Free responses of GFL converters to 2 Hz disturbances at $t = 1.0\,\mathrm{s}$

3.4.2 Multiple-Converter System

Three multiple-converter scenarios are designed to test the accuracy and effectiveness of the proposed modeling framework for larger converter-dominated power systems:

- **Case 4**: three GFM converters operated in islanded mode;
- **Case 5**: parallel connected GFM converter and GFL converter supply an induction machine;
- **Case 6**: modified IEEE 13-bus system with four GFL converters.

In Case 4, three GFM converters are operated in islanded mode to supply a common resistive load (see Figure 3.28). In practice, except for the passive loads, induction machine loads exhibiting highly nonlinear couplings between dynamics of power, voltage and frequency, are important units in power systems. Completely neglecting the interaction between dynamic loads and power sources can result in unrealistic stability evaluation results. Therefore, Case 5 is designed to study the interaction between different types of converters and dynamic loads. To this end, the PHIL test setup is reconfigured as shown in Figure 3.29. Two converters are controlled in grid-following mode and VSG mode, respectively. For the sake of flexibility,

Table 3.3: Control Parameters of the single GFM Converter

Symbol	Description	Value
S_r	Power reference	1 kW
k_P	Active power droop coefficient	320 W · s/rad
k_Q	Reactive power droop coefficient	207 Var/V
τ	Current control time constant	0.5 ms
PM	Desired phase margin of the voltage control	45°
K_{ffv}	Voltage feedforward gain	0.75 A/V

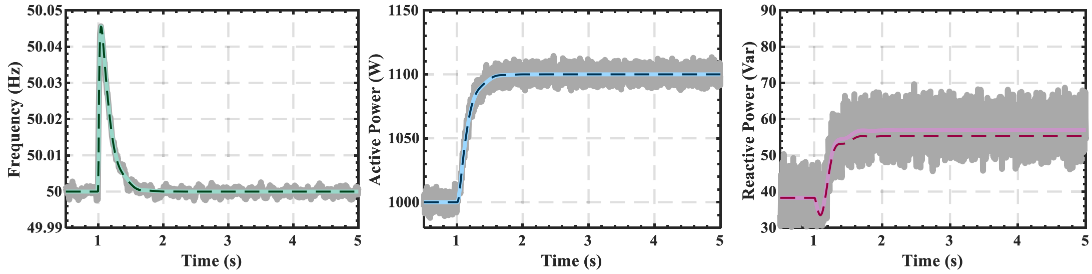

(a) $J = 0.0132\ \mathrm{kg} \cdot \mathrm{m}^2$ and $Z_v = 5.6\ \mathrm{mH}\ +\ 0.1\ \Omega$

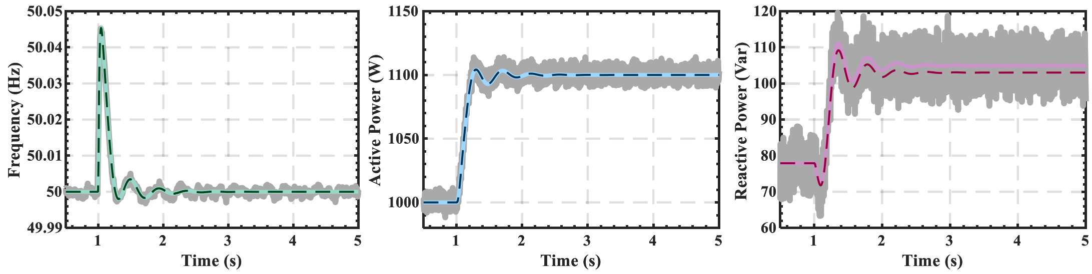

(b) $J = 0.0132\ \mathrm{kg} \cdot \mathrm{m}^2$ and virtual impedance Z_v is disabled

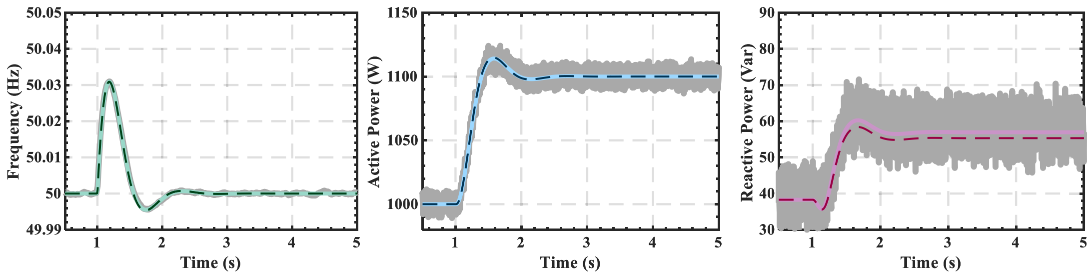

(c) $J = 0.132\ \mathrm{kg} \cdot \mathrm{m}^2$ and $Z_v = 5.6\ \mathrm{mH}\ +\ 0.1\ \Omega$

Figure 3.27: Forced responses of the VSG converter to 100 W power reference step at $t = 1.0\,\mathrm{s}$

a third converter is used as an emulator of the induction machine, which makes it possible to easily change electrical and mechanical constants of the induction machine for parameter studies. In Case 6, the modified IEEE 13-bus system shown in Figure 3.30 is adopted to further validate the scalability of the proposed power flow and small-signal modeling methodology.

Multiple Grid-Forming Converters in Islanded Mode

The three VSG converters in Figure 3.28 share the same control parameters listed in Table 3.3. Parameters of the load and branches are given in Figure 3.28. The steady-state values of the system frequency and the filter capacitor voltages of converters are calculated by using

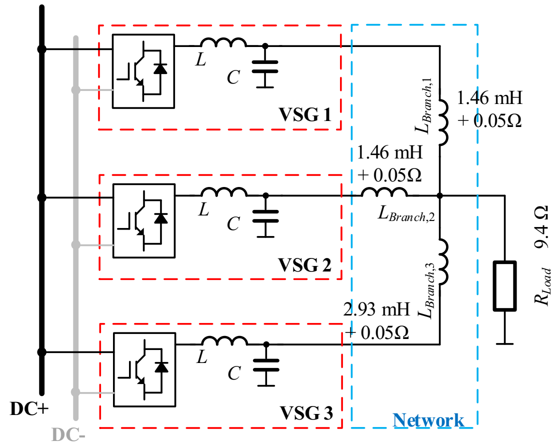

Figure 3.28: Configuration of the multiple-converter test system for Case 4

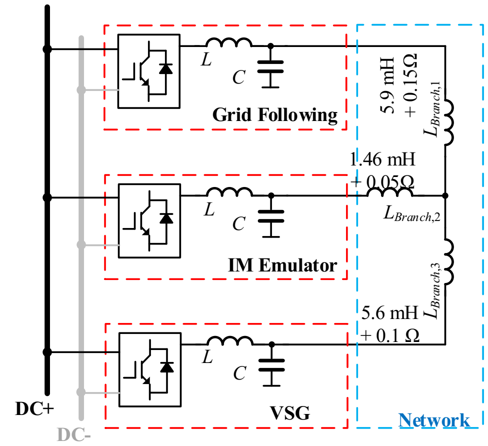

Figure 3.29: Configuration of the multiple-converter test system for Case 5

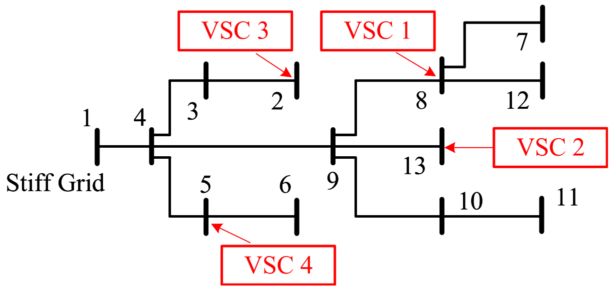

Figure 3.30: Topology of the modified IEEE 13-bus system

the proposed power flow analysis. As given in Table 3.4, the maximum percentage deviation between the results obtained from the power flow analysis and the numerical simulation in MATLAB/Simulink is smaller than 1.1%, which confirms the accuracy of the analytical method. The error comes from the assumption that the impedance $X = R + j\omega_0 L$ is calculated with the nominal frequency ω_0.

Around the steady-state operation trajectory, the small-signal model is developed following the systematic procedure described in Section 3.2. After the system reaches steady state, an active power reference step of 200 W is given to VSG 1 to excite forced responses. The overlap of the waveforms obtained from the small-signal model, the average model and the measurement can be observed in Figure 3.31. Similar to the single-GFM-converter case shown in Figure 3.27, it is seen that poorly damped low-frequency oscillations between the VSG converters can appear as the inertia constant increases. Deviations between the reactive power responses obtained from the average model and experimental tests may result from errors in the nominal value and nonlinearities of the physical line impedance.

Table 3.4: Steady-state Values of the Frequency and Filter Capacitor Voltages

	Simulink Simulation		Power Flow Analysis		Percent Deviation (%)	
	Mag. (V)	Angle (rad)	Mag. (V)	Angle (rad)	Mag.	Angle
$V_{\alpha\beta c,1}$	97.0733	0	96.0233	0	1.0816	0
$V_{\alpha\beta c,2}$	97.0733	0	96.0233	0	1.0816	0
$V_{\alpha\beta c,3}$	97.0700	0.0163	96.0201	0.0164	1.0817	0.1867
f	50.2486	N/A	50.2540	N/A	0.0106	N/A

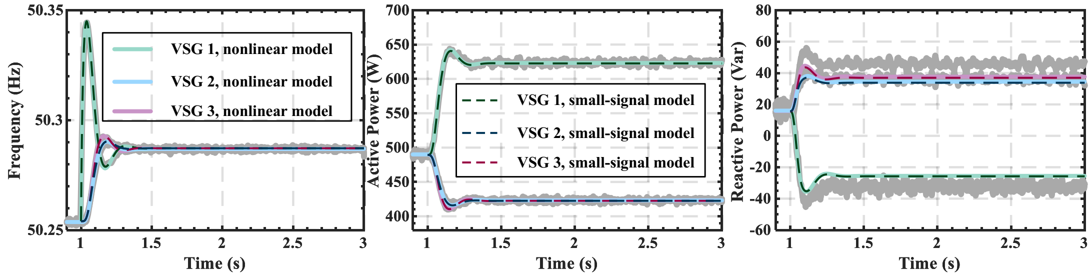

(a) $J = 0.0132\ \mathrm{kg \cdot m^2}$

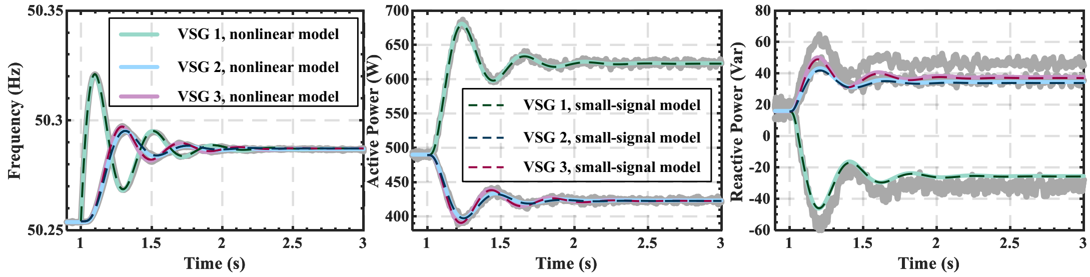

(b) $J = 0.066\ \mathrm{kg \cdot m^2}$

Figure 3.31: Forced responses of three VSG converters to 200 W power reference step given to VSG 1 at $t = 1.0$ s

Interaction between Dynamic Loads and Different Types of Converters

In Figure 3.29, power references of the GFL converter and the GFM converter are set to be 600 W and 400 W, respectively. Inertia constants of the VSG converter and the induction machine are $J = 0.00132\ \mathrm{kg \cdot m^2}$ and $J_{IM} = 0.00686\ \mathrm{kg \cdot m^2}$. Other control parameters are the same as those of Case 1 and Case 3. The steady-state operation trajectory is obtained from the numerical simulation in MATLAB/Simulink. The small-signal model of the induction machine is given in the Appendix B. After the system reaches steady state, a -20% induction machine load torque jump is applied to excite forced responses. Dynamic evolution of the grid-following converter frequency, VSG converter frequency, induction machine stator current and rotor speed obtained from the small-signal model, the nonlinear model and experimental measurements are plotted in Figure 3.32. The overlap between theoretical and experimental results confirms again the effectiveness and accuracy of the proposed modeling framework.

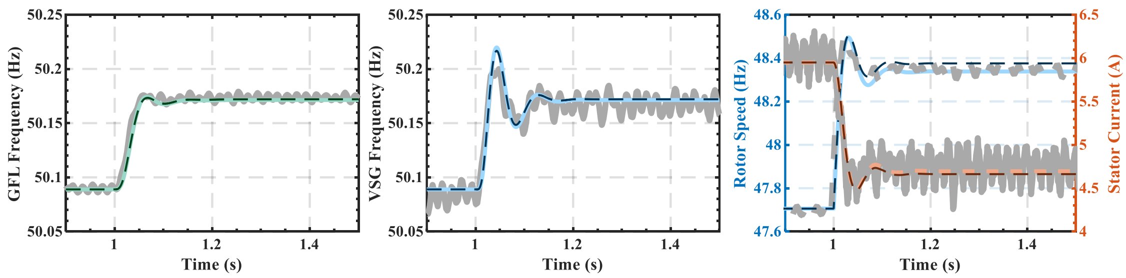

Figure 3.32: Forced responses of converters and induction motor to 0.2 pu load torque jump

Modified IEEE 13-bus System

In this subsection, the power flow and small-signal modeling framework are tested with the modified IEEE 13-bus system. The system is scaled to a voltage rating of 400 V (phase-phase root-mean-square value), and the stiff grid is assumed to contain 0.5 pu negative-sequence voltage. As shown in Figure 3.30, four Type I GFL converters are integrated into the distribution network. Parameters of branches and loads are listed in Table 3.5 and Table 3.6. The comparison between simulation (indicated by "Sim") and power flow (indicated by "PF") calculation results shown in Figure 3.33 confirms the accuracy of the proposed method. Figure 3.34 and Figure 3.35 show time-domain dynamic responses of the PLL frequency and the grid-side filter inductor current of all VSCs to a 5% active power reference step of VSC 1 at 1.0 s. Dynamic evolutions of the small-signal model agrees well with the nonlinear average model. It is noted that the system becomes unstable as the PLL bandwidth increases to 40 Hz. Nevertheless, by initializing all state variables with the results of the power flow analysis, the simulation can be started from the equilibrium, allowing the distinction between instability due to the absence of equilibrium and small-signal instability.

Table 3.5: Branch Parameters of the Modified IEEE 13-Bus System

From	To	Value	From	To	Value
1	4	$0.1313\ \Omega + 0.4178$ mH	7	8	$0.0755\ \Omega + 0.2404$ mH
2	3	$0.0755\ \Omega + 0.2404$ mH	8	9	$0.0752\ \Omega + 0.2394$ mH
3	4	$0.1259\ \Omega + 0.4007$ mH	9	10	$0.0756\ \Omega + 0.2406$ mH
4	5	$0.0713\ \Omega + 0.2269$ mH	10	11	$0.0756\ \Omega + 0.2406$ mH
5	6	$0.01\ \Omega + 0.03183$ mH	8	12	$0.2034\ \Omega + 0.6475$ mH
4	9	$0.1313\ \Omega + 0.4178$ mH	9	13	$0.0656\ \Omega + 0.2089$ mH

Table 3.6: Load Parameters of the Modified IEEE 13-Bus System

Connection Bus	Value	Connection Bus	Value
3	$66.07\ \Omega + 154.6$ mH	10	$56.90\ \Omega + 160.9$ mH
6	$28.36\ \Omega + 65.44$ mH	11	$15.79\ \Omega + 27.54$ mH
7	$83.34\ \Omega + 124.8$ mH	12	$93.15\ \Omega + 199.2$ mH
9	$11.30\ \Omega + 20.54$ mH	-	-

3.5 Summary

In this chapter, a systematic procedure is developed to build the small-signal model of converter-dominated power systems considering balanced and unbalanced operations. The Wirtinger calculus is introduced for the fully complex-domain modeling. The stationary reference frame is selected as the common basis for the implementation of the component connection method. Compared to the classical real-domain modeling in the rotational reference frame, following unique benefits can be observed

1. The complex variable in the original coordinate inherently contains the sequence information, i.e., positive (negative) frequency component refers to positive (negative) sequence component. In contrast, the dq frame is a fictitious coordinate, it is not

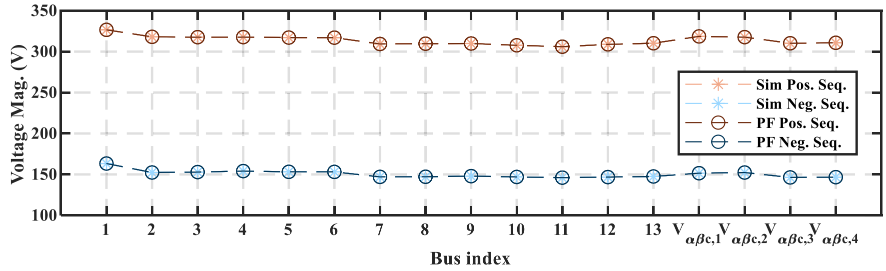

(a) Voltage Magnitude

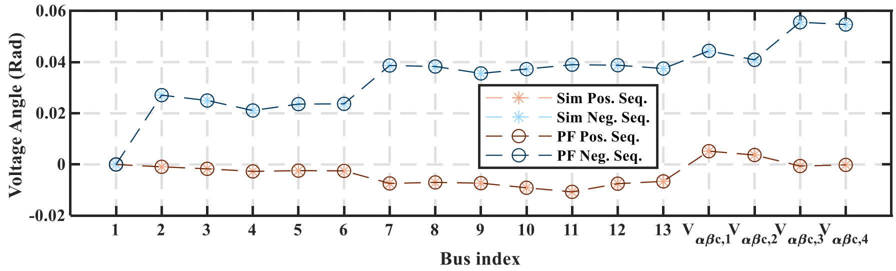

(b) Voltage Phase Angle

Figure 3.33: Steady-state bus voltages of the modified IEEE 13-Bus system

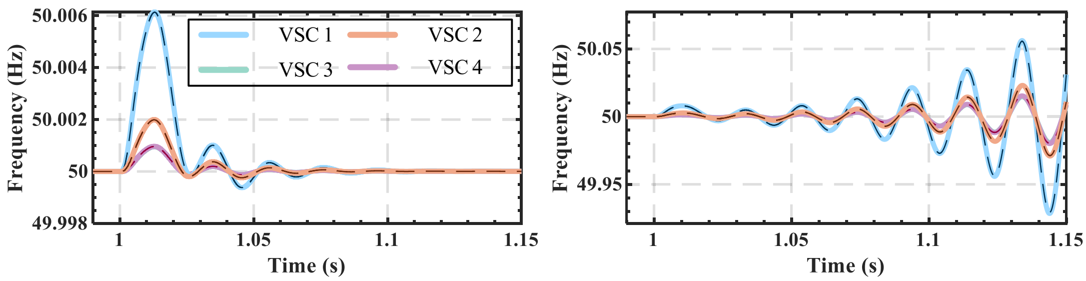

Figure 3.34: Dynamic responses of the PLL estimated frequency to a 5% active power reference step of VSC 1 (Solid lines – average model. Dashed lines – small signal model) Left: PLL bandwidth is 30 Hz. Right: PLL bandwidth is 40 Hz

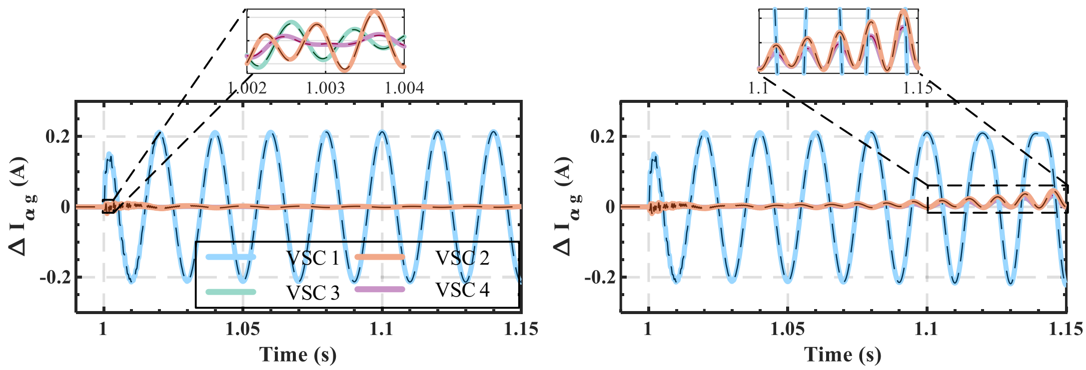

Figure 3.35: Dynamic responses of the α-component of the grid-side inductor current to a 5% active power reference step of VSC 1 (Solid lines – average model. Dashed lines – small signal model) Left: PLL bandwidth is 30 Hz. Right: PLL bandwidth is 40 Hz

straightforward to link a single real-valued component to the description of three-phase systems.

2. For the derivation of the small-signal model, the complex-valued description can simplify the calculation. For instance, the linearization of the current reference calculation and the frame transformation in the complex domain is simpler than that in the real domain.

3. To build small-signal models in the *dq* frame, one converter needs to be selected to provide a common rotational reference frame for the Park respectively inverse Park transformation. This becomes nonintuitive when the system is operated under unbalanced or harmonically distorted conditions. This shortcoming is overcome by selecting the stationary reference frame as the common reference frame.

To verify the accuracy of the proposed modeling method, a systematic software framework is developed based on the MATLAB/Simulink platform. A PHIL test setup is used for the experimental validation. The effectiveness of the proposed modeling methodology is confirmed by tests performed on both single-converter and multi-converter systems.

4

Small-Signal Stability Analysis

This chapter focuses on the stability analysis of the complex-valued LTP small-signal model derived in Chapter 3. First, the widely used eigenanalysis/modal analysis framework for LTI systems is reviewed. A time-domain physical interpretation is proposed to link the dynamic characteristics of LTI and LTP systems. Then, the modal analysis is generalized for the LTP systems. Definitions of the damping ratio, participation factor and eigenvalue sensitivity are accordingly modified for the evaluation of dynamic performance of the LTP systems. Moreover, two accurate and efficient truncation order selection methods are developed for the eigenvalue and eigenvector calculation of the LTP systems. The chapter closes with applications of the above techniques to the stability analysis of both grid-following and grid-forming converter systems.

4.1 Modal Analysis for the Linear Time-Invariant System

The modal analysis is proved to be a useful tool for the stability analysis of a general N-dimensional LTI system

$$\begin{aligned} \Delta\dot{\boldsymbol{x}} &= \boldsymbol{A}\Delta\boldsymbol{x} + \boldsymbol{B}\Delta\boldsymbol{u} \\ \Delta\boldsymbol{y} &= \boldsymbol{C}\Delta\boldsymbol{x} + \boldsymbol{D}\Delta\boldsymbol{u} \end{aligned} \tag{4.1}$$

where $\Delta\boldsymbol{x}$, $\Delta\boldsymbol{u}$ and $\Delta\boldsymbol{y}$ are state, input and output vectors. $\boldsymbol{A}$, $\boldsymbol{B}$, $\boldsymbol{C}$ and $\boldsymbol{D}$ are defined as the system, input, output and feedforward matrices respectively, which are all time invariant. Since the inputs and outputs do not change the stability of the LTI system, solving the free response problem

$$\Delta\dot{\boldsymbol{x}} = \boldsymbol{A}\Delta\boldsymbol{x}, \text{ with } \Delta\boldsymbol{x}(t_0) = \Delta\boldsymbol{x}_0 \tag{4.2}$$

is sufficient for the stability evaluation. t_0 denotes the start time instance.

The mathematical foundation of the modal analysis is the eigen/spectral decomposition of the system matrix

$$\boldsymbol{A} = \boldsymbol{R}\boldsymbol{\Lambda}\boldsymbol{R}^{-1} = \underbrace{\begin{bmatrix} \boldsymbol{r}_1 & \boldsymbol{r}_2 & \cdots & \boldsymbol{r}_N \end{bmatrix}}_{\boldsymbol{R}} \underbrace{\begin{bmatrix} \lambda_1 & & & \\ & \lambda_2 & & \\ & & \ddots & \\ & & & \lambda_N \end{bmatrix}}_{\boldsymbol{\Lambda}} \underbrace{\begin{bmatrix} \boldsymbol{l}_1 \\ \boldsymbol{l}_2 \\ \vdots \\ \boldsymbol{l}_N \end{bmatrix}}_{\boldsymbol{R}^{-1}}. \tag{4.3}$$

Here, the system matrix $\boldsymbol{A}$ is assumed to be diagonalizable, which is a common case for the small-signal models of power systems. The diagonal matrix $\boldsymbol{\Lambda}$ is defined as the eigenvalue matrix. $\boldsymbol{R}$ and $\boldsymbol{R}^{-1}$ are the right eigenvector and left eigenvector matrices. The ith eigenvalue (or mode) λ_i, the ith right eigenvector $\boldsymbol{r}_i$ (the ith column of $\boldsymbol{R}$) and the ith left eigenvector $\boldsymbol{l}_i$ (the ith row of $\boldsymbol{R}^{-1}$) satisfy the relation

$$\boldsymbol{A}\boldsymbol{r}_i = \lambda_i \boldsymbol{r}_i \tag{4.4a}$$

$$\boldsymbol{l}_i\boldsymbol{A} = \lambda_i \boldsymbol{l}_i \tag{4.4b}$$

$$\boldsymbol{l}_i\boldsymbol{r}_j = \sum\nolimits_{k=1}^{N} l_{ik} r_{kj} = \begin{cases} 1, & \text{if } i = j \\ 0, & \text{if } i \neq j \end{cases} \tag{4.4c}$$

where l_{ik} is the kth element of $\boldsymbol{l}_i$, that is the element in the ith row and kth column of $\boldsymbol{R}^{-1}$. r_{kj} is the kth element of $\boldsymbol{r}_j$, namely the element in the kth row and jth column of $\boldsymbol{R}$.

Stability and Damping Ratio

Applying the space transformation

$$\Delta\boldsymbol{x} = \boldsymbol{R}\Delta\boldsymbol{z}, \tag{4.5}$$

the physical system Eq. (4.2) is transformed into the so-called modal space

$$\frac{d}{dt}(\boldsymbol{R}\Delta\boldsymbol{z}) = \boldsymbol{A}(\boldsymbol{R}\Delta\boldsymbol{z}) \;\Rightarrow\; \Delta\dot{\boldsymbol{z}} = \underbrace{\boldsymbol{R}^{-1}\boldsymbol{A}\boldsymbol{R}}_{\boldsymbol{\Lambda}}\Delta\boldsymbol{z}$$

$$\Downarrow$$

$$\underbrace{\begin{bmatrix} \Delta\dot{z}_1 \\ \Delta\dot{z}_2 \\ \vdots \\ \Delta\dot{z}_N \end{bmatrix}}_{\Delta\dot{\boldsymbol{z}}} = \underbrace{\begin{bmatrix} \lambda_1 & & & \\ & \lambda_2 & & \\ & & \ddots & \\ & & & \lambda_N \end{bmatrix}}_{\boldsymbol{\Lambda}=\boldsymbol{R}^{-1}\boldsymbol{A}\boldsymbol{R}} \underbrace{\begin{bmatrix} \Delta z_1 \\ \Delta z_2 \\ \vdots \\ \Delta z_N \end{bmatrix}}_{\Delta\boldsymbol{z}}. \tag{4.6}$$

It is seen that the state variables $\{\Delta z_i, i = 1, ..., N\}$ are decoupled, and the ith state variable Δz_i can be directly solved

$$\Delta z_i = \Delta z_{i0} e^{\lambda_i (t - t_0)},\; t \in [t_0,\;\; \infty) \tag{4.7}$$

where $\Delta z_{i0} = \Delta z_i\,(t_0)$ is the initial condition of Δz_i.

Let the initial condition of $\Delta\boldsymbol{x}$ be the unit vector along the kth axis,

$$\Delta\boldsymbol{x}_0 = \boldsymbol{e}_k = \left[\begin{array}{ccccccc} \underbrace{0}_{\text{1st}} & \cdots & 0 & \underbrace{1}_{k\text{th}} & 0 & \cdots & \underbrace{0}_{N\text{th}} \end{array}\right]^T, \tag{4.8}$$

namely the kth element of $\Delta\boldsymbol{x}_0$ is one and others are zero. Then, the initial value of Δz_i can be obtained from

$$\underbrace{\begin{bmatrix} \Delta z_1 \\ \vdots \\ \Delta z_i \\ \vdots \\ \Delta z_N \end{bmatrix}}_{\Delta\boldsymbol{z}} = \underbrace{\begin{bmatrix} \boldsymbol{l}_1 \\ \vdots \\ \boldsymbol{l}_i \\ \vdots \\ \boldsymbol{l}_N \end{bmatrix}}_{\boldsymbol{R}^{-1}} \underbrace{\begin{bmatrix} \Delta x_1 \\ \vdots \\ \Delta x_i \\ \vdots \\ \Delta x_N \end{bmatrix}}_{\Delta\boldsymbol{x}} = \underbrace{\begin{bmatrix} l_{11} & \cdots & l_{1i} & \cdots & l_{1N} \\ \vdots & & \vdots & & \vdots \\ l_{i1} & \cdots & l_{ii} & \cdots & l_{iN} \\ \vdots & & \vdots & & \vdots \\ l_{N1} & \cdots & l_{Ni} & \cdots & l_{NN} \end{bmatrix}}_{\boldsymbol{R}^{-1}} \underbrace{\begin{bmatrix} \Delta x_1 \\ \vdots \\ \Delta x_i \\ \vdots \\ \Delta x_N \end{bmatrix}}_{\Delta\boldsymbol{x}}. \tag{4.9}$$

$$\Downarrow$$

$$\Delta z_i\left(t_0\right) = \Delta z_{i0} = \boldsymbol{l}_i \Delta\boldsymbol{x}_0 = l_{ik}$$

Returning to Eq. (4.5), the response of the kth physical state variable is given by

$$\underbrace{\begin{bmatrix} \Delta x_1 \\ \vdots \\ \Delta x_k \\ \vdots \\ \Delta x_N \end{bmatrix}}_{\Delta\boldsymbol{x}} = \underbrace{\begin{bmatrix} \boldsymbol{r}_1 & \boldsymbol{r}_2 & \cdots & \boldsymbol{r}_N \end{bmatrix}}_{\boldsymbol{R}} \underbrace{\begin{bmatrix} \Delta z_1 \\ \vdots \\ \Delta z_k \\ \vdots \\ \Delta z_N \end{bmatrix}}_{\Delta\boldsymbol{z}} = \underbrace{\begin{bmatrix} r_{11} & \cdots & r_{1k} & \cdots & r_{1N} \\ \vdots & & \vdots & & \vdots \\ r_{k1} & \cdots & r_{kk} & \cdots & r_{kN} \\ \vdots & & \vdots & & \vdots \\ r_{N1} & \cdots & r_{Nk} & \cdots & r_{NN} \end{bmatrix}}_{\boldsymbol{R}} \underbrace{\begin{bmatrix} \Delta z_1 \\ \vdots \\ \Delta z_k \\ \vdots \\ \Delta z_N \end{bmatrix}}_{\Delta\boldsymbol{z}}.$$

$$\Downarrow$$

$$\Delta x_k = \textstyle\sum_{i=1}^{N} r_{ki}\Delta z_i = \sum_{i=1}^{N} r_{ki} l_{ik} e^{\lambda_i (t-t_0)} \tag{4.10}$$

It is noted that the free response of Δx_k is the superposition of N oscillation modes $\{\lambda_i, i = 1, ..., N\}$. The system is stable if the real parts of all eigenvalues are negative. When the system is stable, defining

$$\lambda_i = \sigma_i + j\omega_i, \tag{4.11}$$

the damping performance of the ith oscillation mode λ_i is quantified by the damping factor σ_i and the damping ratio

$$\xi_i = \frac{-\sigma_i}{\sqrt{\sigma_i^2 + \omega_i^2}}. \tag{4.12}$$

Specifically, the amplitude of the state decays to $1/e$ or 37% of the initial value in $1/\left|\sigma_i\right|$ seconds or $1/(2\pi\xi_i)$ cycles of oscillation.

Participation Factor

From Eq. (4.9) and (4.10), l_{ik} quantifies the significance of the initial condition of the kth state Δx_k to excite the ith mode λ_i. r_{ki} reflects the observability of the ith mode in the kth state. Their product

$$p_{ki} = r_{ki} l_{ik} \tag{4.13}$$

is defined as the participation factor of the kth state in the ith mode, and conversely. Physically it is consistent with the initial value of the ith oscillation mode observed in the dynamic evolution of Δx_k, as given in Eq. (4.10).

Eigenvalue Sensitivity

Another important tool within the classical modal analysis framework is the eigenvalue sensitivity analysis. Let φ be an arbitrary parameter in the system matrix $\boldsymbol{A}$, the partial derivative of Eq. (4.4a) with respect to φ is

$$\begin{gathered}\frac{\partial(\boldsymbol{A}\boldsymbol{r}_i)}{\partial\varphi}=\frac{\partial\left(\lambda_i\boldsymbol{r}_i\right)}{\partial\varphi}\\ \Downarrow\\ \frac{\partial\boldsymbol{A}}{\partial\varphi}\boldsymbol{r}_i+\boldsymbol{A}\frac{\partial\boldsymbol{r}_i}{\partial\varphi}=\frac{\partial\lambda_i}{\partial\varphi}\boldsymbol{r}_i+\lambda_i\frac{\partial\boldsymbol{r}_i}{\partial\varphi}\end{gathered}. \tag{4.14}$$

Multiplying both sides of Eq. (4.14) with $\boldsymbol{l_i}$ and inserting Eq. (4.4b) and (4.4c), the sensitivity of λ_i with respect to φ is obtained

$$\begin{gathered}\boldsymbol{l}_i\frac{\partial\boldsymbol{A}}{\partial\varphi}\boldsymbol{r}_i+\boldsymbol{l}_i\boldsymbol{A}\frac{\partial\boldsymbol{r}_i}{\partial\varphi}=\frac{\partial\lambda_i}{\partial\varphi}\underbrace{\boldsymbol{l}_i\boldsymbol{r}_i}_{1}+\lambda_i\boldsymbol{l}_i\frac{\partial\boldsymbol{r}_i}{\partial\varphi}\\ \Downarrow\\ \frac{\partial\lambda_i}{\partial\varphi}=\boldsymbol{l}_i\frac{\partial\boldsymbol{A}}{\partial\varphi}\boldsymbol{r}_i\end{gathered}. \tag{4.15}$$

Let φ be the element in the ith row and kth column of $\boldsymbol{A}$, namely A_{ik}, the sensitivity of λ_i with respect to A_{ik} is

$$\begin{gathered}\frac{\partial\lambda_i}{\partial A_{ik}}=\boldsymbol{l}_i\frac{\partial\boldsymbol{A}}{\partial A_{ik}}\boldsymbol{r}_i=\underbrace{\begin{bmatrix} l_{i1} & \cdots & l_{ik} & \cdots & l_{iN}\end{bmatrix}}_{\boldsymbol{l}_i}\begin{array}{c} \quad k\text{th} \\ \quad\downarrow \\ \underbrace{\begin{bmatrix} 0 & \cdots & 0 & \cdots & 0\\ \vdots & & \vdots & & \vdots\\ 0 & \cdots & 1 & \cdots & 0\\ \vdots & & \vdots & & \vdots\\ 0 & \cdots & 0 & \cdots & 0\end{bmatrix}}_{\frac{\partial\boldsymbol{A}}{\partial A_{ik}}}\end{array}\begin{array}{c}\\ \\ \\ \leftarrow i\text{th}\\ \\ \\ \end{array}\underbrace{\begin{bmatrix} r_{1i}\\ \vdots\\ r_{ki}\\ \vdots\\ r_{Ni}\end{bmatrix}}_{\boldsymbol{r}_i}\\ \Downarrow\\ \frac{\partial\lambda_i}{\partial A_{ik}}=l_{ik}r_{ki}\end{gathered} \tag{4.16}$$

which is the same as the participation factor given by Eq. (4.13).

Eigenvalue sensitivity information can be used for the control parameter tuning. Specifically, when the feedback loop gain between the ith and the kth state variables is changed by ΔA_{ik}, as shown in Figure 4.1, its impact on the change of the eigenvalue λ_i can be predicted by

$$\Delta\lambda_i=\Delta A_{ik}\frac{\partial\lambda_i}{\partial A_{ik}}. \tag{4.17}$$

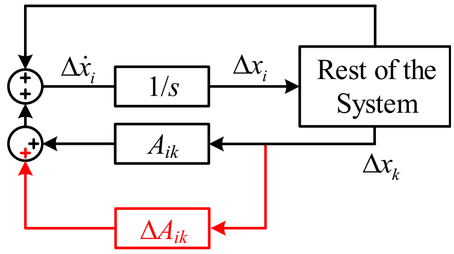

Figure 4.1: Physical meaning of the eigenvalue sensitivity

This provides guidance for control parameter optimization to move critical eigenvalues towards the left-half of the complex plane, as will be presented in Chapter 6.

4.2 Time-Domain Physical Interpretation of the LTP System

The classical modal analysis reviewed above can reveal the dynamic behavior of an LTI system in detail, however, it cannot be directly applied to the stability analysis of the LTP model of converter-dominated power systems. To generalize the modal analysis to LTP systems, a time-domain physical interpretation is proposed for comparison of the dynamic characteristics of LTI and LTP systems.

Linear Time-Invariant System

Applying the rotational transformation

$$\Delta \boldsymbol{x}_h = e^{-jh\omega_0 t}\Delta \boldsymbol{x}, \tag{4.18}$$

in other words observing the system in a new coordinate frame rotating the original one by $e^{-jh\omega_0 t}$, the state-space description of the LTI system given by Eq. (4.2) becomes

$$\begin{gathered} \frac{d}{dt}\Bigg(\underbrace{e^{jh\omega_0 t}\Delta \boldsymbol{x}_h}_{\Delta \boldsymbol{x}}\Bigg) = \boldsymbol{A}\Bigg(\underbrace{e^{jh\omega_0 t}\Delta \boldsymbol{x}_h}_{\Delta \boldsymbol{x}}\Bigg) \\ \Downarrow \\ \Delta\dot{\boldsymbol{x}}_h = (\boldsymbol{A} - jh\omega_0 \boldsymbol{I})\Delta \boldsymbol{x}_h \end{gathered} \tag{4.19}$$

where ω_0 is constant, h is an integer and $\boldsymbol{I}$ is the identity matrix. It is seen that the rotational transformation with fixed frequency $h\omega_0$ is linear. Equation (4.2) and (4.19) are fully decoupled, and both can independently describe the LTI physical system. Obviously, eigenvalues of Eq. (4.19), $\{\lambda_i - jh\omega_0, i = 1, ..., N\}$, are frequency-shifted versions of those of Eq. (4.2).

Linear Time-Periodic System

For the free response problem of a general N-dimensional LTP system

$$\Delta\dot{\boldsymbol{x}} = \boldsymbol{A}(t)\Delta \boldsymbol{x}, \text{ with } \Delta \boldsymbol{x}(t_0) = \Delta \boldsymbol{x}_0 \tag{4.20}$$

the system matrix $\boldsymbol{A}(t)$ becomes time periodic with the fundamental period $T_0 = 2\pi/\omega_0$. If not specified otherwise, the time variable (t) is used to distinguish the time-periodic matrices and vectors from time-invariant ones.

Inserting the Fourier series expansion

$$\boldsymbol{A}(t) = \sum\nolimits_{k=-\infty}^{\infty} \boldsymbol{A}_k e^{jk\omega_0 t}$$

and using the notation defined in Eq. (4.18), the state-space model Eq. (4.20) can be reformulated as

$$\begin{gathered}\Delta\dot{\boldsymbol{x}} = \sum\nolimits_{k=-\infty}^{\infty} \boldsymbol{A}_k e^{jk\omega_0 t}\Delta\boldsymbol{x} = \boldsymbol{A}_0\Delta\boldsymbol{x} + \sum\nolimits_{k\neq 0} \boldsymbol{A}_k \underbrace{e^{jk\omega_0 t}\Delta\boldsymbol{x}}_{\Delta\boldsymbol{x}_{-k}} \\ \Downarrow \\ \Delta\dot{\boldsymbol{x}} = \boldsymbol{A}_0\Delta\boldsymbol{x} + \sum\nolimits_{k\neq 0} \boldsymbol{A}_k\Delta\boldsymbol{x}_{-k}\end{gathered} \tag{4.21}$$

and in the rotated coordinate frame

$$\Delta\dot{\boldsymbol{x}}_h = (\boldsymbol{A}_0 - jh\omega_0\boldsymbol{I})\Delta\boldsymbol{x}_h + \sum\nolimits_{k\neq 0} \boldsymbol{A}_k\Delta\boldsymbol{x}_{h-k}. \tag{4.22}$$

Writing Eq. (4.21) and (4.22) in the matrix form given by Eq. (4.23), the N-dimensional LTP system is equivalently described as an infinite-dimensional LTI system with couplings between observations in the original and rotated coordinate frames, i.e., $\Delta\boldsymbol{x}$ and $\{\Delta\boldsymbol{x}_h, h \in \mathbb{Z}\}$.

$$\begin{bmatrix} \vdots \\ \Delta\dot{\boldsymbol{x}}_{-1} \\ \Delta\dot{\boldsymbol{x}} \\ \Delta\dot{\boldsymbol{x}}_1 \\ \vdots \end{bmatrix} = \begin{bmatrix} \ddots & \vdots & \vdots & \vdots & \iddots \\ \cdots & \boldsymbol{A}_0 + j\omega_0\boldsymbol{I} & \boldsymbol{A}_{-1} & \boldsymbol{A}_{-2} & \cdots \\ \cdots & \boldsymbol{A}_1 & \boldsymbol{A}_0 & \boldsymbol{A}_{-1} & \cdots \\ \cdots & \boldsymbol{A}_2 & \boldsymbol{A}_1 & \boldsymbol{A}_0 - j\omega_0\boldsymbol{I} & \cdots \\ \iddots & \vdots & \vdots & \vdots & \ddots \end{bmatrix} \begin{bmatrix} \vdots \\ \Delta\boldsymbol{x}_{-1} \\ \Delta\boldsymbol{x} \\ \Delta\boldsymbol{x}_1 \\ \vdots \end{bmatrix} \tag{4.23}$$

The same as the LTI system, both $\Delta\boldsymbol{x}$ and $\{\Delta\boldsymbol{x}_h, h \in \mathbb{Z}\}$ can fully capture dynamic evolutions of the LTP physical system. If λ_i is predominantly related to $\Delta\boldsymbol{x}$, the frequency-shifted eigenvalue $\lambda_i - jh\omega_0$ will dominate dynamics of $\Delta\boldsymbol{x}_h$. Therefore, it can be expected that eigenvalues of Eq. (4.23) will formulate N vertical lines in the complex plane. Different from the LTI systems, due to the frequency coupling effect, oscillations associated with $\lambda_i - jh\omega_0$ can also appear in $\Delta\boldsymbol{x}$. Considering symmetry, the contribution of $\lambda_i - jh\omega_0$ in $\Delta\boldsymbol{x}$ is the same as that of λ_i in $\Delta\boldsymbol{x}_h$. These intuitive inferences derived from the proposed time-domain physical interpretation will be mathematically proved in the next section. For the evaluation and improvement of the damping performance of the LTP system, major concerns are to calculate eigenvalues λ_i most relevant to $\Delta\boldsymbol{x}$ and quantify the contribution of $\lambda_i - jh\omega_0$.

4.3 Generalized Modal Analysis for Linear Time-Periodic Systems

4.3.1 Eigenvalues and Eigenvectors of LTP Systems

To evaluate the stability and damping performance of the LTP system, the analytical solution of the free response problem of the LTP system Eq. (4.20) is derived in this subsection.

According to the Floquet theory [90], there exists a time-periodic transformation matrix $\boldsymbol{R}(t)$

$$\Delta \boldsymbol{x} = \boldsymbol{R}(t)\Delta \boldsymbol{z} \tag{4.24}$$

which transforms Eq. (4.20) into a new state space where the system matrix $\boldsymbol{Q}$ is a time-invariant diagonal matrix

$$\begin{gathered}
\tfrac{d}{dt}\left(\boldsymbol{R}(t)\Delta \boldsymbol{z}\right) = \boldsymbol{R}(t)\Delta \dot{\boldsymbol{z}} + \dot{\boldsymbol{R}}(t)\Delta \boldsymbol{z} = \boldsymbol{A}(t)\left(\boldsymbol{R}(t)\Delta \boldsymbol{z}\right) \\
\Downarrow \\
\underbrace{\begin{bmatrix} \Delta \dot{z}_1 \\ \Delta \dot{z}_2 \\ \vdots \\ \Delta \dot{z}_N \end{bmatrix}}_{\Delta \dot{\boldsymbol{z}}} = \underbrace{\begin{bmatrix} \lambda_1 & & & \\ & \lambda_2 & & \\ & & \ddots & \\ & & & \lambda_N \end{bmatrix}}_{\boldsymbol{Q}=\boldsymbol{R}^{-1}(t)(\boldsymbol{A}(t)\boldsymbol{R}(t)-\dot{\boldsymbol{R}}(t))} \underbrace{\begin{bmatrix} \Delta z_1 \\ \Delta z_2 \\ \vdots \\ \Delta z_N \end{bmatrix}}_{\Delta \boldsymbol{z}} \quad .
\end{gathered} \tag{4.25}$$

Similar to Eq. (4.6), this new state space can be regarded as the modal space of the LTP system, where Δz_i can be directly solved

$$\Delta z_i = \Delta z_{i0} e^{\lambda_i (t-t_0)}. \tag{4.26}$$

The initial condition Δz_{i0} is obtained from the transformation

$$\Delta \boldsymbol{z}_0 = \boldsymbol{R}^{-1}\left(t_0\right)\Delta \boldsymbol{x}_0. \tag{4.27}$$

Defining

$$\boldsymbol{R}(t) = [\boldsymbol{r}_1(t),\ \ \boldsymbol{r}_2(t),\ \ \ldots,\ \ \boldsymbol{r}_N(t)]$$

and considering the transformation given by Eq. (4.24), the free response of Eq. (4.20) is formulated by the superposition of N independent fundamental solutions

$$\Delta \boldsymbol{x}_i, i = 1, ..., N$$

related to the N diagonal elements in $\boldsymbol{Q}$

$$\Delta \boldsymbol{x} = \underbrace{\begin{bmatrix} \boldsymbol{r}_1(t) & \boldsymbol{r}_2(t) & \cdots & \boldsymbol{r}_N(t) \end{bmatrix}}_{\boldsymbol{R}(t)} \underbrace{\begin{bmatrix} \Delta z_1 \\ \Delta z_2 \\ \vdots \\ \Delta z_N \end{bmatrix}}_{\Delta \boldsymbol{z}} = \sum\nolimits_{i=1}^{N} \underbrace{\Delta z_{i0} e^{\lambda_i (t-t_0)} \boldsymbol{r}_i(t)}_{\Delta \boldsymbol{x}_i} \tag{4.28}$$

where $\boldsymbol{r}_i(t)$ is the ith column of $\boldsymbol{R}(t)$.

Each fundamental solution $\Delta \boldsymbol{x}_i$ satisfies Eq. (4.20), which means

$$\frac{d}{dt}\left(\underbrace{\Delta z_{i0} e^{\lambda_i(t-t_0)} \boldsymbol{r}_i(t)}_{\Delta \boldsymbol{x}_i}\right) = \boldsymbol{A}(t)\left(\underbrace{\Delta z_{i0} e^{\lambda_i(t-t_0)} \boldsymbol{r}_i(t)}_{\Delta \boldsymbol{x}_i}\right)$$
$$\Downarrow \tag{4.29}$$
$$\Delta z_{i0} e^{-\lambda_i t_0}\left(e^{\lambda_i t}\dot{\boldsymbol{r}}_i(t) + \lambda_i e^{\lambda_i t}\boldsymbol{r}_i(t)\right) = \Delta z_{i0} e^{-\lambda_i t_0}\boldsymbol{A}(t) e^{\lambda_i t}\boldsymbol{r}_i(t)$$

so that

$$\lambda_i \boldsymbol{r}_i(t) = \boldsymbol{A}(t)\boldsymbol{r}_i(t) - \dot{\boldsymbol{r}}_i(t) \quad . \tag{4.30}$$

The time-periodic matrix $\boldsymbol{A}(t)$ and the vector $\boldsymbol{r}_i(t)$ have the Fourier series expansion:

$$\begin{aligned} \boldsymbol{A}(t) &= \sum\nolimits_{k=-\infty}^{\infty} \boldsymbol{A}_k e^{jk\omega_0 t} \\ \boldsymbol{r}_i(t) &= \sum\nolimits_{h=-\infty}^{\infty} \boldsymbol{r}_i^h e^{jh\omega_0 t} \\ \dot{\boldsymbol{r}}_i(t) &= \sum\nolimits_{h=-\infty}^{\infty} jh\omega_0 \cdot \boldsymbol{r}_i^h e^{jh\omega_0 t} \end{aligned} \tag{4.31}$$

where the Fourier series coefficient $\boldsymbol{A}_k$ is associated with the kth order harmonic of $\boldsymbol{A}(t)$, and the Fourier series coefficient $\boldsymbol{r}_i^h$ is associated with the hth order harmonic of $\boldsymbol{r}_i(t)$. The subscript i in $\boldsymbol{r}_i(t)$ indicates that $\boldsymbol{r}_i(t)$ is the ith LTP eigenvector, namely the ith column of $\boldsymbol{R}(t)$.

Inserting Eq. (4.31) into Eq. (4.30), yields

$$\sum\nolimits_{h=-\infty}^{\infty}\left(\left(\lambda_i + jh\omega_0\right)\boldsymbol{r}_i^h - \sum\nolimits_{k=-\infty}^{\infty}\boldsymbol{A}_k \boldsymbol{r}_i^{h-k}\right) e^{jh\omega_0 t} = 0 \tag{4.32}$$

which is valid for any time instance t, therefore, items in the bracket must be zero, namely Eq. (4.33) holds for all $h \in \mathbb{Z}$.

$$\left(\lambda_i + jh\omega_0\right)\boldsymbol{r}_i^h = \sum\nolimits_{k=-\infty}^{\infty}\boldsymbol{A}_k \boldsymbol{r}_i^{h-k} \tag{4.33}$$

Equation (4.33) can be formulated into the matrix form

$$\lambda_i \begin{bmatrix} \vdots \\ \boldsymbol{r}_i^{-1} \\ \boldsymbol{r}_i^0 \\ \boldsymbol{r}_i^1 \\ \vdots \end{bmatrix} = \begin{bmatrix} \ddots & \vdots & \vdots & \vdots & \iddots \\ \cdots & \boldsymbol{A}_0 + j\omega_0\boldsymbol{I} & \boldsymbol{A}_{-1} & \boldsymbol{A}_{-2} & \cdots \\ \cdots & \boldsymbol{A}_1 & \boldsymbol{A}_0 & \boldsymbol{A}_{-1} & \cdots \\ \cdots & \boldsymbol{A}_2 & \boldsymbol{A}_1 & \boldsymbol{A}_0 - j\omega_0\boldsymbol{I} & \cdots \\ \iddots & \vdots & \vdots & \vdots & \ddots \end{bmatrix} \begin{bmatrix} \vdots \\ \boldsymbol{r}_i^{-1} \\ \boldsymbol{r}_i^0 \\ \boldsymbol{r}_i^1 \\ \vdots \end{bmatrix} \tag{4.34}$$

which can be compactly written as

$$\lambda_i \mathcal{R}_i = (\mathcal{A} - \mathcal{N})\mathcal{R}_i \tag{4.35}$$

by defining

$$\mathcal{R}_i = \begin{bmatrix} \vdots \\ \boldsymbol{r}_i^{-1} \\ \boldsymbol{r}_i^{0} \\ \boldsymbol{r}_i^{1} \\ \vdots \end{bmatrix} \quad \mathcal{A} = \begin{bmatrix} \ddots & \vdots & \vdots & \vdots & \iddots \\ \cdots & \boldsymbol{A}_0 & \boldsymbol{A}_{-1} & \boldsymbol{A}_{-2} & \cdots \\ \cdots & \boldsymbol{A}_1 & \boldsymbol{A}_0 & \boldsymbol{A}_{-1} & \cdots \\ \cdots & \boldsymbol{A}_2 & \boldsymbol{A}_1 & \boldsymbol{A}_0 & \cdots \\ \iddots & \vdots & \vdots & \vdots & \ddots \end{bmatrix} \quad \mathcal{N} = \begin{bmatrix} \ddots & & & & \\ & \boldsymbol{N}_{-1} & & & \\ & & \boldsymbol{N}_0 & & \\ & & & \boldsymbol{N}_1 & \\ & & & & \ddots \end{bmatrix}. \tag{4.36}$$

N_k is an N-dimensional diagonal square matrix with diagonal elements equal to $jk\omega_0$. It is seen that Eq. (4.34) and (4.35) define a standard eigenvalue problem. Specifically, λ_i is the eigenvalue of the infinite matrix $\mathcal{A}-\mathcal{N}$ associated with the eigenvector $\mathcal{R}_i$ consisting of Fourier series coefficients of the vector $\boldsymbol{r}_i(t)$.

It can be easily confirmed that the pair of the complex value $\lambda_i + jk\omega_0$ and the vector $e^{-jk\omega_0 t}\boldsymbol{r}_i(t)$ satisfy the relation Eq. (4.30), therefore, the complex value $\lambda_i + jk\omega_0$ is also the eigenvalue of $\mathcal{A}-\mathcal{N}$, and the corresponding eigenvector is the Fourier series coefficient vector of $e^{-jk\omega_0 t}\boldsymbol{r}_i(t)$. Following the same procedure, it can be identified that the other elements in the matrix $\boldsymbol{Q}$ and their frequency-shifted copies are also the eigenvalues of $\mathcal{A}-\mathcal{N}$. This leads to the conclusion that the eigenvalue plot of the infinite matrix $\mathcal{A}-\mathcal{N}$ consists of N vertical lines, as qualitatively demonstrated in Figure 4.2.

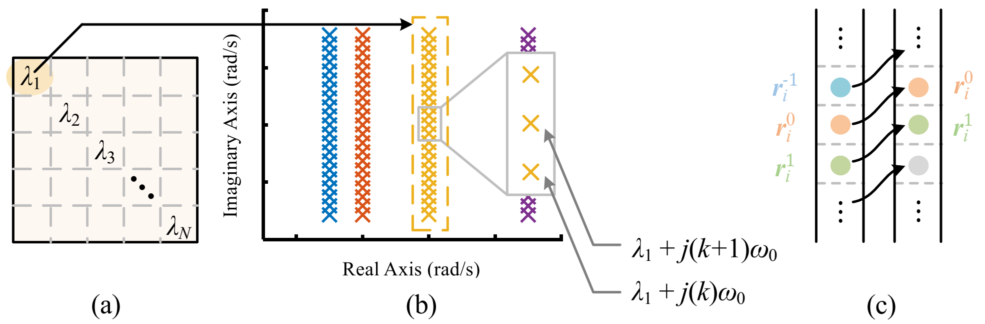

Figure 4.2: Qualitative eigenvalue loci of $\mathcal{A}-\mathcal{N}$. Each element of the diagonal matrix $\boldsymbol{Q}$ (a) corresponds to one vertical line in the Eigenvalue map (b). (c) Eigenvectors of $\mathcal{A}-\mathcal{N}$ associated with $\lambda_1 + jk\omega_0$ (left) and $\lambda_i + j(k+1)\omega_0$ (right)

Returning to the ith fundamental solution

$$\Delta \boldsymbol{x}_i = \Delta z_{i0} \cdot e^{\lambda_i (t-t_0)} \cdot \boldsymbol{r}_i(t), \tag{4.37}$$

it can also be expressed by the frequency-shifted eigenvalue $\lambda_i + jk\omega_0$ and the associated eigenvector $e^{-jk\omega_0 t}\boldsymbol{r}_i(t)$

$$\Delta \boldsymbol{x}_i = {\color{blue}e^{jk\omega_0 t_0}} \Delta z_{i0} \cdot e^{(\lambda_i + jk\omega_0)(t-t_0)} \cdot e^{-jk\omega_0 t}\boldsymbol{r}_i(t). \tag{4.38}$$

The blue term in Eq. (4.38) results from the frequency shifting of the left eigenvector from $\boldsymbol{l}_i$ to $e^{jk\omega_0 t}\boldsymbol{l}_i$.

Defining

$$\lambda_i = \sigma_i + j\omega_i, \tag{4.39}$$

and employing the Fourier series expansion of $\boldsymbol{r}_i(t)$ in Eq. (4.31), the ith fundamental solution $\Delta\boldsymbol{x}_i$ becomes

$$\Delta\boldsymbol{x}_i = \Delta z_{i0} \sum\nolimits_{h=-\infty}^{\infty} \boldsymbol{r}_i^h e^{\sigma_i(t-t_0)} e^{-j\omega_i t_0} e^{j(\omega_i + h\omega_0)t} \tag{4.40}$$

Two conclusions can be drawn from Eq. (4.38) and (4.40):

1. The eigenvalues in each vertical line shown in Figure 4.2 provide redundant information. Together with the eigenvector, one arbitrary eigenvalue on the vertical line is enough to determine the corresponding fundamental solution.

2. Each fundamental solution can contain multiple oscillation components sharing the same damping factor σ_i, while their oscillation frequencies differ by integer multiples of the fundamental frequency ω_0. For the LTI system, only one oscillation frequency is associated with each damping factor (see Eq. (4.10)), since the transformation matrix $\boldsymbol{R}$ of the LTI system is constant.

It is noted that the matrix $\mathcal{A}-\mathcal{N}$ is exactly the same as the system matrix of the state-space model given by Eq. (4.23). The conclusions stated above prove the intuitive guess derived based on the physical explanation in Section 4.2.

In this thesis, λ_i is defined as LTP eigenvalue or LTP mode, and the associated time-periodic eigenvector $\boldsymbol{r}_i(t)$ is called LTP eigenvector.

Analysis Example - Lossy Mathieu equation

In order to illustrate the usefulness of the analysis method described above, the lossy Mathieu equation is taken as an example. A two-dimensional lossy Mathieu equation can be generally described by

$$\underbrace{\frac{d}{dt}\begin{bmatrix} x_1 \\ x_2 \end{bmatrix}}_{\dot{\boldsymbol{x}}} = \underbrace{\begin{bmatrix} 0 & 1 \\ -5+\beta\cos\omega_0 t & -2\zeta \end{bmatrix}}_{\boldsymbol{A}(t)} \underbrace{\begin{bmatrix} x_1 \\ x_2 \end{bmatrix}}_{\boldsymbol{x}} . \tag{4.41}$$

The non-zero Fourier series coefficients of $\boldsymbol{A}(t)$ are

$$\boldsymbol{A}_{-1} = \begin{bmatrix} 0 & 0 \\ \beta/2 & 0 \end{bmatrix}, \quad \boldsymbol{A}_0 = \begin{bmatrix} 0 & 1 \\ -5 & -2\zeta \end{bmatrix}, \quad \boldsymbol{A}_1 = \begin{bmatrix} 0 & 0 \\ \beta/2 & 0 \end{bmatrix} . \tag{4.42}$$

In this example, the parameter values are selected to be

$$\zeta = 0.8, \quad \beta = 8, \quad \omega_0 = 2 \ .$$

For this two-dimensional system, two LTP eigenvalues can be determined by using the method that will be introduced in Section 4.4

$$\boldsymbol{Q} = \begin{bmatrix} \lambda_1 & \\ & \lambda_2 \end{bmatrix} = \begin{bmatrix} -0.1782 & \\ & -1.4218 \end{bmatrix} \tag{4.43}$$

together with two LTP eigenvectors

$$\boldsymbol{r}_1(t) = \left\{ \begin{array}{l} \underbrace{\begin{bmatrix} -0.0005-0.0005j \\ -0.0041+0.0041j \end{bmatrix}}_{\boldsymbol{r}_2^{-4}} e^{-j4\omega_0 t} + \underbrace{\begin{bmatrix} 0.0061+0.0091j \\ 0.0533-0.0381j \end{bmatrix}}_{\boldsymbol{r}_2^{-3}} e^{-j3\omega_0 t} + \underbrace{\begin{bmatrix} -0.0301-0.0817j \\ -0.3213+0.1349j \end{bmatrix}}_{\boldsymbol{r}_2^{-2}} e^{-j2\omega_0 t} \\ + \underbrace{\begin{bmatrix} -0.0230+0.2581j \\ 0.5203+0.0000j \end{bmatrix}}_{\boldsymbol{r}_2^{-1}} e^{-j1\omega_0 t} + \underbrace{\begin{bmatrix} 0.1863+0.1442j \\ -0.0332-0.0257j \end{bmatrix}}_{\boldsymbol{r}_2^{0}} + \underbrace{\begin{bmatrix} 0.2441-0.0871j \\ 0.1306+0.5037j \end{bmatrix}}_{\boldsymbol{r}_2^{1}} e^{j1\omega_0 t} \\ + \underbrace{\begin{bmatrix} -0.0866-0.0086j \\ 0.0499-0.3449j \end{bmatrix}}_{\boldsymbol{r}_2^{2}} e^{j2\omega_0 t} + \underbrace{\begin{bmatrix} 0.0103+0.0036j \\ -0.0235+0.0612j \end{bmatrix}}_{\boldsymbol{r}_2^{3}} e^{j3\omega_0 t} + \underbrace{\begin{bmatrix} -0.0006-0.0004j \\ 0.0029-0.0050j \end{bmatrix}}_{\boldsymbol{r}_2^{4}} e^{j4\omega_0 t} \end{array} \right\}.$$

$$\boldsymbol{r}_2(t) = \left\{ \begin{array}{l} \underbrace{\begin{bmatrix} 0.0006-0.0001j \\ -0.0018-0.0046j \end{bmatrix}}_{\boldsymbol{r}_1^{-4}} e^{-j4\omega_0 t} + \underbrace{\begin{bmatrix} -0.0086+0.0033j \\ 0.0322+0.0467j \end{bmatrix}}_{\boldsymbol{r}_1^{-3}} e^{-j3\omega_0 t} + \underbrace{\begin{bmatrix} 0.0602-0.0419j \\ -0.2531-0.1813j \end{bmatrix}}_{\boldsymbol{r}_1^{-2}} e^{-j2\omega_0 t} \\ + \underbrace{\begin{bmatrix} -0.1088+0.1894j \\ 0.5333-0.0517j \end{bmatrix}}_{\boldsymbol{r}_1^{-1}} e^{-j1\omega_0 t} + \underbrace{\begin{bmatrix} -0.1983+0.0096j \\ 0.2819-0.0136j \end{bmatrix}}_{\boldsymbol{r}_1^{0}} + \underbrace{\begin{bmatrix} -0.1265-0.1780j \\ 0.5359+0.0000j \end{bmatrix}}_{\boldsymbol{r}_1^{1}} e^{j1\omega_0 t} \\ + \underbrace{\begin{bmatrix} 0.0640+0.0359j \\ -0.2344+0.2049j \end{bmatrix}}_{\boldsymbol{r}_1^{2}} e^{j2\omega_0 t} + \underbrace{\begin{bmatrix} -0.0089-0.0025j \\ 0.0275-0.0496j \end{bmatrix}}_{\boldsymbol{r}_1^{3}} e^{j3\omega_0 t} + \underbrace{\begin{bmatrix} 0.0006+0.0001j \\ -0.0014+0.0048j \end{bmatrix}}_{\boldsymbol{r}_1^{4}} e^{j4\omega_0 t} \end{array} \right\}$$

Let the initial condition at $t_0 = 0$ be

$$\boldsymbol{x}_0 = \begin{bmatrix} x_{10} \\ x_{20} \end{bmatrix} = \begin{bmatrix} 1 \\ 0 \end{bmatrix}.$$

The free response of the state variable x_1 is shown in Figure 4.3. It is seen that the dynamic evolution of x_1 is the superposition of two LTP modes, namely λ_1 (see Figure 4.3(a)) and λ_2 (see Figure 4.3(b)). Each LTP mode contains five oscillation components with oscillation frequencies differing by integer multiples of ω_0.

4.3.2 Stability and Damping Ratio

From the analytical solution of the free response of the LTP system given by Eq. (4.40), it can be concluded that the system stability is determined by the real part of the LTP eigenvalue:

- If $\sigma_i < 0$ holds for all i, all LTP oscillation modes are exponentially damped, thus, the system is asymptotically stable.
- If $\sigma_i = 0$, the ith LTP mode is an undamped oscillation, the system is marginally stable.
- If $\sigma_i > 0$, the corresponding LTP mode increases exponentially, so the system is unstable.

When the ith LTP eigenvector $\boldsymbol{r}_i(t)$ has non-zero Fourier series coefficients up to the Hth order, the ith fundamental solution $\Delta\boldsymbol{x}_i$ becomes

$$\Delta\boldsymbol{x}_i = \Delta z_{i0} \sum\nolimits_{h=-H}^{H} \boldsymbol{r}_i^h e^{\sigma_i(t-t_0)} e^{-j\omega_i t_0} e^{j(\omega_i + h\omega_0)t} \tag{4.44}$$

which contains $(2H+1)$ oscillation components. The damping ratio of ith LTP mode is generalized as a vector

$$\boldsymbol{\xi}_i = \begin{bmatrix} \xi_i^{-H} & \cdots & \xi_i^0 & \cdots & \xi_i^H \end{bmatrix}^T. \tag{4.45}$$

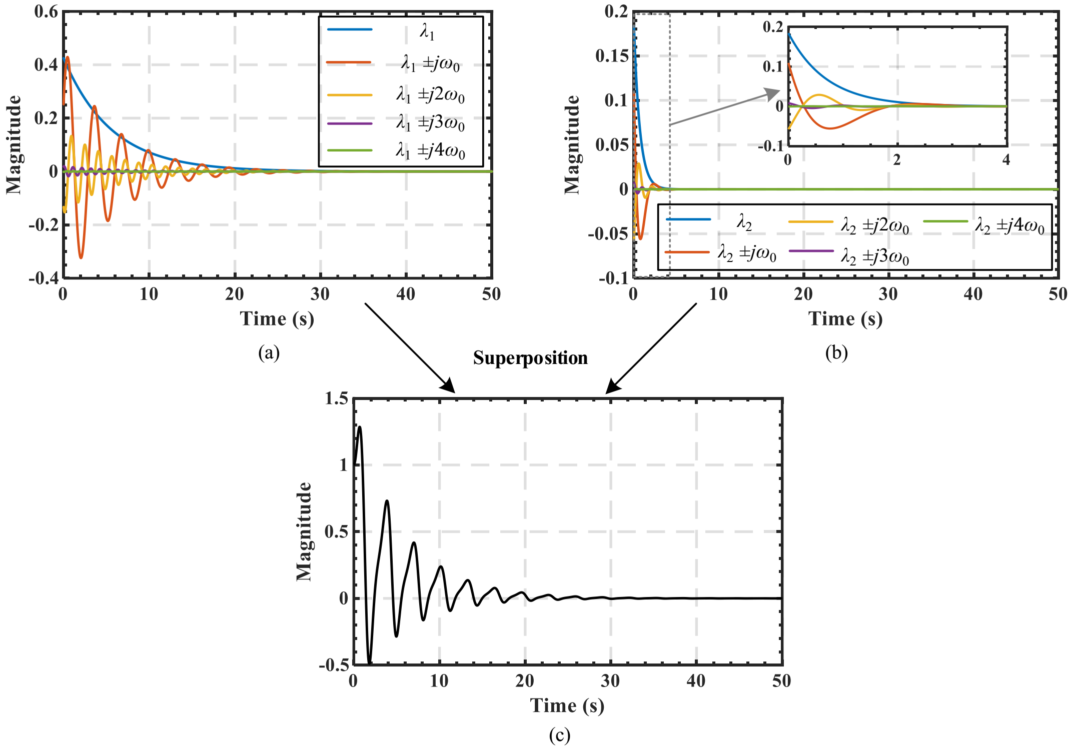

Figure 4.3: Free response of x_1 to an initial condition of $\begin{bmatrix} 1 & 0 \end{bmatrix}^T$ at $t_0 = 0\,\mathrm{s}$. The dynamic evolution of x_1 shown in (c) is the superposition of two LTP modes, namely λ_1 in (a) and λ_2 in (b). Each LTP mode corresponds to five oscillation components.

ξ_i^h given by

$$\xi_i^h = \frac{-\sigma_i}{\sqrt{\sigma_i^2 + (\omega_i + h\omega_0)^2}} \tag{4.46}$$

is the damping ratio of the hth oscillation component of the ith LTP mode.

For LTI systems, ξ_i^h equals zero unless $h = 0$, since the eigenvector $\boldsymbol{r}_i$ is time invariant. This makes the LTI system a special case of the LTP system.

4.3.3 Participation Factor Analysis

To determine the relative participation of the ith LTP mode in the kth state, similar to the case of the LTI systems, the initial condition $\Delta\boldsymbol{x}_0$ is chosen to be the unit vector along the kth axis, namely $\boldsymbol{e}_k$ in Eq. (4.8). Let $\boldsymbol{l}_i(t)$ be the ith row of $\boldsymbol{R}^{-1}(t)$, the initial condition of

Δz_i is obtained from

$$\underbrace{\begin{bmatrix} \Delta z_1 \\ \vdots \\ \Delta z_i \\ \vdots \\ \Delta z_N \end{bmatrix}}_{\Delta \boldsymbol{z}} = \underbrace{\begin{bmatrix} \boldsymbol{l}_1(t) \\ \vdots \\ \boldsymbol{l}_i(t) \\ \vdots \\ \boldsymbol{l}_N(t) \end{bmatrix}}_{\boldsymbol{R}^{-1}(t)} \underbrace{\begin{bmatrix} \Delta x_1 \\ \vdots \\ \Delta x_i \\ \vdots \\ \Delta x_N \end{bmatrix}}_{\Delta \boldsymbol{x}} = \underbrace{\begin{bmatrix} l_{11}(t) & \cdots & l_{1i}(t) & \cdots & l_{1N}(t) \\ \vdots & & \vdots & & \vdots \\ l_{i1}(t) & \cdots & l_{ii}(t) & \cdots & l_{iN}(t) \\ \vdots & & \vdots & & \vdots \\ l_{N1}(t) & \cdots & l_{Ni}(t) & \cdots & l_{NN}(t) \end{bmatrix}}_{\boldsymbol{R}^{-1}(t)} \underbrace{\begin{bmatrix} \Delta x_1 \\ \vdots \\ \Delta x_i \\ \vdots \\ \Delta x_N \end{bmatrix}}_{\Delta \boldsymbol{x}}$$

$$\Downarrow$$

$$\Delta z_{i0} = \Delta z_i(t_0) = \boldsymbol{l}_i\,(t_0)\,\boldsymbol{e}_k = l_{ik}\,(t_0) = \textstyle\sum_{h=-\infty}^{\infty} l_{ik}^h e^{jh\omega_0 t_0} \tag{4.47}$$

where $l_{ik}(t_0)$ represents the kth element of $\boldsymbol{l}_i(t_0)$, and gives the contribution of the initial condition of Δx_k to the ith LTP mode. $l_{ik}(t_0)$ varies in a periodic manner on the start time instance t_0, and l_{ik}^h denotes its hth order Fourier series coefficient.

Then, the dynamic response of the kth state of $\Delta \boldsymbol{x}$ in Eq. (4.28) becomes

$$\Delta x_k = \sum_{i=1}^{N} l_{ik}\,(t_0)\,r_{ki}\,(t) e^{\lambda_i (t-t_0)} \tag{4.48}$$

where $r_{ki}(t)$ is the kth element of the column vector $\boldsymbol{r}_i(t)$. Inserting the Fourier series expansion

$$r_{ki}\,(t) = \sum_{h=-\infty}^{\infty} r_{ki}^h e^{jh\omega_0 t}$$

yields

$$\Delta x_k = \sum_{i=1}^{N} \sum_{h=-\infty}^{\infty} \underbrace{l_{ik}\,(t_0)\,r_{ki}^h e^{jh\omega_0 t_0}}_{\Delta x_{ki}^h (t_0)} e^{(\lambda_i + jh\omega_0)(t-t_0)} \tag{4.49}$$

It is seen that the initial value of the hth oscillation component of the ith LTP mode

$$\Delta x_{ki}^h\,(t_0) = l_{ik}\,(t_0)\,r_{ki}^h e^{jh\omega_0 t_0}$$

is a time-period function of t_0. Formulating the Fourier series coefficients of $l_{ik}(t)$ in vector form

$$\boldsymbol{l}_{ik} = \begin{bmatrix} \cdots & l_{ik}^{-h} & \cdots & l_{ik}^{-1} & l_{ik}^0 & l_{ik}^1 & \cdots & l_{ik}^h & \cdots \end{bmatrix}^T,$$

the upper bound of $l_{ik}(t_0)$ is given by the L_1-norm $|\boldsymbol{l}_{ik}|_1$. Using the upper limit of $\Delta x_{ki}^h\,(t_0)$, the participation factor of the hth oscillation component of the ith LTP mode in the kth state is defined as

$$p_{ki}^h = \frac{|\boldsymbol{l}_{ik}|_1 \cdot \left| r_{ki}^h \right|}{\sum_{i=1}^{N} \sum_{h=-\infty}^{\infty} |\boldsymbol{l}_{ik}|_1 \cdot \left| r_{ki}^h \right|}. \tag{4.50}$$

The entire contribution of the ith LTP mode in the kth state is defined as

$$p_{ki} = \frac{\sum_{h=-\infty}^{\infty} |\boldsymbol{l}_{ik}|_1 \cdot \left| r_{ki}^h \right|}{\sum_{i=1}^{N} \sum_{h=-\infty}^{\infty} |\boldsymbol{l}_{ik}|_1 \cdot \left| r_{ki}^h \right|}. \tag{4.51}$$

An alternative definition of the participation factor can be developed by considering the average value of $\Delta x_{ki}^{h}(t_0)$ over one fundamental period T_0, namely

$$p_{ki}^{h} = \int_{t_0=0}^{T_0} \Delta x_{ki}^{h}(t_0) dt_0 = \int_{t_0=0}^{T_0} l_{ik}(t_0) r_{ki}^{h} e^{jh\omega_0 t_0} dt_0 = l_{ik}^{-h} r_{ki}^{h}. \tag{4.52}$$

Accordingly, the total participation factor of the ith LTP mode in the kth state is defined as

$$p_{ki} = \sum\nolimits_{h=-\infty}^{\infty} p_{ki}^{h} = \sum\nolimits_{h=-\infty}^{\infty} l_{ik}^{-h} r_{ki}^{h}. \tag{4.53}$$

It can be confirmed that the sum of participation factors of the ith LTP mode (state) in all states (modes) is one.

Analysis Example - Type I grid-following converter (DSRF-PLL plus PI current control)

For the sake of clarity, the free response of the Type I GFL converter is solved to demonstrate the application of the participation factor given by Eq. (4.50) and (4.51). Key control and physical parameters are listed in Table 4.1. Non-zero Fourier coefficients of $\boldsymbol{A}(t)$ are indicated by colored dots in Figure 4.4. Extra non-zero elements caused by the negative-sequence grid voltage are marked with black dots. In other words, those terms indicated by black dots become zeros when the three-phase grid voltage is balanced.

Table 4.1: Parameters of the Type I Grid-Following Converter for Participation Analysis

Symbol	Description	Value
SCR	Short-circuit ratio	3
BW	Bandwidth of the DSRF-PLL	20 Hz
τ	Time constant of the PI current controller	1 ms
S_r	Power reference	1.2 kW
V_p	Magnitude of the positive-sequence grid voltage	100 V
V_n	Magnitude of the negative-sequence grid voltage	50 V

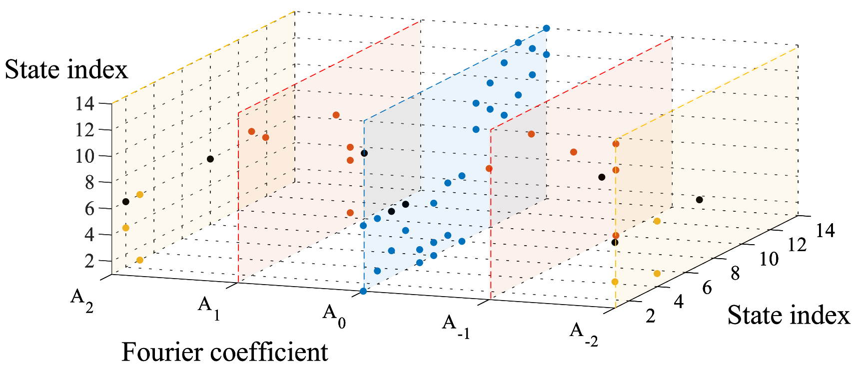

Figure 4.4: Distribution of non-zero Fourier coefficients of the 14-dimensional time-periodic matrix $\boldsymbol{A}(t)$. Each colored surface corresponds to a 14×14 Fourier series coefficient of $\boldsymbol{A}(t)$, and their non-zero elements are denoted by dots. Extra black dots result from the negative-sequence grid voltage.

After the system reaches steady state, a 1 Hz disturbance is applied to the state variable $\Delta\eta$ of the DSRF-PLL. The free responses obtained from the nonlinear average model and the small-signal model are shown in Figure 4.5. It can be observed that the evolution of $\Delta\eta$ is dominated by an oscillation component at the frequency of 12.99 Hz (0.077 s) for a low PLL bandwidth BW $= 20$ Hz. The influence of the starting time instance is negligible. As the PLL bandwidth BW increases to 33 Hz, the time-periodic impact of the starting time instance t_0, can be observed in the response of $\Delta\eta$. Additionally, more oscillation frequencies appear.

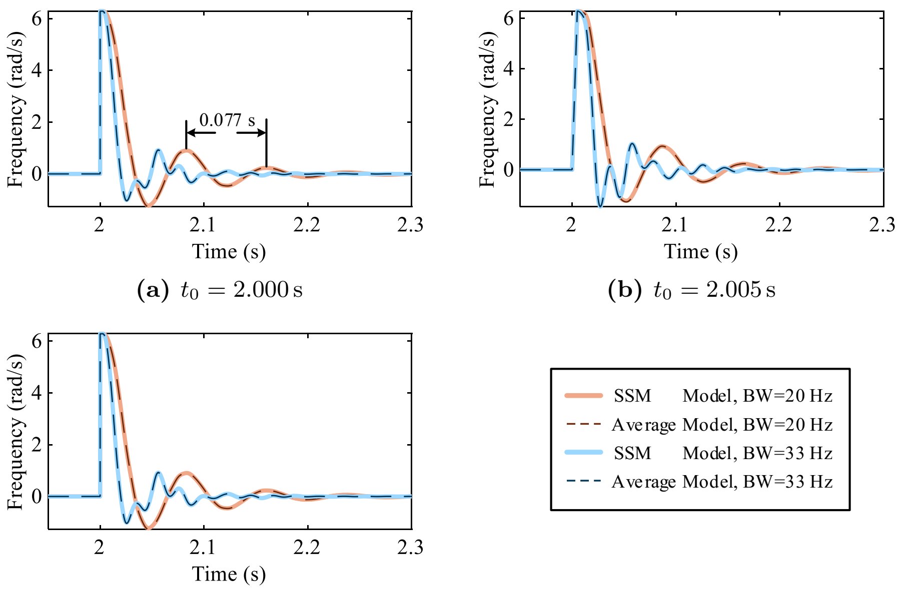

(a) $t_0 = 2.000$ s **(b)** $t_0 = 2.005$ s **(c)** $t_0 = 2.020$ s

Figure 4.5: Free response of PLL estimated frequency $\Delta\eta$ to initial condition $\Delta\eta_0 = 2\pi$ at different starting time instances

Figure 4.6(a) and Figure 4.7(a) show the LTP eigenvalue maps for different PLL bandwidths. The 14 LTP eigenvalues are marked with red dots. According to Eq. (4.44), each LTP eigenvalue/mode is related to multiple oscillation components. Those oscillation components corresponding to nonzero $\boldsymbol{r}_i^h$ are marked with dots and stars in Figure 4.6(b) and Figure 4.7(b). In Figure 4.6(b), only LTP mode 1 and mode 3 are plotted, since mode 2 and mode 4 have the same damping factor (i.e., real part) and conjugate frequencies (i.e., imaginary part), the same goes for Figure 4.7(b). Based on Eq. (4.50), the participation factor of each LTP mode in the state $\Delta\eta$ is computed and given by the stacked bar plots in Figure 4.6(c) and Figure 4.7(c). In Figure 4.6(b), LTP mode 1 has eight oscillation components (marked with one red dot and seven different colored stars), the participation factor of each oscillation component of mode 1 is given by the first stacked bar in Figure 4.6(c). The color of the stacked bar is consistent with that of the dots and stars in Figure 4.6(b). It can be observed that only one pair of oscillation components in LTP mode 1 and 2 ($\lambda_{1,2} = -17 \pm j81.5$) has critical damping ratio ($\xi^0_{1,2} = 0.20$). The oscillation frequency is consistent with the free response shown in Figure 4.5. As BW increases to 33 Hz, more oscillation components having critical damping ratio appear in LTP mode 1/2 ($-21.8 \pm j346.4$ and $-21.8 \pm j281.9$) and mode 3/4 ($-36.8 \pm j101.5$), as shown in Figure 4.7(b). This explains the more oscillatory free response for BW $= 33$ Hz in Figure 4.5.

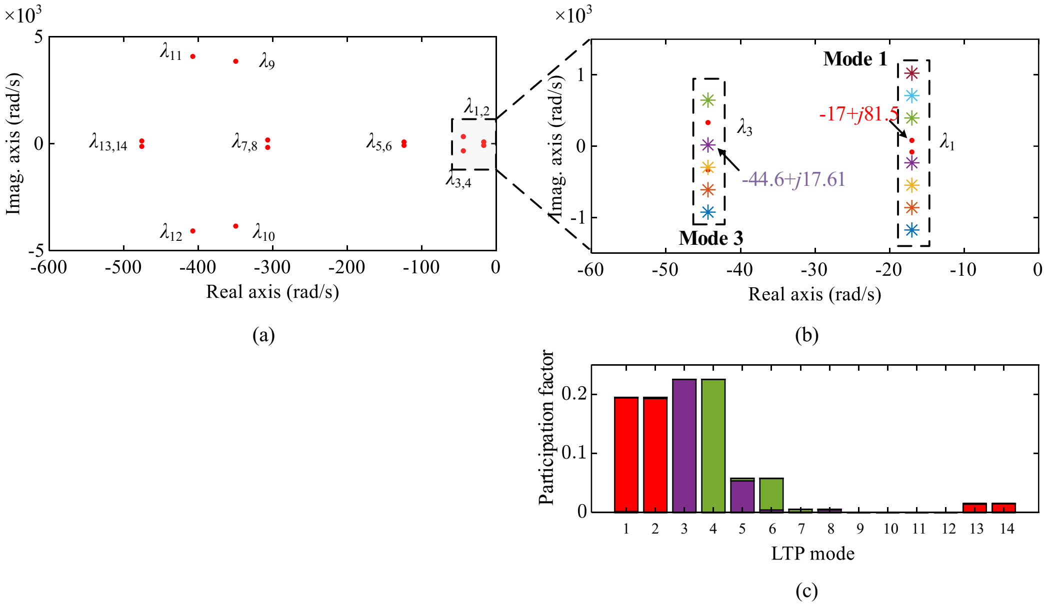

Figure 4.6: Small-signal analysis for $BW = 20\,\text{Hz}$. (a) LTP eigenvalue map. (b) Oscillation components of each LTP mode. (c) PF of each LTP mode in state $\Delta\eta$.

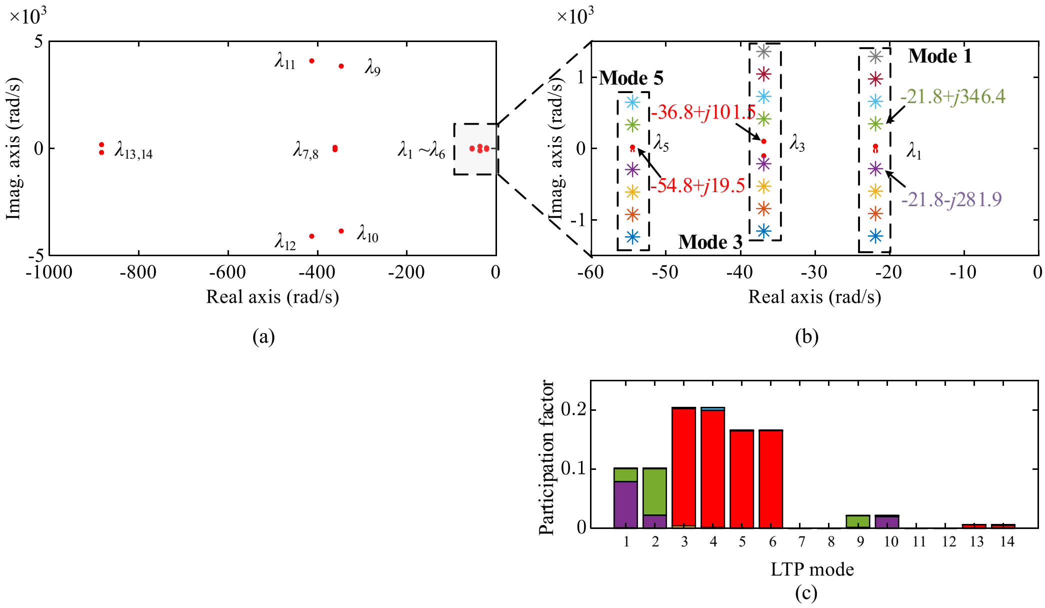

Figure 4.7: Small-signal analysis for $BW = 33\,\text{Hz}$. (a) LTP eigenvalue map. (b) Oscillation components of each LTP mode. (c) PF of each LTP mode in state $\Delta\eta$.

4.3.4 Sensitivity Analysis

This subsection aims to compute the sensitivity of the LTP eigenvalue with respect to an arbitrary parameter. From Eq. (4.25), the system matrix $\boldsymbol{A}(t)$ of the LTP system satisfies

$$\boldsymbol{A}(t)\,\boldsymbol{R}(t) - \dot{\boldsymbol{R}}(t) = \boldsymbol{R}(t)\,\boldsymbol{Q} \tag{4.54}$$

Considering

$$\begin{gathered}\boldsymbol{R}(t)\boldsymbol{R}^{-1}(t) = \boldsymbol{I} \\ \Downarrow \\ \frac{d}{dt}\left(\boldsymbol{R}(t)\boldsymbol{R}^{-1}(t)\right) = \dot{\boldsymbol{R}}(t)\boldsymbol{R}^{-1}(t) + \boldsymbol{R}(t)\dot{\boldsymbol{R}}^{-1}(t) = \boldsymbol{0}\end{gathered},$$

the adjoint equation can be derived from Eq. (4.54)

$$\boldsymbol{R}^{-1}(t)\,\boldsymbol{A}(t) + \dot{\boldsymbol{R}}^{-1}(t) = \boldsymbol{Q}\boldsymbol{R}^{-1}(t) \tag{4.55}$$

Equation (4.54) and (4.55) give that the ith diagonal element of $\boldsymbol{Q}$, the ith column of $\boldsymbol{R}(t)$ and the ith row of $\boldsymbol{R}^{-1}(t)$, namely λ_i, $\boldsymbol{r}_i(t)$ and $\boldsymbol{l}_i(t)$, satisfy the relation

$$\boldsymbol{A}(t)\,\boldsymbol{r}_i(t) - \dot{\boldsymbol{r}}_i(t) = \lambda_i \boldsymbol{r}_i(t) \tag{4.56a}$$

$$\boldsymbol{l}_i(t)\,\boldsymbol{A}(t) + \dot{\boldsymbol{l}}_i(t) = \lambda_i \boldsymbol{l}_i(t) \tag{4.56b}$$

Taking partial derivatives of both sides of Eq. (4.56a) with respect to an arbitrary parameter φ, yields

$$\frac{\partial \boldsymbol{A}(t)}{\partial \varphi}\boldsymbol{r}_i(t) + \boldsymbol{A}(t)\frac{\partial \boldsymbol{r}_i(t)}{\partial \varphi} - \frac{\partial \dot{\boldsymbol{r}}_i(t)}{\partial \varphi} = \frac{\partial \lambda_i}{\partial \varphi}\boldsymbol{r}_i(t) + \lambda_i \frac{\partial \boldsymbol{r}_i(t)}{\partial \varphi}. \tag{4.57}$$

Multiplying both sides of Eq. (4.57) by $\boldsymbol{l}_i(t)$ and substituting the relation given by Eq. (4.56b), it becomes

$$\begin{aligned} \frac{\partial \lambda_i}{\partial \varphi} &= \boldsymbol{l}_i(t)\frac{\partial \boldsymbol{A}(t)}{\partial \varphi}\boldsymbol{r}_i(t) - \left(\dot{\boldsymbol{l}}_i(t)\frac{\partial \boldsymbol{r}_i(t)}{\partial \varphi} + \boldsymbol{l}_i(t)\frac{\partial \dot{\boldsymbol{r}}_i(t)}{\partial \varphi}\right) \\ &= \boldsymbol{l}_i(t)\frac{\partial \boldsymbol{A}(t)}{\partial \varphi}\boldsymbol{r}_i(t) - \frac{d}{dt}\left(\boldsymbol{l}_i(t)\frac{\partial \boldsymbol{r}_i(t)}{\partial \varphi}\right) \end{aligned}. \tag{4.58}$$

The term

$$\frac{d}{dt}\left(\boldsymbol{l}_i(t)\frac{\partial \boldsymbol{r}_i(t)}{\partial \varphi}\right)$$

contains no time-invariant elements, therefore, the time-independent eigenvalue sensitivity is determined by

$$\frac{\partial \lambda_i}{\partial \varphi} = \left\{\boldsymbol{l}_i(t)\frac{\partial \boldsymbol{A}(t)}{\partial \varphi}\boldsymbol{r}_i(t)\right\}^0 \tag{4.59}$$

where the operator $\{\ \}^0$ extracts the DC component, namely the average value of $\boldsymbol{l}_i(t)\frac{\partial \boldsymbol{A}(t)}{\partial \varphi}\boldsymbol{r}_i(t)$ over one fundamental period T_0. It is seen that the LTP eigenvalue sensitivity is the same as the participation factor given by Eq. (4.52) and (4.53). The physical meaning of the LTP eigenvalue sensitivity is the same as that of the LTI system.

4.4 LTP Eigenvalue Calculation

The proposed generalized modal analysis can provide insightful characterization of the dynamic performance of the LTP system. However, the calculation of the LTP eigenvalue matrix $\boldsymbol{Q}$ and the transformation matrix $\boldsymbol{R}(t)$ in Eq. (4.25) remains an open topic. Currently, there are mainly two categories of LTP eigenvalue computation methods.

The first category is to calculate the N-dimensional monodromy matrix $\boldsymbol{\Phi}(T_0, 0)$ [58] by solving a matrix differential equation

$$\dot{\boldsymbol{\Phi}}(t,\ 0) = \boldsymbol{A}(t)\,\boldsymbol{\Phi}(t,\ 0) \quad \text{with } \boldsymbol{\Phi}(0,\ 0) = \boldsymbol{I} \tag{4.60}$$

There exists the following relation between the LTP eigenvalues of $\boldsymbol{A}(t)$ and eigenvalues of $\boldsymbol{\Phi}(T_0, 0)$

$$\underbrace{\begin{bmatrix} e^{\lambda_1 T_0} & & & \\ & e^{\lambda_2 T_0} & & \\ & & \ddots & \\ & & & e^{\lambda_N T_0} \end{bmatrix}}_{e^{\boldsymbol{Q} T_0}} = \underbrace{\begin{bmatrix} \lambda_{\boldsymbol{\Phi},\,1} & & & \\ & \lambda_{\boldsymbol{\Phi},\,2} & & \\ & & \ddots & \\ & & & \lambda_{\boldsymbol{\Phi},\,N} \end{bmatrix}}_{\mathrm{eig}\{\boldsymbol{\Phi}(T_0,\,0)\}} \tag{4.61}$$

which gives another interpretation of the stability criterion, that is the LTP system is asymptotically stable when magnitudes of all eigenvalues of $\boldsymbol{\Phi}(T_0, 0)$ are smaller than unity.

According to Eq. (4.61), the LTP eigenvalue λ_i can be solved from

$$e^{\lambda_i T_0} = \lambda_{\boldsymbol{\Phi},\,i}. \tag{4.62}$$

By choosing an appropriate ordinary differential equation solver, eigenvalue calculation results to any required degree of accuracy can be derived from $\boldsymbol{\Phi}(T_0, 0)$. Yet, it fails to provide more insightful quantification of the system dynamics, e.g., damping, sensitivity and participation information. Additionally, for large-scale converter-dominated power systems, the numerical integration of the high-dimensional system matrix can be time-consuming.

The second category is to solve the eigenvalue problem of Eq. (4.34). Since numerical implementation and calculation of the eigenvalues of an infinite matrix is impossible, the matrix $\mathcal{A} - \mathcal{N}$ must be truncated. Two questions should be answered:

1. whether the eigenvalues of the truncated matrix converge to those of the infinite matrix;

2. how to choose the minimum truncation order H_{min} to balance the trade-off between numerical accuracy and efficiency.

Practical power electronic systems have limited bandwidth and energy, thus, $\boldsymbol{A}(t)$ and $\boldsymbol{r}_i(t)$ given in Eq. (4.31) have finite non-zero Fourier series terms. For such systems, it has been rigorously proved in [94] that eigenvalues of the truncated matrix converge to those of the non-truncated one as the truncation order approaches infinity.

Eigenvalue Sorting Method

To determine the minimum truncation order H_{min}, the eigenvalue sorting method is used in most references. The principle is to increase the truncation order H until N unchanged eigenvalues are found in the fundamental strip $-\omega_0/2 < \mathrm{Im}\{\lambda_i\} < \omega_0/2$. For the single Type I grid-following converter system with control and physical parameters specified in Table 4.2, the eigenvalues of $\mathcal{A} - \mathcal{N}$ for different truncation orders are plotted in Figure 4.8. A high truncation order of 50 is used as a benchmark, of which the eigenvalues form eight vertical lines in the complex plane. Further increasing H does not change the location of the lines. It can be observed from Figure 4.8 that

- Within the fundamental strip, more and more eigenvalues converge to the vertical lines as the truncation order increases.

- No matter how large H is, the truncation will always result in eigenvalues away from the vertical lines (see the zoomed in plot). Such eigenvalues should not be considered for the stability evaluation. With the eigenvalue sorting method those eigenvalues can only be graphically distinguished.

- On each vertical line, either one pure real-valued eigenvalue or two complex-conjugate eigenvalues within the fundamental strip should be selected as the LTP eigenvalues. The truncation order is considered to be sufficient when N LTP eigenvalues are determined. For the test case, a truncation order of 14 is needed, which results in a square matrix with the dimension of $14 \cdot (2 \cdot 14 + 1) = 406$.

Table 4.2: Parameters of the Type I Grid-Following Converter for the Study of the LTP Eigenvalue Calculation Algorithm

Symbol	Description	Value
SCR	Short-circuit ratio	3
BW	Bandwidth of the DSRF-PLL	20 Hz
τ	Time constant of the PI current controller	0.5 ms
S_r	Power reference	1.2 kW
V_p	Magnitude of the positive-sequence grid voltage	100 V
V_n	Magnitude of the negative-sequence grid voltage	50 V

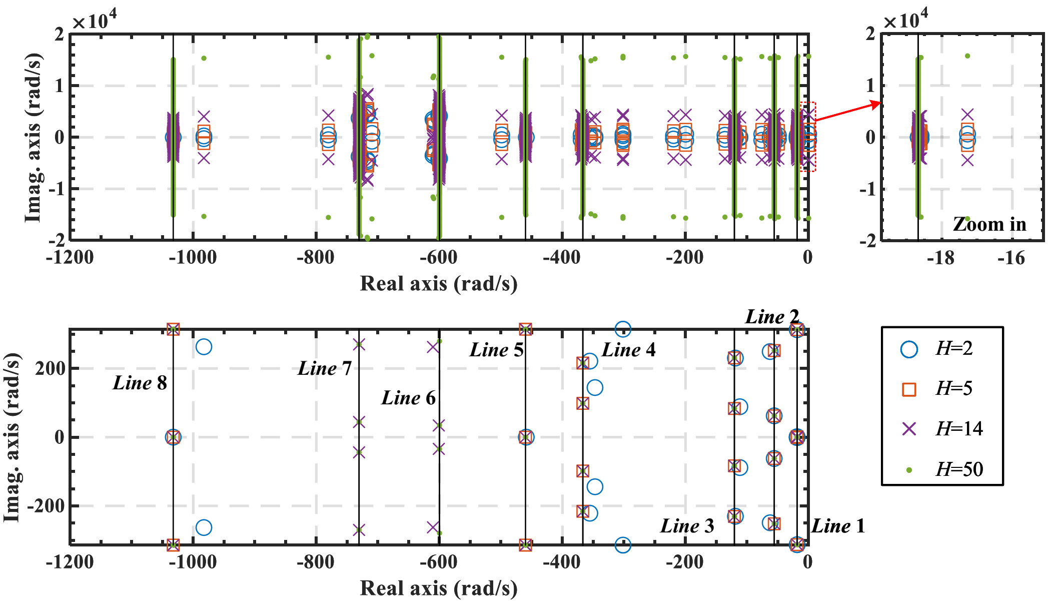

Figure 4.8: Convergence process of the eigenvalue sorting method. All eigenvalues of $\mathcal{A} - \mathcal{N}$ for different truncation orders (top). Eigenvalues located in the fundamental strip (bottom).

Eigenvector Sorting Method

The eigenvalue sorting method ignores the rate of convergence of eigenvalues and can result in unnecessarily high truncation orders. Specifically, in Figure 4.8, a high truncation order of 14 is needed to see the converged eigenvalues on Line 6 and 7 in the fundamental strip ($-\omega_0/2 < \text{Im}\{\lambda_i\} < \omega_0/2$). However, in the frequency range from 3000 to 5000 rad/s, $H = 5$ is already sufficient to determine the converged eigenvalues (see Figure 4.9). To tackle the issue of the eigenvalue sorting methods, one eigenvector sorting method is proposed in [95]. The basic idea behind is that the N eigenvectors, whose nonzero terms are symmetric about the DC component and within the truncation order, are less influenced by the truncation. Thus, the associated N eigenvalues converge faster. For a truncation order H, to select those N eigenvectors from the $N(2H+1)$ eigenvectors of the truncated matrix $\mathcal{A}-\mathcal{N}$, the $N(2H+1)$ weighted mean values

$$w_i = \frac{\sum_{h=-H}^{H} h\left|\boldsymbol{r}_i^h\right|_1}{\sum_{h=-H}^{H} \left|\boldsymbol{r}_i^h\right|_1} \tag{4.63}$$

are calculated. The weighted means of $\boldsymbol{r}_i(t)$ and $e^{jk\omega_0 t}\boldsymbol{r}_i(t)$, namely w_i and w_{i+k}, satisfy $w_{i+k} = w_i + k$. The N eigenvectors whose weighted means are closest to zero are selected. More details of the eigenvector sorting method are given in Algorithm 1.

Algorithm 1 Eigenvector Sorting Method

Initialization of the truncation order: $H_{min} = 1$
repeat
    Calculate eigenvalues and eigenvectors of truncated matrix $\boldsymbol{\mathcal{A}}-\boldsymbol{\mathcal{N}}$
    Calculate weighted means of all eigenvectors based on Eq. (4.63)
    Determine the N eigenvectors with the weighted means closest to zero, store the associated N eigenvalues
    Update the truncation order $H_{min} = H_{min} + 1$
until changes of the N eigenvalues between two iterations (l and $l+1$) satisfy

$$\frac{|\lambda_i^{l+1}-\lambda_i^l|}{|\lambda_i^{l+1}|}\cdot 100\% \le \delta,\ i\in[1,\ N]$$

Output: minimum truncation order H_{min}, converged N eigenvectors and eigenvalues

Figure 4.9 shows the convergence process of the eigenvector sorting method. The high truncation order $H = 50$ is again used as the benchmark. In each iteration step, the selected N LTP eigenvalues are marked with circles. A truncation order $H = 5$ is found to be sufficient to determine the LTP eigenvalues, considering a tolerance of $\delta = 0.01\%$. Compared with the eigenvalue sorting method, the eigenvector sorting method shows faster convergence speed.

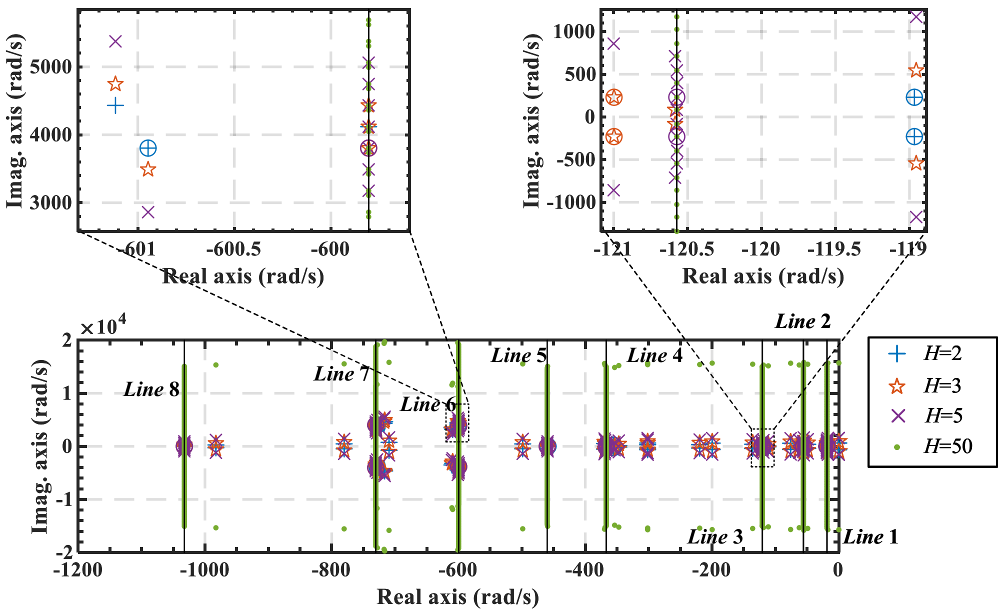

Figure 4.9: Eigenvalue map of $\mathcal{A}-\mathcal{N}$ for different truncation orders H. The selected eigenvalues in each step of the eigenvector sorting method are marked with circles.

Adaptive LTP Eigenvalue Computation Methods

Though the eigenvector sorting method exhibits better convergence performance, no rigorous mathematical proof has been achieved yet, and the impact of changing the truncation order H has not been quantitatively evaluated. To bridge the knowledge gap, two adaptive truncation order selection methods are developed to pave the way for easier application of the LTP theory.

The first method is inspired by the fact that Eq. (4.30) is difficult to solve but easy to validate. Assuming that a truncation order of H is selected, a convergence error index for the ith eigenvalue λ_i and the corresponding eigenvector

$$\mathcal{R}_i = \begin{bmatrix} \boldsymbol{r}_i^{-H} \\ \vdots \\ \boldsymbol{r}_i^{0} \\ \vdots \\ \boldsymbol{r}_i^{H} \end{bmatrix} \tag{4.64}$$

of the truncated matrix $\mathcal{A} - \mathcal{N}$ is defined as

$$\varepsilon_i = \left\| \lambda_i \boldsymbol{r}_i(t) - (\boldsymbol{A}(t)\boldsymbol{r}_i(t) - \dot{\boldsymbol{r}}_i(t)) \right\|_1 \tag{4.65}$$

where $\boldsymbol{r}_i(t)$ is an N-dimensional time-periodic vector derived from Fourier synthesis of the Fourier series coefficient vector $\mathcal{R}_i$

$$\boldsymbol{r}_i(t) = \sum\nolimits_{k=-H}^{H} \boldsymbol{r}_i^k e^{jk\omega_0 t}. \tag{4.66}$$

The operator $\|\boldsymbol{x}(t)\|_1$ gives the L_1 norm of the Fourier series coefficient vector of the time-periodic signal $\boldsymbol{x}(t)$. The index ε_i quantifies the absolute error between the actual (frequency-shifted) LTP eigenvalue/eigenvector and their approximation obtained from the truncated matrix. The eigenvalue/eigenvector whose convergence error index does not exceed a pre-defined threshold value δ is regarded as converged. It can be expected that, with the increasing of the truncation order H, more eigenvalues converge and form several vertical lines in the complex plane. The eigenvalue with the smallest convergence error in each line is selected as LTP eigenvalue, and the Fourier synthesis of the corresponding eigenvector is chosen as LTP eigenvector. For the N-dimensional matrix $\boldsymbol{A}(t)$, the truncation order H stops increasing until N LTP eigenvalues are determined.

The same setting given in Table 4.2 is used to demonstrate the convergence process of the proposed method. Figure 4.10 plots all eigenvalues of $\mathcal{A} - \mathcal{N}$ for different truncation orders. Converged eigenvalues are indicated by markers with higher visibility, and the selected LTP eigenvalues (i.e., eigenvalues with the smallest convergence error in each line) are indicated by circles. Four LTP eigenvalues (marked with red circles) have already converged for $H = 5$, while the other ten need a higher truncation order of seven. It is seen that the proposed adaptive truncation order selection method can deal with the difference between rates of convergence of LTP eigenvalues. The wrong eigenvalues caused by the truncation effect can be distinguished by using the proposed convergence error index.

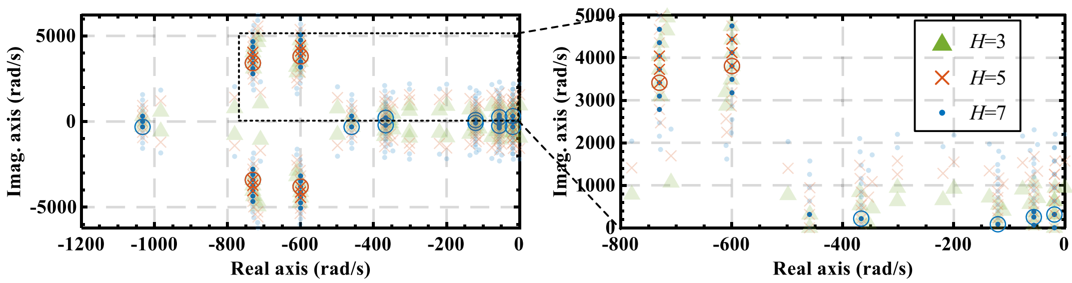

Figure 4.10: Convergence process of the truncation order selection method

To validate the accuracy of the proposed adaptive truncation order selection method, more test scenarios are generated by choosing different PLL bandwidths and current controller time constants. The balanced grid voltage is also considered for comparison. The monodromy matrix $\boldsymbol{\Phi}(T_0, 0)$ obtained by using MATLAB ode45 function with a simulation time step $MaxStep = 0.0001\,\mathrm{s}$ is used as benchmark, considering the relation between LTP eigenvalues of $\boldsymbol{A}(t)$ and eigenvalues of $\boldsymbol{\Phi}\,(T_0,\ 0)$ given by Eq. (4.61). For different combinations of PLL bandwidth BW and current controller time constant τ, the maximum percentage deviation between $e^{\boldsymbol{Q}T_0}$ and eigenvalues of $\boldsymbol{\Phi}(T_0, 0)$ is calculated

$$\max\left\{\left|\frac{e^{\lambda_i T_0} - \lambda_{\Phi,\, i}}{\lambda_{\Phi,\, i}}\right| \times 100\% \quad \middle|\ i = 1,\ \cdots,\ 14\right\}. \tag{4.67}$$

The result is plotted in Figure 4.11 for a threshold value of $\delta = 0.001$. It should be clarified that $e^{\boldsymbol{Q}T_0}$ and eigenvalues of $\boldsymbol{\Phi}(T_0, 0)$ are sorted in descending order of magnitude before the calculation of the percentage deviation.

As shown in Figure 4.11, the maximum percentage deviation is smaller than 0.03 %, which confirms the accuracy of the proposed methodology. Figure 4.12 shows maps of required truncation orders for the determination of the 14 LTP eigenvalues and eigenvectors. It is seen that $H = 2$ is sufficient for the balanced scenario, while higher truncation orders (up to seven) are needed for the unbalanced scenario, where the required truncation order is predominantly influenced by the PLL bandwidth.

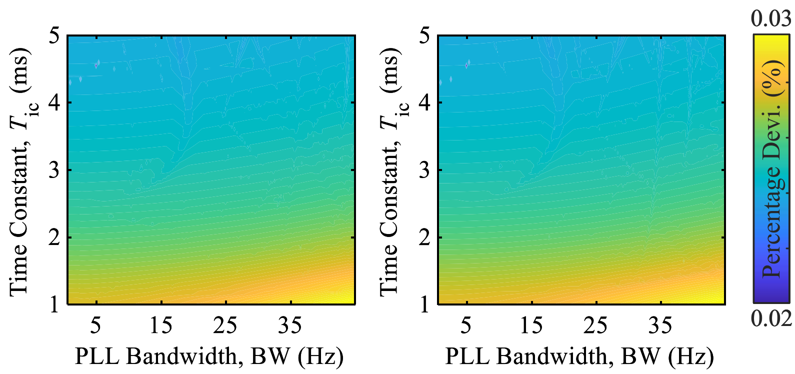

Figure 4.11: Maximum percentage deviation between $e^{\boldsymbol{Q}T_0}$ and eigenvalues of $\boldsymbol{\Phi}(T_0, 0)$. Left: Balanced scenario. Right: Unbalanced scenario.

To test the scalability of the proposed method, a second case study is carried out on the modified IEEE 13-bus system with four Type I grid-following converters shown in Figure 3.30.

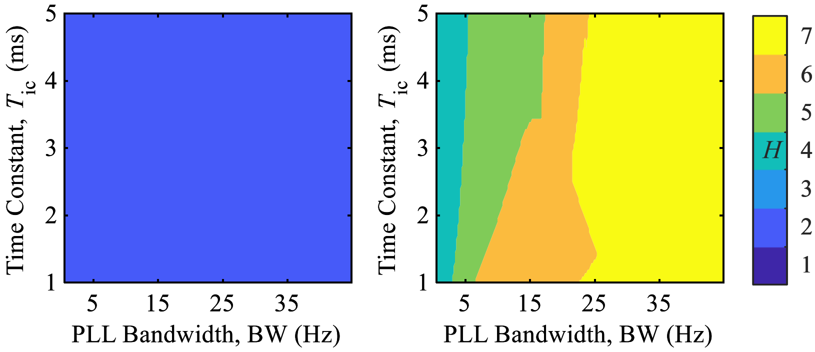

Figure 4.12: Maps of required truncation order for different parameter combinations. Left: Balanced scenario. Right: Unbalanced scenario.

The LTP small-signal model with 94 states is obtained by using the modeling framework presented in Chapter 3. Four cases listed in Table 4.3 are considered, and the required truncation order is determined using the proposed method.

Table 4.3: Parameters of Different Test Cases of the IEEE 13-bus System

Index	Grid Voltage	BW (Hz)	τ (ms)	Truncation Order
Case 1	balanced	20	1	3
Case 2	unbalanced with 0.5 pu negative-sequence component	30	1	3
Case 3	balanced	30	1	7
Case 4	unbalanced with 0.5 pu negative-sequence component	40	1	8

The agreement between diagonal elements of $e^{\boldsymbol{Q}T_0}$ and eigenvalues of the monodromy matrix $\boldsymbol{\Phi}(T_0, 0)$ can be observed in Figure 4.13. For all cases, the maximum percentage deviation is smaller than 0.03%, which validates the correctness of the proposed method. It is noted that four eigenvalues of $\boldsymbol{\Phi}(T_0, 0)$ of Case 4 locate outside the unit circle, which indicates that the system is unstable. It is consistent with the time-domain simulation results shown in Figure 3.34 and Figure 3.35.

The second adaptive LTP eigenvalue calculation method is inspired by the proposed time-domain physical interpretation in Section 4.2. According to the classical LTI theory, oscillation modes commonly exhibit different degrees of controllability and observability in state variables of the LTI system. As for the equivalent representation of the LTP system given by Eq. (4.23), if λ_i can only be excited and examined in $\Delta\boldsymbol{x}$, it will be one of the eigenvalues of $\boldsymbol{A}_0$, namely λ_i is immune to the frequency coupling effect. When the impact of the frequency coupling becomes not negligible, λ_i can be obtained from the modified selective modal analysis given in Algorithm 2.

At the core of Algorithm 2 are an iteration aimed at computing the eigenvalue λ_i and an adaptive truncation order selection method. First, grouping state observations in Eq. (4.23) into two categories

$$\Delta\boldsymbol{x}_r = [\Delta\boldsymbol{x}]$$

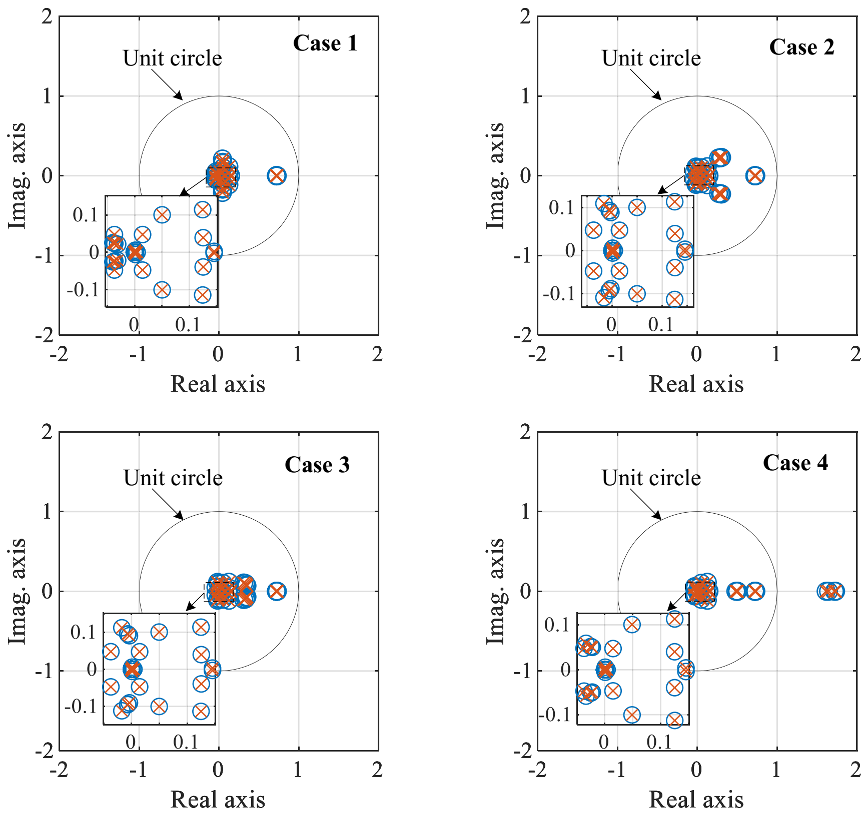

Figure 4.13: Distribution of diagonal elements of $e^{\boldsymbol{Q}T_0}$ (blue circles) and eigenvalues of $\boldsymbol{\Phi}(T_0, 0)$ (orange crosses).

and

$$\Delta \boldsymbol{x}_z = [\Delta \boldsymbol{x}_{-H};\ \ldots\ ;\ \Delta \boldsymbol{x}_{-2};\ \Delta \boldsymbol{x}_{-1};\ \Delta \boldsymbol{x}_1;\ \Delta \boldsymbol{x}_2;\ \ldots\ ;\ \Delta \boldsymbol{x}_H]$$

Correspondingly, Eq. (4.23) can be reformulated as

$$\begin{bmatrix} \Delta \dot{\boldsymbol{x}}_r \\ \Delta \dot{\boldsymbol{x}}_z \end{bmatrix} = \begin{bmatrix} \boldsymbol{A}_0 & \boldsymbol{\mathcal{A}}_{12} \\ \boldsymbol{\mathcal{A}}_{21} & \boldsymbol{\mathcal{A}}_{22} \end{bmatrix} \begin{bmatrix} \Delta \boldsymbol{x}_r \\ \Delta \boldsymbol{x}_z \end{bmatrix} \tag{4.68}$$

The color of the partitioned matrices is consistent with that in Eq. (4.23). At the kth iteration, $\Delta \dot{\boldsymbol{x}}_z$ is approximated by $\lambda_i^k \Delta \boldsymbol{x}_z$, where λ_i^k is the estimation of λ_i at the kth iteration step. This makes the second row of Eq. (4.68) algebraic, yielding an N-dimensional reduced-order system

$$\begin{gathered} \begin{bmatrix} \Delta \dot{\boldsymbol{x}}_r \\ \lambda_i^k \Delta \boldsymbol{x}_z \end{bmatrix} = \begin{bmatrix} \boldsymbol{A}_0 & \boldsymbol{\mathcal{A}}_{12} \\ \boldsymbol{\mathcal{A}}_{21} & \boldsymbol{\mathcal{A}}_{22} \end{bmatrix} \begin{bmatrix} \Delta \boldsymbol{x}_r \\ \Delta \boldsymbol{x}_z \end{bmatrix} \\ \Downarrow \\ \Delta \dot{\boldsymbol{x}}_r = \left(\boldsymbol{A}_0 + \underbrace{\boldsymbol{\mathcal{A}}_{12} \left(\lambda_i^k \boldsymbol{I} - \boldsymbol{\mathcal{A}}_{22} \right)^{-1} \boldsymbol{\mathcal{A}}_{21}}_{\boldsymbol{G}} \right) \Delta \boldsymbol{x}_r \end{gathered} \tag{4.69}$$

The truncation order H, i.e., the number of rotated coordinate frames in $\Delta \boldsymbol{x}_z$ providing redundant observations of the physical LTP system, is adaptively increased until $\boldsymbol{G}$ converges. Then, the next estimation λ_i^{k+1} of λ_i is determined from the eigenvalue analysis of Eq. (4.69).

Algorithm 2

Group observations in different coordinate frames:
  e.g., $\Delta\boldsymbol{x}_r = [\Delta\boldsymbol{x}]$ and $\Delta\boldsymbol{x}_z = [\Delta\boldsymbol{x}_{-H};\ \dots\ ;\ \Delta\boldsymbol{x}_{-1};\ \Delta\boldsymbol{x}_1;\ \dots\ ;\ \Delta\boldsymbol{x}_H]$
Determine initial guess of LTP eigenvalues:
  Eigenvalue calculation of A_0, $\{\lambda_i^0, i \in [1,\ N]\}$
for $i \leftarrow 1 : N$ **do**
  Initialize the iteration index $k = 0$
  repeat
    Increase the truncation order H until $\boldsymbol{G}$ in Eq. (4.69) does not change
    Compute eigenvalues of $\boldsymbol{A}_0 + \boldsymbol{G}$, set λ_i^{k+1} as the one closest to λ_i^k
    Update the iteration index $k = k + 1$
  until the value of λ_i^k converges
end for
Output: converged N eigenvalues and eigenvectors

The local convergence of Algorithm 2 for λ_i is guaranteed when the magnitude of the coefficient ρ_i defined as

$$\rho_i = \frac{\boldsymbol{l}_i \boldsymbol{r}_i}{\boldsymbol{l}_i \frac{\partial \boldsymbol{G}}{\partial \lambda_i} \boldsymbol{r}_i} = \frac{\boldsymbol{l}_i \boldsymbol{r}_i}{-\boldsymbol{l}_i \boldsymbol{\mathcal{A}}_{12} (\lambda_i \boldsymbol{I} - \boldsymbol{\mathcal{A}}_{22})^{-2} \boldsymbol{\mathcal{A}}_{21} \boldsymbol{r}_i} \tag{4.70}$$

is larger than unity. ρ_i is the ratio between participation factors of λ_i in $\Delta\boldsymbol{x}_r$ and $\Delta\boldsymbol{x}_z$. Considering symmetry, it is also the ratio of participation factors of λ_i and $\{\lambda_i - jh\omega_0\}$ in $\Delta\boldsymbol{x}_r$. $\boldsymbol{l}_i$ and $\boldsymbol{r}_i$ are the N-dimensional left and right eigenvectors of Eq. (4.69), associated with λ_i. Actually, the magnitude of ρ_i quantifies the strength of the frequency coupling effect. Smaller $|\rho_i|$ indicates comparable contribution of λ_i and $\{\lambda_i - jh\omega_0\}$ in $\Delta\boldsymbol{x}_r(t)$, namely stronger frequency coupling effect. When $|\rho_i|$ approaches unity, observations in rotated coordinate frames should be incrementally moved from $\Delta\boldsymbol{x}_z$ to $\Delta\boldsymbol{x}_r$ to make the algorithm converge.

Again the Type I grid-following converter with the parameters listed in Table 4.2 is used to test Algorithm 2. The result is demonstrated in Figure 4.14. Blue crosses indicate the LTP eigenvalues obtained by using the first adaptive method. Orange dots are the initial guess of the LTP eigenvalues. Red circles are the converged LTP eigenvalues determined by using Algorithm 2.

To quantify the impact of the frequency coupling effect on the relevant LTP eigenvalues, the participation ratio given by Eq. (4.70) and the percentage deviation between the initial guess and the true LTP eigenvalue are calculated. It is observed from Table 4.4 that comparably accurate prediction of λ_{1-4} and λ_{10-14} can be obtained from eigenvalue calculation of $\boldsymbol{A}_0$, while $\lambda_{5,6}$, $\lambda_{7,8}$ and λ_9 are highly influenced by the frequency coupling effect. Observations in rotated coordinates, $\Delta\boldsymbol{x}_{-2}$ and $\Delta\boldsymbol{x}_2$, need to be added into $\Delta\boldsymbol{x}_r$ of Algorithm 2 for the computation of λ_{5-9}. In other words, the contribution of $\lambda_{5-9} \pm 2j\omega_0$ in the dynamics of $\Delta\boldsymbol{x}$ is not negligible.

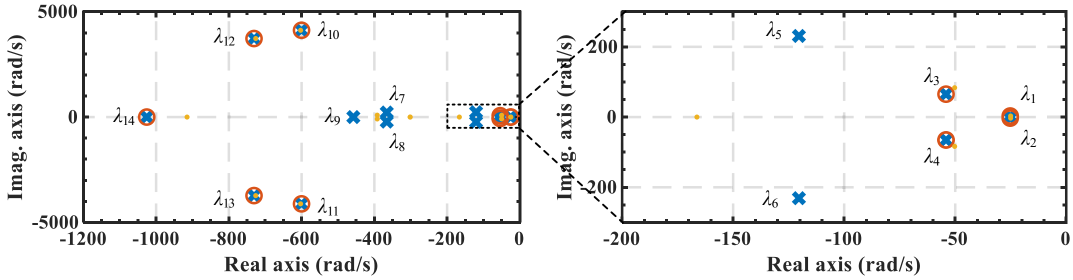

(a) $\Delta \boldsymbol{x}_r = [\Delta \boldsymbol{x}]$, $\lambda_{5,6}$, $\lambda_{7,8}$ and λ_9 cannot be obtained

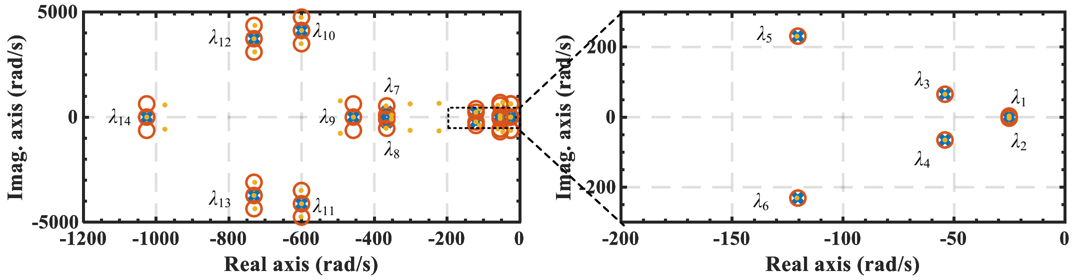

(b) $\Delta \boldsymbol{x}_r = [\Delta \boldsymbol{x}_{-2};\ \Delta \boldsymbol{x};\ \Delta \boldsymbol{x}_2]$, all LTP eigenvalues can be determined

Figure 4.14: LTP eigenvalue map of the Type I grid-following converter obtained by using Algorithm 2 with different groupings of the state observation

Table 4.4: Coupling Effect Quantification of LTP Eigenvalue

Eigenvalue	Value	Participation Factor Ratio	Percentage Deviation (%)
$\lambda_{1,2}$	$-25.23 \pm j3.031$	6851	0.74
$\lambda_{3,4}$	$-54.14 \pm j65.23$	48.61	22.1
$\lambda_{5,6}$	$-120.4 \pm j231.0$	2.384	N/A
$\lambda_{7,8}$	$-365.9 \pm j216.8$	2.313	N/A
λ_9	-457.8	2.389	N/A
$\lambda_{10,11}$	$-600.2 \pm j4120$	1387	0.07
$\lambda_{12,13}$	$-730.8 \pm j3727$	734.0	0.13
λ_{14}	-1026	42.15	10.8

4.5 Case Study

4.5.1 Grid-Following Converter

Based on the generalized modal analysis method, the dynamic characteristics of the two types of grid-following converters are investigated and compared in this subsection. As a base case, the time constant of the current controller is chosen to be $\tau = 0.5\,\text{ms}$. A bandwidth of $\text{BW} = 20\,\text{Hz}$ is designed for the DSRF-PLL and DSOGI-PLL. The grid strength quantified by the short-circuit ratio is initially set to be $\text{SCR} = 3.6$. These three variables build the parameter space for the stability investigation.

LTP Eigenvalue-Based Stability Analysis

Figure 4.15 shows the eigenvalue map of the two different grid-following converter systems operated under balanced conditions. Considering that oscillations related to left half-plane eigenvalues far away from the imaginary axis decay rapidly and do not threaten the system stability, only the three pairs of complex conjugate LTP eigenvalues with real parts larger than $-200\,\mathrm{rad/s}$ are considered. Participation factors of those six eigenvalues are shown in Figure 4.16. Participation factors of state variables belonging to the same control or physical unit (PLL, current controller as well as filter and grid) are summarized.

The participation factor analysis reveals that, under weak grid conditions, the system stability is influenced by the strong interaction between dynamics of the PLL, current control and power networks, instead of being dominated by one single unit. This highlights the necessity of full-order-model-based analysis. Moreover, the Type II grid-following converter is immune to the frequency coupling effect. In other words, there exists a rotational transformation with fixed frequency which can transform the LTP small-signal model of the Type II grid-following converter to an LTI one. In contrast, the small-signal model of the Type I grid-following converter is time periodic, this is an intrinsic difference between them.

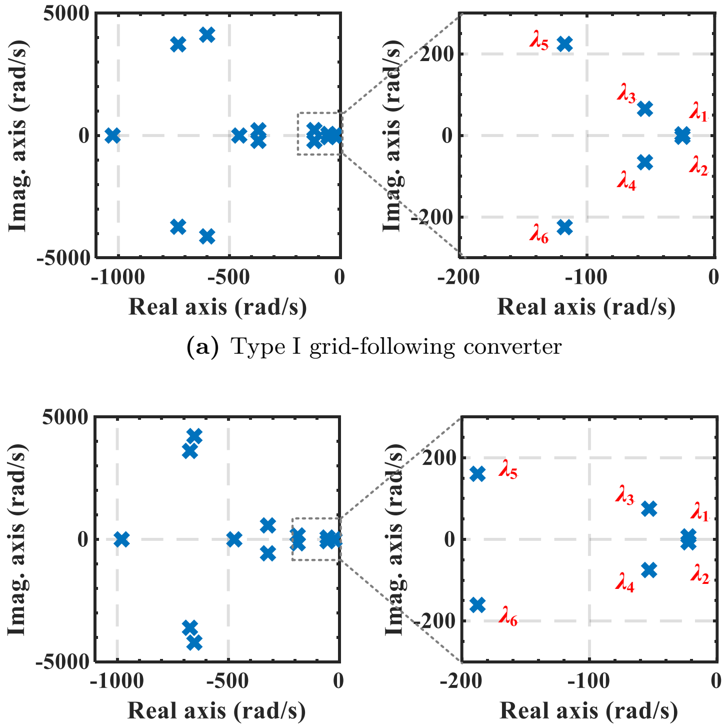

(a) Type I grid-following converter

(b) Type II grid-following converter

Figure 4.15: LTP eigenvalue map of the grid-following converter

The small-signal analysis results given by Figure 4.15 and Figure 4.16 are only valid in the vicinity of the steady-state operation trajectory determined by the initial parameters. To gain a global overview of the impact of the interaction between the PLL, the current control and the network on the system stability, the PLL bandwidth BW is swept from 20 Hz to 50 Hz, the current control time constant τ from 0.5 ms to 3.5 ms, and SCR from 3 to 2. As summarized in Table 4.5, following conclusions can be drawn from the movement of eigenvalues shown in Figure 4.17 and Figure 4.18:

1. As the SCR decreases from 3 to 2, $\lambda_{3,\,4}$ of both types of converters approximate the imaginary axis from the left side (see Zoom 2 in Figure 4.17(a) and Figure 4.17(b)), i.e., the system stability margin becomes smaller, while $\lambda_{1,\,2}$ and $\lambda_{5,\,6}$ are comparably less influenced.

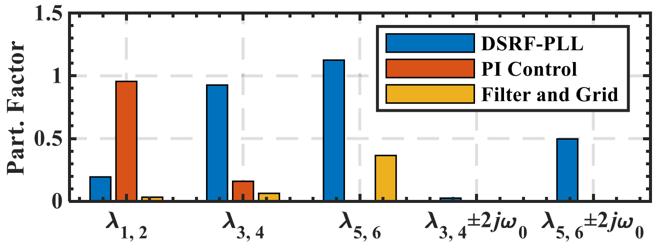

(a) Type I grid-following converter

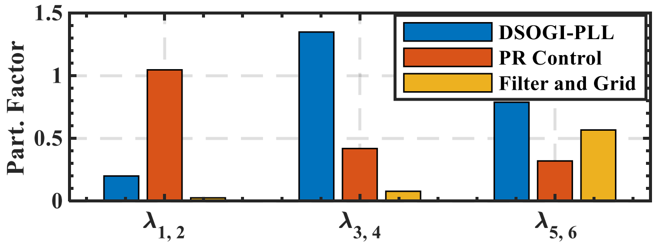

(b) Type II grid-following converter

Figure 4.16: Magnitude of participation factors of the grid-following converter

2. Slower current controllers make $\lambda_{3,\,4}$ of both types of converters migrate towards the right-half plane (see Figure 4.18), and even makes the Type I grid-following converter unstable (see Zoom 2 in Figure 4.18(a)). Additionally, larger τ can result in poorly damped low-frequency (1-2 Hz) oscillations of Type II converter, indicated by the movement of $\lambda_{1,\,2}$ shown in Zoom 1 in Figure 4.18(b).

3. The PLL bandwidth BW has large impact on $\lambda_{3,\,4}$ and $\lambda_{5,\,6}$. Specifically, a higher BW can help to counteract the impact of weaker grids and slower current controls on $\lambda_{3,\,4}$ (see Zoom 2 in Figure 4.17 and Figure 4.18). However, increasing BW moves $\lambda_{5,\,6}$ towards the right-half plane (see Zoom 3 in Figure 4.17 and Figure 4.18), and can even lead to the instability of the Type I grid-following converter.

Table 4.5: Impact of Parameter Changes on the System Stability

Eigenvalue	Oscillation Frequency	Type I Grid-Following Converter	Type II Grid-Following Converter
$\lambda_{1,\,2}$	$<$ 4 Hz	-	τ ($\rightarrow$)
$\lambda_{3,\,4}$	6 $\sim$ 20 Hz	SCR ($\leftarrow$) τ ($\rightarrow$, instability) BW ($\leftarrow$)	SCR ($\leftarrow$) τ ($\rightarrow$) BW ($\leftarrow$)
$\lambda_{5,\,6}$	about 50 Hz	BW ($\rightarrow$, instability)	BW($\rightarrow$)

Arrows in Table 4.5 indicate the direction of movement of eigenvalues, as corresponding parameters increase.

Influence of the Unbalanced Operation

The influence of the grid imbalance is investigated by considering following two scenarios:

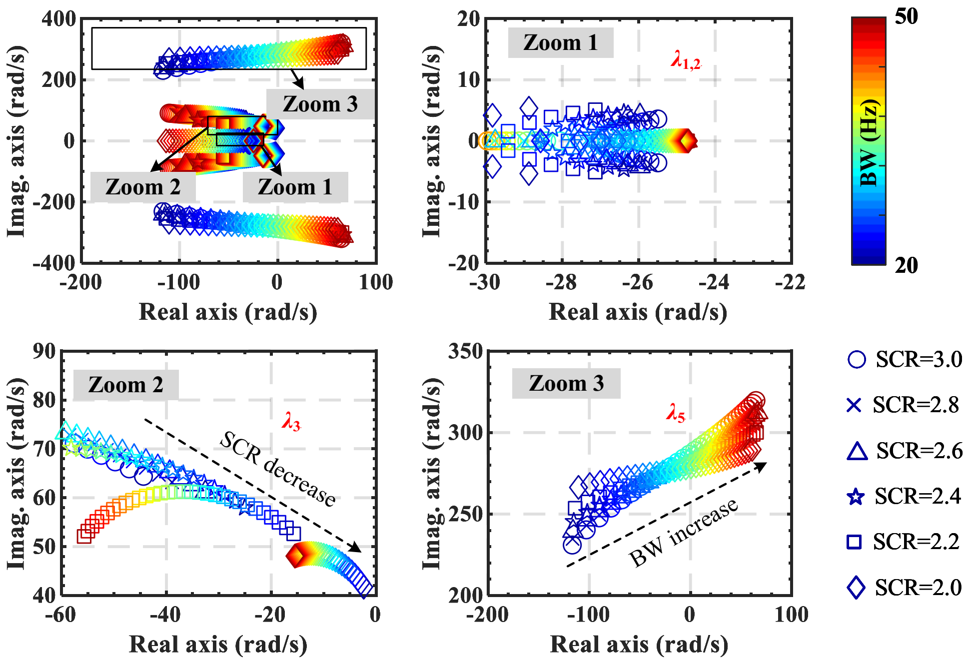

(a) Type I grid-following converter

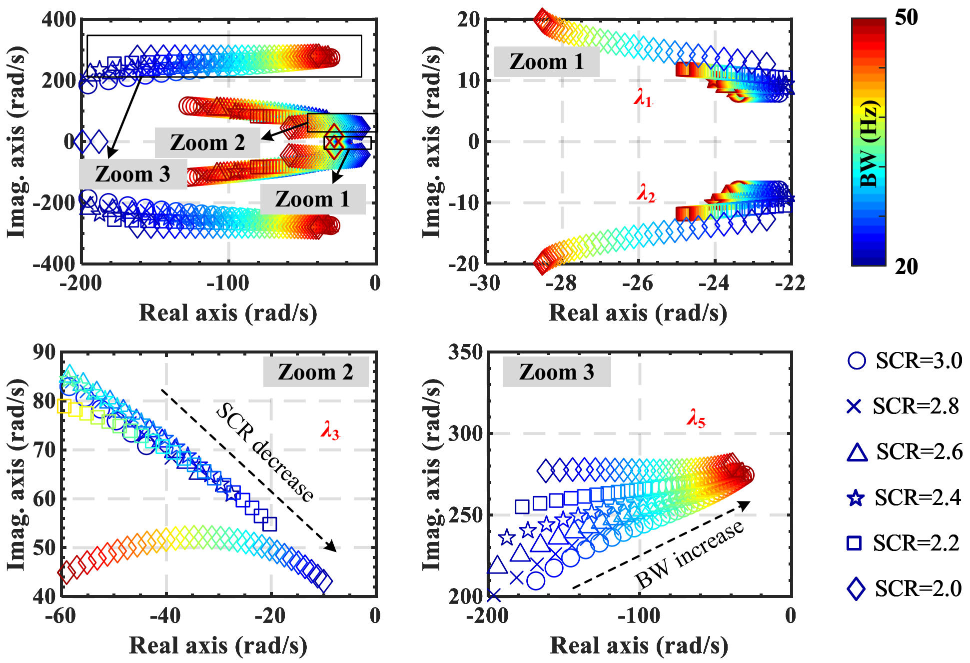

(b) Type II grid-following converter

Figure 4.17: Eigenvalue locus of the grid-following converter for different combinations of SCR and BW

1. Unbalanced stiff grid voltage: A negative-sequence voltage is assumed to exist in the grid, and the ratio $k_V = V_{g-}/V_{g+}$ is swept in the range of 0 to 1, where V_{g+} and V_{g-} refer to magnitudes of the positive and negative sequence grid voltages.

2. Unbalanced grid impedance: The inductance of phase a of the grid line impedance is increased by a multiple k_Z varying from 1 to 3.

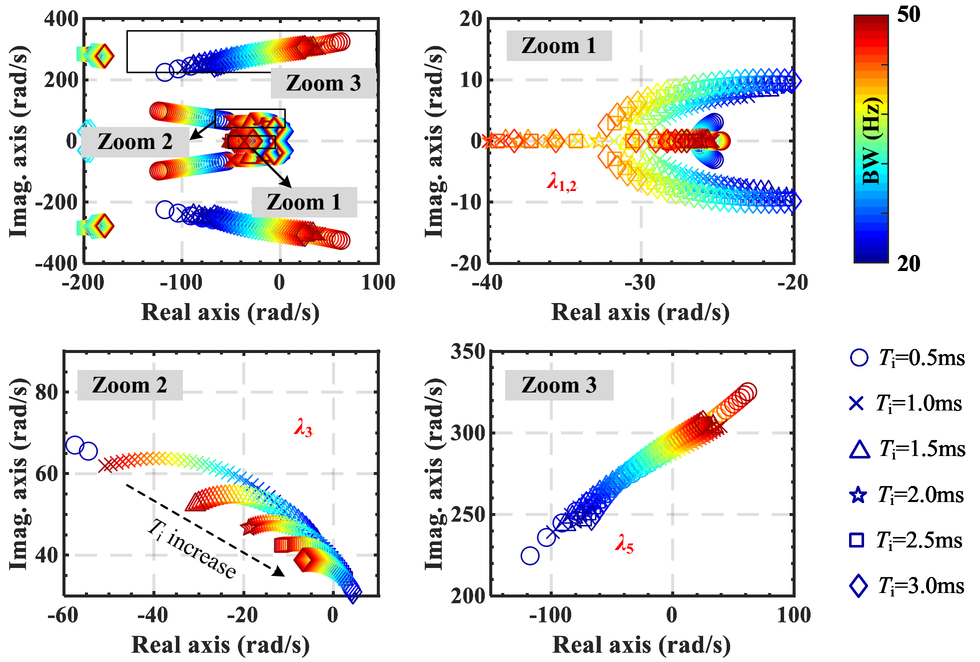

(a) Type I grid-following converter

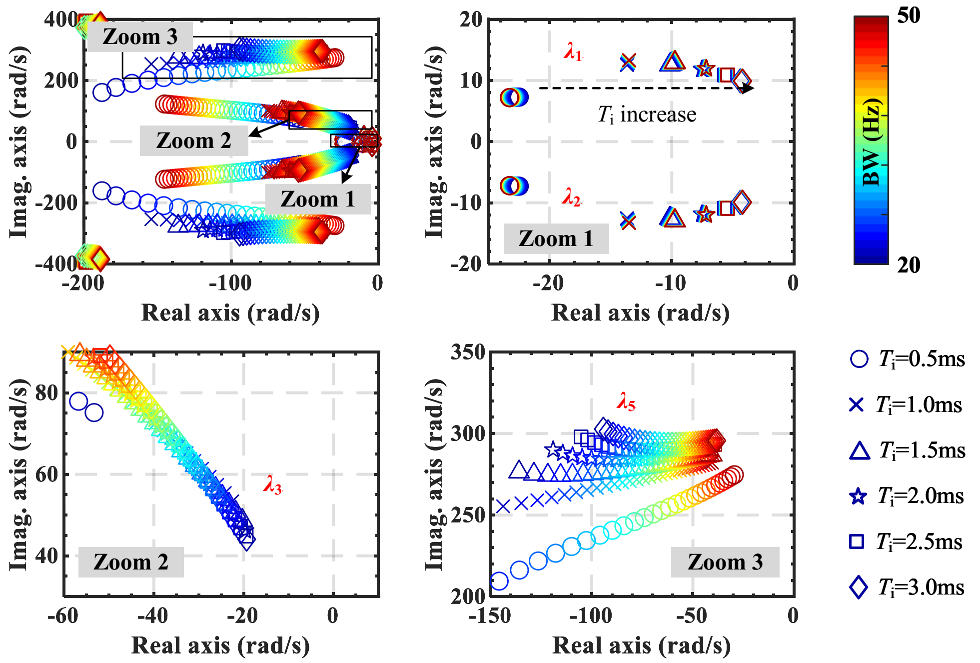

(b) Type II grid-following converter

Figure 4.18: Eigenvalue locus of the grid-following converter for different combinations of τ and BW

In the presence of the grid imbalance, small-signal models of both types of converters become LTP. Figure 4.19 presents the eigenvalue locus with the varying parameter k_V. It is observed that the increasing of k_V causes the bifurcation of $\lambda_{5,\,6}$, which threatens the stability of the Type I grid-following converter with higher PLL bandwidth. $\lambda_{1,\,2}$ and $\lambda_{3,\,4}$ are immune to the presence of negative sequence grid voltage. The parameter sweep result of k_Z is demonstrated in Figure 4.20. $\lambda_{1,\,2}$ and $\lambda_{5,\,6}$ remain almost unchanged, while $\lambda_{3,\,4}$

travel towards the right-half plane as k_Z increases, which is similar to the eigenvalue movement pattern of reducing the SCR shown in Figure 4.17.

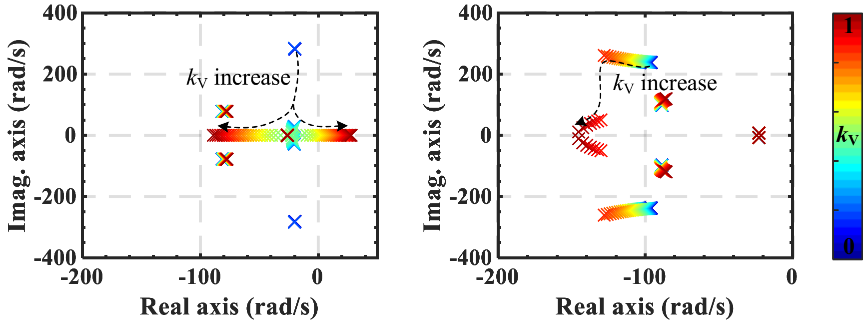

Figure 4.19: Eigenvalue locus for BW = 30 Hz and different k_V. Left: Type I grid-following converter. Right: Type II grid-following converter

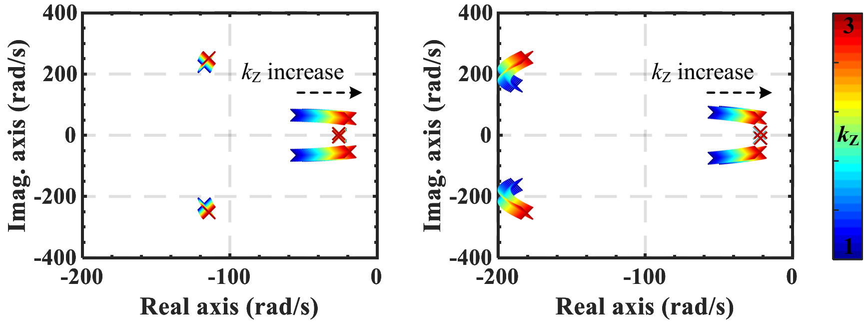

Figure 4.20: Eigenvalue locus for different k_Z. Left: Type I grid-following converter. Right: Type II grid-following converter

The real-life grid imbalance caused by faults or asymmetric loads can be treated as the combination of voltage and impedance imbalance. Systematic investigations on the practical imbalanced scenarios considering also the dual-sequence current control [116] deserve further investigation, but are out of the scope of this thesis.

Comparison between LTI and LTP Stability Analysis Results

To further confirm the necessity of the application of the LTP theory, the LTI models developed in [29, 31, 32] which neglect the angle and frequency feedback dynamics of the DSRF-PLL and DSOGI-PLL are used for comparison in a stability analysis.

For two different grid strengths, SCR = 3 and SCR = 5, eigenvalues of both types of grid-following converters are calculated for various combinations of PLL bandwidth BW and current control time constant τ. Real parts of the right-most eigenvalues are plotted in Figure 4.21 and Figure 4.22. It can be observed that neglecting the phase angle feedback of the DSRF-PLL can result in wrong stability assessment results, neglecting the frequency feedback of the DSOGI-PLL gives overoptimistic stability assessment results. Additionally, only the LTP models can be used for the stability analysis under unbalanced conditions.

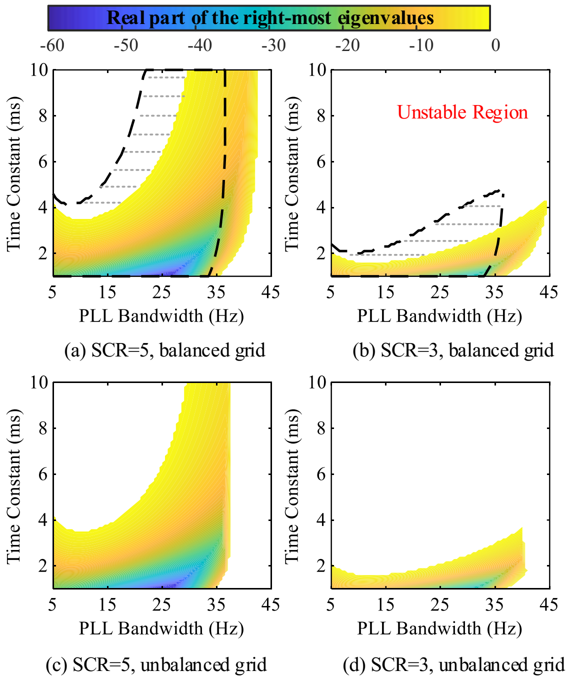

(a) SCR=5, balanced grid (b) SCR=3, balanced grid (c) SCR=5, unbalanced grid (d) SCR=3, unbalanced grid

Figure 4.21: Real part of the right-most eigenvalues of the Type I grid-following converter for different parameter combinations. White areas are the unstable region. Dashed black lines indicate stability boundaries determined based on conventional LTI models.

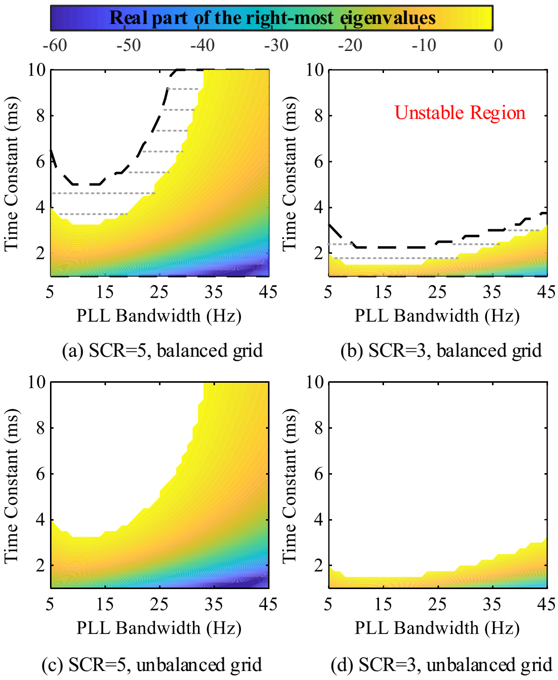

(a) SCR=5, balanced grid (b) SCR=3, balanced grid (c) SCR=5, unbalanced grid (d) SCR=3, unbalanced grid

Figure 4.22: Real part of the right-most eigenvalues of the Type II grid-following converter for different parameter combinations. White areas are the unstable region. Dashed black lines indicate stability boundaries determined based on conventional LTI models.

Time-Domain Validation

To validate the eigenvalue-based stability analysis results, time-domain dynamic responses obtained from the analytical small-signal model, the numerical nonlinear average model and experimental measurements are compared. After the system reaches steady state, a power reference step of $-200\,\mathrm{W}$ is given to the converter. Forced responses of $\Delta\eta$, real parts of the grid-side current and the capacitor voltage for different control parameter combinations are shown in Figure 4.23 to Figure 4.25. The consistency between dynamic responses obtained from the nonlinear average MATLAB/Simulink model, the analytical small-signal model and experimental measurements confirms the accuracy of the linear small-signal model. For the base case ($\tau = 0.5\,\mathrm{ms}$ and $\mathrm{BW} = 20\,\mathrm{Hz}$), the two types of converters demonstrate similar dynamic characteristics, as shown in Figure 4.23 and Figure 4.25. As τ increases to $3\,\mathrm{ms}$, the Type I GFL converter becomes unstable (see Figure 4.26). In contrast, the Type II grid-following converter remains stable, and the low-frequency oscillation corresponding to $\lambda_{1,\,2}$ can be observed in Figure 4.24.

To verify the instability caused by a higher DSRF-PLL bandwidth, the bandwidth BW of the Type I grid-following converter is increased from 20 Hz to 35 Hz at $t = 1.0\,\mathrm{s}$, the exponentially amplified evolution of and the real part of the grid-side current can be observed in Figure 4.27.

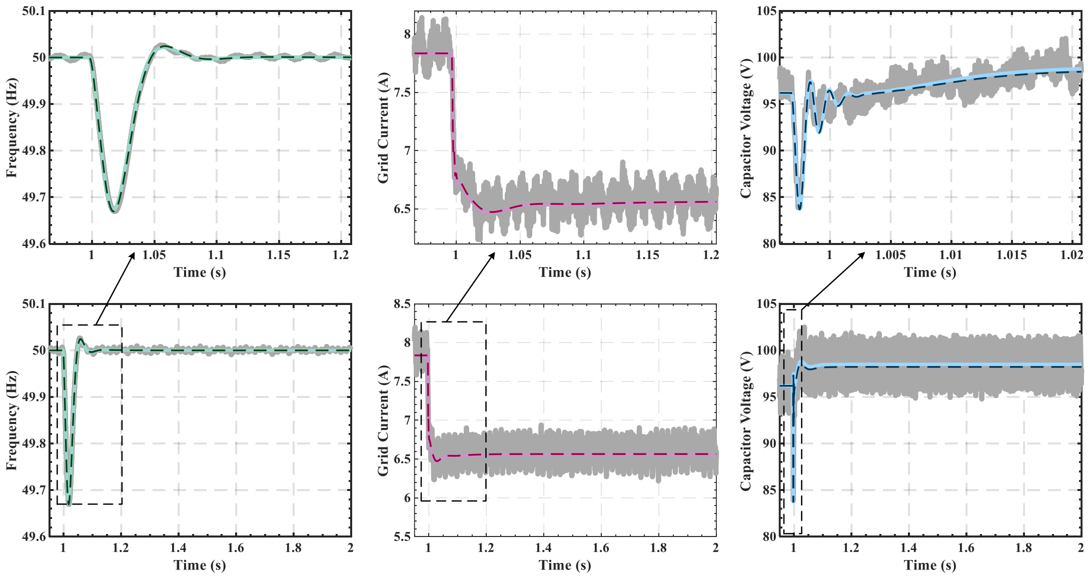

Figure 4.23: Forced responses of the Type II GFL converter to a $-200\,\mathrm{W}$ power reference step at $t = 1.0\,\mathrm{s}$ for BW $= 20\,\mathrm{Hz}$ and $\tau = 0.5\,\mathrm{ms}$. Grey lines: measurements. Solid lines:nonlinear average model. Dashed lines:small-signal model

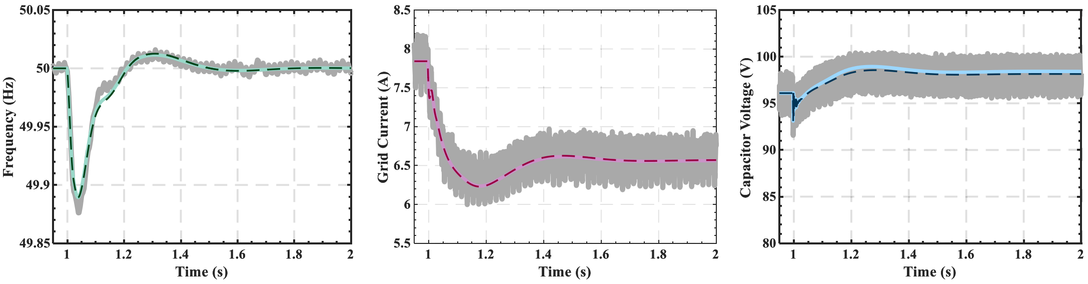

Figure 4.24: Forced responses of the Type II GFL converter to a $-200\,\mathrm{W}$ power reference step at $t = 1.0\,\mathrm{s}$ for BW $= 20\,\mathrm{Hz}$ and $\tau = 3\,\mathrm{ms}$. Grey lines: measurements. Solid lines:nonlinear average model. Dashed lines:small-signal model

4.5.2 Grid-Forming Converter

In this subsection, the eigenvalue-based stability analysis is carried out for the single grid-forming converter system shown in Figure 3.11. The control and physical parameters of the base case are given in Table 4.6. The 16 eigenvalues shown in Figure 4.28 can be generally divided into four groups according to their locations in the complex plane. Participation factors of the twelve oscillation modes are given in Figure 4.29. The other four over damped modes do not threaten the system stability.

It can be observed from Figure 4.29 that the high-frequency eigenvalues in Group IV are related to the LCL resonance. Three pairs of oscillations modes exist in Group I. $\lambda_{1,\,2}$ is merely related to the outer power loop. $\lambda_{3,\,4}$ and $\lambda_{5,\,6}$ mainly contribute to the dynamics of the cascaded voltage-current loop. Moreover, $\lambda_{7,\,8}$ in Group II is influenced by the interaction between the inner control loop and the LCL passive components.

To study the impact of parameter changes on the system stability, the inertia constant J, droop coefficients k_P and k_Q, the virtual impedance $Z_v = R_v + j\omega_0 L_v$, the current controller

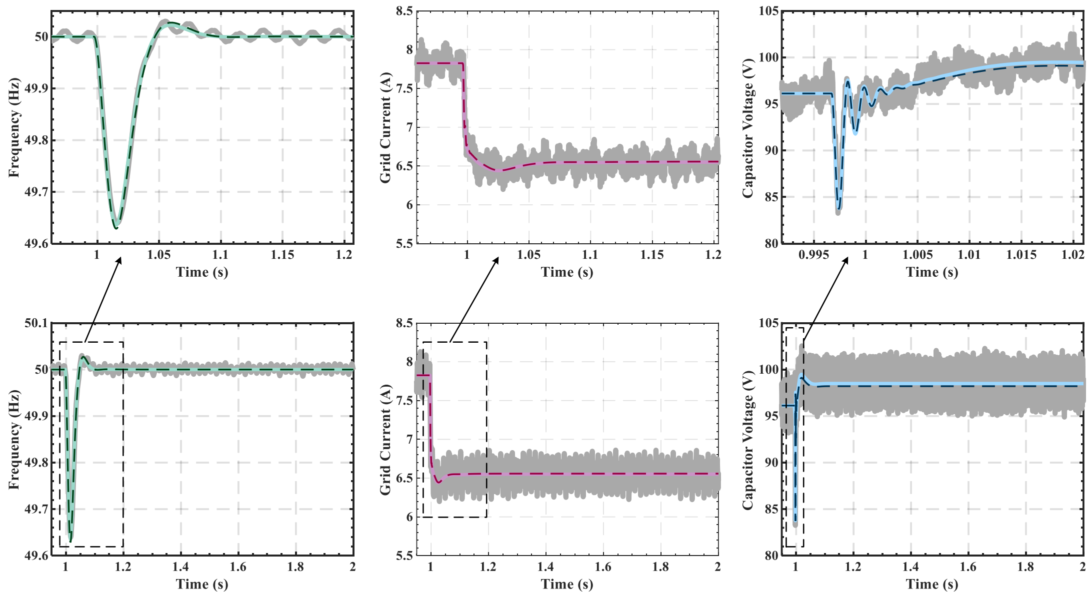

Figure 4.25: Forced responses of the Type I GFL converter to a −200 W power reference step at $t = 1.0\,\mathrm{s}$ for BW = 20 Hz and $\tau = 0.5\,\mathrm{ms}$. Grey lines: measurements. Solid lines:nonlinear average model. Dashed lines:small-signal model

Table 4.6: Base Case Parameters of the GFM Converter

Symbol	Description	Value
SCR	Short-circuit ratio	5
S_r	Power reference	1 kW
k_P	Active power droop coefficient	320 W · s/rad
k_Q	Reactive power droop coefficient	207 Var/V
J	Inertia constant	0.132 kg · m^2
τ	Current control time constant	0.5 ms
PM	Desired phase margin of the voltage control	45°
Z_v	Virtual impedance	5.6 mH + 0.1 Ω

time constant τ and the desired voltage control phase margin PM are changed in the following ranges:

- J is swept from 0.08 kg · m^2 to 0.41 kg · m^2, corresponding to the inertia time constant H changes from 2 s to 9.5 s.
- k_P is swept from 127 W · s/rad to 637 W · s/rad, which means that 100% active power change corresponds to the change from 5% to 1% of the nominal frequency.
- k_Q is swept from 200 Var/V to 2000 Var/V, which means that 100% reactive power change corresponds to the change from 10% to 1% of the nominal voltage.
- SCR is swept from 2 to 17.
- Z_v is swept from 20% to 100% of the converter-side filter inductance.
- τ is swept from 0.5 ms to 3 ms.
- PM is swept from 30° to 60°.

Figure 4.30 and Figure 4.31 show the eigenvalue loci for different combinations of the inertia constant J and the droop coefficients k_P and k_Q. It can be observed that $\lambda_{1,\,2}$ migrate towards the right half plane with decreasing oscillation frequency and damping ratio as the

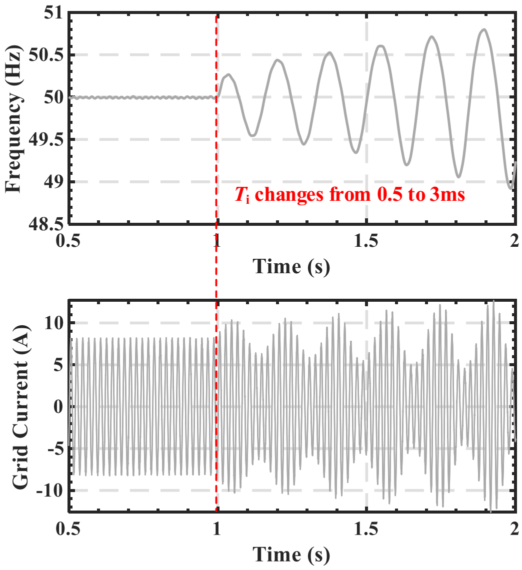

Figure 4.26: Measurements of the Type I grid-following converter for the increase of τ

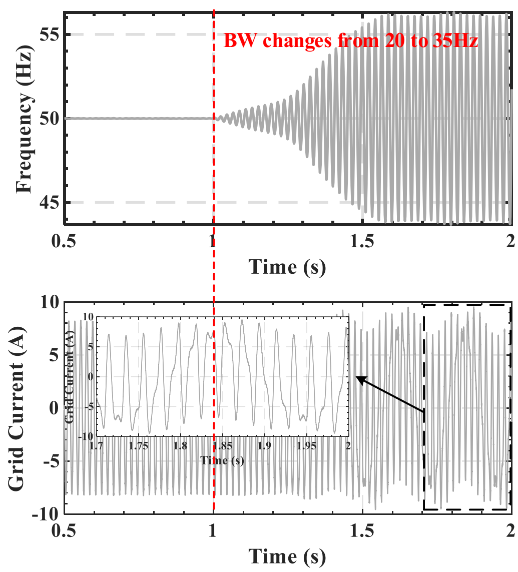

Figure 4.27: Measurements of the Type I grid-following converter for the increase of BW

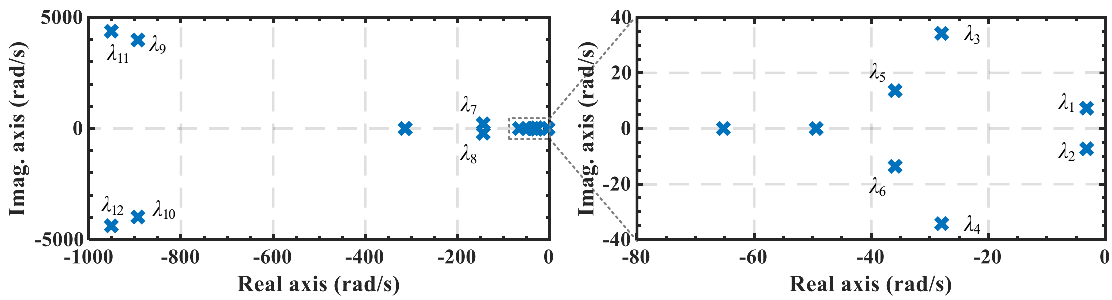

Figure 4.28: LTP eigenvalue map of the grid-forming converter

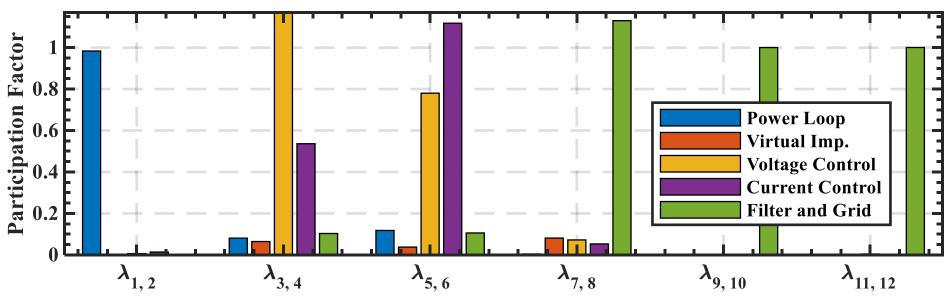

Figure 4.29: Magnitude of participation factors of the grid-forming converter

inertia constant J increases. Large active power droop coefficient k_P can improve the damping performance of those modes. The impact of k_Q on $\lambda_{1,\,2}$ is negligible.

Figure 4.32 shows the eigenvalue loci for different combinations of SCR and virtual impedance Z_v. As SCR increases (the grid becomes stronger), $\lambda_{1,\,2}$ migrate towards the right half plane with increasing oscillation frequency and decreasing damping ratio. To ensure the system stability, large virtual impedances should be selected. Moreover, the increasing of the SCR also makes $\lambda_{3,\,4}$ approach the imaginary axis from the left side, which degrades the damping performance of the system.

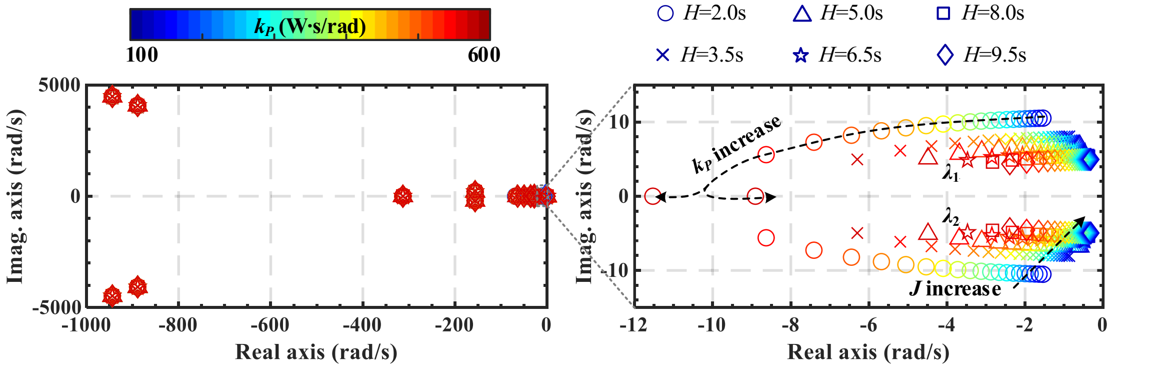

Figure 4.30: Eigenvalue locus of the GFM converter for different combinations of k_P and J

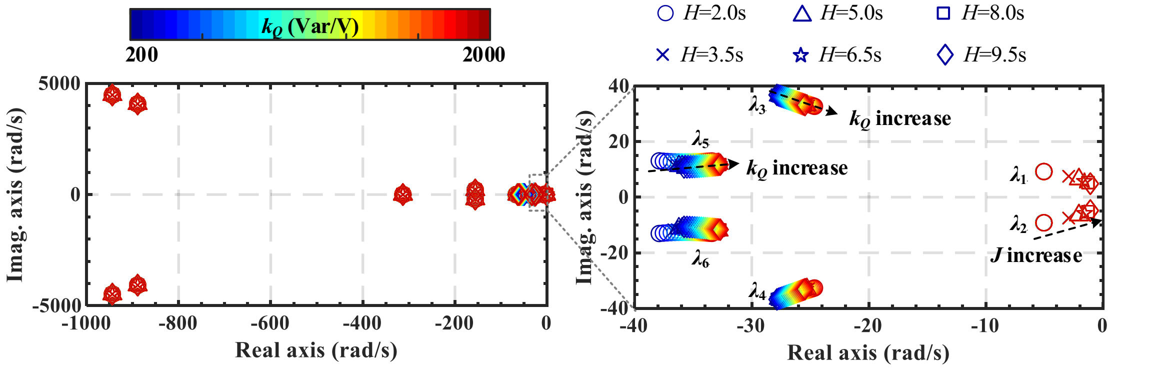

Figure 4.31: Eigenvalue locus of the GFM converter for different combinations of k_Q and J

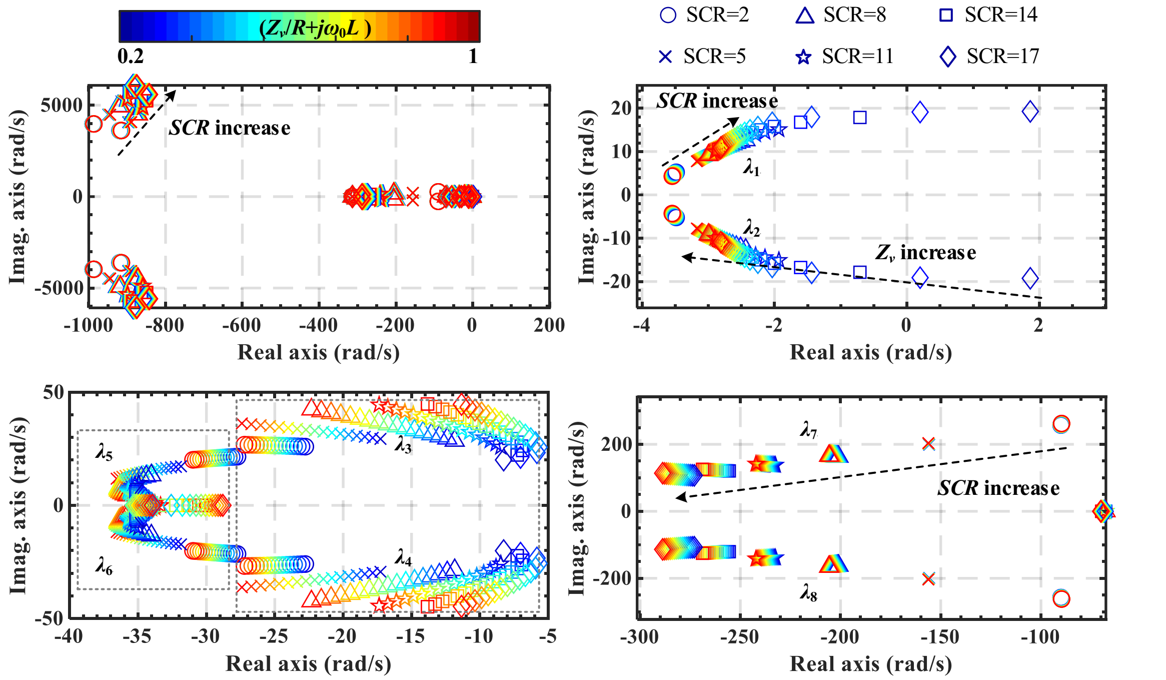

Figure 4.32: Eigenvalue locus of the GFM converter for different combinations of SCR and Z_v

Figure 4.33 shows the movement of the eigenvalues for different inner loop control parameters. It is seen that the inner loop can interact with the low-frequency power loop mode $\lambda_{1,\,2}$ as the inner current control loop becomes slower. Fast current control is desired to guarantee the system stability and damping of the high-frequency oscillation modes λ_{9-12}.

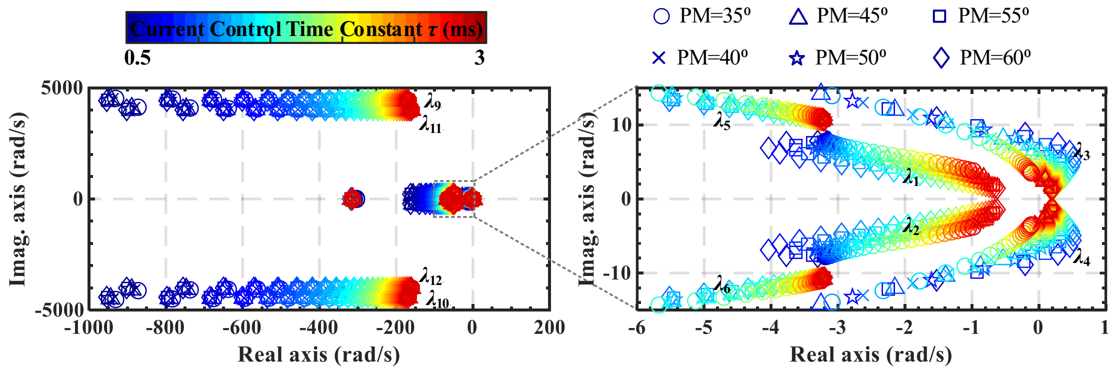

Figure 4.33: Eigenvalue locus of the GFM converter for different combinations of τ and PM

Time-Domain Validation

To verify the eigenvalue-based stability analysis results, time-domain forced responses have been performed by applying 200 W active power reference step to the VSG converter for different control parameters. Figure 4.34 - Figure 4.36 show the forced responses for different outer power loop control parameters. It is seen that the dynamic evolution becomes more oscillatory as the inertia constant increases. Larger active power droop coefficient is beneficial for improving the damping, while the influence of the reactive power droop coefficient is negligible. Moreover, it is seen from Figure 4.37 and Figure 4.38 that reducing the virtual impedance can cause the instability. The negative impact of a slower inner current controller on the system stability can be confirmed by the dynamic responses shown in Figure 4.39.

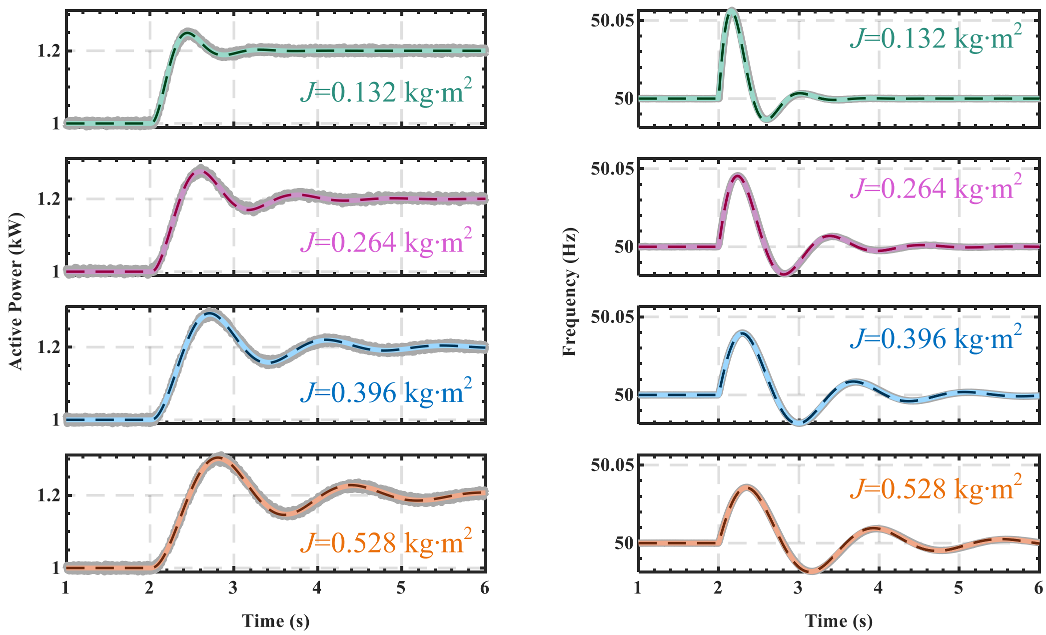

(a) Active Power **(b)** Frequency

Figure 4.34: Forced responses of the VSG converter for different inertia constants

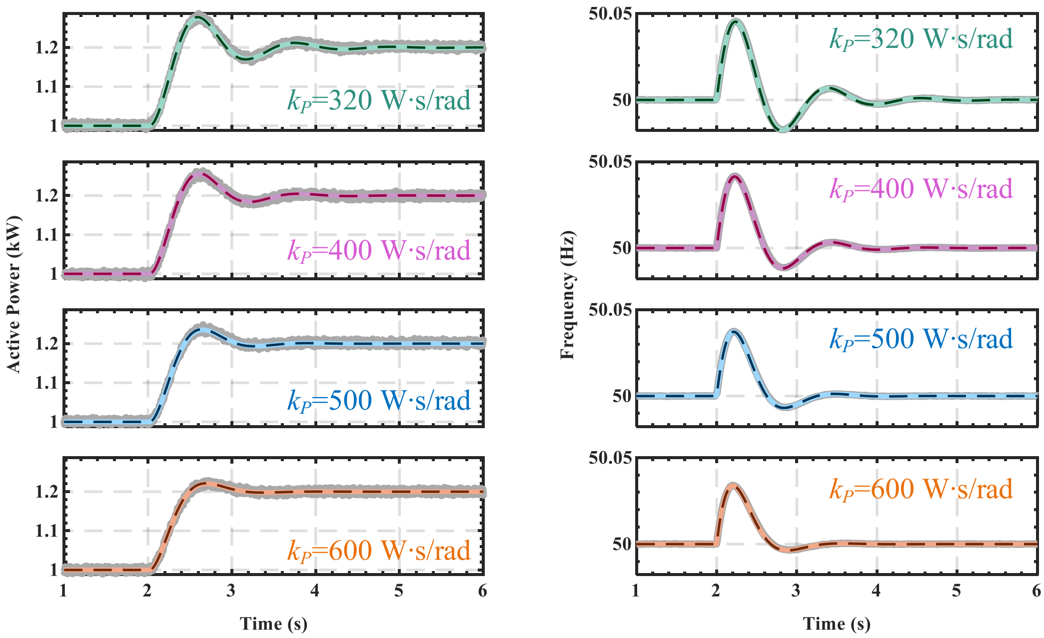

(a) Active Power **(b)** Frequency

Figure 4.35: Forced responses of the VSG converter for $J = 0.264\ \mathrm{kg} \cdot \mathrm{m}^2$ different active power droop coefficients

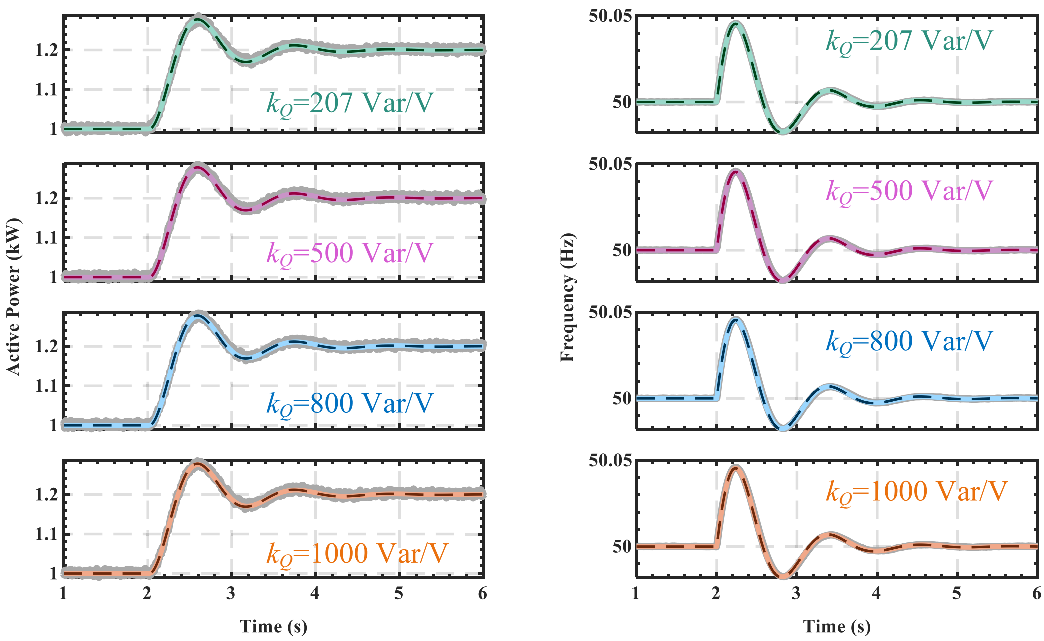

(a) Active Power **(b)** Frequency

Figure 4.36: Forced responses of the VSG converter for $J = 0.264\ \mathrm{kg} \cdot \mathrm{m}^2$ and different reactive power droop coefficients

4.6 Summary

This chapter generalizes the classical modal analysis to the linear time-periodic systems by deriving the analytical free-response solution. The proposed indices, including damping ratio,

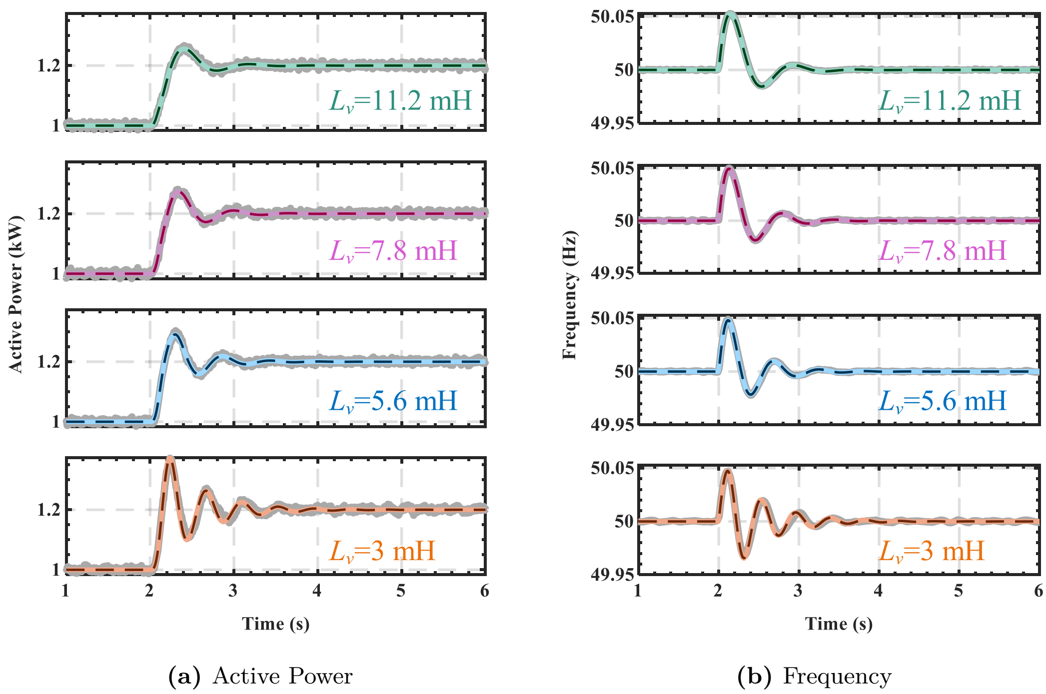

Figure 4.37: Forced responses of the VSG converter for different virtual impedances

participation factor and eigenvalue sensitivity, can provide insightful description and assessment of dynamic performance of LTP systems. Two iterative LTP eigenvalue calculation algorithms are developed to balance the trade-off between computational accuracy and efficiency. The participation factor ratio is defined as a measure of the strength of the frequency coupling effect, which answers when the LTP theory must be applied. Based on the proposed LTP modal analysis, the stability of both grid-following and grid-forming converters are examined, and the major findings are:

- Higher bandwidth of DSRF-PLL and DSOGI-PLL can counteract the negative impact of weaker grids and slower current controls on the system stability. However, it brings poorly damped or even amplified oscillations around the fundamental frequency.

- The Type II grid-following converter (DSOGI-PLL plus PR current control) has a larger stability margin and is more robust than Type I GFL converter (DSRF-PLL plus PI current control) against grid voltage imbalances.

- Under strong grid conditions, the grid-forming converter with inner cascaded voltage-current control can encounter instability problems. A large virtual impedance needs to be used to ensure the system stability. Moreover, fast current control is generally desired to guarantee the damping of high-frequency oscillation modes and weaken the interaction between outer and inner loops.

All theoretical analysis has been validated by simulation results and experimental tests.

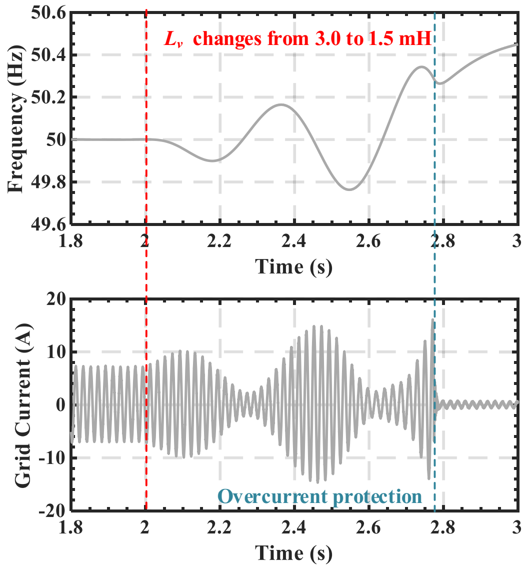

Figure 4.38: Instability of the VSG converter caused by small virtual impedance

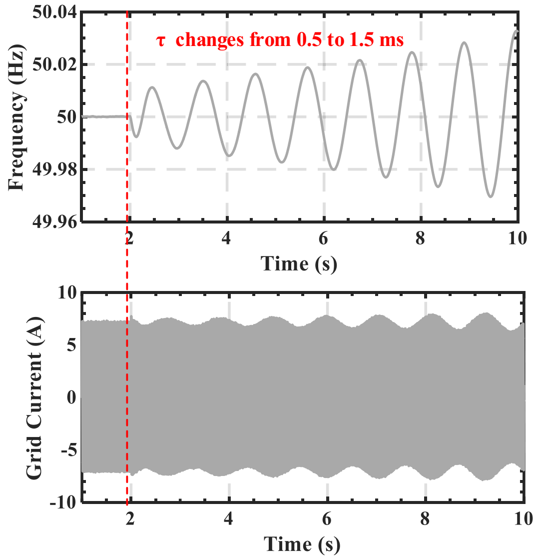

Figure 4.39: Instability of the VSG converter caused by slow inner current control

5

Harmonic Resonance Analysis

This chapter deals with the harmonic resonance investigation of the converter-dominated power systems considering unbalanced operations. Initially, the closed-form analytical solution of the forced response of the LTP system is deduced. According to this, the impedance model of the grid-following converter and the unbalanced network are derived to fully capture the frequency coupling effect. Then, the LTP resonance mode analysis is developed by describing the system with a time-periodic impedance matrix to identify the resonance frequencies. Based on the eigenanalysis of the time-periodic impedance matrix, the definition of the participation factor is modified to determine the propagation areas and corresponding severity of a certain resonance. In addition, the impact of the converter controller and the grid imbalance on the resonance characteristics are evaluated by using a sensitivity analysis method. The proposed methodology is tested on an exemplary multiple-converter system.

5.1 Forced Response of the LTP System

As discussed in Section 4.3, the LTP eigenvalues of the time-periodic system matrix $\boldsymbol{A}(t)$ provide the intrinsic stability characteristic of the LTP system. For the resonance analysis, we are interested in the terminal equivalent impedance or admittance of converters, namely the steady-state transfer functions between voltages and currents. To obtain the relevant transfer functions, the forced response of the N-dimensional LTP system

$$\Delta\dot{\boldsymbol{x}} = \boldsymbol{A}\left(t\right)\Delta\boldsymbol{x} + \boldsymbol{B}\left(t\right)\Delta\boldsymbol{u} \tag{5.1a}$$

$$\Delta\boldsymbol{y} = \boldsymbol{C}\left(t\right)\Delta\boldsymbol{x} + \boldsymbol{D}\left(t\right)\Delta\boldsymbol{u} \tag{5.1b}$$

is investigated in this section.

Based on the generalized modal analysis explained in Section 4.3, the forced response of the LTP system can be derived following two steps shown in Figure 5.1:

1. In the first step, the physical input $\Delta\boldsymbol{x}$ is transformed into an LTI modal space, and the steady-state response of state variables in the modal space, namely $\Delta\boldsymbol{z}$, is derived.

2. In the second step, $\Delta \boldsymbol{z}$ is transformed back into the physical space to obtain the physical output $\Delta \boldsymbol{y}$.

STEP 1

Applying the space transformation described with the LTP eigenvector matrix $\boldsymbol{R}(t)$, Eq. (5.1a) is transformed into the modal space

$$
\begin{gathered}
\Delta \dot{\boldsymbol{x}} = \boldsymbol{A}(t)\,\Delta \boldsymbol{x} + \boldsymbol{B}(t)\,\Delta \boldsymbol{u} \\
\Downarrow \Delta \boldsymbol{x} = \boldsymbol{R}(t)\Delta \boldsymbol{z} \\
\Delta \dot{\boldsymbol{z}} = \boldsymbol{Q}\Delta \boldsymbol{z} + \boldsymbol{f}(t)\,\Delta \boldsymbol{u} = \underbrace{\boldsymbol{R}^{-1}(t)\left(\boldsymbol{A}(t)\,\boldsymbol{R}(t) - \dot{\boldsymbol{R}}(t)\right)}_{\boldsymbol{Q}}\Delta \boldsymbol{z} + \underbrace{\boldsymbol{R}^{-1}(t)\,\boldsymbol{B}(t)}_{\boldsymbol{f}(t)}\Delta \boldsymbol{u}
\end{gathered} \quad . \tag{5.2}
$$

In the modal space, Eq. (5.2) describes an LTI system, since the diagonal LTP eigenvalue matrix $\boldsymbol{Q}$ is constant.

Without loss of generality, let the physical input $\Delta \boldsymbol{u}$ contain a single component at the frequency of ω, namely

$$\Delta \boldsymbol{u} = \boldsymbol{U}e^{j\omega t} \tag{5.3}$$

where $\boldsymbol{U}$ is a constant vector, which gives the magnitude and phase angle of the input vector $\Delta \boldsymbol{u}$. The time-periodic matrix

$$\boldsymbol{f}(t) = \sum\nolimits_{p=-\infty}^{\infty} \boldsymbol{f}^p e^{jp\omega_0 t}$$

transforms the single-frequency physical input $\Delta \boldsymbol{u}$ to a multiple-frequency input in the modal space

$$\Delta \boldsymbol{u}_{modal} = \boldsymbol{f}(t)\,\Delta \boldsymbol{u} = \sum\nolimits_{p=-\infty}^{\infty} \boldsymbol{f}^p \boldsymbol{U} e^{j(\omega + p\omega_0)t}. \tag{5.4}$$

The Fourier series coefficient $\boldsymbol{f}^p$ is associated with the pth order harmonic of $\boldsymbol{f}(t)$.

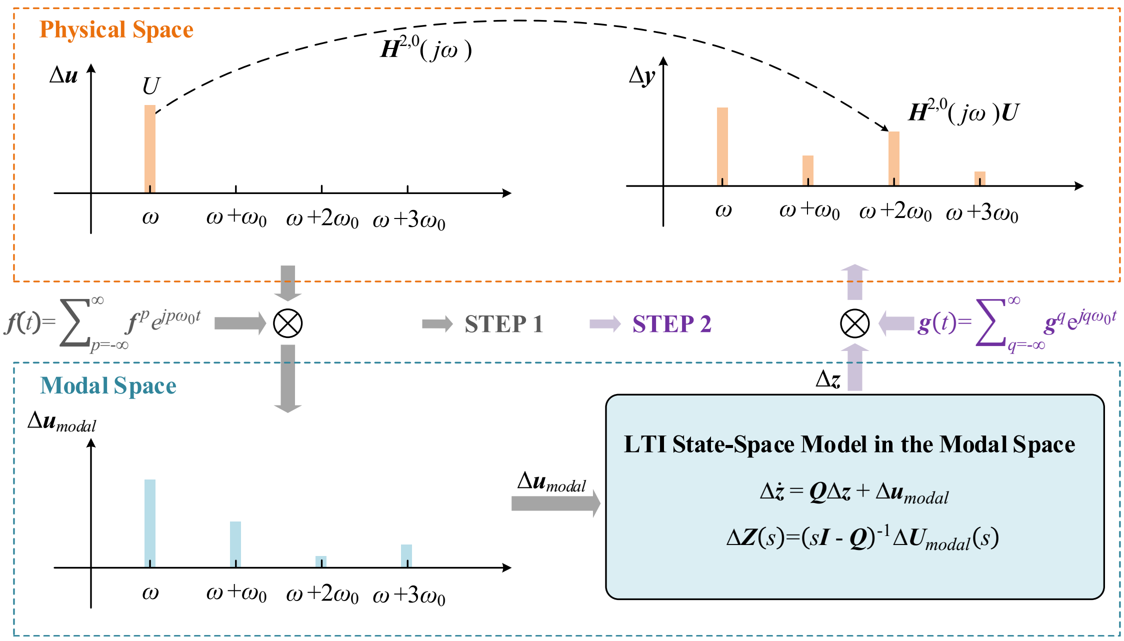

Figure 5.1: Qualitative forced response of the LTP system

In the LTI modal space, the steady-state relation between $\Delta \boldsymbol{z}$ and $\Delta \boldsymbol{u}_{modal}$ can be easily derived

$$\Delta \boldsymbol{Z}(s) = (s\boldsymbol{I} - \boldsymbol{Q})^{-1} \Delta \boldsymbol{U}_{modal}(s) \tag{5.5}$$

where $\Delta \boldsymbol{Z}(s)$ and $\Delta \boldsymbol{U}_{modal}(s)$ are the Laplace transformation of $\Delta \boldsymbol{z}$ and $\Delta \boldsymbol{u}_{modal}$. $\boldsymbol{I}$ stands for the N-dimensional identity matrix. To obtain the steady-state response of $\Delta \boldsymbol{z}$ to $\Delta \boldsymbol{u}$, Eq. (5.4) needs to be inserted into Eq. (5.5), and yields

$$\Delta \boldsymbol{z} = \sum\nolimits_{p=-\infty}^{\infty} \left(j\left(\omega + p\omega_0\right)\boldsymbol{I} - \boldsymbol{Q}\right)^{-1} \boldsymbol{f}^p \boldsymbol{U} e^{j(\omega + p\omega_0)t} \tag{5.6}$$

STEP 2

In STEP 1, the steady-state response of the state vector $\Delta \boldsymbol{z}$ in the modal space to the input vector $\Delta \boldsymbol{u}$ in the physical space is deduced. STEP 2 aims to further derive the output vector $\Delta \boldsymbol{y}$ in the physical space based on Eq. (5.1b) and the transformation $\Delta \boldsymbol{x} = \boldsymbol{R}(t)\Delta \boldsymbol{z}$.

Since both $\boldsymbol{C}(t)$ and $\boldsymbol{R}(t)$ are time-periodic matrices, their product defined as $\boldsymbol{g}(t)$ will also be time-periodic, which has the Fourier series expansion

$$\boldsymbol{g}(t) = \boldsymbol{C}(t)\boldsymbol{R}(t) = \sum\nolimits_{q=-\infty}^{\infty} \boldsymbol{g}^q e^{jq\omega_0 t}. \tag{5.7}$$

Then, the steady-state forced response $\Delta \boldsymbol{y}$ in Eq. (5.1b) can be obtained with the inverse transformation from the modal space to the physical space

$$\begin{aligned}
\Delta \boldsymbol{y} &= \boldsymbol{C}(t)\Delta \boldsymbol{x} = \boldsymbol{C}(t)\boldsymbol{R}(t)\Delta \boldsymbol{z} = \boldsymbol{g}(t)\Delta \boldsymbol{z} \\
&= \sum\nolimits_{q=-\infty}^{\infty} \boldsymbol{g}^q e^{jq\omega_0 t} \underbrace{\sum\nolimits_{p=-\infty}^{\infty} \left(j\left(\omega + p\omega_0\right)\boldsymbol{I} - \boldsymbol{Q}\right)^{-1} \boldsymbol{f}^p \boldsymbol{U} e^{j(\omega + p\omega_0)t}}_{\Delta \boldsymbol{z}} \\
&= \sum\nolimits_{q=-\infty}^{\infty} \underbrace{\left(\sum\nolimits_{p=-\infty}^{\infty} \boldsymbol{g}^p \left(j\left(\omega + (q-p)\omega_0\right)\boldsymbol{I} - \boldsymbol{Q}\right)^{-1} \boldsymbol{f}^{(q-p)}\right)}_{\boldsymbol{H}^{q,0}(j\omega)} \boldsymbol{U} e^{j(\omega + q\omega_0)t} \\
&= \sum\nolimits_{q=-\infty}^{\infty} \boldsymbol{H}^{q,0}(j\omega)\boldsymbol{U} e^{j(\omega + q\omega_0)t} \\
&= \sum\nolimits_{q=-\infty}^{\infty} \boldsymbol{Y}^q(j\omega) e^{j(\omega + q\omega_0)t}
\end{aligned} \tag{5.8}$$

The zero output matrix $\boldsymbol{D}(t)$ in Eq. (5.1b) is dropped, since, for the LTP small-signal model of the converter-dominated power systems, the output variables are part of the state variables.

Equation (5.8) reveals the unique characteristic of the LTP system, that the input $\Delta \boldsymbol{u}$ at a single frequency ω will excite the steady-state responses of $\Delta \boldsymbol{y}$ with multiple components at the frequencies of $\{\omega + q\omega_0,\ q \in \mathbb{Z}\}$. The transfer function $\boldsymbol{H}^{q,0}(j\omega)$ maps the input $\Delta \boldsymbol{u} = \boldsymbol{U}e^{j\omega t}$ to the harmonic component $\boldsymbol{Y}^q e^{j(\omega+q\omega_0)t}$ in the output $\Delta \boldsymbol{y}$, namely

$$\boldsymbol{Y}^q(j\omega) e^{j(\omega+q\omega_0)t} = \boldsymbol{H}^{q,0}(j\omega)\boldsymbol{U} e^{j(\omega+q\omega_0)t} = \boldsymbol{H}^{q,0}(j\omega)\boldsymbol{U} e^{j\omega t} \tag{5.9}$$

Discussion on Transfer function of LTP System

In Eq. (5.8), the inverse calculation of the diagonal matrix can be easily obtained

$$\left(j\left(\omega+\left(q-p\right)\omega_0\right)\boldsymbol{I}-\boldsymbol{Q}\right)^{-1}=\begin{bmatrix}\frac{1}{j(\omega+(q-p)\omega_0)-\lambda_1} & & & \\ & \frac{1}{j(\omega+(q-p)\omega_0)-\lambda_2} & & \\ & & \ddots & \\ & & & \frac{1}{j(\omega+(q-p)\omega_0)-\lambda_N}\end{bmatrix}.$$

Then, $\boldsymbol{H}^{q,0}\left(j\omega\right)$ can be expressed as the superposition of the N LTP eigenvalues/modes

$$\boldsymbol{H}^{q,0}\left(j\omega\right)=\sum\nolimits_{i=1}^{N}\left(\sum\nolimits_{p=-\infty}^{\infty}\frac{1}{j\left(\omega+\left(q-p\right)\omega_0\right)-\lambda_i}\boldsymbol{g}_i{}^{p}\boldsymbol{f}_i{}^{q-p}\right). \tag{5.10}$$

It gives that the transfer functions of the LTP system consist of N clusters of first-order transfer functions, and the ith cluster is

$$\left\{\frac{1}{j\left(\omega+\left(q-p\right)\omega_0\right)-\lambda_i},\ q,p\in\mathbb{Z}\right\}. \tag{5.11}$$

The residue of

$$\frac{1}{j\left(\omega+\left(q-p\right)\omega_0\right)-\lambda_i} \tag{5.12}$$

is $\boldsymbol{g}_i^p\boldsymbol{f}_i^{q-p}$, where $\boldsymbol{g}_i^p$ is the ith column of $\boldsymbol{g}^p$, and $\boldsymbol{f}_i^{q-p}$ is the ith row of $\boldsymbol{f}^{q-p}$. The LTI system can be regarded as a special case of the LTP system, where $\boldsymbol{g}_i^0\boldsymbol{f}_i^0$ is the only non-zero residue.

The input and output of the classical LTI system share the same frequency. However, for the LTP systems, it can be concluded from Eq. (5.8) that the only possibility to make the input $\Delta\boldsymbol{u}$ and the output $\Delta\boldsymbol{y}$ of the LTP system share the same harmonic space is to set the input as

$$\Delta\boldsymbol{u}=\sum\nolimits_{p=-\infty}^{\infty}\boldsymbol{U}^{p}e^{j(\omega+p\omega_0)t} \tag{5.13}$$

which contains infinite harmonic components, of which the frequencies are differing by integer multiples of ω_0. Then, the spectra of $\Delta\boldsymbol{u}$ and the output

$$\Delta\boldsymbol{y}=\sum\nolimits_{q=-\infty}^{\infty}\boldsymbol{Y}^{q}e^{j(\omega+q\omega_0)t}$$

are linked by

$$\begin{bmatrix}\vdots\\ \boldsymbol{Y}^{-1}\\ \boldsymbol{Y}^{0}\\ \boldsymbol{Y}^{+1}\\ \vdots\end{bmatrix}=\underbrace{\begin{bmatrix}\ddots & \vdots & \vdots & \vdots & \iddots\\ \cdots & \boldsymbol{H}^{-1,-1}\left(j\omega\right) & \boldsymbol{H}^{-1,0}\left(j\omega\right) & \boldsymbol{H}^{-1,+1}\left(j\omega\right) & \cdots\\ \cdots & \boldsymbol{H}^{0,-1}\left(j\omega\right) & \boldsymbol{H}^{0,0}\left(j\omega\right) & \boldsymbol{H}^{0,+1}\left(j\omega\right) & \cdots\\ \cdots & \boldsymbol{H}^{+1,-1}\left(j\omega\right) & \boldsymbol{H}^{+1,0}\left(j\omega\right) & \boldsymbol{H}^{+1,+1}\left(j\omega\right) & \cdots\\ \iddots & \vdots & \vdots & \vdots & \ddots\end{bmatrix}}_{\boldsymbol{H}_{HTM}(j\omega)}\begin{bmatrix}\vdots\\ \boldsymbol{U}^{-1}\\ \boldsymbol{U}^{0}\\ \boldsymbol{U}^{+1}\\ \vdots\end{bmatrix}. \tag{5.14}$$

The elementary transfer function matrix $\boldsymbol{H}^{q,p}\left(j\omega\right)$ in $\boldsymbol{H}_{HTM}\left(j\omega\right)$ gives the relation

$$\boldsymbol{Y}^{q}=\boldsymbol{H}^{q,p}\left(j\omega\right)\boldsymbol{U}^{p}. \tag{5.15}$$

Actually, the information stored in the transfer function matrix $\boldsymbol{H}_{HTM}(j\omega)$ is highly redundant. To illustrate this, similar to Eq. (5.3), the input $\Delta \boldsymbol{u}$ is again assumed to contain a single component while the frequency is shifted to $\omega + h\omega_0$, namely

$$\Delta \boldsymbol{u} = \boldsymbol{U} e^{j(\omega + h\omega_0)t}. \tag{5.16}$$

Then, the steady-state output can be derived by replacing ω with $\omega + h\omega_0$ in Eq. (5.8)

$$\Delta \boldsymbol{y} = \sum_{q=-\infty}^{\infty} \underbrace{\left(\sum_{p=-\infty}^{\infty} \boldsymbol{g}^p \left(j\left(\omega + (q-p+h)\,\omega_0\right) \boldsymbol{I} - \boldsymbol{Q} \right)^{-1} \boldsymbol{f}^{q-p} \right)}_{\boldsymbol{H}^{q+h,h}(j\omega)} \boldsymbol{U} e^{j(\omega + (q+h)\omega_0)t} \tag{5.17}$$

where the transfer function $\boldsymbol{H}^{q+h,h}(j\omega)$ maps the input $\Delta \boldsymbol{u} = \boldsymbol{U} e^{j(\omega + h\omega_0)t}$ to the output component $\boldsymbol{Y}^{q+h} e^{j(\omega + (q+h)\omega_0)t}$ and satisfies the relation

$$\boldsymbol{H}^{q+h,h}(j\omega) = \boldsymbol{H}^{q,0}\left(j\left(\omega + h\omega_0\right)\right) \tag{5.18}$$

It can be concluded that transfer functions on diagonals of $\boldsymbol{H}_{HTM}(j\omega)$ are frequency-shifted versions of each other. Knowing one column or one row of $\boldsymbol{H}_{HTM}(j\omega)$ is sufficient for the determination of the harmonic transfer relation.

Formally $\boldsymbol{H}_{HTM}(j\omega)$ in Eq. (5.14) is the same as that in Eq. (2.5) obtained by applying the harmonic balance principle. The vital contribution of this section is that the analytical closed-form expression of $\boldsymbol{H}_{HTM}(j\omega)$ is deduced by using the generalized modal analysis, and the impractical inverse calculation of the infinite transfer function matrix is avoided.

5.2 Impedance Modeling of Converter-Dominated Power Systems

5.2.1 Impedance Modeling of the Voltage Source Converters

The LTP state-space model of the grid-following and grid-forming converters have been derived in Section 3.2. Based on the fundamentals introduced in Section 5.1, the equivalent admittance/impedance of the single-converter system observed at the grid connection point is derived in this subsection.

Assuming that the voltage at the grid connection point $\Delta v_{\alpha\beta g}$ contains infinite harmonic components differing by integer multiples of ω_0

$$\begin{aligned} \Delta v_{\alpha\beta g} &= \sum_{p=-\infty}^{\infty} V_{\alpha\beta g}^{p} e^{j(\omega + p\omega_0)t} \\ \Delta v_{\alpha\beta g}^{*} &= \sum_{p=-\infty}^{\infty} \left(V_{\alpha\beta g}^{p}\right)^{*} e^{j(-\omega - p\omega_0)t}, \end{aligned}$$

the steady-state response of the grid-side inductor current $\Delta i_{\alpha\beta g}$ will have the same form

$$\begin{aligned} \Delta i_{\alpha\beta g} &= \sum_{p=-\infty}^{\infty} I_{\alpha\beta g}^{p} e^{j(\omega + p\omega_0)t} \\ \Delta i_{\alpha\beta g}^{*} &= \sum_{p=-\infty}^{\infty} \left(I_{\alpha\beta g}^{p}\right)^{*} e^{j(-\omega - p\omega_0)t}. \end{aligned}$$

Defining the voltage and current Fourier series coefficient vectors

$$\boldsymbol{\mathcal{V}} = \left[\underbrace{\cdots \;\; V_{\alpha\beta g}^{-1} \;\; V_{\alpha\beta g}^{0} \;\; V_{\alpha\beta g}^{1} \;\; \cdots}_{original\ coordinate} \;\; \underbrace{\cdots \;\; \left(V_{\alpha\beta g}^{1}\right)^{*} \;\; \left(V_{\alpha\beta g}^{0}\right)^{*} \;\; \left(V_{\alpha\beta g}^{-1}\right)^{*} \;\; \cdots}_{conjugate\ coordinate} \right]^{T}$$

$$\boldsymbol{\mathcal{I}} = \left[\underbrace{\cdots \;\; I_{\alpha\beta g}^{-1} \;\; I_{\alpha\beta g}^{0} \;\; I_{\alpha\beta g}^{1} \;\; \cdots}_{original\ coordinate} \;\; \underbrace{\cdots \;\; \left(I_{\alpha\beta g}^{1}\right)^{*} \;\; \left(I_{\alpha\beta g}^{0}\right)^{*} \;\; \left(I_{\alpha\beta g}^{-1}\right)^{*} \;\; \cdots}_{conjugate\ coordinate} \right]^{T},$$

the harmonic transfer matrix of the single-converter system can be defined as

$$\boldsymbol{\mathcal{I}} = \underbrace{\begin{bmatrix} \boldsymbol{H}_{O,O}(j\omega) & \boldsymbol{H}_{O,C}(j\omega) \\ \boldsymbol{H}_{C,O}(j\omega) & \boldsymbol{H}_{C,C}(j\omega) \end{bmatrix}}_{\boldsymbol{H}_{VSC}(j\omega)} \boldsymbol{\mathcal{V}}. \tag{5.19}$$

$\boldsymbol{H}_{VSC}(j\omega)$ is the equivalent admittance of the single-converter system observed at the grid connected point. It is divided into four blocks, i.e., $\boldsymbol{H}_{O,O}(j\omega)$, $\boldsymbol{H}_{O,C}(j\omega)$, $\boldsymbol{H}_{C,O}(j\omega)$ and $\boldsymbol{H}_{C,C}(j\omega)$. The subscript O and C indicate the original and conjugate coordinates. $\boldsymbol{H}_{O,C}(j\omega)$ and $\boldsymbol{H}_{C,O}(j\omega)$ reflect the coupling between the original and conjugate coordinates caused by the asymmetric control of the PLLs in the grid-following converter and the power control loop in the grid-forming converter.

Theoretically the four blocks in $\boldsymbol{H}_{VSC}(j\omega)$ are all infinite-dimensional matrices, for instance, $\boldsymbol{H}_{O,C}(j\omega)$ is given by

$$\boldsymbol{H}_{O,C}(j\omega) = \begin{bmatrix} \ddots & \vdots & \vdots & \vdots & \iddots \\ \cdots & H_{O,C}^{-1,\,-1}(j\omega) & H_{O,C}^{-1,\,0}(j\omega) & H_{O,C}^{-1,\,1}(j\omega) & \cdots \\ \cdots & H_{O,C}^{0,\,-1}(j\omega) & H_{O,C}^{0,\,0}(j\omega) & H_{O,C}^{0,\,1}(j\omega) & \cdots \\ \cdots & H_{O,C}^{1,\,-1}(j\omega) & H_{O,C}^{1,\,0}(j\omega) & H_{O,C}^{1,\,1}(j\omega) & \cdots \\ \iddots & \vdots & \vdots & \vdots & \ddots \end{bmatrix}$$

where $H_{O,C}^{q,\,p}(-j\omega)$ maps the input voltage harmonic

$$\left(V_{\alpha\beta g}^{-p}\right)^{*} e^{j(-\omega+p\omega_0)t}$$

in the conjugate coordinate to the output current harmonic

$$I_{\alpha\beta g}^{q} e^{j(-\omega+q\omega_0)t}$$

in the original coordinate. Specifically, let the input voltage contain only 1 V positive-sequence component at the frequency ω. Except for

$$\Delta v_{\alpha\beta g} = 1e^{j\omega t},$$

the output current is also excited by

$$\Delta v_{\alpha\beta g}^{*} = 1e^{-j\omega t}.$$

This is defined as the **sequence coupling effect**. Additionally, due to the time-periodic operation trajectory, the current response contains multiple harmonics at the frequencies of $\{\omega + q\omega_0, q \in \mathbb{Z}\}$ and $\{-\omega + q\omega_0, q \in \mathbb{Z}\}$, quantified by

$$\left\{H_{O,O}^{n,\,0}(j\omega), n \in \mathbb{Z}\right\} \text{ and } \left\{H_{O,C}^{n,\,0}(-j\omega), n \in \mathbb{Z}\right\},$$

respectively. This is defined as the **frequency shift effect**.

Table 5.1: Parameters of the Single Type I Grid-Following Converter System

Symbol	Description	Value
L / R	Converter-side filter inductance	$5.6\,\text{mH}$ / $0.1\,\Omega$
C	Filter capacitor	$16\,\mu\text{F}$
BW	PLL bandwidth	$25\,\text{Hz}$
τ	Time constant of the current control	$1\,\text{ms}$
L_g / R_g	Grid-side line impedance	$1.5\,\text{mH}$ / $0.001\,\Omega$
S_r	Power reference	$2\,\text{kW}$
$v_{\alpha\beta g}$	Voltage at the grid connection point	$(100e^{j\omega_0 t} + 50e^{-j\omega_0 t})\text{V}$

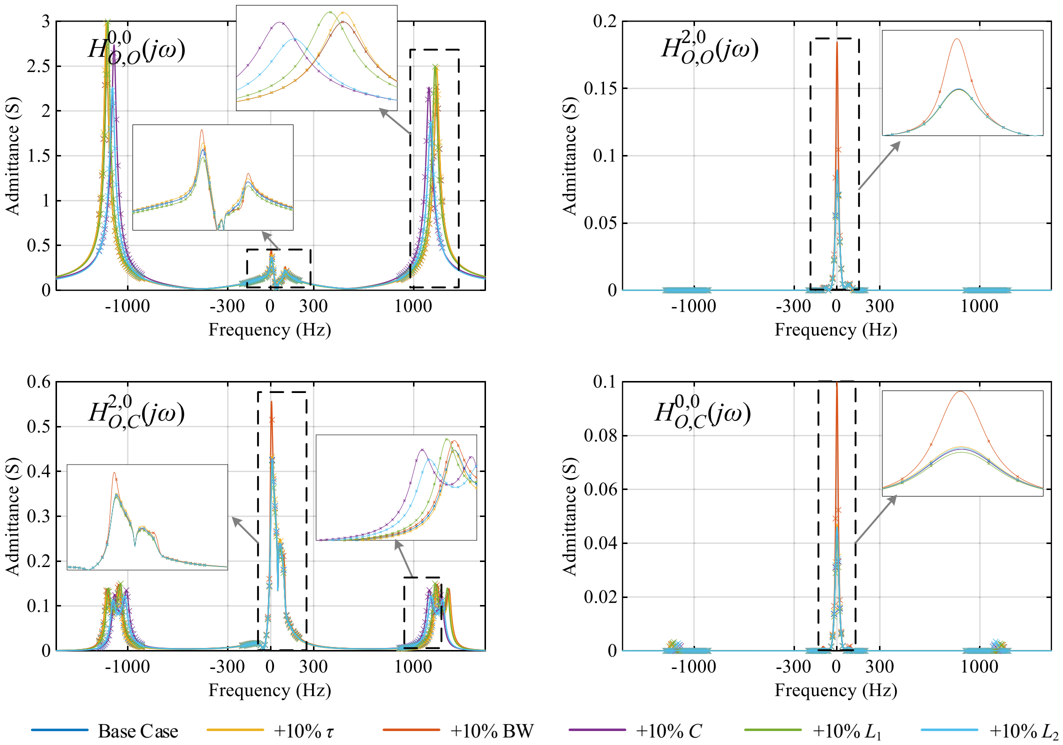

Figure 5.2: Equivalent admittances of the Type I grid-following converter for changes of different control and physical parameters. Solid lines: analytical results. Crosses: frequency sweep results.

For the sake of clarity, the equivalent admittance of the Type I grid-following converter is derived and evaluated. Table 5.1 lists initial values of the key control and physical parameters. The unbalanced grid voltage contains 0.5 pu negative-sequence component. The nonlinear large-signal model is implemented in MATLAB/Simulink. The frequency sweep method is used to evaluate the accuracy of the harmonic transfer matrix $\boldsymbol{H}_{VSC}\,(j\omega)$ given in Eq. (5.19). The basic principle of the frequency sweep method is that a voltage disturbance $\Delta v_{\alpha\beta g}$ at different frequencies (one frequency at a time) is injected into $v_{\alpha\beta g}$, then, the spectrum of the steady-state current response $\Delta i_{\alpha\beta g}$ is obtained to calculate equivalent admittances. The equivalent admittances with maximum magnitudes larger than 0.1 S are shown in Figure 5.2 with solid lines. The crosses in Figure 5.2 denote frequency sweep simulation results. The maximum relative percentage error between analytical and frequency sweeping results is smaller than 0.05%, which verifies the correctness and accuracy of the proposed harmonic transfer matrix model. Additionally, control parameters and LCL filter parameters are respectively increased by 10% of the initial values to investigate the individual influence of the current control time constant τ, PLL bandwidth BW, and LCL parameters on the equivalent admittances, as shown in Figure 5.2. It is seen that:

1. Parameters of the LCL filter have larger impact on resonance peaks and resonance frequencies of $H_{O,O}^{0,\,0}(j\omega)$ and $H_{O,C}^{2,\,0}(j\omega)$ in the high frequency range (around 1000 Hz), while their influence in the low frequency range (below 300 Hz) is comparably small.

2. Time constant τ of the current controller mainly influences the damping of resonance peaks. The system gets less damped as the time constant increases.

3. The bandwidth BW of the DSRF-PLL influences all four impedances merely in the low frequency range.

5.2.2 Impedance Modeling of Power Networks and Loads

In the frequency domain, a three-phase branch (or load) can be described with

$$\begin{bmatrix} I_a(j\omega) \\ I_b(j\omega) \\ I_c(j\omega) \end{bmatrix} = \underbrace{\begin{bmatrix} Y_a(j\omega) & & \\ & Y_b(j\omega) & \\ & & Y_c(j\omega) \end{bmatrix}}_{\boldsymbol{Y}_{abc}(j\omega)} \begin{bmatrix} V_a(j\omega) \\ V_b(j\omega) \\ V_c(j\omega) \end{bmatrix} \tag{5.20}$$

where $[I_a(j\omega),\ I_b(j\omega),\ I_c(j\omega)]^T$ and $[V_a(j\omega),\ V_b(j\omega),\ V_c(j\omega)]^T$ are the Fourier transformation of the branch current and nodal voltage vectors, $[i_a,\ i_b,\ i_c]^T$ and $[v_a,\ v_b,\ v_c]^T$. $Y_a(j\omega)$, $Y_b(j\omega)$ and $Y_c(j\omega)$ denote the admittance of each phase. The corresponding two-phase description given by

$$\begin{bmatrix} I_\alpha(j\omega) \\ I_\beta(j\omega) \end{bmatrix} = \underbrace{\begin{bmatrix} Y_{\alpha\alpha}(j\omega) & Y_{\alpha\beta}(j\omega) \\ Y_{\beta\alpha}(j\omega) & Y_{\beta\beta}(j\omega) \end{bmatrix}}_{\boldsymbol{Y}_{\alpha\beta}(j\omega)} \begin{bmatrix} V_\alpha(j\omega) \\ V_\beta(j\omega) \end{bmatrix}$$

can be obtained by applying Clarke respectively inverse Clarke transformation

$$\begin{aligned} &\boldsymbol{Y}_{\alpha\beta}(j\omega) = \boldsymbol{T}_{Clarke}\boldsymbol{Y}_{abc}(j\omega)\boldsymbol{T}_{Clarke}^{-1} \\ &\begin{bmatrix} I_\alpha(j\omega) \\ I_\beta(j\omega) \end{bmatrix} = \boldsymbol{T}_{Clarke}\begin{bmatrix} I_a(j\omega) \\ I_b(j\omega) \\ I_c(j\omega) \end{bmatrix}; \quad \begin{bmatrix} V_\alpha(j\omega) \\ V_\beta(j\omega) \end{bmatrix} = \boldsymbol{T}_{Clarke}\begin{bmatrix} V_a(j\omega) \\ V_b(j\omega) \\ V_c(j\omega) \end{bmatrix} \end{aligned}$$

Then, the complex-domain impedance model of the branch can be derived

$$\begin{bmatrix} I(j\omega) \\ I^*(j\omega) \end{bmatrix} = \underbrace{\begin{bmatrix} Y_{O,O}(j\omega) & Y_{O,C}(j\omega) \\ Y_{C,O}(j\omega) & Y_{C,C}(j\omega) \end{bmatrix}}_{\boldsymbol{Y}_{OC}(j\omega)=\boldsymbol{T}_{r2c}\boldsymbol{Y}_{\alpha\beta}(j\omega)\boldsymbol{T}_{r2c}^{-1}} \begin{bmatrix} V(j\omega) \\ V^*(j\omega) \end{bmatrix} \tag{5.21}$$

where $\{V(j\omega),\ I(j\omega)\}$ and $\{V^*(j\omega),\ I^*(j\omega)\}$ denote the branch voltage and current in the original and conjugate coordinates, respectively. When the branch is symmetric, i.e., $Y_a(j\omega) = Y_b(j\omega) = Y_c(j\omega)$, it can be described by merely using variables in either the original coordinate or the conjugate coordinate, since $Y_{O,C}(j\omega) = Y_{C,O}(j\omega) = 0$. However, when the branch becomes unbalanced, non-zero $Y_{O,C}(j\omega)$ and $Y_{C,O}(j\omega)$ cause the same sequence coupling effect as the unbalanced control units of the voltage source converters. It can be expected that the frequency shift effect can also appear when a nonlinearity of the branch (e.g., saturation) is considered.

For the sake of consistency, the harmonic transfer matrix of the branch can be obtained by extending each entry of $\boldsymbol{Y}_{OC}(j\omega)$ into an infinite matrix according to Eq. (5.18), for instance

$$\begin{aligned} H_{O,O}^{q,p}(j\omega) &= \begin{cases} Y_{O,O}(j\omega + jp\omega_0) & \text{if } \ p = q \\ 0 & \text{if } \ p \neq q \end{cases} \\ H_{O,C}^{q,p}(j\omega) &= \begin{cases} Y_{O,C}(j\omega + jp\omega_0) & \text{if } \ p = q \\ 0 & \text{if } \ p \neq q \end{cases} \end{aligned}. \tag{5.22}$$

So far, the harmonic transfer matrix of basic elements in the converter-dominated grid have been deduced, which can precisely capture the frequency coupling effect. In the next section, these impedance models are used to investigate the resonance characteristics.

5.3 LTP-Theory Based Harmonic Resonance Analysis

5.3.1 Review of the Conventional Resonance Mode Analysis

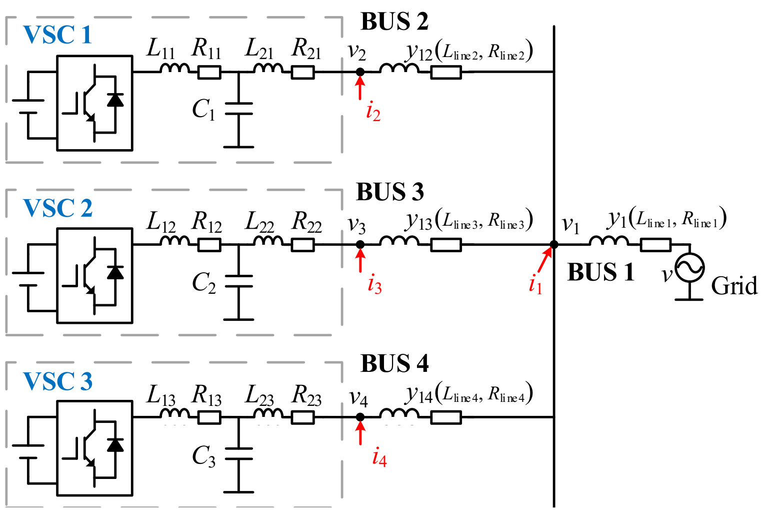

Figure 5.3: Topology of a grid-connected multiple-converter system

Figure 5.3 shows an exemplary grid-connected three-converter system. When the three-phase branches are symmetric, the conventional resonance modal analysis method can be used to investigate the parallel resonance of the passive network. The process is given as follows:

$$\begin{gathered}
\underbrace{\begin{bmatrix} I_1(j\omega) \\ I_2(j\omega) \\ I_3(j\omega) \\ I_4(j\omega) \end{bmatrix}}_{\boldsymbol{I}(j\omega)} = \underbrace{\begin{bmatrix} Y_{11}(j\omega) & Y_{12}(j\omega) & Y_{13}(j\omega) & Y_{14}(j\omega) \\ Y_{21}(j\omega) & Y_{22}(j\omega) & Y_{23}(j\omega) & Y_{24}(j\omega) \\ Y_{31}(j\omega) & Y_{32}(j\omega) & Y_{33}(j\omega) & Y_{34}(j\omega) \\ Y_{41}(j\omega) & Y_{42}(j\omega) & Y_{43}(j\omega) & Y_{44}(j\omega) \end{bmatrix}}_{\boldsymbol{Y}(j\omega)} \underbrace{\begin{bmatrix} V_1(j\omega) \\ V_2(j\omega) \\ V_3(j\omega) \\ V_4(j\omega) \end{bmatrix}}_{\boldsymbol{V}(j\omega)} \\
\Downarrow \\
\boldsymbol{V}(j\omega) = \boldsymbol{Y}^{-1}(j\omega)\,\boldsymbol{I}(j\omega) = \boldsymbol{Z}(j\omega)\,\boldsymbol{I}(j\omega)
\end{gathered} \tag{5.23}$$

where $\boldsymbol{V}(j\omega)$ gives the nodal voltage at the frequency of ω, and $\boldsymbol{I}(j\omega)$ is the nodal current injection vector. $\boldsymbol{Y}(j\omega)$ and $\boldsymbol{Z}(j\omega)$ are the network admittance and impedance matrices, which are frequency dependent. The element of $\boldsymbol{Y}(j\omega)$ is formulated by

$$Y_{mn} = \begin{cases} y_m + \sum_{n=1,\ldots,N_{Bus},\, n\neq m} y_{mn}, & if\ m = n \\ -y_{mn}, & if\ m \neq n \end{cases}$$

where y_{mn} denotes the admittance between the mth bus and the nth bus, of course, it is non-zero only when a physical connection exists between the two buses. The term y_m accounts for the admittance of linear loads connected to the mth bus as well as the admittance-to-stiff-grid in Figure 5.3.

Applying eigen decomposition to the network impedance matrix $\boldsymbol{Z}(j\omega)$ in Eq. (5.23), yields

$$\begin{aligned}
\boldsymbol{Z}(j\omega) &= \boldsymbol{R}(j\omega)\boldsymbol{\Lambda}(j\omega)\boldsymbol{R}^{-1}(j\omega) \\
&= \boldsymbol{R}(j\omega) \underbrace{\begin{bmatrix} \lambda_1(j\omega) & & & \\ & \lambda_2(j\omega) & & \\ & & \lambda_3(j\omega) & \\ & & & \lambda_4(j\omega) \end{bmatrix}}_{\boldsymbol{\Lambda}(j\omega)} \underbrace{\boldsymbol{L}(j\omega)}_{\triangleq \boldsymbol{R}^{-1}(j\omega)} .
\end{aligned}$$

$\boldsymbol{\Lambda}(j\omega)$ is the eigenvalue matrix of $\boldsymbol{Z}(j\omega)$, $\boldsymbol{R}(j\omega)$ and $\boldsymbol{L}(j\omega)$ are the corresponding right and left eigenvector matrices. The four eigenvalues/modes are named the modal impedances. A sharp parallel resonance will only occur when $\boldsymbol{Z}(j\omega)$ has eigenvalues/modes with very large magnitude, i.e., $\boldsymbol{Y}(j\omega)$ approaches singular. The peak of the magnitude of the eigenvalue is defined as the resonance mode, and the corresponding frequency is called the resonance frequency.

Figure 5.4 qualitatively demonstrates the basic principle of the conventional resonance mode analysis method, where ω^p $(p \in \mathbb{Z})$ denotes $\omega + p\omega_0$. Imagine that the physical current

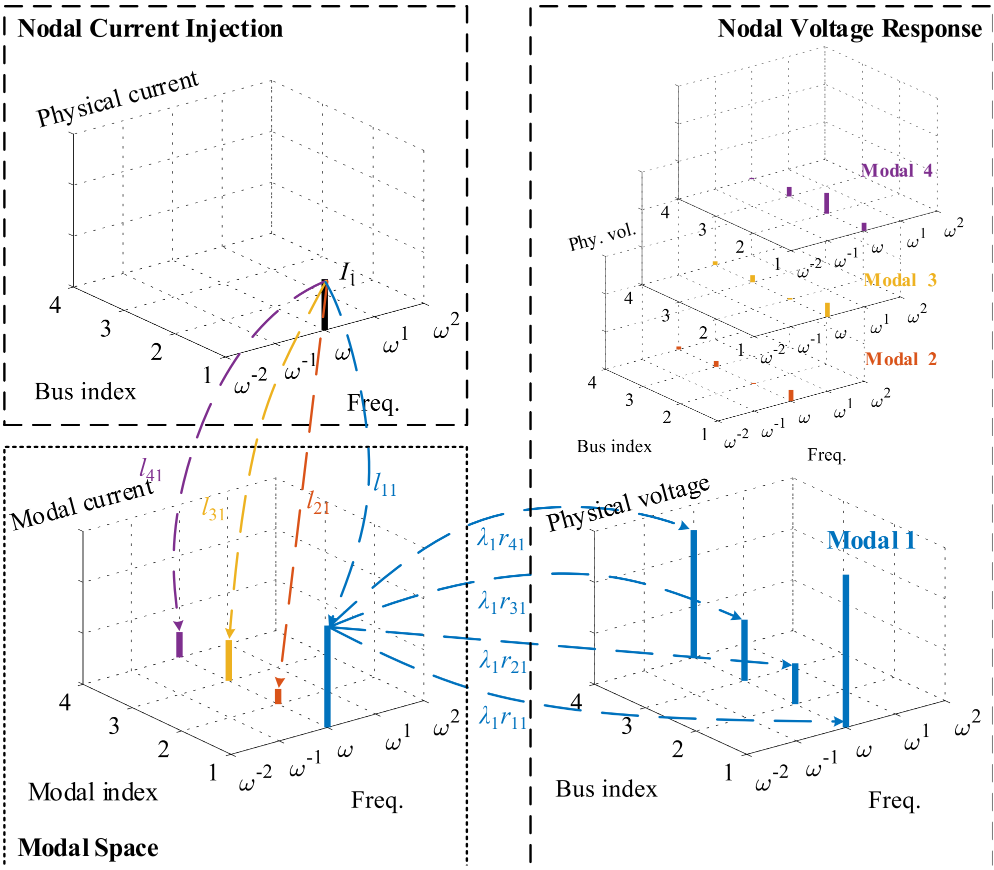

Figure 5.4: Basic principle of the conventional resonance mode analysis method

injection vector $\boldsymbol{I}(j\omega)$ has only one non-zero element at Bus 1, namely

$$\boldsymbol{I}(j\omega) = \begin{bmatrix} I_1 \\ 0 \\ 0 \\ 0 \end{bmatrix},$$

the corresponding nodal voltage response can be obtained following two steps. First, $\boldsymbol{L}(j\omega)$ projects $\boldsymbol{I}(j\omega)$ into the modal space, described by

$$\underbrace{\begin{bmatrix} J_1 \\ J_2 \\ J_3 \\ J_4 \end{bmatrix}}_{\boldsymbol{J}(j\omega)} = \underbrace{\begin{bmatrix} l_{11}(j\omega) & l_{12}(j\omega) & l_{13}(j\omega) & l_{14}(j\omega) \\ l_{21}(j\omega) & l_{22}(j\omega) & l_{23}(j\omega) & l_{24}(j\omega) \\ l_{31}(j\omega) & l_{32}(j\omega) & l_{33}(j\omega) & l_{34}(j\omega) \\ l_{41}(j\omega) & l_{42}(j\omega) & l_{43}(j\omega) & l_{44}(j\omega) \end{bmatrix}}_{\boldsymbol{L}(j\omega)} \underbrace{\begin{bmatrix} I_1 \\ 0 \\ 0 \\ 0 \end{bmatrix}}_{\boldsymbol{I}(j\omega)} = \begin{bmatrix} l_{11}I_1 \\ l_{21}I_1 \\ l_{31}I_1 \\ l_{41}I_1 \end{bmatrix} \tag{5.24}$$

where $l_{mn}(j\omega)$ characterizes the significance of the current injection at the nth bus to excite the mth modal current J_m.

Next, the physical nodal voltage response is given by the superposition of four modes

$$\begin{aligned}\boldsymbol{V}(j\omega) &= \underbrace{[\boldsymbol{r}_1(j\omega)\ \boldsymbol{r}_2(j\omega)\ \boldsymbol{r}_3(j\omega)\ \boldsymbol{r}_4(j\omega)]}_{\boldsymbol{R}(j\omega)} \underbrace{\begin{bmatrix} \lambda_1(j\omega) & & & \\ & \lambda_2(j\omega) & & \\ & & \lambda_3(j\omega) & \\ & & & \lambda_4(j\omega) \end{bmatrix}}_{\boldsymbol{\Lambda}(j\omega)} \underbrace{\begin{bmatrix} J_1 \\ J_2 \\ J_3 \\ J_4 \end{bmatrix}}_{\boldsymbol{J}(j\omega)} \\ &= \sum\nolimits_{m=1}^{4} \lambda_m(j\omega)\, \boldsymbol{r}_m(j\omega)\, J_m \end{aligned} \tag{5.25}$$

where $\boldsymbol{r}_m(j\omega)$ denotes the mth column of $\boldsymbol{R}(j\omega)$.

As shown in Figure 5.4, without loss of generality, it is assumed that λ_1 exhibits a resonance mode at the resonance frequency ω. Its magnitude is much larger than that of λ_2, λ_3 and λ_4. Then, the nodal voltage $\boldsymbol{V}(j\omega)$ can be approximated by

$$\underbrace{\begin{bmatrix} V_1 \\ V_2 \\ V_3 \\ V_4 \end{bmatrix}}_{\boldsymbol{V}(j\omega)} = \sum\nolimits_{m=1}^{4} \lambda_m(j\omega)\, \boldsymbol{r}_m(j\omega)\, J_m \approx \lambda_1(j\omega) \underbrace{\begin{bmatrix} r_{11}(j\omega) \\ r_{21}(j\omega) \\ r_{31}(j\omega) \\ r_{41}(j\omega) \end{bmatrix}}_{\boldsymbol{r}_1(j\omega)} J_1 \tag{5.26}$$

where $r_{nm}(j\omega)$, the nth element of $\boldsymbol{r}_m(j\omega)$, quantifies the observability of the mth modal voltage at the nth Bus. The excitability and observability are combined into the participation factor, which is the product of $l_{mn}(j\omega)$ and $r_{nm}(j\omega)$.

Recently, the influence of the grid-following converter is considered in [101, 102] by adding its equivalent impedance in the diagonal entries of $\boldsymbol{Y}(j\omega)$, yet the dynamic of the non-holomorphic control units of the VSC (e.g., PLL) is neglected, and only balanced operation conditions are considered.

5.3.2 LTP-Theory Based Generalized RMA method

Time-Periodic Impedance Matrix

To precisely investigate harmonic resonance characteristics of the system shown in Figure 5.3 considering also unbalanced conditions, the harmonic transfer matrices of the converter and the network derived in Section 5.2 should be used to build the admittance and impedance matrices, yielding

$$\boldsymbol{Z} = \boldsymbol{Y}^{-1} = \begin{bmatrix} \boldsymbol{Z}_{1O,1O} & \cdots & \boldsymbol{Z}_{1O,4O} & \boldsymbol{Z}_{1O,1C} & \cdots & \boldsymbol{Z}_{1O,4C} \\ \vdots & \ddots & \vdots & \vdots & \ddots & \vdots \\ \boldsymbol{Z}_{4O,1O} & \cdots & \boldsymbol{Z}_{4O,4O} & \boldsymbol{Z}_{4O,1C} & \cdots & \boldsymbol{Z}_{4O,4C} \\ \boldsymbol{Z}_{1C,1O} & \cdots & \boldsymbol{Z}_{1C,4O} & \boldsymbol{Z}_{1C,1C} & \cdots & \boldsymbol{Z}_{1C,4C} \\ \vdots & \ddots & \vdots & \vdots & \ddots & \vdots \\ \boldsymbol{Z}_{4C,1O} & \cdots & \boldsymbol{Z}_{4C,4O} & \boldsymbol{Z}_{4C,1C} & \cdots & \boldsymbol{Z}_{4C,4C} \end{bmatrix} \tag{5.27}$$

where the elementary impedance

$$\boldsymbol{Z}_{mO,nO} = \begin{bmatrix} \ddots & \vdots & \vdots & \vdots & \\ \cdots & Z_{mO,nO}^{-1,\,-1} & Z_{mO,nO}^{-1,\,0} & Z_{mO,nO}^{-1,\,1} & \cdots \\ \cdots & Z_{mO,nO}^{0,\,-1} & Z_{mO,nO}^{0,\,0} & Z_{mO,nO}^{0,\,1} & \cdots \\ \cdots & Z_{mO,nO}^{1,\,-1} & Z_{mO,nO}^{1,\,0} & Z_{mO,nO}^{1,\,1} & \cdots \\ & \vdots & \vdots & \vdots & \ddots \end{bmatrix} \tag{5.28}$$

quantifies the relation between the spectrum of the current injected at the nth bus

$$\boldsymbol{I}_n = \begin{bmatrix} \cdots & I_n^{-2} & I_n^{-1} & I_n^{0} & I_n^{1} & I_n^{2} & \cdots \end{bmatrix}^T$$

and that of the nodal voltage at the mth bus

$$\boldsymbol{V}_m = \begin{bmatrix} \cdots & V_m^{-2} & V_m^{-1} & V_m^{0} & V_m^{1} & V_m^{2} & \cdots \end{bmatrix}^T.$$

Specifically, $Z_{mO,nO}^{p,\,q}(j\omega)$ maps the current harmonic

$$I_n^q e^{j(\omega+q\omega_0)t}$$

to the voltage harmonic

$$V_m^p e^{j(\omega+p\omega_{\mathrm{n}})t}$$

by

$$V_m^p = I_n^q \cdot Z_{m\mathrm{O},n\mathrm{O}}^{p,\,q}(j\omega)\,. \tag{5.29}$$

The physical meaning of other entries in Eq. (5.27) is defined in the same way. For the sake of brevity, $j\omega$ for the description of frequency dependence is omitted.

Now, assume the current injected at each bus only contains the harmonic component at the frequency ω, namely

$$\begin{aligned} \boldsymbol{I}_1 &= \begin{bmatrix} \cdots & 0 & 0 & I_1^0 & 0 & 0 & \cdots \end{bmatrix}^T \\ \boldsymbol{I}_2 &= \begin{bmatrix} \cdots & 0 & 0 & I_2^0 & 0 & 0 & \cdots \end{bmatrix}^T \\ \boldsymbol{I}_3 &= \begin{bmatrix} \cdots & 0 & 0 & I_3^0 & 0 & 0 & \cdots \end{bmatrix}^T \\ \boldsymbol{I}_4 &= \begin{bmatrix} \cdots & 0 & 0 & I_4^0 & 0 & 0 & \cdots \end{bmatrix}^T. \end{aligned} \tag{5.30}$$

It gives that the infinite-dimensional nodal current injection vector

$$\boldsymbol{I} = [(\boldsymbol{I}_1)^T \quad (\boldsymbol{I}_2)^T \quad (\boldsymbol{I}_3)^T \quad (\boldsymbol{I}_4)^T \quad (\boldsymbol{I}_1^*)^T \quad (\boldsymbol{I}_2^*)^T \quad (\boldsymbol{I}_3^*)^T \quad (\boldsymbol{I}_4^*)^T]^T$$

has only eight non-zero terms, thus, $\boldsymbol{I}$ can be reduced to an eight-dimensional column vector

$$\boldsymbol{I} = \begin{bmatrix} I_1^0 & I_2^0 & I_3^0 & I_4^0 & \left(I_1^0\right)^* & \left(I_2^0\right)^* & \left(I_3^0\right)^* & \left(I_4^0\right)^* \end{bmatrix}^T.$$

Next, nodal voltage spectrum is determined by the central column of Eq. (5.28), yielding

$$\underbrace{\begin{bmatrix} \boldsymbol{V}_1 \\ \boldsymbol{V}_2 \\ \boldsymbol{V}_3 \\ \boldsymbol{V}_4 \\ \boldsymbol{V}_1^* \\ \boldsymbol{V}_2^* \\ \boldsymbol{V}_3^* \\ \boldsymbol{V}_4^* \end{bmatrix}}_{\boldsymbol{V}} = \begin{bmatrix} \vdots & \vdots & \vdots & \vdots & \vdots & \vdots & \vdots & \vdots \\ Z_{1O,1O}^{-1,\,0} & Z_{1O,2O}^{-1,\,0} & Z_{1O,3O}^{-1,\,0} & Z_{1O,4O}^{-1,\,0} & Z_{1O,1C}^{-1,\,0} & Z_{1O,2C}^{-1,\,0} & Z_{1O,3C}^{-1,\,0} & Z_{1O,4C}^{-1,\,0} \\ Z_{1O,1O}^{0,\,0} & Z_{1O,2O}^{0,\,0} & Z_{1O,3O}^{0,\,0} & Z_{1O,4O}^{0,\,0} & Z_{1O,1C}^{0,\,0} & Z_{1O,2C}^{0,\,0} & Z_{1O,3C}^{0,\,0} & Z_{1O,4C}^{0,\,0} \\ Z_{1O,1O}^{1,\,0} & Z_{1O,2O}^{1,\,0} & Z_{1O,3O}^{1,\,0} & Z_{1O,4O}^{1,\,0} & Z_{1O,1C}^{1,\,0} & Z_{1O,2C}^{1,\,0} & Z_{1O,3C}^{1,\,0} & Z_{1O,4C}^{1,\,0} \\ \vdots & \vdots & \vdots & \vdots & \vdots & \vdots & \vdots & \vdots \\ \vdots & \vdots & \vdots & \vdots & \vdots & \vdots & \vdots & \vdots \\ Z_{4C,1O}^{-1,\,0} & Z_{4C,2O}^{-1,\,0} & Z_{4C,3O}^{-1,\,0} & Z_{4C,4O}^{-1,\,0} & Z_{4C,1C}^{-1,\,0} & Z_{4C,2C}^{-1,\,0} & Z_{4C,3C}^{-1,\,0} & Z_{4C,4C}^{-1,\,0} \\ Z_{4C,1O}^{0,\,0} & Z_{4C,2O}^{0,\,0} & Z_{4C,3O}^{0,\,0} & Z_{4C,4O}^{0,\,0} & Z_{4C,1C}^{0,\,0} & Z_{4C,2C}^{0,\,0} & Z_{4C,3C}^{0,\,0} & Z_{4C,4C}^{0,\,0} \\ Z_{4C,1O}^{1,\,0} & Z_{4C,2O}^{1,\,0} & Z_{4C,3O}^{1,\,0} & Z_{4C,4O}^{1,\,0} & Z_{4C,1C}^{1,\,0} & Z_{4C,2C}^{1,\,0} & Z_{4C,3C}^{1,\,0} & Z_{4C,4C}^{1,\,0} \\ \vdots & \vdots & \vdots & \vdots & \vdots & \vdots & \vdots & \vdots \end{bmatrix} \underbrace{\begin{bmatrix} I_1^0 \\ I_2^0 \\ I_3^0 \\ I_4^0 \\ \left(I_1^0\right)^* \\ \left(I_2^0\right)^* \\ \left(I_3^0\right)^* \\ \left(I_4^0\right)^* \end{bmatrix}}_{\boldsymbol{I}}. \tag{5.31}$$

The impedance matrix in Eq. (5.31) has eight columns and theoretically an infinite number of rows. The eigenvalues of the matrix are not defined. However, if the frequency coupling effect is described in the time domain, Eq. (5.29) becomes

$$V_m^p e^{j(\omega+p\omega_0)t} = I_n^q e^{j(\omega+q\omega_0)t} \cdot Z_{mO,nO}^{p,\,q}\left(j\omega\right) e^{j(p-q)\omega_0 t}.$$

By treating the entries in each column of the impedance matrix in Eq. (5.31) as Fourier series coefficients, the time-domain nodal voltage can be derived as

$$\begin{aligned} \boldsymbol{v}\left(t\right) &= \boldsymbol{Z}\left(j\omega t\right)\boldsymbol{i}\left(t\right) \\ \boldsymbol{v}\left(t\right) &= \left[v_1\left(t\right) \;\; v_2\left(t\right) \;\; v_3\left(t\right) \;\; v_4\left(t\right) \;\; v_1^*\left(t\right) \;\; v_2^*\left(t\right) \;\; v_3^*\left(t\right) \;\; v_4^*\left(t\right)\right]^T \\ \boldsymbol{i}\left(t\right) &= \left[I_1^0 e^{j\omega t} \;\; I_2^0 e^{j\omega t} \;\; I_3^0 e^{j\omega t} \;\; I_4^0 e^{j\omega t} \;\; \left(I_1^0\right)^* e^{-j\omega t} \;\; \left(I_2^0\right)^* e^{-j\omega t} \left(I_3^0\right)^* e^{-j\omega t} \;\; \left(I_4^0\right)^* e^{-j\omega t}\right]^T \\ \boldsymbol{Z}\left(j\omega t\right) &= \begin{bmatrix} \boldsymbol{Z}_{OO}\left(j\omega t\right) & \boldsymbol{Z}_{OC}\left(-j\omega t\right) \\ \boldsymbol{Z}_{CO}\left(j\omega t\right) & \boldsymbol{Z}_{CC}\left(-j\omega t\right) \end{bmatrix}^{8\times 8} \end{aligned} \tag{5.32}$$

where

$$\boldsymbol{Z}_{OO}\left(j\omega t\right) = \begin{bmatrix} Z_{1O,1O}\left(j\omega t\right) & Z_{1O,2O}\left(j\omega t\right) & Z_{1O,3O}\left(j\omega t\right) & Z_{1O,4O}\left(j\omega t\right) \\ Z_{2O,1O}\left(j\omega t\right) & Z_{2O,2O}\left(j\omega t\right) & Z_{2O,3O}\left(j\omega t\right) & Z_{2O,4O}\left(j\omega t\right) \\ Z_{3O,1O}\left(j\omega t\right) & Z_{3O,2O}\left(j\omega t\right) & Z_{3O,3O}\left(j\omega t\right) & Z_{3O,4O}\left(j\omega t\right) \\ Z_{4O,1O}\left(j\omega t\right) & Z_{4O,2O}\left(j\omega t\right) & Z_{4O,3O}\left(j\omega t\right) & Z_{4O,4O}\left(j\omega t\right) \end{bmatrix}$$

$$\boldsymbol{Z}_{OC}\left(-j\omega t\right) = \begin{bmatrix} Z_{1O,1C}\left(-j\omega t\right) & Z_{1O,2C}\left(-j\omega t\right) & Z_{1O,3C}\left(-j\omega t\right) & Z_{1O,4C}\left(-j\omega t\right) \\ Z_{2O,1C}\left(-j\omega t\right) & Z_{2O,2C}\left(-j\omega t\right) & Z_{2O,3C}\left(-j\omega t\right) & Z_{2O,4C}\left(-j\omega t\right) \\ Z_{3O,1C}\left(-j\omega t\right) & Z_{3O,2C}\left(-j\omega t\right) & Z_{3O,3C}\left(-j\omega t\right) & Z_{3O,4C}\left(-j\omega t\right) \\ Z_{4O,1C}\left(-j\omega t\right) & Z_{4O,2C}\left(-j\omega t\right) & Z_{4O,3C}\left(-j\omega t\right) & Z_{4O,4C}\left(-j\omega t\right) \end{bmatrix}$$

are time-periodic matrices with

$$\begin{aligned} Z_{mO,nO}\left(j\omega t\right) &= \textstyle\sum_{p=-\infty}^{\infty} Z_{mO,nO}^{p,\,0}\left(j\omega\right) e^{jp\omega_0 t} \\ Z_{mO,nC}\left(-j\omega t\right) &= \textstyle\sum_{p=-\infty}^{\infty} Z_{mO,nC}^{p,\,0}\left(-j\omega\right) e^{jp\omega_0 t}. \end{aligned}$$

Generalized Resonance Mode Analysis

If the harmonic current at ω is only injected into Bus 1, the nodal voltage response is obtained from Eq. (5.32)

$$\begin{bmatrix} v_1(t) \\ v_2(t) \\ v_3(t) \\ v_4(t) \end{bmatrix} = \boldsymbol{Z}_{OO}(j\omega t) \begin{bmatrix} I_1^0 e^{j\omega t} \\ 0 \\ 0 \\ 0 \end{bmatrix} + \boldsymbol{Z}_{OC}(-j\omega t) \begin{bmatrix} \left(I_1^0\right)^* e^{-j\omega t} \\ 0 \\ 0 \\ 0 \end{bmatrix}. \tag{5.33}$$

Taking $\boldsymbol{Z}_{OO}(j\omega t)$ as an example, according to Eq. (4.25), it has the eigen decomposition

$$\begin{aligned} \boldsymbol{Z}_{OO}(j\omega t) &= \left(\boldsymbol{R}_{OO}(j\omega t)\,\boldsymbol{\Lambda}_{OO}(j\omega) + \dot{\boldsymbol{R}}_{OO}(j\omega t)\right)\boldsymbol{L}_{OO}(j\omega t) \\ \boldsymbol{L}_{OO}(j\omega t) &= \boldsymbol{R}_{OO}^{-1}(j\omega t) \end{aligned} \tag{5.34}$$

where the LTP eigenvalue/mode matrix

$$\boldsymbol{\Lambda}_{OO}(j\omega) = \begin{bmatrix} \lambda_{OO,1}(j\omega) & & & \\ & \lambda_{OO,2}(j\omega) & & \\ & & \lambda_{OO,3}(j\omega) & \\ & & & \lambda_{OO,4}(j\omega) \end{bmatrix}$$

is a constant diagonal matrix. The corresponding LTP eigenvector matrix and its inverse, namely

$$\begin{aligned} \boldsymbol{R}_{OO}(j\omega t) &= \begin{bmatrix} \boldsymbol{r}_{OO,1}(j\omega t) & \boldsymbol{r}_{OO,2}(j\omega t) & \boldsymbol{r}_{OO,3}(j\omega t) & \boldsymbol{r}_{OO,4}(j\omega t) \end{bmatrix} \\ &= \begin{bmatrix} r_{1O,1O}(j\omega t) & r_{1O,2O}(j\omega t) & r_{1O,3O}(j\omega t) & r_{1O,4O}(j\omega t) \\ r_{2O,1O}(j\omega t) & r_{2O,2O}(j\omega t) & r_{2O,3O}(j\omega t) & r_{2O,4O}(j\omega t) \\ r_{3O,1O}(j\omega t) & r_{3O,2O}(j\omega t) & r_{3O,3O}(j\omega t) & r_{3O,4O}(j\omega t) \\ r_{4O,1O}(j\omega t) & r_{4O,2O}(j\omega t) & r_{4O,3O}(j\omega t) & r_{4O,4O}(j\omega t) \end{bmatrix} \end{aligned}$$

and

$$\begin{aligned} \boldsymbol{L}_{OO}(j\omega t) &= \begin{bmatrix} \boldsymbol{l}_{OO,1}(j\omega t) \\ \boldsymbol{l}_{OO,2}(j\omega t) \\ \boldsymbol{l}_{OO,3}(j\omega t) \\ \boldsymbol{l}_{OO,4}(j\omega t) \end{bmatrix} \\ &= \begin{bmatrix} l_{1O,1O}(j\omega t) & l_{1O,2O}(j\omega t) & l_{1O,3O}(j\omega t) & l_{1O,4O}(j\omega t) \\ l_{2O,1O}(j\omega t) & l_{2O,2O}(j\omega t) & l_{2O,3O}(j\omega t) & l_{2O,4O}(j\omega t) \\ l_{3O,1O}(j\omega t) & l_{3O,2O}(j\omega t) & l_{3O,3O}(j\omega t) & l_{3O,4O}(j\omega t) \\ l_{4O,1O}(j\omega t) & l_{4O,2O}(j\omega t) & l_{4O,3O}(j\omega t) & l_{4O,4O}(j\omega t) \end{bmatrix}, \end{aligned}$$

are time periodic.

As shown in Figure 5.5, $l_{mO,1O}(j\omega t) = \sum_p l_{mO,1O}^p e^{jp\omega_0 t}$, the element in the mth row and 1st column of $\boldsymbol{L}_{OO}(j\omega t)$, projects $I_1^0 e^{j\omega t}$ into the modal currents $J_m(t)$ containing multiple

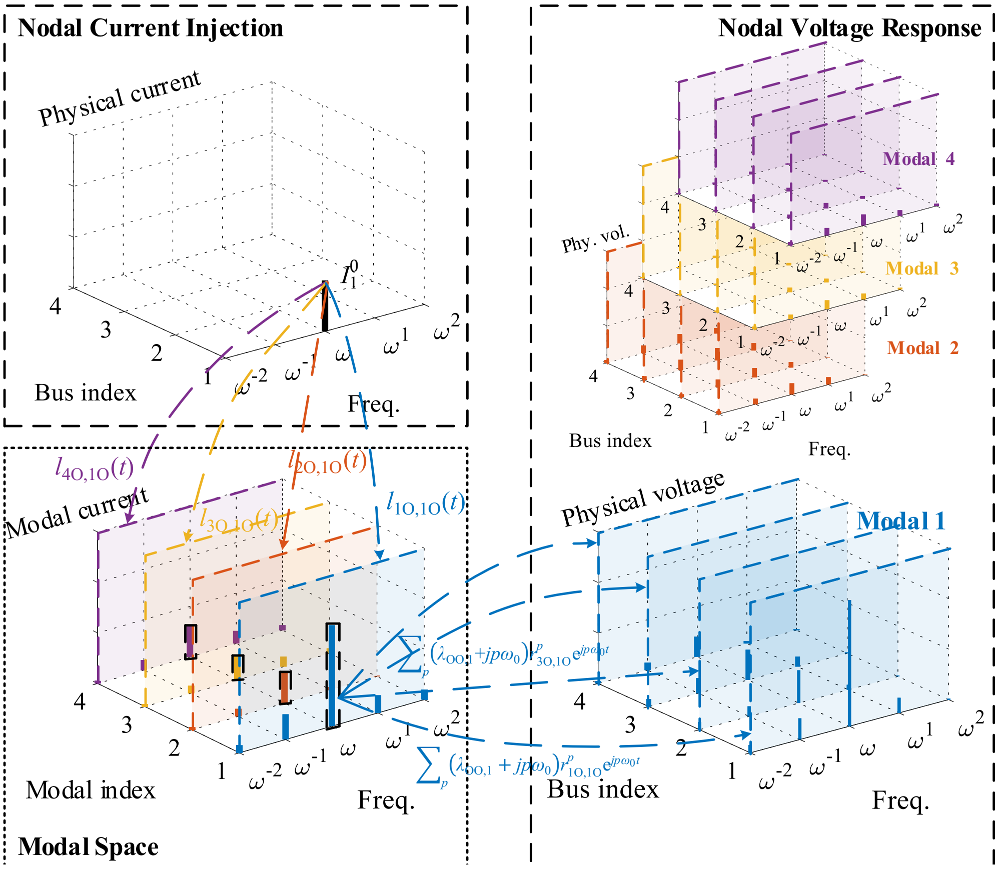

Figure 5.5: Basic principle of the LTP theory-based generalized resonance mode analysis method

harmonics, given by

$$\boldsymbol{J}\left(j\omega t\right)=\begin{bmatrix} J_1\left(t\right) \\ J_2\left(t\right) \\ J_3\left(t\right) \\ J_4\left(t\right) \end{bmatrix}=\begin{bmatrix} \sum_p J_1^p e^{j(\omega+p\omega_0)t} \\ \sum_p J_2^p e^{j(\omega+p\omega_0)t} \\ \sum_p J_3^p e^{j(\omega+p\omega_0)t} \\ \sum_p J_4^p e^{j(\omega+p\omega_0)t} \end{bmatrix}=I_1^0 e^{j\omega t}\begin{bmatrix} \sum_p l_{1O,1O}^p e^{jp\omega_0 t} \\ \sum_p l_{2O,1O}^p e^{jp\omega_0 t} \\ \sum_p l_{3O,1O}^p e^{jp\omega_0 t} \\ \sum_p l_{4O,1O}^p e^{jp\omega_0 t} \end{bmatrix}. \tag{5.35}$$

For modal currents at ω (also applies to other frequencies), namely

$$\boldsymbol{J}\left(j\omega t\right)=\begin{bmatrix} J_1^0 e^{j\omega t} & J_2^0 e^{j\omega t} & J_3^0 e^{j\omega t} & J_4^0 e^{j\omega t} \end{bmatrix}^T$$

the corresponding nodal voltage response is given by the superposition of four LTP modes

$$\begin{aligned}\begin{bmatrix} v_1\left(t\right) \\ v_2\left(t\right) \\ v_3\left(t\right) \\ v_4\left(t\right) \end{bmatrix}&=\left(\boldsymbol{R}_{OO}\left(j\omega t\right)\boldsymbol{\Lambda}_{OO}\left(j\omega\right)+\dot{\boldsymbol{R}}_{OO}\left(j\omega t\right)\right)\boldsymbol{J}\left(j\omega t\right) \\ &=\sum\nolimits_{m=1}^{4}\left(\lambda_{OO,m}\left(j\omega\right)\boldsymbol{r}_{OO,m}\left(j\omega t\right)+\dot{\boldsymbol{r}}_{OO,m}\left(j\omega t\right)\right)J_m^0 e^{j\omega t}\end{aligned} \tag{5.36}$$

where $\boldsymbol{r}_{OO,m}(j\omega t)$ denotes the mth column of $\boldsymbol{R}_{OO}(j\omega t)$. Inserting the Fourier series expansion of $\boldsymbol{r}_{OO,m}(j\omega t)$, Eq. (5.36) becomes

$$\begin{bmatrix} v_1(t) \\ v_2(t) \\ v_3(t) \\ v_4(t) \end{bmatrix} = \begin{pmatrix} J_1^0 e^{j\omega t} \sum_p \left(\lambda_{OO,1}(j\omega) + jp\omega_0\right) \boldsymbol{r}_{OO,1}^p e^{jp\omega_0 t} \\ +J_2^0 e^{j\omega t} \sum_p \left(\lambda_{OO,2}(j\omega) + jp\omega_0\right) \boldsymbol{r}_{OO,2}^p e^{jp\omega_0 t} \\ +J_3^0 e^{j\omega t} \sum_p \left(\lambda_{OO,3}(j\omega) + jp\omega_0\right) \boldsymbol{r}_{OO,3}^p e^{jp\omega_0 t} \\ +J_4^0 e^{j\omega t} \sum_p \left(\lambda_{OO,4}(j\omega) + jp\omega_0\right) \boldsymbol{r}_{OO,4}^p e^{jp\omega_0 t} \end{pmatrix} \tag{5.37}$$

where $\boldsymbol{r}_{OO,m}^p$ is the pth order Fourier coefficient of $\boldsymbol{r}_{OO,m}(j\omega t)$. Comparing Eq. (5.35) and (5.37) with Eq. (5.24) and (5.25), it is seen that $l_{mO,nO}(j\omega t)$ and $r_{nO,mO}(j\omega t)$ characterize the excitability and observability of the mth LTP mode at the nth bus, where $r_{nO,mO}(j\omega t)$ is the nth element of $\boldsymbol{r}_{OO,m}(j\omega t)$.

The generalization of the resonance mode definition for the LTP system is not straightforward, since each LTP mode is associated with a group of multipliers, for instance, $\{\lambda_{OO,m}(j\omega) + jp\omega_0,\ p \in \mathbb{Z}\}$ is related to the mth LTP mode. Inspired by following two facts:

1. the definition of LTP resonance mode should be compatible with LTI systems.
2. $\boldsymbol{r}_{OO,m}^p$ decreases to zero as p approaches infinity.

the mth LTP modal impedance is defined as

$$\lambda_m(j\omega) \triangleq \max\left\{ \frac{\left|\boldsymbol{r}_{OO,m}^p\right|_1}{\left|\boldsymbol{r}_{OO,m}^0\right|_1} \cdot \left|\lambda_{OO,m}(j\omega) + jp\omega_0\right|,\ \ p \in \mathbb{Z} \right\}. \tag{5.38}$$

The LTP resonance mode is accordingly defined as the peak of LTP modal impedances. For the test system, it is found $\lambda_m(j\omega) = |\lambda_{OO,m}(j\omega)|$. In Figure 5.5, it is assumed that λ_1 exhibits a peak value (i.e., an LTP resonance mode) at ω, and it is much larger than λ_2, λ_3 and λ_4.

Similarly, the other impedance matrix $\boldsymbol{Z}_{OC}(-j\omega t)$ in Eq. (5.33) has also the eigen decomposition with LTP eigenvalue and eigenvector matrices, i.e., $\boldsymbol{\Lambda}_{OC}(j\omega)$, $\boldsymbol{R}_{OC}(-j\omega t)$ and $\boldsymbol{L}_{OC}(-j\omega t)$. It can be expected that the coupling of original and conjugate coordinates caused by the non-holomorphic control or unbalanced physical components may introduce new LTP resonance modes, indicated by the LTP resonance mode of $\boldsymbol{Z}_{OC}(-j\omega t)$.

Sensitivity Analysis

To detect the affected area and the most involved buses of a particular resonance mode, the participation factor analysis can be used. According to previous analysis, $l_{mO,nO}(j\omega t)$ and $r_{nO,mO}(j\omega t)$ characterize the excitability and observability of mode m of $\boldsymbol{Z}_{OO}(j\omega t)$ at Bus n. Similarly, $l_{mO,nC}(-j\omega t)$ and $r_{nO,mC}(-j\omega t)$ characterize the excitability and observability of the mth mode of $\boldsymbol{Z}_{OC}(-j\omega t)$ at the nth bus. Then, participation factors of the mth mode of

$\boldsymbol{Z}_{OO}(j\omega t)$ and $\boldsymbol{Z}_{OC}(-j\omega t)$ at the nth bus are defined as

$$\begin{aligned} PF_{nO,mO} &= \frac{\left\| l_{mO,nO}\left(j\omega t\right) \cdot r_{nO,mO}\left(j\omega t\right) \right\|_1}{\sum_{b=1}^{4} \left\| l_{mO,bO}\left(j\omega t\right) \cdot r_{bO,mO}\left(j\omega t\right) \right\|_1} \\ PF_{nO,mC} &= \frac{\left\| l_{mO,nC}\left(j\omega t\right) \cdot r_{nO,mC}\left(j\omega t\right) \right\|_1}{\sum_{b=1}^{4} \left\| l_{mO,bC}\left(j\omega t\right) \cdot r_{bO,mC}\left(j\omega t\right) \right\|_1} \end{aligned}. \tag{5.39}$$

Generally, the larger the participation factor of a bus is, the greater the risk of resonance.

Harmonic resonance results from the energy exchange between capacitive and inductive elements. Thus, all parameter changes that influence the system admittance or impedance will affect the system resonance characteristics. Sensitivity analysis is a useful tool to determine the impact of a network component or a converter control parameter on the resonance frequency and the resonance mode. In this paper, a local sensitivity analysis method, one-at-a-time (OAT) [117], is used, since it is easy to implement and requires relatively low computational effort. In the OAT method, the individual system parameter x_i is varied in the vicinity of its nominal value X_i, and the corresponding sensitivity is defined as the ratio of the relative variation of the output y to the percentage change of x_i, given by

$$S_i = (X_i/y) \cdot (\partial y/\partial x_i) \tag{5.40}$$

where y stands for the resonance frequency and the resonance mode, while x_i is the network parameter and the converter control parameter.

5.4 Case Study

In this section, the proposed generalized resonance mode analysis method is tested and validated using the three-converter system shown in Figure 5.3. The converter and network parameters are listed in Table 5.2 and Table 5.3. The model is implemented in MATLAB/Simulink and simulated with the real-time simulator OP5600. Parallel harmonic resonance studies are carried out based on the generalized resonance mode analysis method. The accuracy of the analytical admittance/impedance model and the effectiveness of the generalized resonance mode analysis method are validated by frequency sweep simulation results.

Table 5.2: Parameters of the Converters

Symbol	Description	VSC 1	VSC 2	VSC 3
L / R	Converter-side filter inductance	5.6 mH / 0.1 Ω	5.6 mH / 0.1 Ω	7 mH / 0.1 Ω
C	Filter capacitor	16 μF	16 μF	30 μF
BW	Bandwidth of the DSRF-PLL		25 Hz	
τ	Time constant of the current controller		1 ms	
S_r	Power reference	2 kW	2 kW	3 kW
L_g / R_g	Grid-side filter inductor	1.5 mH / 1 mΩ	1 mH / 1 mΩ	1.5 mH / 1 mΩ

The network is first assumed to be balanced. The results of the generalized resonance mode analysis are shown in Figure 5.6. No critical resonance modes are introduced by $\boldsymbol{Z}_{OC}(-j\omega t)$ under this test scenario, thus, they are omitted. In the conventional analysis, the resonance

Table 5.3: Parameter of the Network

Symbol	Description	Value
y_1	Line impedance between Bus 1 and the stiff grid	$1\ \text{mH} + 1\ \text{m}\Omega$
y_{12}	Line impedance between Bus 1 and Bus 2	
y_{13}	Line impedance between Bus 1 and Bus 3	$0.5\ \text{mH} + 1\ \text{m}\Omega$
y_{14}	Line impedance between Bus 1 and Bus 4	

frequency and modal impedance of positive and negative sequence components are the same. However, it is noted in Figure 5.6 that the negative sequence component has smaller resonance frequencies and larger modal impedances, which is caused by the non-holomorphic control units of the grid-following converters. This effect becomes more obvious as the line impedance L_{line1} increases from 1 mH to 2 mH, where the resonance frequency approaches the bandwidth of the PLL. Another observation is that an additional resonance peak at 96 Hz is introduced by the larger grid impedance. This resonance mode is strongly linked to system stability, which has been intensively studied in Chapter 4. The focus of this chapter is the system steady-state resonance behavior in a higher frequency range.

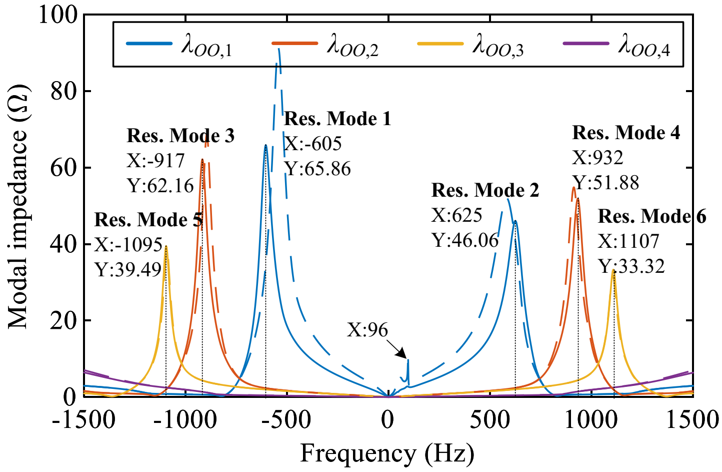

Figure 5.6: Modal impedances of the test system for different grid impedances. Solid lines: $L_{line1} = 1\,\text{mH}$. Dashed lines: $L_{line1} = 2\,\text{mH}$.

Application of the Generalized RMA Method

Following the definition given by Eq. (5.39), the participation factor calculation results are listed in Table 5.4. It can be concluded that all buses are involved in the resonance mode 1 and 2, while the key participating buses for resonance mode 3 and 4 are Bus 1, 2 and 3. Moreover, resonance mode 5 and 6 are mainly related to Bus 3. The participation factor analysis results can be validated by the frequency sweep method: injecting a current disturbance at each bus and checking whether the corresponding nodal voltage resonances appear.

In fact, the voltage response information is stored in the analytical impedance matrices $\boldsymbol{Z}_{OO}(j\omega t)$ and $\boldsymbol{Z}_{OC}(-j\omega t)$, as discussed in Section 5.3.2. Specifically, assume the current disturbance is injected at Bus 2, Figure 5.7 shows the magnitude of the impedances in $\boldsymbol{Z}_{OO}(j\omega t)$ from Bus 2 to all the buses. Here, solid lines denote the analytical results, and the crosses denote frequency sweep simulation results. For instance, $Z_{1O,\,2O}^{0,\,0}(j\omega)$ maps the current disturbance

$I_2^0 e^{j\omega t}$ at Bus 2 to the voltage response $V_1^0 e^{j\omega t}$ at Bus 1. Additionally, $\boldsymbol{Z}_{OC}(-j\omega t)$ also contains non-zero terms, $Z^{2,\,0}_{mO,\,2C}(-j\omega)$, which maps $(I_2^0)^* e^{-j\omega t}$ at Bus 2 to $V_m^2 e^{j(-\omega+2\omega_0)t}$ at Bus m. The maximum magnitude of $Z^{2,\,0}_{mO,\,2C}(-j\omega)$ is smaller than $3\,\Omega$, thus, they are ignored here. It can be observed from Figure 5.7 that all four impedances exhibit peak values at the resonance frequencies of resonance mode 1 and 2, which means that these resonances can be easily excited and observed at Bus 2. Furthermore, among the four impedances, $Z^{0,\,0}_{4O,\,2O}(j\omega)$ has the largest values at - 605 and 625 Hz, namely the corresponding observability at Bus 4 is stronger, which is consistent with the result in Table 5.4 that Bus 4 has a larger participation factor for resonance mode 1 and 2 (0.3825 and 0.3886). Similarly, it is seen that resonance mode 3 and 4 can also be easily excited at Bus 2, which indicate the resonance modes observability, share the same order of participation factors. As for resonance mode 5 and 6, all impedances are comparably small, which means it is difficult to excite and observe resonance mode 5 and 6 at Bus 2. Nevertheless, the stronger participation of Bus 3 can still be confirmed by the fact that $Z^{0,\,0}_{3O,\,2O}(j\omega)$ is much larger than the other three impedances at -1095 and 1107 Hz.

Table 5.4: Participation Factor Analysis Results under Symmetric Condition

Resonance Mode	**Frequency (Hz)**	**Participation Factor of each Bus**			
		1	**2**	**3**	**4**
1	-605	**0.1938**	**0.2124**	**0.2119**	**0.3825**
2	625	**0.1938**	**0.2096**	**0.2096**	**0.3886**
3	-917	**0.1676**	**0.4719**	**0.3335**	0.0281
4	932	**0.1689**	**0.4670**	**0.3352**	0.0306
5	-1095	0.0721	0.0319	**0.8831**	0.0251
6	1107	0.0735	0.0329	**0.8853**	0.0258

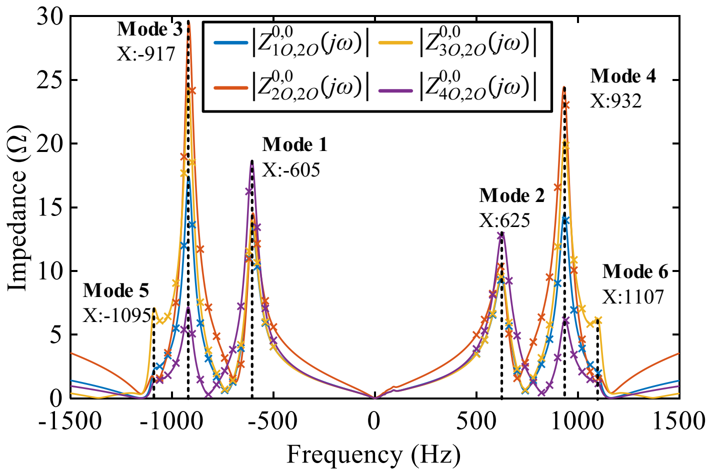

Figure 5.7: Impedances from Bus 2 to all the buses. Solid lines: analytical results. Crosses: frequency sweep results.

Influence of the Grid Imbalance

In this subsection, the influence of the grid imbalance is investigated by considering the following two cases:

- unbalanced grid voltage containing negative sequence component.
- unbalanced three-phase grid impedance.

First, the effect of the unbalanced grid voltage is investigated by sweeping the unbalance ratio $D = V_{-}/V_{+}$, where V_{-} and V_{+} represent the magnitude of the negative and positive sequence components of the grid voltage. Figure 5.8 shows the movement of the modal impedance for different values of D. It is identified that the grid voltage imbalance has only a small impact in the frequency range below 150 Hz, while the resonance frequency and modal impedance at higher frequencies are immune to the appearance of the negative sequence grid voltage.

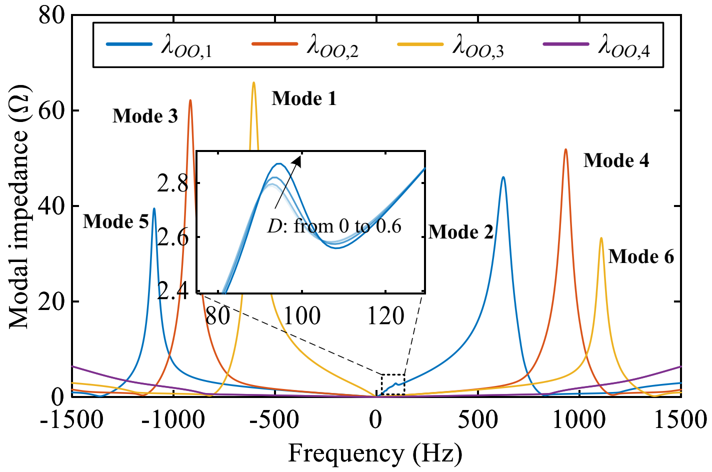

Figure 5.8: Modal impedances for different unbalance ratios D

Then, the grid imbalance is introduced by modifying the impedance L_{line1} ($L_a = 3\,\mathrm{mH}$, $L_b = L_c = 1\,\mathrm{mH}$). Applying the generalized resonance mode analysis method, the modal impedance of $\boldsymbol{Z}_{OO}(j\omega t)$ and $\boldsymbol{Z}_{OC}(-j\omega t)$ are shown in Figure 5.9. Compared to Figure 5.6, it can be observed that, among the first six resonance modes, resonance mode 5 and 6 are almost unaffected, while the resonance frequency and modal impedance of other modes decrease to varying degrees. Additionally, an extra resonance mode (resonance mode 7) at 535 Hz appears. Meanwhile, one modal impedance of $\boldsymbol{Z}_{OC}(-j\omega t)$ becomes critical and exhibits peak values at ±556 and ±908 Hz, i.e., resonance mode 8, 9, 10 and 11. According to Eq. (5.32), the resonance mode associated with $\boldsymbol{Z}_{OC}(-j\omega t)$ indicates that the current injection $I_n^0 e^{j\omega t}$ at the nth bus will excite voltage resonances $\left\{V_m^p e^{j(-\omega+p\omega_0)t},\ p \in \mathbb{Z}\right\}$ at the mth bus, and the relation is quantified by the entries of $\boldsymbol{Z}_{OC}(-j\omega t)$, for instance, $V_m^p = Z_{mO,nC}^{p,0}(-j\omega)\left(I_n^0\right)^*$.

The participation factor calculation results are listed in Table 5.5. As for the newly introduced resonance modes, it is identified that all the buses are involved in resonance mode 7, 8 and 9, while Bus 4 is excluded from resonance mode 10 and 11. Similarly, the impedance matrices $\boldsymbol{Z}_{OO}(j\omega t)$ and $\boldsymbol{Z}_{OC}(-j\omega t)$ are used to validate the participation factor analysis results, as shown in Figure 5.10. The comparison between the impedances from Bus 2 to all

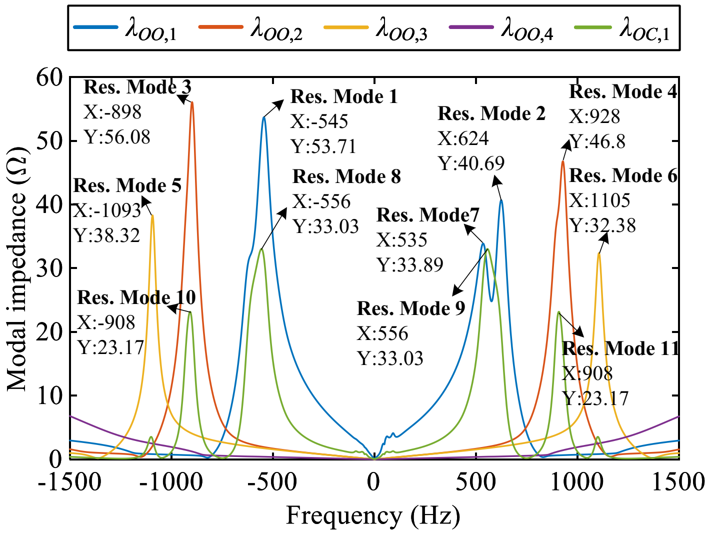

Figure 5.9: Modal impedances under unbalanced grid impedance condition

Table 5.5: Participation Factor Analysis Results under unbalanced Condition

Resonance Mode	Frequency (Hz)	Participation Factor of each Bus 1	2	3	4
1	-545	**0.2175**	**0.2293**	**0.2294**	**0.3249**
2	624	**0.2011**	**0.2102**	**0.2102**	**0.3806**
3	-898	**0.1829**	**0.4491**	**0.3442**	0.0249
4	928	**0.1776**	**0.4571**	**0.3362**	0.0307
5	-1093	0.0759	0.0381	**0.8737**	0.0263
6	1105	0.0769	0.0393	**0.8767**	0.027
7	535	**0.223**	**0.2328**	**0.2333**	**0.3121**
8	-556	**0.222**	**0.2275**	**0.2277**	**0.3243**
9	556	**0.222**	**0.2275**	**0.2277**	**0.3243**
10	-908	**0.1869**	**0.4452**	**0.344**	0.0273
11	908	**0.1869**	**0.4452**	**0.344**	0.0273

the buses at the resonance frequency of each resonance mode confirms the bus participation information given in Table 5.5. Again, the agreement between analytical results (solid lines) and frequency sweep simulation results (crosses) in Figure 5.10 confirms the accuracy and effectiveness of the proposed methodology. To give an intuitive illustration of the frequency coupling effect, one of the frequency sweep simulation results is shown in Figure 5.11: 1 A (0.1 pu) negative-sequence current disturbance at 550 Hz (−11 pu) is injected at Bus 2, the corresponding steady-state voltage responses at each bus are shown in Figure 5.11. As expected, the nodal voltage at each bus contains harmonic components at ±650, ±550 and ±450 Hz. The impedances obtained from the bus voltages and the injected current agree well with the analytical results.

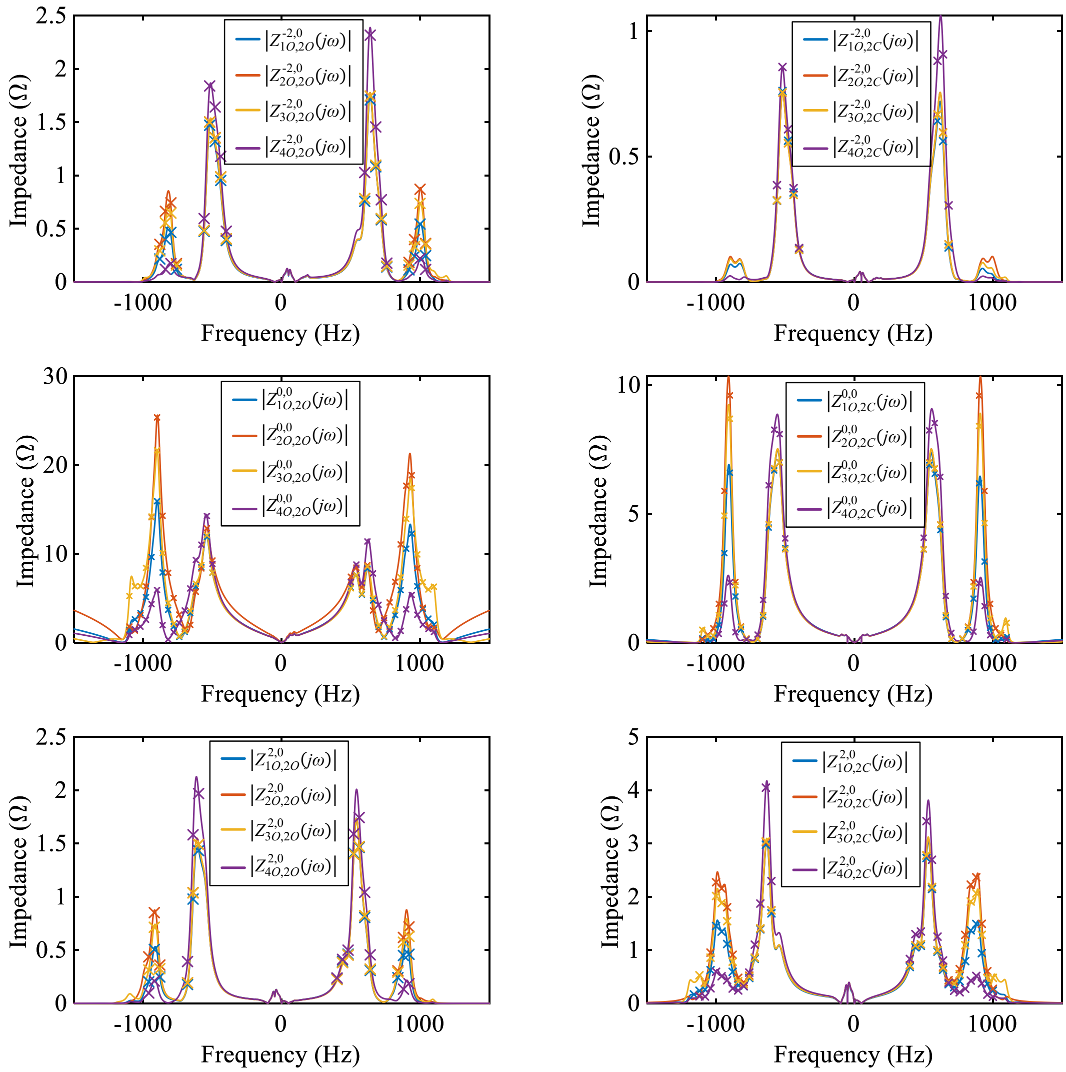

Figure 5.10: Impedances from Bus 2 to all the buses under the unbalanced grid impedance condition. Solid lines: analytical results. Crosses: frequency sweep results.

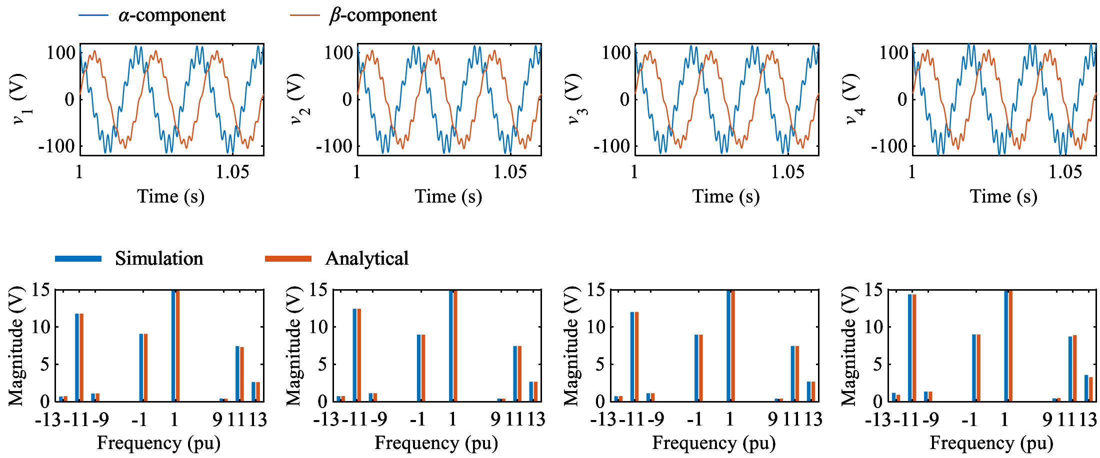

Figure 5.11: Voltage responses at each bus to a 1 A 550 Hz negative-sequence current disturbance at Bus 2. Top: Steady-state time domain waveforms. Bottom: Comparison between the frequency spectrums of the simulation and analytical results.

Sensitivity Analysis

The above presented results indicate that the generalized resonance mode analysis method is a useful tool to identify the resonance frequencies of a converter-dominated grid, considering balanced and unbalanced operation conditions. The proposed participation factor analysis can further characterize the excitability and observability of the individual resonance mode. In this section, the OAT method is used to assess the impact of system parameters on each resonance mode and the corresponding resonance frequency. The sensitivity indices of following parameters are evaluated:

1. Physical Components: line impedances $L_{line\ i}$ and LCL filter of each VSC L_{1i}, C_i, L_{2i};

2. Control Parameters: Time constant of the converter's current controller τ_i and the designed bandwidth (BW_i) of the DSRF-PLL.

The index i stands for the ith line or converter.

Taking the unbalanced line impedance $L_{line1} = \{L_a = 3\,\text{mH}, L_b = L_c = 1\,\text{mH}\}$ as an example, the value of L_a is swept in the range of [90%, 110%] of 3 mH, and the movement of the modal impedances is shown in Figure 5.12. Then, the impact of L_a on each resonance is quantified by the resonance frequency and the resonance mode sensitivity indices, S_f and S_λ, as shown in Figure 5.13. All resonance frequency indices S_f indicate negative values, which means the resonance modes move towards lower frequencies as L_a increases. Another observation is that the resonance modes resulting from $\boldsymbol{Z}_{OC}(-j\omega t)$, that is, resonance mode 8, 9, 10 and 11, are highly sensitive to L_a, and enlarge as the grid imbalance becomes more severe. Meanwhile, large L_a can damp resonance mode 1, 3 and 4 to some extent, since their sensitivity indices S_λ are negative.

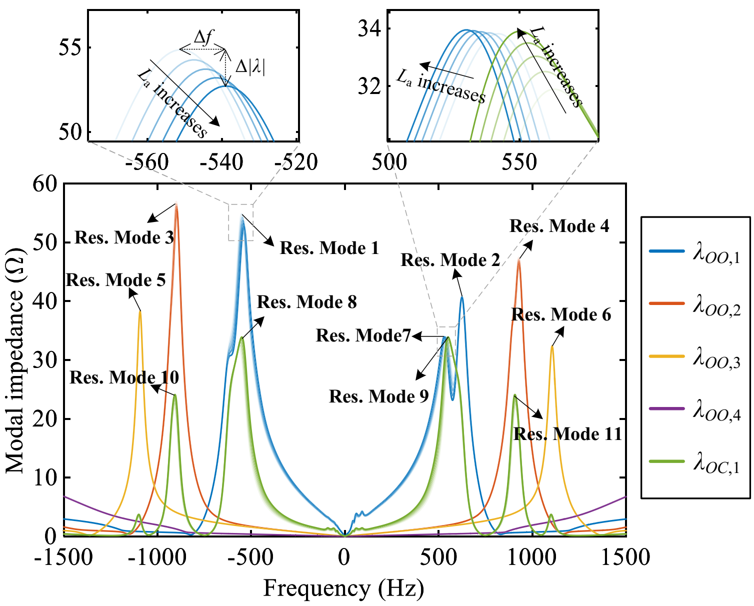

Figure 5.12: Modal impedances for different L_a

The sensitivity indices of other parameters are calculated following the same procedure and demonstrated by the heatmaps in Figure 5.14 and Figure 5.15. The following observations can be obtained from Figure 5.14 and Figure 5.15:

1. Harmonic resonances are mainly affected by a few parameters, while most parameters have little or negligible impact on the resonance frequencies and the resonance modes. The resonance frequency sensitivity indices agree quite well with the PF analysis results,

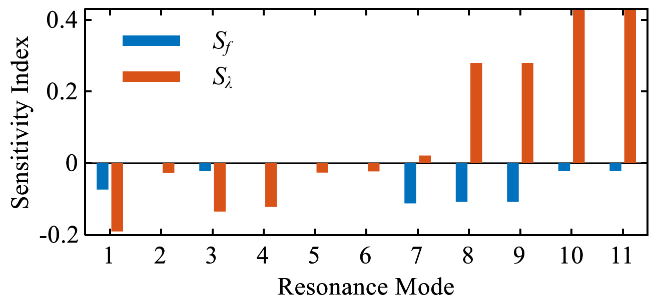

Figure 5.13: Sensitivity indices of L_a to all the resonance modes

i.e., the network components related to the bus with the largest PF will have larger S_f. For instance, Bus 4 is most involved in resonance mode 7, 8 and 9 as given in Table 5.5, the parameters of converter 3, e.g., L_{13}, C_3 and τ_3, indicate comparably larger resonance frequency sensitivity indices.

2. All physical components have negative sensitivity indices S_f, while the sensitivity indices S_f and S_λ of the control parameters are positive. It predicts that the resonance frequencies will decrease when the values of capacitor and inductor are increased; both the resonance frequencies and resonance modes become larger as the grid-following converter's current controller becomes slower. It is noteworthy that some physical components have bidirectional resonance mode sensitivities. For instance, the resonance mode sensitivities of C_1 at resonance mode 5 and 10 are positive and negative, respectively. It implies that these two resonance modes cannot be simultaneously damped by merely increasing/decreasing C_1. This property should be carefully considered for designing resonance mitigation strategies.

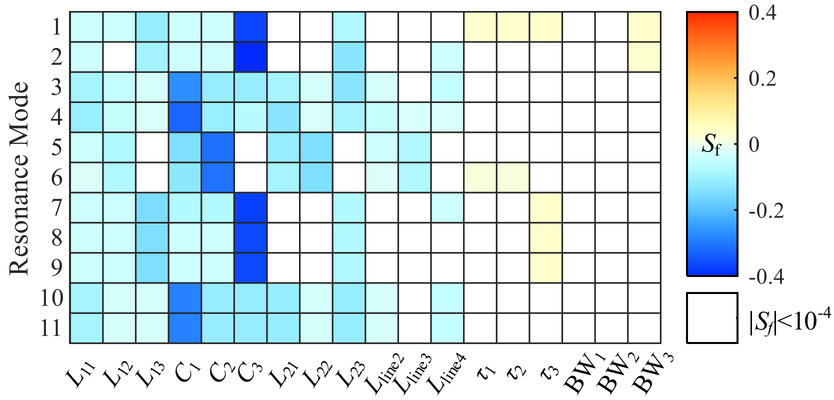

Figure 5.14: Resonance frequency sensitivity analysis results.

Harmonic resonance only occurs when the frequencies generated by the harmonic sources are close to the resonance frequencies with large resonance modes. Therefore, based on the sensitivity indices, the resonance mitigation scheme can be developed by optimizing the system parameters to decrease the resonance modes and shift the resonance frequencies away from the frequency contents of the harmonic sources.

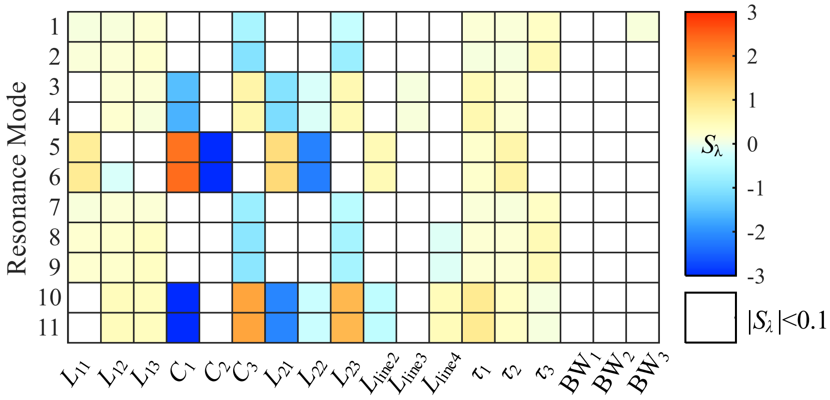

Figure 5.15: Resonance mode sensitivity analysis results.

5.5 Summary

This chapter presents a systematic methodology for the harmonic resonance analysis of converter dominated power systems. Unlike the classical RMA for the legacy power system, the admittance/impedance matrix is represented by a time-periodic matrix obtained from the reformulation of the HTMs to fully capture frequency coupling effects. The proposed generalized RMA can accurately evaluate the effects of the non-holomorphic control units and the unbalanced operation conditions on the resonance characteristics. The results of case studies indicate that the DSRF-PLL of the grid-following converter can cause the difference of harmonic resonances for positive and negative sequences, and the grid impedance imbalance will introduce extra resonance modes. In addition, sensitivity analysis is used to assess the impact of individual parameters on the resonance frequency and the resonance mode, which provides useful information for resonance mitigation. Potential applications of the proposed method include: harmonic resonance analysis of large-scale modern power systems with diverse converters under different operation conditions, investigation of the impact of other nonlinear control units, e.g., PWM, on the resonance behavior, and optimized design of passive and active damping strategies.

6

Sensitivity-Based Stability Improvement

In previous chapters, the eigenvalue sensitivity analysis and participation analysis have been proved to be useful tools for the identification of the most influential parameters and states affecting the small-signal stability of converter-dominated power systems. In this chapter, sensitivity and participation analysis are used as design-oriented tools to improve stability margins and damping performance. Based on eigenvalue and damping ratio sensitivities, a linear optimization problem is formulated and solved iteratively to achieve automatic tuning of control parameters. Additionally, guided by the participation analysis, an auxiliary damping loop design rule is proposed for the scenarios where the control parameters cannot be freely alternated. Experimental tests have been carried out on both grid-following converters and grid-forming converters to validate the effectiveness of the proposed methodology.

6.1 Sensitivity-Based Parameter Optimization

The LTI and LTP eigenvalue sensitivity analysis results provide linear approximation of the movement of eigenvalues as physical and control parameters are modified. Take the Type I GFL converter as an example, as the proportional gain k_p of the PI controller in the DSRF-PLL is swept in the range of $[-20\%,\ 20\%]$ of the initially designed value, the 14 LTP eigenvalues can be predicted with

$$\lambda_i = \lambda_{i0} + \tfrac{\partial \lambda_i}{\partial k_p} \Delta k_p, \quad i = 1, \ldots, 14 \tag{6.1}$$

where λ_{i0} is the initial value of the ith LTP eigenvalue, which are marked with black circles in Figure 6.1. The crosses give their sensitivity-based predictions when k_p is changed. Meanwhile, the system matrix is updated for each new value of k_p. Corresponding LTP eigenvalues are recalculated, and the results are plotted as dots in Figure 6.1. The agreement of LTP eigenvalues obtained from the prediction and recalculation confirms the effectiveness of the proposed LTP eigenvalue sensitivity index $\frac{\partial \lambda_i}{\partial k_p}$ used in Eq. (6.1). Nevertheless, it should be clarified that the eigenvalue sensitivity is a linear approximation around the initial control parameters, and the accuracy cannot be guaranteed when the changes of parameter are too large. The increasing deviations between actual LTP eigenvalues and their predictions can be observed in the enlarged plot of Figure 6.1. Such prediction error can be reduced by considering also the second-order eigenvalue sensitivity, however, it brings nonlinearity and computational complexity.

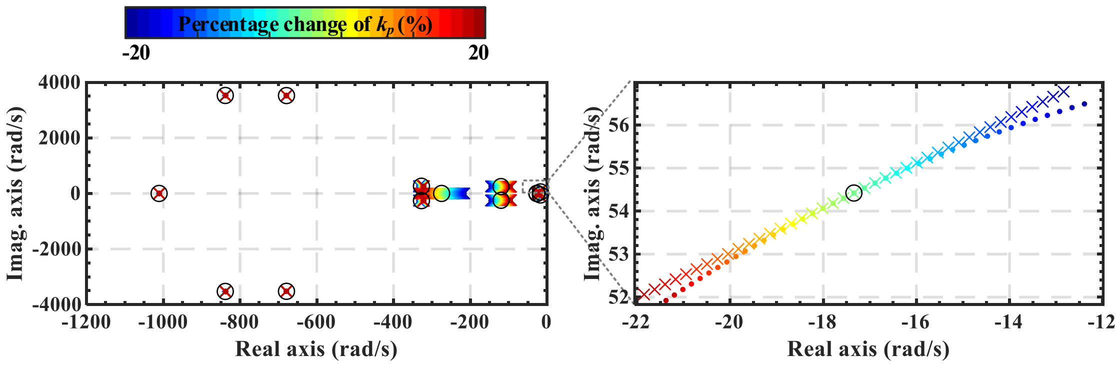

Figure 6.1: Distribution of LTP eigenvalues of Typy I GFL converter system with changes of k_p. Black circles: initial values of the eigenvalues. Crosses: sensitivity-based predictions. Dots: recalculated/true eigenvalues.

According to the modal analysis presented in Chapter 4, the control parameter should be optimized so that all eigenvalues lie in the left-half of the complex plane to ensure the system stability. At the same time, damping ratio of each mode should be as large as possible to achieve smooth dynamic responses. As given by Eq. (4.45), each LTP eigenvalue/mode contains multiple oscillation components and its damping performance is quantified by a damping ratio vector. To give a comprehensive evaluation of the damping performance of one LTP mode, the sum of damping ratios weighted by the first-order norm of the eigenvector is defined

$$\bar{\xi}_i = \sum\nolimits_{h=-H}^{H} \frac{\left|\boldsymbol{r}_i^h\right|_1}{\left|\boldsymbol{r}_i\right|_1} \xi_i^h = \sum\nolimits_{h=-H}^{H} \frac{\left|\boldsymbol{r}_i^h\right|_1}{\left|\boldsymbol{r}_i\right|_1} \frac{-\sigma_i}{\sqrt{\sigma_i^2 + (\omega_i + h\omega_0)^2}}. \tag{6.2}$$

Then, the first-order sensitivity of $\bar{\xi}_i$ with respect to an arbitrary parameter φ is given by

$$\frac{\partial \bar{\xi}_i}{\partial \varphi} = \sum\nolimits_{h=-H}^{H} \frac{\frac{\partial \left|\boldsymbol{r}_i^h\right|_1}{\partial \varphi}\left|\boldsymbol{r}_i\right|_1 - \frac{\partial \left|\boldsymbol{r}_i\right|_1}{\partial \varphi}\left|\boldsymbol{r}_i^h\right|_1}{\left|\boldsymbol{r}_i\right|_1^2} \xi_i^h + \frac{\left|\boldsymbol{r}_i^h\right|_1}{\left|\boldsymbol{r}_i\right|_1} \frac{\partial \xi_i^h}{\partial \varphi} \tag{6.3}$$

where $\frac{\partial \xi_i^h}{\partial \varphi}$ can be determined with the eigenvalue sensitivity

$$\frac{\partial \xi_i^h}{\partial \varphi} = \frac{1}{\sigma_i^2 + (\omega_i + h\omega_0)^2} \left(-\sqrt{\sigma_i^2 + (\omega_i + h\omega_0)^2} \mathrm{Re}\left\{ \frac{\partial \lambda_i}{\partial \varphi} \right\} + \sigma_i \cdot \frac{\sigma_i \mathrm{Re}\left\{ \frac{\partial \lambda_i}{\partial \varphi} \right\} + (\omega_i + h\omega_0)\, \mathrm{Im}\left\{ \frac{\partial \lambda_i}{\partial \varphi} \right\}}{\sqrt{\sigma_i^2 + (\omega_i + h\omega_0)^2}} \right).$$

Moreover, $\frac{\partial \left|\boldsymbol{r}_i^h\right|_1}{\partial \varphi}$ and $\frac{\partial \left|\boldsymbol{r}_i\right|_1}{\partial \varphi}$ in Eq. (6.2) are related to the LTP eigenvector sensitivities, which are deduced as following:

The linear independent LTP eigenvectors and their shifted copies are the basis vectors, therefore, the sensitivity of the ith LTP eigenvector $\boldsymbol{r}_i(t)$ with respect to an arbitrary parameter φ can be generally written as the linear superposition of those basis vectors

$$\frac{\partial \boldsymbol{r}_i(t)}{\partial \varphi} = \sum\nolimits_{j=1}^{N} \sum\nolimits_{h=-H}^{H} \psi_{ij}^h e^{jh\omega_0 t} \boldsymbol{r}_j(t)\;, \quad h \neq 0 \text{ if } j = i \tag{6.4}$$

where ψ_{ij}^{h} denotes a constant coefficient to be determined.

According to Eq. (4.56a), the shifted copies of LTP eigenvalue and eigenvector satisfy the relation

$$\boldsymbol{A}(t)\left(e^{jh\omega_0 t}\boldsymbol{r}_i(t)\right)-\frac{\partial}{\partial t}\left(e^{jh\omega_0 t}\boldsymbol{r}_i(t)\right)=(\lambda_i-jh\omega_0)\left(e^{jh\omega_0 t}\boldsymbol{r}_i(t)\right) \tag{6.5}$$

Taking the partial derivative of Eq. (6.5) with respect to φ, yields

$$\begin{aligned}&\frac{\partial\boldsymbol{A}(t)}{\partial\varphi}\left(e^{jh\omega_0 t}\boldsymbol{r}_i(t)\right)+\boldsymbol{A}(t)\left(e^{jh\omega_0 t}\frac{\partial\boldsymbol{r}_i(t)}{\partial\varphi}\right)-\frac{\partial}{\partial t}\left(e^{jh\omega_0 t}\frac{\partial\boldsymbol{r}_i(t)}{\partial\varphi}\right)\\&=\frac{\partial\lambda_i}{\partial\varphi}\left(e^{jh\omega_0 t}\boldsymbol{r}_i(t)\right)+(\lambda_i-jh\omega_0)\left(e^{jh\omega_0 t}\frac{\partial\boldsymbol{r}_i(t)}{\partial\varphi}\right)\end{aligned} \tag{6.6}$$

Multiplying both sides of Eq. (6.6) with $\boldsymbol{l}_j(t)$ and inserting the relation given by Eq. (4.56b), yields

$$\boldsymbol{l}_j(t)\frac{\partial\boldsymbol{A}(t)}{\partial\varphi}\left(e^{jh\omega_0 t}\boldsymbol{r}_i(t)\right)-\frac{\partial}{\partial t}\left(e^{jh\omega_0 t}\boldsymbol{l}_j(t)\frac{\partial\boldsymbol{r}_i(t)}{\partial\varphi}\right)=(\lambda_i-jh\omega_0-\lambda_j)\left(e^{jh\omega_0 t}\boldsymbol{l}_j(t)\frac{\partial\boldsymbol{r}(t)_i}{\partial\varphi}\right) \tag{6.7}$$

The second term on the left side of Eq. (6.7) contains no DC components, therefore, the constant coefficient ψ_{ij}^{-h} is determined by

$$\psi_{ij}^{-h}=\frac{\left\{\boldsymbol{l}_j(t)\frac{\partial\boldsymbol{A}(t)}{\partial\varphi}\left(e^{jh\omega_0 t}\boldsymbol{r}_i(t)\right)\right\}^0}{\lambda_i-jh\omega_0-\lambda_j} \tag{6.8}$$

Then, $\frac{\partial|\boldsymbol{r}_i^h|_1}{\partial\varphi}$ and $\frac{\partial|\boldsymbol{r}_i|_1}{\partial\varphi}$ can be obtained based on $\frac{\partial\boldsymbol{r}_i(t)}{\partial\varphi}$.

With the eigenvalue and damping ratio sensitivity deduced above, the following linear optimization problem can be formulated for the automatic tuning of control parameters

$$\min_{\Delta\varphi_j}\quad\sigma_{\max} \tag{6.9a}$$

subjected to

$$\sigma_i=\mathrm{Re}\{\lambda_{i0}\}+\sum\nolimits_{j=1}^{M}\frac{\mathrm{Re}\{\partial\lambda_i\}}{\partial\varphi_j}\Delta\varphi_j,\quad i=1,\ldots,N \tag{6.9b}$$

$$\sigma_{\max}\geq\sigma_i \tag{6.9c}$$

$$\bar{\xi}_i=\bar{\xi}_{i0}+\sum\nolimits_{j=1}^{M}\frac{\partial\bar{\xi}_i}{\partial\varphi_j}\Delta\varphi_j,\quad i=1,\ldots,N \tag{6.9d}$$

$$\bar{\xi}_{\min 0}\leq\bar{\xi}_{i0} \tag{6.9e}$$

$$\bar{\xi}_{\min}\leq\bar{\xi}_i \tag{6.9f}$$

$$\bar{\xi}_{\min}\geq\bar{\xi}_{\min 0} \tag{6.9g}$$

$$|\Delta\varphi_j|\leq 1\%\varphi_{j0} \tag{6.9h}$$

The objective function Eq. (6.9a) is to minimize the real part of the right-most LTP eigenvalues. Decision variables $\{\Delta\varphi_i,\ i=1,\cdots,M\}$ are the changes of control parameters with initial values $\{\varphi_{i0},\ i=1,\cdots,M\}$. M stands for the total number of adjustable control parameters. The initial values are determined following the classical design methods described in Chapter 3.

The constraint Eq. (6.9b) gives the linear prediction of the real part of each LTP eigenvalue after control parameters are updated. To guarantee the accuracy of the sensitivity-based linear approximation, changes of parameters are limited by inequalities Eq. (6.9h), namely permissible variance must be within ±1% of the initial values. $\bar{\xi}_{i0}$ denotes the initial value of the comprehensive damping ratio, and its prediction is given by the constraint Eq. (6.9d). The inequality Eq. (6.9g) ensures that the minimum comprehensive damping ratio will not be degraded by updating parameters. This linear optimization problem is solved by using the commercial software GUROBI.

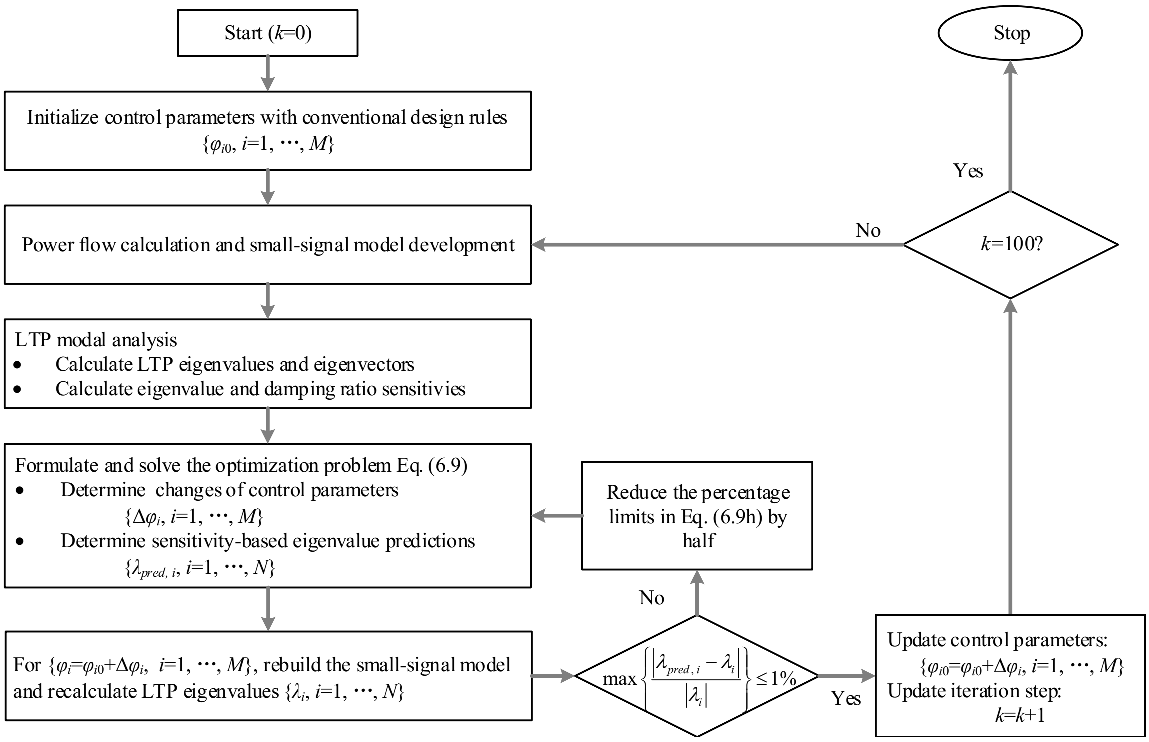

Figure 6.2: Sensitivity-based automatic control parameter optimization framework

Figure 6.2 shows the flowchart of the eigenvalue-sensitivity-based parameter optimization algorithm. In the first step, control parameters are initialized with the conventional tuning procedure. Power flow analysis is performed to determine the steady-state operation trajectory. Then, the small-signal model is established, and the modal analysis is carried out to determine LTP eigenvalues, eigenvectors and corresponding sensitivities. Next, the linear optimization problem given by Eq. (6.9) is formulated and solved. The validity of the sensitivity-based prediction is checked by recalculating eigenvalues with updated parameters. If deviations between actual eigenvalues and their predictions are too large, the linear optimization problem is modified by reducing limits of parameter changes. Specifically, the maximum percentage change of control parameters in Eq. (6.9h) decreases from ±1% to ±0.5%. Otherwise, parameter updates are accepted and the next iteration starts. The algorithm stops when a predefined maximum number of iteration is reached, which is set to be 100.

The proposed design method is tested with the Type I GFL converter system. The current control time constant is fixed to 0.5 ms. Parameters of the DSRF-PLL are selected for optimization, which are initialized to a desired bandwidth of 20 Hz. The grid impedance is adapted to the maximum value of the test bench ($L_g = 17.4\,\mathrm{mH}$ and $R_g = 0.53\,\Omega$). Figure 6.3

shows the movement of eigenvalues for different steady-state operation trajectories. As the active power reference P_r increases, the critical eigenvalues move towards the right half plane with decreasing damping ratio, and eventually enter the unstable region.

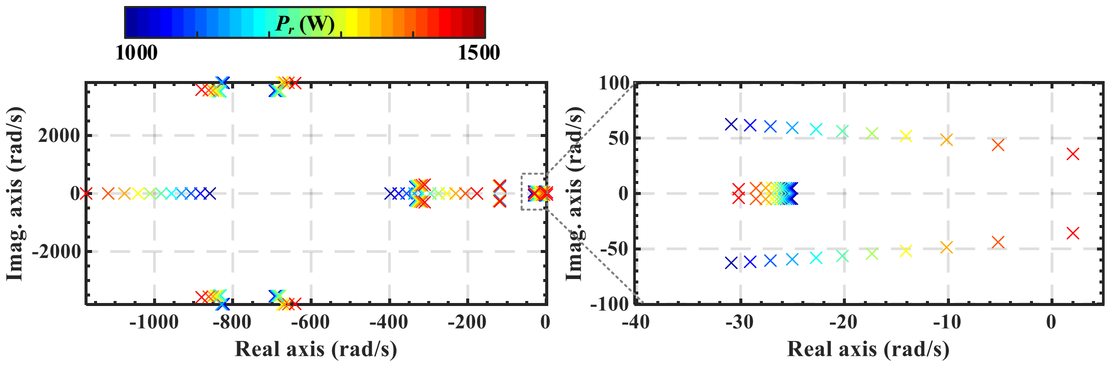

Figure 6.3: Movement of LTP eigenvalues of Typy I GFL converter system for different active power reference P_r

To extend the stability margin, parameters of the DSRF-PLL are optimized with the proposed design method. Another difference worth mentioning from the conventional tuning procedure is that the cutoff frequencies of the four low-pass filters within the DSRF-PLL are treated to be independent rather than sharing the same value, namely the decision variables become

$$\{\Delta\varphi_1,\ \Delta\varphi_2,\ \Delta\varphi_3,\ \Delta\varphi_4,\ \Delta\varphi_5,\ \Delta\varphi_6\} = \{\Delta k_p,\ ,\Delta k_i,\ \Delta\omega_{f1},\ \Delta\omega_{f2},\ \Delta\omega_{f3},\ \Delta\omega_{f4}\}$$

To improve computational efficiency, only damping ratio of LTP eigenvalues with real parts larger than -200 are examined. Figure 6.4 shows the movement of LTP eigenvalues at each iteration. The critical eigenvalues migrate gradually towards the left half plane, which confirms the effectiveness of the proposed methodology. Initial and optimized control parameters are listed in Table 6.1. It is noted that asymmetric tuning the cutoff frequencies of the low-pass filters is beneficial for the system stability.

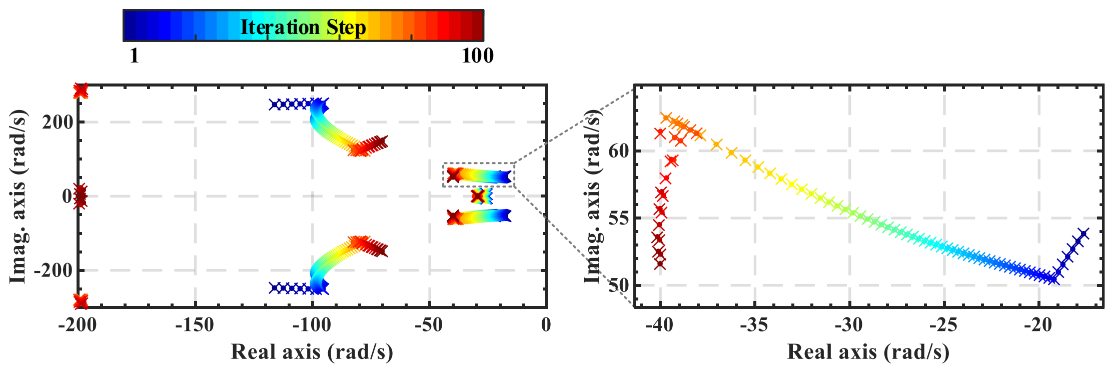

Figure 6.4: Movement of LTP eigenvalues of Type I GFL converter system at each optimization iteration. Crosses: sensitivity-based predictions. Dots: recalculated/true eigenvalues.

Experimental tests have been carried out on the single GFL converter system to verify the effectiveness of the proposed control parameter tuning method. Figure 6.5 and Figure 6.6 show the comparison of time-domain free and forced responses for different DSRF-PLL parameters. The improvement of the stability margin and the damping performance is validated.

Table 6.1: Control parameters of the DSRF-PLL for different iterations

Iteration	k_p	k_i	ω_{f1}	ω_{f2}	ω_{f3}	ω_{f4}
0 (conventional design)	125.7	6580	301.6	301.6	301.6	301.6
50	171.1	9502	180.6	206.9	207.8	207.8
100	176.3	10290	142.5	212.9	155.3	215.8

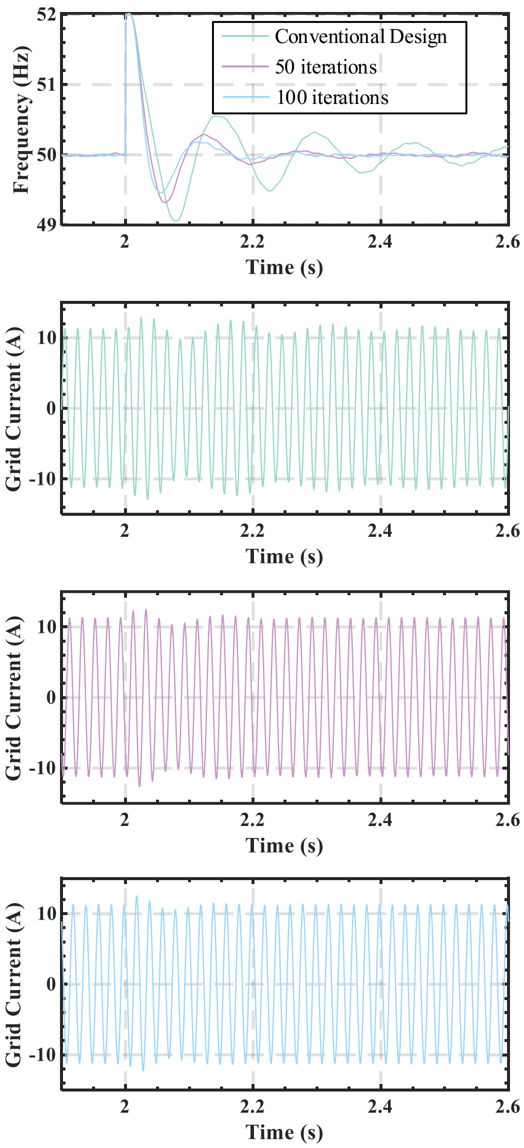

Figure 6.5: Measurements of the Type I GFL to 2 Hz disturbance applied to η at $t = 2.0$ s for different DSRF-PLL parameters

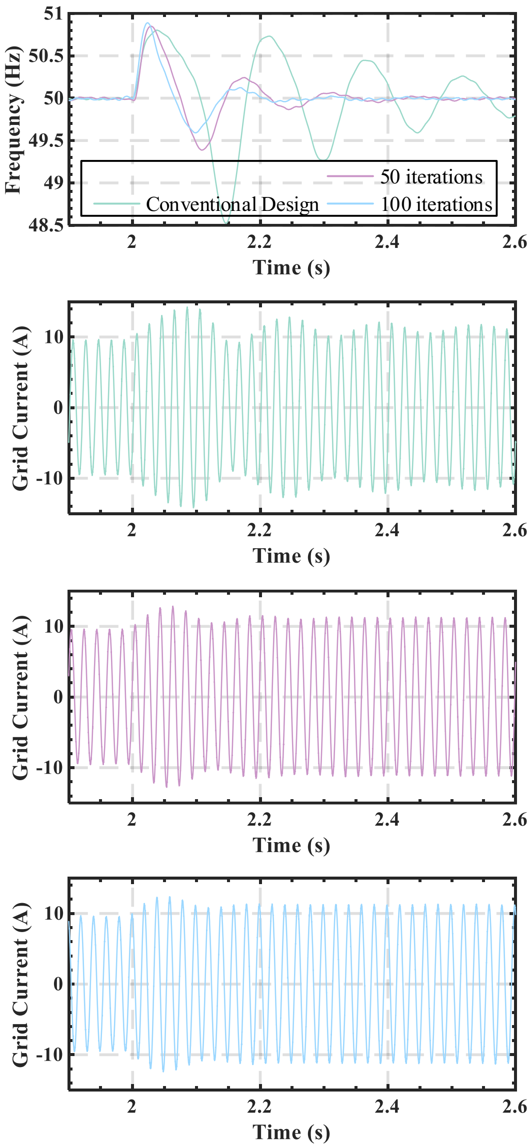

Figure 6.6: Measurements of the Type I GFL to P_r changing from 1300 to 1400 W at $t = 2.0$ s for different DSRF-PLL parameters

6.2 Sensitivity-Based Damping Loop Design

For a given control structure, it may happen that the stability margin cannot be further expanded by adjusting the control parameters alone. Moreover, there exist also application scenarios where the control parameters cannot be freely selected, for instance the droop coefficients of GFM converters are defined by grid codes. For these cases, auxiliary damping loops need to be developed. To this end, the participation factor analysis can provide insightful guidance on the location selection of the damping loop.

Taking the single GFM converter system as an example, Figure 4.29 shows magnitudes of participation factors between state variables and oscillation modes. The right-most low-frequency modes $\lambda_{1,\,2}$ mainly contribute to dynamics of the power control loop, which suggests that a local feedback loop can be added around the state variable ω to improve the damping performance, as shown in Figure 6.7.

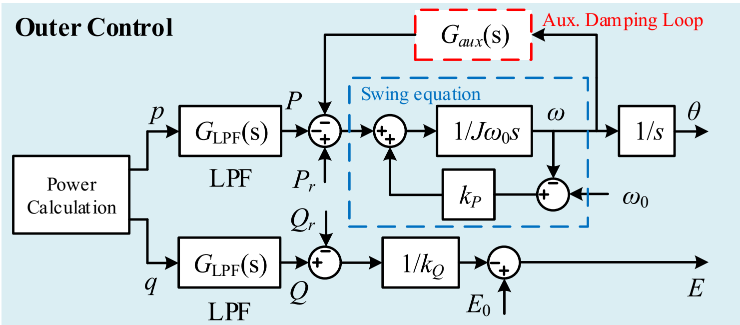

Figure 6.7: Outer control diagram of the VSG converter with auxiliary damping loop

Based on experience in design of the power system stabilizer for conventional rotational generators, the transfer function of the extra feedback loop can be generally expressed as

$$G_{aux}(s) = K_{aux} \cdot \underbrace{\frac{sT_w}{1+sT_w}}_{\text{washout filter}} \cdot \underbrace{\frac{1+sT_1}{1+sT_2}}_{\text{phase compensation}} \tag{6.10}$$

where the phase compensation unit is used to guarantee that the newly introduced control loop provides damping torque to the target oscillation. For the GFM converter a negative feedback is adopted, namely the phase compensation is 180°. The washout filter is a high-pass filter with a time constant of T_w, which allows oscillations at the frequency of $\lambda_{1,\,2}$ to pass, while ensuring that the system steady state is not affected by the use of the damping loop. The value of T_w is commonly in the range of 1 to 20 seconds, here it is set to 5 s. The gain K_{aux} determines the amount of damping introduced by the auxiliary loop. Figure 6.8 plots the eigenvalue loci for different values of K_{aux}. It is observed that the low-frequency mode becomes better damped as K_{aux} increases, and it can even turn into two real-valued eigenvalues. Moreover, the adoption of the auxiliary damping loop brings a pure real eigenvalue near the origin which does not threaten the system stability.

The proposed damping strategy is tested with the three-VSG laboratory prototype microgrid shown in Figure 3.28. The inertia constant J is increased to $0.264\,\mathrm{kg}\cdot\mathrm{m}^2$. To excite dynamic responses, an active power reference step of 600 W is given to VSG 1. The output active and reactive power responses of all three converters are calculated using voltage and current

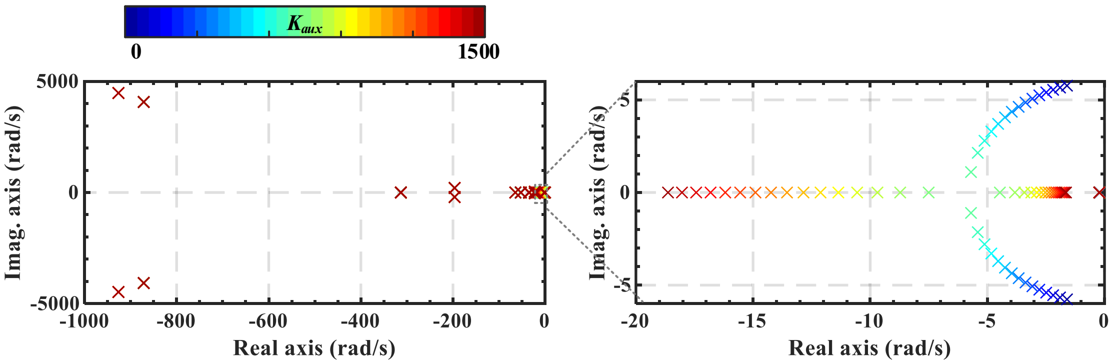

Figure 6.8: Movement of eigenvalues of the single GFM converter system for different values of K_{aux}

measurements, and an apparent low-frequency oscillation between VSGs can be observed from Figure 6.9. To validate the effectiveness of the proposed auxiliary damping loop, the same active power reference step is repeated for different values of K_{aux}, experimental results are plotted in Figure 6.10. Since dynamic responses of all three VSGs' output active and reactive power exhibit the same damping characteristic, only those of VSG 1 are plotted in Figure 6.10. It is seen that, after enabling the auxiliary damping loop, the low-frequency oscillation can be damped well, and the damping gets larger as K_{aux} increases.

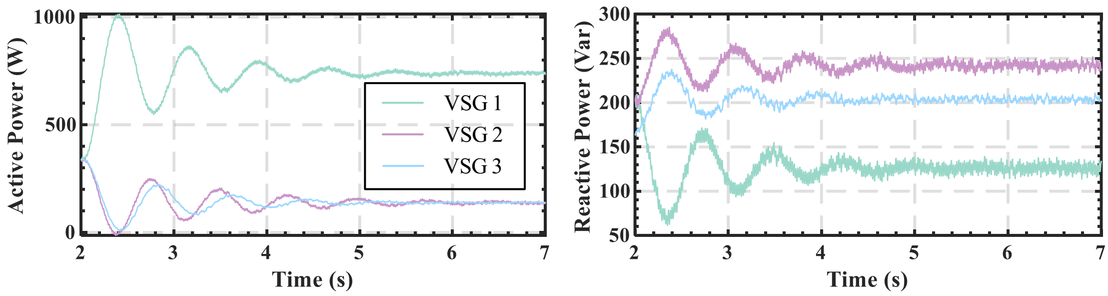

Figure 6.9: Measurement of dynamic responses of VSGs output active power (left) and reactive power (right) to 600 W active power reference step of VSG 1 at $t = 2.0\,\mathrm{s}$

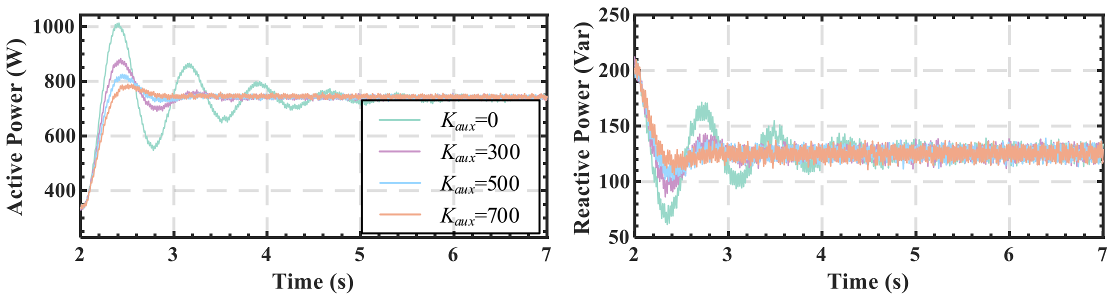

Figure 6.10: Measurement of active and reactive power responses of VSG 1 for different K_{aux}

The sensitivity-based damping loop design principle is also tested with the GFL converters. One conclusion drawn in Section 4.5.1 is that as the grid becomes weaker (namely SCR decreases), LTP eigenvalues $\lambda_{3,\,4}$ in Figure 4.17 threaten the system stability. Those two modes exhibit larger participation factor in dynamics of the PLLs, therefore, adding a negative feedback loop around the state variable η in PLLs (see Figure 6.11) is an efficient way to move $\lambda_{3,\,4}$ towards left.

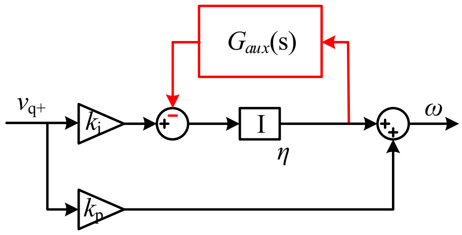

Figure 6.11: Control diagram of the SRF-PLL with auxiliary damping loop

In the test, the operational SCR is reduced to 1.8 by increasing both the power reference and the grid line impedance. After the system reaches steady state, a 2 Hz disturbance is given to the state variable η. Free responses of η are shown in Figure 6.12 and Figure 6.13. It is seen that the Type I GFL converter can be stabilized by the proposed damping loop. Additionally, the damping performance of both types of converters can be improved by increasing the gain K_{aux}. The experimental tests confirm the effectiveness of the proposed damping loop.

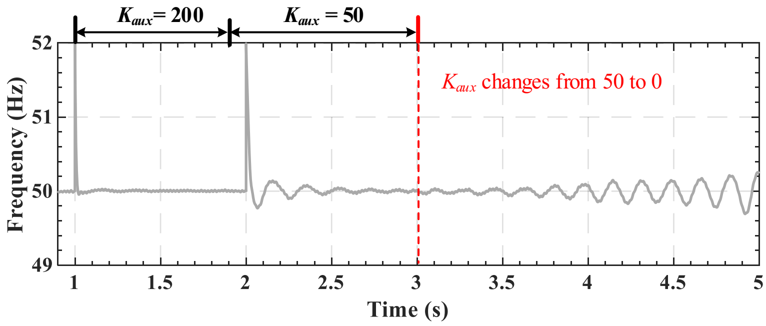

Figure 6.12: Measurement of free response of η of the Type I GFL converter for different values of K_{aux}. 2 Hz disturbance is applied to η at $t = 1.0$ s and $t = 2.0$ s

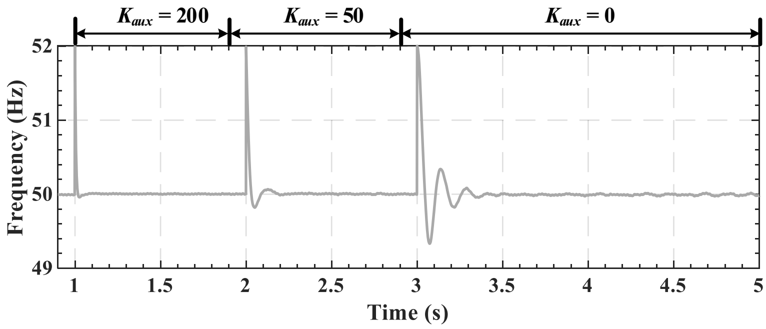

Figure 6.13: Measurement of free response of η of the Type II GFL converter for different values of K_{aux}. 2 Hz disturbance is applied to η at $t = 1.0$ s, $t = 2.0$ s and $t = 3.0$ s

6.3 Summary

In this chapter, the sensitivity and participation analysis are used as design-oriented tools to guide the optimization of control parameters and structures. By using the proposed sensitivity-based optimization method, control parameters are iteratively modified to shift critical eigenvalues towards the left half plane without degrading the damping performance. Though the same effect can be achieved by using a brute force methods (namely iterating over all possible parameter combinations), the proposed method exhibits superior computational efficiency because the sensitivity index indicates the fastest direction in which the critical eigenvalues move towards the left. The application to the Type I GFL converter system reveals that asymmetric tuning of d-channel and q-channel control parameters can improve the system stability. For scenarios where the control parameters are predefined, extra damping loops consisting of the proportional gain, high-pass filter and phase compensation unit can be developed based on the participation analysis results. For both GFL converters and GFM converters, negative feedback around the frequency state variable is an effective way to improve the system stability. Theoretical analysis results have been confirmed with experimental measurements.

7

Conclusion and Outlook

7.1 Conclusions

This thesis aimed at the modeling, stability and resonance analysis of modern converter-dominated power systems. To this end, a modular, scalable and flexible numerical modeling framework is developed on the MATLAB/Simulink platform. To gain detailed and insightful understanding of the system dynamics, small-signal models are derived by using the component connection method. Modal analysis is carried out to identify causes of abnormal resonances and instability. Experimental tests on a laboratory multi-converter PHIL system validate the fidelity of the simulation results. Cross-validation between stability and resonance evaluation results obtained from numerical models, analytical models and hardware measurements confirms the effectiveness of the proposed methodology. The major findings and conclusions are summarized as follows.

- The frequency coupling effect can be classified into the sequence coupling effect and the frequency shift effect. Specifically, unbalanced three-phase branches will result in couplings between voltages and currents at frequencies of ω and $-\omega$. Time periodic operation trajectories caused by grid voltage harmonics will bring couplings at frequencies of ω and $\{\omega + n\omega_0, n \in \mathbb{Z}\}$. The influence of the asymmetric converter controller can be regarded as the superposition of both, for instance, the PLL causes the coupling at frequencies of ω and $-\omega + 2\omega_0$.

- Similar to the LTI system, there exists a time-invariant modal space for the LTP system. The system stability is determined by real parts of the system matrix in the modal space. The eigenvalues of the LTP system are affected by the frequency coupling effect to varying degrees. The major difference between LTP and LTI systems is that the space transformation matrix of the LTP system, namely the LTP eigenvector matrix, is time-periodic.

- The eigenvalue-based stability analysis reveals that the GFL converter with DSOGI-PLL and PR current controller has a larger stability margin. The DSRF-PLL with higher bandwidths can exhibit instability behavior when the input voltage becomes unbalanced. The instability issue of the GFL converter under weak grid conditions can be overcome by the GFM converter, while it is challenging to guarantee the stability of GFM converters connected to strong grids. Moreover, the inner-loop control parameters of the GFM converter can degrade the performance of the outer power loop.

- The results of the generalized resonance mode analysis give that the integration of GFL converters can cause a difference of harmonic resonances for positive and negative sequences. The resonance frequencies and resonance modes are hardly affected by grid voltage imbalances, while the grid impedance imbalance can introduce extra resonance modes.
- The LTP eigenvalue and damping ratio sensitivities can be used to optimize control parameters. It is found that independently tuning the d/α-channel and q/β-channel control parameters can extend the system stability margin. Guided by the participation factor analysis, auxiliary damping loops can be added around the frequency state variable of both GFL and GFM converters to improve the damping performance.

7.2 Future Work

There are still some open questions left unaddressed in this thesis, which are worth to be extended and investigated:

- The proposed power flow analysis does not cover the integration of induction machine loads, constant power loads and GFM converters under unbalanced conditions. To provide the fault-ride-through service, converters are commonly equipped with sequence-decoupling structures and dual sequence current controllers, which should also be further studied to evaluate their impact on the system stability.
- In this thesis, the converters are assumed to be supplied with ideal DC voltage sources. Average models of converters are used for the steady-state and small-signal analysis. In practice, the DC side can be energy storage systems with DC-DC converters, the interaction between DC and AC sides can bring new frequency coupling effects. Moreover, the impact of other nonlinearities including PWM, saturation of controllers and nonlinearity of passive components deserves further investigation.
- The proposed power flow analysis gives whether there is a steady-state operation point or trajectory. The eigenvalue-based small-signal analysis evaluates the system stability near such equilibrium. However, the stability of converter-dominated power systems against large disturbances, namely the transient stability, is still a challenging problem. Dynamic modal analysis could be a promising solution.
- The establishment of the state-space model requires detailed modeling of the converter systems, which could be critical for practical applications. Data-driven system identification techniques should be further investigated to achieve the trade-off between modeling accuracy and privacy protection. The sparse identification of nonlinear dynamical systems (SINDy) technique [118] could be an interesting option.

References

[1] Bettina B.F. Wittneben. “The impact of the Fukushima nuclear accident on European energy policy”. In: *Environmental Science and Policy* 15.1 (2012), pp. 1–3. ISSN: 1462-9011. DOI: https://doi.org/10.1016/j.envsci.2011.09.002.

[2] Philip Sterchele et al. *Paths to a Climate-neutral Energy System*. Tech. rep. Tech. rep. Freiburg, Germany: Fraunhofer Institute for Solar Energy Systems ISE, 2020.

[3] Our World in Data. *BP Statistical Review of World Energy*. 2022. URL: https://ourworldindata.org/grapher/electricity-prod-source-stacked?country=~DEU.

[4] Nikos Hatziargyriou et al. “Definition and Classification of Power System Stability - Revisited and Extended”. In: *IEEE Transactions on Power Systems* 36.4 (2021), pp. 3271–3281. DOI: 10.1109/TPWRS.2020.3041774.

[5] Joan Rocabert et al. “Control of Power Converters in AC Microgrids”. In: *IEEE Transactions on Power Electronics* 27.11 (2012), pp. 4734–4749. DOI: 10.1109/TPEL.2012.2199334.

[6] John M. Uudrill. “Dynamic Stability Calculations for an Arbitrary Number of Interconnected Synchronous Machines”. In: *IEEE Transactions on Power Apparatus and Systems* PAS-87.3 (1968), pp. 835–844. DOI: 10.1109/TPAS.1968.292199.

[7] Hans-Peter Beck and Ralf Hesse. “Virtual synchronous machine”. In: *2007 9th International Conference on Electrical Power Quality and Utilisation*. 2007, pp. 1–6. DOI: 10.1109/EPQU.2007.4424220.

[8] Qing-Chang Zhong and George Weiss. “Synchronverters: Inverters That Mimic Synchronous Generators”. In: *IEEE Transactions on Industrial Electronics* 58.4 (2011), pp. 1259–1267. DOI: 10.1109/TIE.2010.2048839.

[9] J. Driesen and K. Visscher. “Virtual synchronous generators”. In: *2008 IEEE Power and Energy Society General Meeting - Conversion and Delivery of Electrical Energy in the 21st Century*. 2008, pp. 1–3. DOI: 10.1109/PES.2008.4596800.

[10] Catalin Arghir, Taouba Jouini, and Florian Dörfler. “Grid-forming control for power converters based on matching of synchronous machines”. In: *Automatica* 95 (2018), pp. 273–282. ISSN: 0005-1098. DOI: doi.org/10.1016/j.automatica.2018.05.037.

[11] Brian B. Johnson et al. “Synchronization of Parallel Single-Phase Inverters With Virtual Oscillator Control”. In: *IEEE Transactions on Power Electronics* 29.11 (2014), pp. 6124–6138. DOI: 10.1109/TPEL.2013.2296292.

[12] Saeed Golestan, Mohammad Monfared, and Francisco D. Freijedo. “Design-Oriented Study of Advanced Synchronous Reference Frame Phase-Locked Loops”. In: *IEEE Transactions on Power Electronics* 28.2 (2013), pp. 765–778. DOI: 10.1109/TPEL.2012.2204276.

[13] Saeed Golestan et al. “A Study on Three-Phase FLLs”. In: *IEEE Transactions on Power Electronics* 34.1 (2019), pp. 213–224. DOI: 10.1109/TPEL.2018.2826068.

[14] Xiaolong Yue, Xiongfei Wang, and Frede Blaabjerg. “Review of Small-Signal Modeling Methods Including Frequency-Coupling Dynamics of Power Converters”. In: *IEEE Transactions on Power Electronics* 34.4 (2019), pp. 3313–3328. DOI: 10.1109/TPEL.2018.2848980.

[15] Xiongfei Wang and Frede Blaabjerg. “Harmonic Stability in Power Electronic-Based Power Systems: Concept, Modeling, and Analysis”. In: *IEEE Transactions on Smart Grid* 10.3 (2019), pp. 2858–2870. DOI: 10.1109/TSG.2018.2812712.

[16] Prabha Kundur. *Power System Stability and Control.* New York: McGraw-Hill, 1994.

[17] José Ignacio Pérez Arriaga. “Selective modal analysis with applications to electric power systems”. dissertation. Massachusetts Institute of Technology, 1981. URL: https://dspace.mit.edu/handle/1721.1/15875.

[18] Nagaraju Pogaku, Milan Prodanovic, and Timothy C. Green. “Modeling, Analysis and Testing of Autonomous Operation of an Inverter-Based Microgrid”. In: *IEEE Transactions on Power Electronics* 22.2 (2007), pp. 613–625. DOI: 10.1109/TPEL.2006.890003.

[19] Roberto Rosso, Soenke Engelken, and Marco Liserre. “Robust Stability Investigation of the Interactions Among Grid-Forming and Grid-Following Converters”. In: *IEEE Journal of Emerging and Selected Topics in Power Electronics* 8.2 (2020), pp. 991–1003. DOI: 10.1109/JESTPE.2019.2951091.

[20] Diptargha Chakravorty et al. “Small Signal Stability Analysis of Distribution Networks With Electric Springs”. In: *IEEE Transactions on Smart Grid* 10.2 (2019), pp. 1543–1552. DOI: 10.1109/TSG.2017.2772224.

[21] Dharmendra Kumar Dheer et al. “Improvement of Stability Margin of Droop-Based Islanded Microgrids by Cascading of Lead Compensators”. In: *IEEE Transactions on Industry Applications* 55.3 (2019), pp. 3241–3251. DOI: 10.1109/TIA.2019.2897947.

[22] Stefan Leitner et al. “Small-Signal Stability Analysis of an Inverter-Based Microgrid With Internal Model-Based Controllers”. In: *IEEE Transactions on Smart Grid* 9.5 (2018), pp. 5393–5402. DOI: 10.1109/TSG.2017.2688481.

[23] Xiangyu Wu, Chen Shen, and Reza Iravani. “Feasible Range and Optimal Value of the Virtual Impedance for Droop-Based Control of Microgrids”. In: *IEEE Transactions on Smart Grid* 8.3 (2017), pp. 1242–1251. DOI: 10.1109/TSG.2016.2519454.

[24] Wenjuan Du et al. “Dynamic Instability of a Power System Caused by Aggregation of Induction Motor Loads”. In: *IEEE Transactions on Power Systems* 34.6 (2019), pp. 4361–4369. DOI: 10.1109/TPWRS.2019.2920370.

[25] I. J. Perez-Arriaga, G. C. Verghese, and F. C. Schweppe. "Selective Modal Analysis with Applications to Electric Power Systems, Part I: Heuristic Introduction". In: *IEEE Power Engineering Review* PER-2.9 (1982), pp. 29–30. DOI: 10.1109/MPER.1982.5519461.

[26] G. C. Verghese, I. J. Perez-arriaga, and F. C. Schweppe. "Selective Modal Analysis With Applications to Electric Power Systems, Part II: The Dynamic Stability Problem". In: *IEEE Transactions on Power Apparatus and Systems* PAS-101.9 (1982), pp. 3126–3134. DOI: 10.1109/TPAS.1982.317525.

[27] Lennart Harnefors, Massimo Bongiorno, and Stefan Lundberg. "Input-Admittance Calculation and Shaping for Controlled Voltage-Source Converters". In: *IEEE Transactions on Industrial Electronics* 54.6 (2007), pp. 3323–3334. DOI: 10.1109/TIE.2007.904022.

[28] Dong Dong et al. "Analysis of Phase-Locked Loop Low-Frequency Stability in Three-Phase Grid-Connected Power Converters Considering Impedance Interactions". In: *IEEE Transactions on Industrial Electronics* 62.1 (2015), pp. 310–321. DOI: 10.1109/TIE.2014.2334665.

[29] Bo Wen et al. "Analysis of D-Q Small-Signal Impedance of Grid-Tied Inverters". In: *IEEE Transactions on Power Electronics* 31.1 (2016), pp. 675–687. DOI: 10.1109/TPEL.2015.2398192.

[30] Zhiqing Yang. "On the stability of three-phase grid-tied photovoltaic inverter systems : modeling, investigation, and stability-enhanced operation". dissertation. RWTH Aachen University, 2021. URL: https://publications.rwth-aachen.de/record/818957.

[31] Yicheng Liao et al. "Low-Frequency Stability Analysis of Single-Phase System With dq-Frame Impedance Approach—Part I: Impedance Modeling and Verification". In: *IEEE Transactions on Industry Applications* 54.5 (2018), pp. 4999–5011. DOI: 10.1109/TIA.2018.2832027.

[32] Yicheng Liao et al. "Low-Frequency Stability Analysis of Single-Phase System With dq-Frame Impedance Approach—Part II: Stability and Frequency Analysis". In: *IEEE Transactions on Industry Applications* 54.5 (2018), pp. 5012–5024. DOI: 10.1109/TIA.2018.2828386.

[33] Saeed Golestan et al. "dq-Frame Impedance Modeling of Three-Phase Grid-Tied Voltage Source Converters Equipped With Advanced PLLs". In: *IEEE Transactions on Power Electronics* 36.3 (2021), pp. 3524–3539. DOI: 10.1109/TPEL.2020.3017387.

[34] Shike Wang et al. "Small-Signal Modeling and Stability Prediction of Parallel Droop-Controlled Inverters Based on Terminal Characteristics of Individual Inverters". In: *IEEE Transactions on Power Electronics* 35.1 (2020), pp. 1045–1063. DOI: 10.1109/TPEL.2019.2914176.

[35] Hong Gong, Dongsheng Yang, and Xiongfei Wang. "Impact Analysis and Mitigation of Synchronization Dynamics for DQ Impedance Measurement". In: *IEEE Transactions on Power Electronics* 34.9 (2019), pp. 8797–8807. DOI: 10.1109/TPEL.2018.2886096.

[36] Jian Sun. "Impedance-Based Stability Criterion for Grid-Connected Inverters". In: *IEEE Transactions on Power Electronics* 26.11 (2011), pp. 3075–3078. DOI: 10.1109/TPEL.2011.2136439.

[37] Mauricio Cespedes and Jian Sun. “Impedance Modeling and Analysis of Grid-Connected Voltage-Source Converters”. In: *IEEE Transactions on Power Electronics* 29.3 (2014), pp. 1254–1261. DOI: 10.1109/TPEL.2013.2262473.

[38] Jian Sun et al. “A Theory for Harmonics Created by Resonance in Converter-Grid Systems”. In: *IEEE Transactions on Power Electronics* 34.4 (2019), pp. 3025–3029. DOI: 10.1109/TPEL.2018.2869781.

[39] Yicheng Liao and Xiongfei Wang. “Stationary-Frame Complex-Valued Frequency-Domain Modeling of Three-Phase Power Converters”. In: *IEEE Journal of Emerging and Selected Topics in Power Electronics* 8.2 (2020), pp. 1922–1933. DOI: 10.1109/JESTPE.2019.2958938.

[40] Atle Rygg et al. “On the Equivalence and Impact on Stability of Impedance Modeling of Power Electronic Converters in Different Domains”. In: *IEEE Journal of Emerging and Selected Topics in Power Electronics* 5.4 (2017), pp. 1444–1454. DOI: 10.1109/JESTPE.2017.2744988.

[41] Atle Rygg et al. “A Modified Sequence-Domain Impedance Definition and Its Equivalence to the dq-Domain Impedance Definition for the Stability Analysis of AC Power Electronic Systems”. In: *IEEE Journal of Emerging and Selected Topics in Power Electronics* 4.4 (2016), pp. 1383–1396. DOI: 10.1109/JESTPE.2016.2588733.

[42] Shahil Shah and Leila Parsa. “Impedance Modeling of Three-Phase Voltage Source Converters in DQ, Sequence, and Phasor Domains”. In: *IEEE Transactions on Energy Conversion* 32.3 (2017), pp. 1139–1150. DOI: 10.1109/TEC.2017.2698202.

[43] Yicheng Liao and Xiongfei Wang. “Small-Signal Modeling of AC Power Electronic Systems: Critical Review and Unified Modeling”. In: *IEEE Open Journal of Power Electronics* 2 (2021), pp. 424–439. DOI: 10.1109/OJPEL.2021.3104522.

[44] Xiongfei Wang, Lennart Harnefors, and Frede Blaabjerg. “Unified Impedance Model of Grid-Connected Voltage-Source Converters”. In: *IEEE Transactions on Power Electronics* 33.2 (2018), pp. 1775–1787. DOI: 10.1109/TPEL.2017.2684906.

[45] Hendrik Just. “Modeling and control of power converters in weak and unbalanced electric grids”. dissertation. Technische Universität Berlin, 2021. URL: https://verlag.tu-berlin.de/produkt/978-3-7983-3207-2/.

[46] Saeed Golestan et al. “Linear Time-Periodic Modeling, Examination, and Performance Enhancement of Grid Synchronization Systems With DC Component Rejection/Estimation Capability”. In: *IEEE Transactions on Power Electronics* 36.4 (2021), pp. 4237–4253. DOI: 10.1109/TPEL.2020.3018584.

[47] Saeed Golestan et al. “Harmonic Linearization and Investigation of Three-Phase Parallel-Structured Signal Decomposition Algorithms in Grid-Connected Applications”. In: *IEEE Transactions on Power Electronics* 36.4 (2021), pp. 4198–4213. DOI: 10.1109/TPEL.2020.3021723.

[48] S.R. Sanders et al. “Generalized averaging method for power conversion circuits”. In: *IEEE Transactions on Power Electronics* 6.2 (1991), pp. 251–259. DOI: 10.1109/63.76811.

[49] Yelun Peng et al. “Performance Improvement of the Unbalanced Voltage Compensation in Islanded Microgrid Based on Small-Signal Analysis”. In: *IEEE Transactions on Industrial Electronics* 67.7 (2020), pp. 5531–5542. DOI: 10.1109/TIE.2019.2934021.

[50] Zhikang Shuai et al. “Transient Response Analysis of Inverter-Based Microgrids Under Unbalanced Conditions Using a Dynamic Phasor Model”. In: *IEEE Transactions on Industrial Electronics* 66.4 (2019), pp. 2868–2879. DOI: 10.1109/TIE.2018.2844828.

[51] Özgür Can Sakinci and Jef Beerten. “Generalized Dynamic Phasor Modeling of the MMC for Small-Signal Stability Analysis”. In: *IEEE Transactions on Power Delivery* 34.3 (2019), pp. 991–1000. DOI: 10.1109/TPWRD.2019.2898468.

[52] Philip J. Hart et al. “Impact of Harmonics and Unbalance on the Dynamics of Grid-Forming, Frequency-Droop-Controlled Inverters”. In: *IEEE Journal of Emerging and Selected Topics in Power Electronics* 8.2 (2020), pp. 976–990. DOI: 10.1109/JESTPE.2019.2949303.

[53] Stefan Almer. “Control and Analysis of Pulse-Modulated Systems”. dissertation. KTH Royal Institute of Technology in Stockholm, 2008. URL: https://kth.diva-portal.org/smash/record.jsf?pid=diva2%3A13578&dswid=-6014.

[54] Miguel Esparza et al. “Modeling of VSC-Based Power Systems in the Extended Harmonic Domain”. In: *IEEE Transactions on Power Electronics* 32.8 (2017), pp. 5907–5916. DOI: 10.1109/TPEL.2017.2658340.

[55] Uriel Vargas and Abner Ramirez. “Reformulating Extended Harmonic Domain Models for Accurate Representation of Harmonics Dynamics”. In: *IEEE Transactions on Power Delivery* 31.6 (2016), pp. 2562–2564. DOI: 10.1109/TPWRD.2016.2568744.

[56] J.J. Rico, M. Madrigal, and E. Acha. “Dynamic harmonic evolution using the extended harmonic domain”. In: *IEEE Transactions on Power Delivery* 18.2 (2003), pp. 587–594. DOI: 10.1109/TPWRD.2003.809731.

[57] Uriel Vargas and Abner Ramirez. “Extended Harmonic Domain Model of a Wind Turbine Generator for Harmonic Transient Analysis”. In: *IEEE Transactions on Power Delivery* 31.3 (2016), pp. 1360–1368. DOI: 10.1109/TPWRD.2015.2499701.

[58] Norman M Wereley. “Analysis and control of linear periodically time varying systems”. dissertation. Massachusetts Institute of Technology, 1991. URL: https://dspace.mit.edu/handle/1721.1/13761.

[59] JunBum Kwon et al. “Harmonic Interaction Analysis in a Grid-Connected Converter Using Harmonic State-Space (HSS) Modeling”. In: *IEEE Transactions on Power Electronics* 32.9 (2017), pp. 6823–6835. DOI: 10.1109/TPEL.2016.2625802.

[60] JunBum Kwon et al. “Frequency-Domain Modeling and Simulation of DC Power Electronic Systems Using Harmonic State Space Method”. In: *IEEE Transactions on Power Electronics* 32.2 (2017), pp. 1044–1055. DOI: 10.1109/TPEL.2016.2544279.

[61] Jun Bum Kwon et al. “Harmonic Instability Analysis of a Single-Phase Grid-Connected Converter Using a Harmonic State-Space Modeling Method”. In: *IEEE Transactions on Industry Applications* 52.5 (2016), pp. 4188–4200. DOI: 10.1109/TIA.2016.2581154.

[62] Jordan Rel C. Orillaza and Alan R. Wood. “Harmonic State-Space Model of a Controlled TCR”. In: *IEEE Transactions on Power Delivery* 28.1 (2013), pp. 197–205. DOI: 10.1109/TPWRD.2012.2215926.

[63] Jordan Rel Cajudo Orillaza. “Harmonic State Space Model of Three Phase Thyristor Controlled Reactor”. dissertation. University of Canterbury, 2012. URL: https://ir.canterbury.ac.nz/handle/10092/6634.

[64] Valerio Salis et al. “Stability Assessment of Power-Converter-Based AC systems by LTP Theory: Eigenvalue Analysis and Harmonic Impedance Estimation”. In: *IEEE Journal of Emerging and Selected Topics in Power Electronics* 5.4 (2017), pp. 1513–1525. DOI: 10.1109/JESTPE.2017.2714026.

[65] Valerio Salis et al. “Stability Boundary Analysis in Single-Phase Grid-Connected Inverters With PLL by LTP Theory”. In: *IEEE Transactions on Power Electronics* 33.5 (2018), pp. 4023–4036. DOI: 10.1109/TPEL.2017.2714860.

[66] Valerio Salis et al. “Stability Assessment of High-Bandwidth DC Voltage Controllers in Single-Phase Active Front Ends: LTI Versus LTP Models”. In: *IEEE Journal of Emerging and Selected Topics in Power Electronics* 6.4 (2018), pp. 2147–2158. DOI: 10.1109/JESTPE.2018.2810282.

[67] Chen Zhang et al. “Harmonic Transfer-Function-Based Impedance Modeling of a Three-Phase VSC for Asymmetric AC Grid Stability Analysis”. In: *IEEE Transactions on Power Electronics* 34.12 (2019), pp. 12552–12566. DOI: 10.1109/TPEL.2019.2909576.

[68] Yicheng Liao et al. “Complex-Valued Multifrequency Admittance Model of Three-Phase VSCs in Unbalanced Grids”. In: *IEEE Journal of Emerging and Selected Topics in Power Electronics* 8.2 (2020), pp. 1934–1946. DOI: 10.1109/JESTPE.2019.2963004.

[69] Yicheng Liao and Xiongfei Wang. “Small-Signal Modeling of AC Power Electronic Systems: Critical Review and Unified Modeling”. In: *IEEE Open Journal of Power Electronics* 2 (2021), pp. 424–439. DOI: 10.1109/OJPEL.2021.3104522.

[70] Heng Nian et al. “Sequences Domain Impedance Modeling of Three-Phase Grid-Connected Converter Using Harmonic Transfer Matrices”. In: *IEEE Transactions on Energy Conversion* 33.2 (2018), pp. 627–638. DOI: 10.1109/TEC.2017.2761791.

[71] Shahil Shah et al. “Large-Signal Impedance-Based Modeling and Mitigation of Resonance of Converter-Grid Systems”. In: *IEEE Transactions on Sustainable Energy* 10.3 (2019), pp. 1439–1449. DOI: 10.1109/TSTE.2019.2903478.

[72] Piet Vanassche, Georges Gielen, and Willy M Sansen. *Systematic modeling and analysis of telecom frontends and their building blocks*. Vol. 842. Springer Science Business Media, 2006.

[73] Yajun Ma et al. “Stability analysis of modular multilevel converter based on harmonic state-space theory”. In: *IET Power Electronics* 12.15 (2019), pp. 3987–3997.

[74] Philippe De Rua, Özgür Can Sakinci, and Jef Beerten. “Comparative Study of Dynamic Phasor and Harmonic State-Space Modeling for Small-Signal Stability Analysis”. In: *Electric Power Systems Research* 189 (2020), p. 106626. ISSN: 0378-7796. DOI: doi.org/10.1016/j.epsr.2020.106626.

[75] Salvatore D'Arco, Jon Are Suul, and Olav Bjarte Fosso. "Automatic Tuning of Cascaded Controllers for Power Converters Using Eigenvalue Parametric Sensitivities". In: *IEEE Transactions on Industry Applications* 51.2 (2015), pp. 1743–1753. DOI: 10.1109/TIA.2014.2354732.

[76] Ashwin Venkatraman et al. "Improving Dynamic Performance of Low-Inertia Systems Through Eigensensitivity Optimization". In: *IEEE Transactions on Power Systems* 36.5 (2021), pp. 4075–4088. DOI: 10.1109/TPWRS.2021.3062974.

[77] Jenny Z. Zhou et al. "Impact of Short-Circuit Ratio and Phase-Locked-Loop Parameters on the Small-Signal Behavior of a VSC-HVDC Converter". In: *IEEE Transactions on Power Delivery* 29.5 (2014), pp. 2287–2296. DOI: 10.1109/TPWRD.2014.2330518.

[78] Uros Markovic et al. "Understanding Small-Signal Stability of Low-Inertia Systems". In: *IEEE Transactions on Power Systems* 36.5 (2021), pp. 3997–4017. DOI: 10.1109/TPWRS.2021.3061434.

[79] R. David Middlebrook. "Input filter considerations in design and application of switching regulators". In: 1976.

[80] Mohamed Belkhayat. "Stability criteria for AC power systems with regulated loads". dissertation. Purdue University, 1997. URL: https://docs.lib.purdue.edu/dissertations/AAI9821703/.

[81] A. G. J. MAcFARLANE and I. POSTLETHWAITE. "The generalized Nyquist stability criterion and multivariable root loci". In: *International Journal of Control* 25.1 (1977), pp. 81–127. DOI: 10.1080/00207177708922217.

[82] Lennart Harnefors et al. "Passivity-Based Stability Assessment of Grid-Connected VSCs—An Overview". In: *IEEE Journal of Emerging and Selected Topics in Power Electronics* 4.1 (2016), pp. 116–125. DOI: 10.1109/JESTPE.2015.2490549.

[83] Lennart Harnefors et al. "VSC Input-Admittance Modeling and Analysis Above the Nyquist Frequency for Passivity-Based Stability Assessment". In: *IEEE Transactions on Industrial Electronics* 64.8 (2017), pp. 6362–6370. DOI: 10.1109/TIE.2017.2677353.

[84] Yicheng Liao and Xiongfei Wang. "Impedance-Based Stability Analysis for Interconnected Converter Systems With Open-Loop RHP Poles". In: *IEEE Transactions on Power Electronics* 35.4 (2020), pp. 4388–4397. DOI: 10.1109/TPEL.2019.2939636.

[85] Bo Wen et al. "Inverse Nyquist Stability Criterion for Grid-Tied Inverters". In: *IEEE Transactions on Power Electronics* 32.2 (2017), pp. 1548–1556. DOI: 10.1109/TPEL.2016.2545871.

[86] Xiongfei Wang, Frede Blaabjerg, and Poh Chiang Loh. "An impedance-based stability analysis method for paralleled voltage source converters". In: *2014 International Power Electronics Conference (IPEC-Hiroshima 2014 - ECCE ASIA)*. 2014, pp. 1529–1535. DOI: 10.1109/IPEC.2014.6869788.

[87] Lucia Beloqui Larumbe et al. "Impedance Modeling for Three-Phase Inverters With Double Synchronous Reference Frame Current Controller in the Presence of Imbalance". In: *IEEE Transactions on Power Electronics* 37.2 (2022), pp. 1461–1475. DOI: 10.1109/TPEL.2021.3107045.

[88] Heng Wu, Xiongfei Wang, and Łukasz Hubert Kocewiak. "Impedance-Based Stability Analysis of Voltage-Controlled MMCs Feeding Linear AC Systems". In: *IEEE Journal of Emerging and Selected Topics in Power Electronics* 8.4 (2020), pp. 4060–4074. DOI: 10.1109/JESTPE.2019.2911654.

[89] Valerio Salis et al. "Experimental Validation of Harmonic Impedance Measurement and LTP Nyquist Criterion for Stability Analysis in Power Converter Networks". In: *IEEE Transactions on Power Electronics* 34.8 (2019), pp. 7972–7982. DOI: 10.1109/TPEL.2018.2880935.

[90] Barend Julius Bentvelsen. "Modal analysis of structures in time-periodic elastic state". PhD thesis. Sorbonne Université, 2018. URL: https://tel.archives-ouvertes.fr/tel-03461286.

[91] Yang Han et al. "Floquet-Theory-Based Small-Signal Stability Analysis of Single-Phase Asymmetric Multilevel Inverters With SRF Voltage Control". In: *IEEE Transactions on Power Electronics* 35.3 (2020), pp. 3221–3241. DOI: 10.1109/TPEL.2019.2930326.

[92] Pankaj D. Achlerkar and Bijaya Ketan Panigrahi. "New Perspectives on Stability of Decoupled Double Synchronous Reference Frame PLL". In: *IEEE Transactions on Power Electronics* 37.1 (2022), pp. 285–302. DOI: 10.1109/TPEL.2021.3099162.

[93] Yelun Peng et al. "Modeling and Stability Analysis of Inverter-Based Microgrid Under Harmonic Conditions". In: *IEEE Transactions on Smart Grid* 11.2 (2020), pp. 1330–1342. DOI: 10.1109/TSG.2019.2936041.

[94] Jun Zhou, Tomomichi Hagiwara, and Mituhiko Araki. "Spectral characteristics and eigenvalues computation of the harmonic state operators in continuous-time periodic systems". In: *Systems Control Letters* 53.2 (2004), pp. 141–155. ISSN: 0167-6911. DOI: doi.org/10.1016/j.sysconle.2004.03.002.

[95] Arnaud Lazarus and Olivier Thomas. "A harmonic-based method for computing the stability of periodic solutions of dynamical systems". In: *Comptes Rendus Mécanique* 338.9 (2010), pp. 510–517. ISSN: 1631-0721. DOI: doi.org/10.1016/j.crme.2010.07.020.

[96] Task Force on Harrnonics Modeling and Simulation. "Modeling and simulation of the propagation of harmonics in electric power networks. I. Concepts, models, and simulation techniques". In: *IEEE Transactions on Power Delivery* 11.1 (1996), pp. 452–465. DOI: 10.1109/61.484130.

[97] Wilsun Xu et al. "Harmonic resonance mode analysis". In: *IEEE Transactions on Power Delivery* 20.2 (2005), pp. 1182–1190. DOI: 10.1109/TPWRD.2004.834856.

[98] Zhenyu Huang, Yu Cui, and Wilsun Xu. "Application of Modal Sensitivity for Power System Harmonic Resonance Analysis". In: *IEEE Transactions on Power Systems* 22.1 (2007), pp. 222–231. DOI: 10.1109/TPWRS.2006.883678.

[99] Yu Cui and Xiaoyu Wang. "Modal Frequency Sensitivity for Power System Harmonic Resonance Analysis". In: *IEEE Transactions on Power Delivery* 27.2 (2012), pp. 1010–1017. DOI: 10.1109/TPWRD.2012.2185520.

[100] Zhaoyang Li et al. “Probabilistic Harmonic Resonance Assessment Considering Power System Uncertainties”. In: *IEEE Transactions on Power Delivery* 33.6 (2018), pp. 2989–2998. DOI: 10.1109/TPWRD.2018.2846608.

[101] Lucheng Hong et al. “Harmonic Resonance Investigation of a Multi-Inverter Grid-Connected System Using Resonance Modal Analysis”. In: *IEEE Transactions on Power Delivery* 34.1 (2019), pp. 63–72. DOI: 10.1109/TPWRD.2018.2877966.

[102] Esmaeil Ebrahimzadeh et al. “Bus Participation Factor Analysis for Harmonic Instability in Power Electronics Based Power Systems”. In: *IEEE Transactions on Power Electronics* 33.12 (2018), pp. 10341–10351. DOI: 10.1109/TPEL.2018.2803846.

[103] Jie Shen. “Modeling methodologies for analysis and synthesis of controls and modulation schemes for high-power converters with low pulse ratios”. dissertation. RWTH Aachen University, 2013.

[104] Srinivas Ponnaluri. “Generalized design, analysis and control of grid side converters with integrated UPS or Islanding functionality”. dissertation. RWTH Aachen University, 2006.

[105] D.H. Brandwood. “A complex gradient operator and its application in adaptive array theory”. In: *IEE Proceedings H (Microwaves, Optics and Antennas)* 130 (1983), pp. 11–16. ISSN: 2053-7972. DOI: 10.1049/ip-h-1.1983.0004.

[106] Peng Xiao, Keith A. Corzine, and Ganesh Kumar Venayagamoorthy. “Multiple Reference Frame-Based Control of Three-Phase PWM Boost Rectifiers under Unbalanced and Distorted Input Conditions”. In: *IEEE Transactions on Power Electronics* 23.4 (2008), pp. 2006–2017. DOI: 10.1109/TPEL.2008.925205.

[107] P. Rodríguez et al. “New positive-sequence voltage detector for grid synchronization of power converters under faulty grid conditions”. In: *2006 37th IEEE Power Electronics Specialists Conference*. 2006, pp. 1–7. DOI: 10.1109/pesc.2006.1712059.

[108] Hirofumi Akagi, Edson Hirokazu Watanabe, and Mauricio Aredes. *Instantaneous power theory and applications to power conditioning*. John Wiley & Sons, 2017.

[109] Claudio Alberto Busada et al. “Current Controller Based on Reduced Order Generalized Integrators for Distributed Generation Systems”. In: *IEEE Transactions on Industrial Electronics* 59.7 (2012), pp. 2898–2909. DOI: 10.1109/TIE.2011.2167892.

[110] Izudin Džafić, Rabih A. Jabr, and Tarik Hrnjić. “High Performance Distribution Network Power Flow Using Wirtinger Calculus”. In: *IEEE Transactions on Smart Grid* 10.3 (2019), pp. 3311–3319. DOI: 10.1109/TSG.2018.2824018.

[111] Stefan Preitl and Radu-Emil Precup. “An extension of tuning relations after symmetrical optimum method for PI and PID controllers”. In: *Automatica* 35.10 (1999), pp. 1731–1736. ISSN: 0005-1098. DOI: https://doi.org/10.1016/S0005-1098(99)00091-6.

[112] Floyd M Gardner. *Phaselock techniques*. John Wiley & Sons, 2005.

[113] Joachim Holtz and Nikolaos Oikonomou. “Fast Dynamic Control of Medium Voltage Drives Operating at Very Low Switching Frequency—An Overview”. In: *IEEE Transactions on Industrial Electronics* 55.3 (2008), pp. 1005–1013. DOI: 10.1109/TIE.2007.908540.

[114] Maren Kuschke and Kai Strunz. “Energy-Efficient Dynamic Drive Control for Wind Power Conversion With PMSG: Modeling and Application of Transfer Function Analysis”. In: *IEEE Journal of Emerging and Selected Topics in Power Electronics* 2.1 (2014), pp. 35–46. DOI: 10.1109/JESTPE.2013.2293632.

[115] Peter Teske et al. “Power Hardware-in-the-Loop Testbench for Grid-Following and Grid-Forming Inverter Prototyping”. In: *2022 IEEE 13th International Symposium on Power Electronics for Distributed Generation Systems (PEDG)*. 2022, pp. 1–7.

[116] Mads Graungaard Taul et al. “Current Reference Generation Based on Next-Generation Grid Code Requirements of Grid-Tied Converters During Asymmetrical Faults”. In: *IEEE Journal of Emerging and Selected Topics in Power Electronics* 8.4 (2020), pp. 3784–3797. DOI: 10.1109/JESTPE.2019.2931726.

[117] Kazi Nazmul Hasan, Robin Preece, and Jovica V. Milanović. “Priority Ranking of Critical Uncertainties Affecting Small-Disturbance Stability Using Sensitivity Analysis Techniques”. In: *IEEE Transactions on Power Systems* 32.4 (2017), pp. 2629–2639. DOI: 10.1109/TPWRS.2016.2618347.

[118] Steven L. Brunton, Joshua L. Proctor, and J. Nathan Kutz. “Discovering governing equations from data by sparse identification of nonlinear dynamical systems”. In: *Proceedings of the National Academy of Sciences* 113.15 (2016), pp. 3932–3937. DOI: 10.1073/pnas.1517384113.

List of Figures

List of Tables

A

Wirtinger Calculus

Let $z = x + jy$, for x and y real, denote a complex number and let

$$f(z) = F(x, y) = f_{\text{Re}}(x, y) + 1j \cdot f_{\text{Im}}(x, y)$$

be a general complex-valued function of the complex number z. In standard complex analysis courses, $f(z)$ is defined as differentiable/holomorphic when the limit

$$\frac{\partial f}{\partial z} = \lim_{\Delta z \to 0} \frac{f(z + \Delta z) - f(z)}{\Delta z}$$

exists for Δz approaches zero from any directions.

Setting

$$\Delta z = \Delta x + j\Delta y$$

two possible paths for $\Delta z \to 0$ are considered. The first path goes in the horizontal direction with $\Delta y = 0$ and $\Delta x \to 0$ yielding

$$\begin{aligned}
\frac{\partial f}{\partial z} &= \lim_{\Delta x \to 0} \frac{F(x + \Delta x, y) - F(x, y)}{\Delta x} \\
&= \lim_{\Delta x \to 0} \left\{ \frac{f_{\text{Re}}(x + \Delta x, y) - f_{\text{Re}}(x, y)}{\Delta x} + j \frac{f_{\text{Im}}(x + \Delta x, y) - f_{\text{Im}}(x, y)}{\Delta x} \right\}. \\
&= \frac{\partial f_{\text{Re}}(x, y)}{\partial x} + j \frac{\partial f_{\text{Im}}(x, y)}{\partial x}
\end{aligned} \tag{A.1}$$

The second path goes in the vertical direction with $\Delta x = 0$ and $\Delta y \to 0$ yielding

$$\begin{aligned}
\frac{\partial f}{\partial z} &= \lim_{\Delta y \to 0} \frac{F(x, y + \Delta y) - F(x, y)}{j\Delta y} \\
&= \lim_{\Delta y \to 0} \left\{ \frac{f_{\text{Re}}(x, y + \Delta y) - f_{\text{Re}}(x, y)}{j\Delta y} + j \frac{f_{\text{Im}}(x, y + \Delta y) - f_{\text{Im}}(x, y)}{j\Delta y} \right\}. \\
&= \frac{\partial f_{\text{Re}}(x, y)}{j\partial y} + \frac{\partial f_{\text{Im}}(x, y)}{\partial y}
\end{aligned} \tag{A.2}$$

When $f(z)$ is differentiable/holomorphic, both expressions (Eq. A.1 and Eq. A.2) should be the same, namely

$$\begin{aligned}\frac{\partial f_{\mathrm{Re}}(x,y)}{\partial x} &= \frac{\partial f_{\mathrm{Im}}(x,y)}{\partial y}\\ \frac{\partial f_{\mathrm{Re}}(x,y)}{\partial y} &= -\frac{\partial f_{\mathrm{Im}}(x,y)}{\partial x}\end{aligned}$$

which is the Cauchy-Riemann condition. It is proved that if the partial derivatives of f_{Re} and f_{Im} with respect to x and y are continuous, the Cauchy-Riemann condition are sufficient for $f(z)$ being holomorphic.

As presented in Chapter 3, the complex conjugate operator, magnitude calculation function, real and imaginary extraction operator do not satisfy the Cauchy-Riemann condition. The complex partial derivative defined above must be extended. To this end, the total differential of the bivariate function $F(x,y)$ is first deduced

$$\begin{aligned}\Delta F &= \frac{\partial F(x,y)}{\partial x}\Delta x + \frac{\partial F(x,y)}{\partial y}\Delta y\\ &= \frac{\partial f_{\mathrm{Re}}(x,y)}{\partial x}\Delta x + j\frac{\partial f_{\mathrm{Im}}(x,y)}{\partial x}\Delta x + \frac{\partial f_{\mathrm{Re}}(x,y)}{\partial y}\Delta y + j\frac{\partial f_{\mathrm{Im}}(x,y)}{\partial y}\Delta y\end{aligned}.$$

Inserting the relation

$$\begin{aligned}\Delta x &= \frac{1}{2}(\Delta z + \Delta z^*)\\ \Delta y &= \frac{1}{2j}(\Delta z - \Delta z^*)\end{aligned}$$

yields

$$\begin{aligned}\Delta F &= \frac{1}{2}\left[\frac{\partial}{\partial x}(f_{\mathrm{Re}}(x,y) + jf_{\mathrm{Im}}(x,y)) - j\frac{\partial}{\partial y}(f_{\mathrm{Re}}(x,y) + jf_{\mathrm{Im}}(x,y))\right]\Delta z\\ &+ \frac{1}{2}\left[\frac{\partial}{\partial x}(f_{\mathrm{Re}}(x,y) + jf_{\mathrm{Im}}(x,y)) + j\frac{\partial}{\partial y}(f_{\mathrm{Re}}(x,y) + jf_{\mathrm{Im}}(x,y))\right]\Delta z^*.\\ &= \frac{1}{2}\left(\frac{\partial}{\partial x} - j\frac{\partial}{\partial y}\right)F(x,y)\,\Delta z + \frac{1}{2}\left(\frac{\partial}{\partial x} + j\frac{\partial}{\partial y}\right)F(x,y)\,\Delta z^*\end{aligned}$$

The Wirtinger derivatives are introduced by defining

$$\begin{aligned}\frac{\partial}{\partial z} &\triangleq \frac{1}{2}\left(\frac{\partial}{\partial x} - j\frac{\partial}{\partial y}\right)\\ \frac{\partial}{\partial z^*} &\triangleq \frac{1}{2}\left(\frac{\partial}{\partial x} + j\frac{\partial}{\partial y}\right)\end{aligned} \tag{A.3}$$

then the differential of the complex function $f(z)$ can be written as

$$\Delta f = \frac{\partial f(z)}{\partial z}\Delta z + \frac{\partial f(z)}{\partial z^*}\Delta z^*.$$

It can be immediately derived from Eq. (A.3)

$$\frac{\partial}{\partial z}z^* = \frac{\partial}{\partial z^*}z = 0$$

which means that z^* can be regarded as a constant value when differentiating $f(z)$ with respect to z, namely calculating $\frac{\partial f(z)}{\partial z}$. The same goes for $\frac{\partial f(z)}{\partial z^*}$.

B

Small-Signal Model of Induction machine

For the sake of consistency, stator and rotor currents of the induction machine instead of fluxes are used as state variables for the modeling of induction machines. Transform rotor currents into the stationary reference frame of the stator, dynamics of the induction machine can be described by the state-space equation

$$\begin{aligned} v_{\alpha\beta s} &= r_s i_{\alpha\beta s} + L_s \tfrac{d}{dt} i_{\alpha\beta s} + L_m \tfrac{d}{dt} i_{\alpha\beta r} \\ v_{\alpha\beta r} &= r_r i_{\alpha\beta r} + L_m \tfrac{d}{dt} i_{\alpha\beta s} + L_r \tfrac{d}{dt} i_r - j\omega_r \left(L_m i_{\alpha\beta s} + L_r i_r \right) \end{aligned} \tag{B.1}$$

where L_s and r_s are the stator inductance and resistance. L_r and r_r are the rotor inductance and resistance. L_m denotes the linkage inductance. ω_r is the electrical speed of the rotor. $v_{\alpha\beta s}$ and $i_{\alpha\beta s}$ are the stator voltage and current. $i_{\alpha\beta r}$ is the rotor current. All rotor variables are referred to the stator windings.

The electromagnetic torque is given by

$$T_{el} = \frac{3}{2} n_p L_m \mathrm{Im} \left\{ i_{\alpha\beta s} \cdot i^*_{\alpha\beta r} \right\} \tag{B.2}$$

where n_p is the pole pair number. Let T_L denote the load torque, the swing dynamic of the induction machine is given by

$$\dot{\omega}_r = \frac{\left(T_{el} - T_{load} \right) n_p}{J_{IM}} \tag{B.3}$$

where J_{IM} is the inertia constant of the induction machine.

By linearizing Eq. (B.1) - Eq. (B.3) around steady-state operation trajectories, time-periodic small-signal model of the induction machine can be obtained

$$\begin{aligned}
&\Delta\dot{\boldsymbol{x}}_{IM}(t) = \boldsymbol{A}_{IM}(t)\,\Delta\boldsymbol{x}_{IM}(t) + \boldsymbol{B}_{IM}(t)\begin{bmatrix}\Delta v_{\alpha\beta s}(t)\\ \Delta v^{*}_{\alpha\beta s}(t)\end{bmatrix}\\
&\underbrace{\begin{bmatrix}\Delta i_{\alpha\beta s}(t)\\ \Delta i^{*}_{\alpha\beta s}(t)\end{bmatrix}}_{\Delta\boldsymbol{y}_{IM}(t)} = \underbrace{\begin{bmatrix}1 & 0 & 0 & 0 & 0\\ 0 & 1 & 0 & 0 & 0\end{bmatrix}}_{\boldsymbol{C}_{IM}(t)}\Delta\boldsymbol{x}_{IM}(t)
\end{aligned} \tag{B.4}$$

where the stator current is selected as output $\boldsymbol{y}_{IM}$. The state vector is given by

$$\Delta\boldsymbol{x}_{IM}(t) = \left[\Delta i_{\alpha\beta s}(t)\,,\ \Delta i^{*}_{\alpha\beta s}(t)\,,\ \Delta i_{\alpha\beta r}(t)\,,\ \Delta i^{*}_{\alpha\beta r}(t)\,,\ \omega_r\right]^T$$